FABRICATION OF 2-DIMENSIONAL MOLYBDENUM DISULFIDE (MOS_2) AND TUNGSTEN DISULFIDE (WS_2) BASED MATERIALS FOR FIELD EMISSION APPLICATIONS

TAMIE LOH AI-JIA

(B. Eng. (Hons.) National University of Singapore)

A THESIS SUBMITTED

FOR THE DEGREE OF DOCTOR OF PHILOSOPHY

DEPARTMENT OF MATERIALS SCIENCE & ENGINEERING

NATIONAL UNIVERSITY OF SINGAPORE

2016

DECLARATION

I hereby declare that this thesis is my original work and it has been written by me in its entirety. I have duly acknowledged all the sources of information which have been used in the thesis.

This thesis has also not been submitted for any degree in any university previously.

Tamie Loh Ai Jia

April 2016

ACKNOWLEDGEMENTS

Pursuing a Ph.D. for the past four years has been, for me, both a frustrating and enjoyable experience. There have been many hardships along the way, and I could not possibly have come this far without the support of the all the people I have met on my long journey. Though a mere expression of gratitude will never be enough to repay them, I still wish give my thanks to all those who have helped me in one way or another.

First, I would like to express my deepest gratitude to my supervisor, Dr. Daniel Chua, who has been the single most important influence in my pursuit of research and innovation. He offered me the life-changing opportunity to explore my interest in research back when I was just a second year undergraduate in NUS. As a Ph.D. student within his group, he not only provided me with invaluable guidance and counsel, but also gave me the freedom to pursue independent work and always encouraged me to learn new skills to add to my repertoire. I thank him for his patience and understanding during the rough periods when setbacks keep piling on one after another. I am also grateful to him for the numerous overseas opportunities that he has given me, through which I have gained many priceless experiences.

Special thanks are also given to Prof. Andrew Wee and Prof Sow Chong Haur from the Department of Physics, as well as to Prof. Gong Hao for their generosity in allowing me to use their equipment, which have been instrumental in my research.

I would like to express my sincerest thanks to Mr. Suradi from the Physics workshop for his assistance in assembling key equipment components. I would also like to thank Mr. Chen Gin Seng from the Department of Physics for his support and guidance. Without his help to fix broken equipment, my projects would have been

impossible to complete. In addition, I would like to thank Mr. Wong How Kwong from the Department of Physics for his assistance in managing my lab in Science faculty.

My sincere thanks goes to the Department of Materials Science & Engineering for providing an ideal environment in which I could conduct research freely and safely. In particular, I would like to thank Mr. Henche Kuan, Ms. He Jian, Ms. Agnes Lim, Ms. Serene Chooi, Mr. Chan Yew Weng, Mr. Chen Qun, Mr. Roger Lee, and Ms. Yang Fengzhen for their considerable help and guidance throughout all these years.

My life as a graduate student would certainly be less fulfilling if it were not for my wonderful group of colleagues and friends. I am deeply grateful to Dr. Chen Ting and Dr. Wang Hongyu, both of whom mentored me when I first began delving into research. I am just as grateful Dr. Angel Koh for her guidance and patience in teaching me how to operate the pulsed laser deposition. I would also like to thank Dr. Pham Kien Cuong for joining me in many exceedingly useful discussions where we bounced ideas off each other. Special thanks goes to Mr. Vincent Lee for his generous assistance and for lending an ear whenever I feel down and/or frustrated. Further thanks are given to Mr. Royston Tan, Dr. Tang Zhe and Dr. Hu Yan, all of whom have helped me in one way or another during my difficult journey.

Last but not least, I would like to express my heartfelt gratitude to my family, especially my parents, for their unconditional love and support in my research endeavour.

Tamie Loh

Singapore, May 2016

Table of Contents

Summary

The isolation of graphene and discovery of its remarkable properties have led to renewed interest in inorganic two-dimensional (2D) materials with unique electronic and optical attributes. Of these, MoS_2 and WS_2 are among the most widely studied for their potential applications in nanoscale electronics. However, controlled fabrication and understanding of the growth mechanism of 2D MoS_2 and WS_2 need to be established before these emerging materials can be realized for practical applications. While techniques such as chemical vapour deposition (CVD) and exfoliation have been extensively investigated, the controlled synthesis of highly crystalline MoS_2 and WS_2 atomic layers is still a challenge, and studies on solid-state formation of MoS_2 and WS_2 through physical vapour deposition (PVD) techniques remain severely limited.

The aims of this project are to understand the growth mechanism of MoS_2 and WS_2 using PVD techniques such as pulsed laser deposition (PLD) and sputtering, and to fabricate MoS_2- and WS_2-based field emitters. To achieve these objectives, the first chapter details investigations on the growth of few-layer MoS_2 on metal substrates by PLD and the effects of parameters such as laser energy, deposition time and cooling rate on the crystalline quality of the resulting film. The growth process of MoS_2 on metal substrates was also elucidated as occurring through conventional epitaxy. With the knowledge acquired from this experiments, MoS_2-coated metal nanocones were fabricated with enhanced field emission properties as compared to pristine nanocones. This was attributed to a reduction in the effective barrier to field emission due to the formation of a low Schottky barrier and charge transfer from the metal to MoS_2.

In the second chapter, the use of PLD was extended to fabricate WS_2 on metal substrates to produce films consisting of a mixture of 1T- and 2H-WS_2. Factors

influencing the phasic composition of the film such as growth temperature, metal buffer thickness, deposition time, laser energy and type of metal used were also investigated. Briefly, the hybrid 1T-2H structure was formed only on the noble metals Ag and Au, and is believed to be induced by electron doping of the WS_2 lattice. The 1T-phase was also observed to completely convert to 2H-WS_2 after annealing. In the final part of this chapter, WS_2-coated Ag nanocones were fabricated for field emission purposes. It was observed that the as-fabricated WS_2-coated Ag nanocones gave enhanced field emission properties over that of bare nanocones and annealed samples. This due to the formation of low resistance contacts between Ag and the metallic 1T-phase, as well as a low Schottky barrier at the interface between 1T- and 2H-WS_2, both of which contributed to lowering of the effective barrier height for electron emission.

In the final chapter, ultrathin MoS_2 and WS_2 were grown as an encapsulating shell on carbon nanotubes (CNT) for field emission purposes. In both cases, the initial shell was composed of M oxides (M = Mo or W) that converted to MS_2 nanoflakes with increasing deposition times. Both the oxide and MS_2 shell led to improved field emission performance over that of pristine CNTs. For the oxide coating, the lowering of the effective barrier height was primarily due to the formation of a Schottky barrier. For the MS_2 nanoflakes, it was mainly the high density of sharp tips acting as additional emission sites that led to high external field enhancement and thus decreased the potential barrier for electron emission.

Through the information gained from these experiments, MoS_2 and WS_2 growth from solid sources using PLD and sputtering were better understood and thus field emitters based on these materials can be optimized to achieve better performance.

List of Tables

List of Figures

List of Abbreviations

0D	Zero dimensional
1D	One dimensional
2D	Two dimensional
3D	Three dimensional
AFM	Atomic force microscopy
AR	Angle-resolved
CCD	Charge-coupled device
CNT	Carbon nanotube
CVD	Chemical vapour deposition
DC	Direct current
DFT	Density functional theory
EDX	Energy dispersive spectroscopy
FE	Field emission
FEG	Field emission gun
FET	Field effect transistor
F-N	Fowler-Nordheim
FWHM	Full width half maximum
HER	Hydrogen evolution rection
ITO	Indium tin oxide
LIBS	Laser induced breakdown spectroscopy
LTE	Local thermodynamic equilibrium
min	Minutes
MW	Multi-walled

NIST	National Institute of Standards and Technology
PECVD	Plasma Enhanced Chemical Vapour Deposition
PL	Photoluminescence
PLD	Pulsed laser deposition
PVD	Physical vapour deposition
RF	Radio frequency
RMS	Root mean square
rpm	Revolutions per minute
RF	Radio frequency
RSD	Relative standard deviation
s	Seconds
SEM	Scanning electron microscope
TEM	Transmission electron microscopy
TMD	Transition metal dichalcogenide
UHV	Ultra-high vacuum
VLS	Vapour-liquid-solid
VS	Vapour-solid
XPS	X-ray photoelectron spectroscopy
XRD	X-Ray diffraction

List of Publications

1. **Loh, T. A. J.**; Chua, D. H. C. Dual-functional Magnetic and Field Emission Properties of γ-Fe_2O_3 Coated Carbon Nanotubes Core-shell Structures. *ECS J. Solid State Science and Tech.* **2014**, 3, M11-M17.
2. **Loh, T. A. J.**; Chua, D. H. C. Pulsed Laser Fabricated Few-layer MoS_2 on Silver. *Chem. Phys. Lett.* **2014**, 610-611, 284-287.
3. **Loh, T. A. J.**; Chua, D. H. C. Growth Mechanism of Pulsed Laser Fabricated Few-layer MoS_2 on Metal Substrates. *ACS Appl. Mater. and Interfaces* **2014**, 6, 15966-15871.
4. **Loh, T. A. J.**; Chua, D. H. C.; Wee, A. T. S. One-step Synthesis of Few-layer WS_2 by Pulsed Laser Deposition, *Sci. Rep.* **2015**, 5, 18116.
5. **Loh, T. A. J**.; Chua, D. H. C. Origin of Hybrid 1T- and 2H-WS_2 Ultrathin Layers by Pulsed Laser Deposition, *J. Phys. Chem. C.* **2015**, 119, 27496–27504.
6. **Loh, T. A. J.**, Tanemura, M.; Chua, D. H. C. Ultrathin MoS_2 and WS_2 Layers on Silver Nanocones as Field Electron Emitters, *Appl. Phys. Lett.* **2016**, 109, 133102.
7. **Loh, T. A. J.**; Ooi, Y. J.; Chua, D. H. C. WS_2 Nano-petals and Nano-bristles Supported on Carbon Nanotubes for Field Emission Applications. **2016**, Under Revision.
8. **Loh, T. A. J.;** Chua, D. H. C.; Shankar, A.; Jagota, A. Insight into DNA-SWCNT hybrid structure via XPS surface analysis. **2016**, Under Revision.
9. Murawala*, A. P.; **Loh*, T. A. J.** and Chua, D. H. C. Synthesis of MoS_2 Nano-petal Forest Supported on Carbon Nanotubes for Enhanced Field Emission Performance. *J. Appl. Phys.* **2014**, 116, 114305.

10. Chen, T.; Pan, L.; **Loh, T. A. J.**; Chua, D. H. C.; Yao, Y.; Chen, Q.; Li, D.; Qin, W. and Sun, Z. Porous nitrogen-doped carbon microspheres as anode materials for lithium ion batteries. *Dalton Trans.* **2014**, 43, 14931-14935.
11. Lee, W. S. V.; Peng, E.; **Loh, T. A. J.**; X. Huang; Xue, J. M. Few-layers MoS_2 Anchored Graphene Aerogel Paper for Free-Standing Electrode Materials. *Nanoscale*, **2016**, 8, 8042-8047.

Conference Presentations:

1. Poster presentation *"X-Ray Photoelectron Spectroscopy Investigation of 0D, 1D and 2D Carbon-based Nanomaterials"* Carbon-based Nano-Materials and Devices, Hualien, Taiwan, 3^{rd} – 8^{th} November 2013.
2. Poster presentation "Pulsed Laser Fabricated Few-layer MoS_2 on Metal Substrates" 2015 Materials Research Society Spring Meeting, San Francisco, California, USA, 6^{th} – 10^{th} April 2015.

**These authors contributed equally to this work.*

Chapter 1

Introduction

Over the last few years, extensive efforts have been devoted to studying graphene analogues of layered inorganic materials such as MoS_2 and WS_2. In this chapter, the background and properties of MoS_2 and WS_2 are reviewed in section 1.1 and 1.2 respectively. Material fabrication methods are then discussed in section 1.3. The theory of field emission as well as the application of MoS_2 and WS_2 as potential field emitters are reviewed in Section 1.4. Finally, the motivations and objectives of this project are detailed in section 1.5.

1.1 MoS_2 and WS_2 Analogues of Graphene

Within the emerging class of ultrathin two-dimensional (2D) layered materials, graphene has undoubtedly attracted the most attention due to its remarkable mechanical and electronic properties.[1,2] However, the intrinsic limitations of graphene such as the lack of a bandgap necessary for efficient high performance field effect transistors (FET) and the difficulty in altering the band gap without negatively impacting its electrical properties has motivated research on other 2D materials. Of these, molybdenum disulfide (MoS_2) and tungsten disulfide (WS_2), from the family of layered transition metal dichalcogenides (TMD), have received the most interest. As a consequences of its easy availability in nature as molybdenite, MoS_2 been widely studied since the 1960s for applications in dry lubrication,[3] batteries,[4,5] as well as photocatalysis and photovoltaics[6,7]. It is only very recently that 2D ultrathin layers of both MoS_2 and WS_2

have generated interest for their promising semiconducting properties and potential applications in nanoelectronics and optoelectronics.

The layered structure of MoS_2 and WS_2 is formed by the stacking of three atomic layers of S-M-S atoms,[8] where M = Mo or W, as illustrated in Figure 1.1(a). The planar projection shows a perfect hexagonal lattice of S atoms, with each M atom coordinated to six S atoms in a trigonal prismatic geometry. Depending on the arrangement of the S atoms, two kinds of hexagonal S-M-S layers are possible: prismatic D_{3h}-MS_6 or octahedral O_h-MS_6.[9,10] Individual layers interact by weak van der Waals interactions and may be stacked in a variety of ways. For example, bulk MoS_2 and WS_2 naturally occur as a mixture of two stable polymorphs based on D_{3h}-MS_6 units: the hexagonal 2H-MS_2 and the rhombohedral modification 3R-MS_2. The 3R-polytype is less stable and thus transforms into the 2H-polytype upon heating. As the number of layers decreases to one however, there is no variety of stacking different layers. Thus, monolayer MoS_2 and WS_2 only have the two phases of 2H-MS_2 and 1T-MS_2 (octahedral O_h). These two phases exhibit different electronic structures, with 2H-MS_2 behaving as a semiconductor while the 1T-phase is metallic.[10] Theoretical calculations predict that the 2H-polytype is more thermodynamically stable, and hence the 1T-phase converts to the former upon heating via atomic plane gliding, which involves a transversal displacement of one of the S planes.[11] Due to this instability of the octahedral 1T-phase, it has not been found in nature. Figure 1.1(b) shows the schematics of the three different structural polytypes.

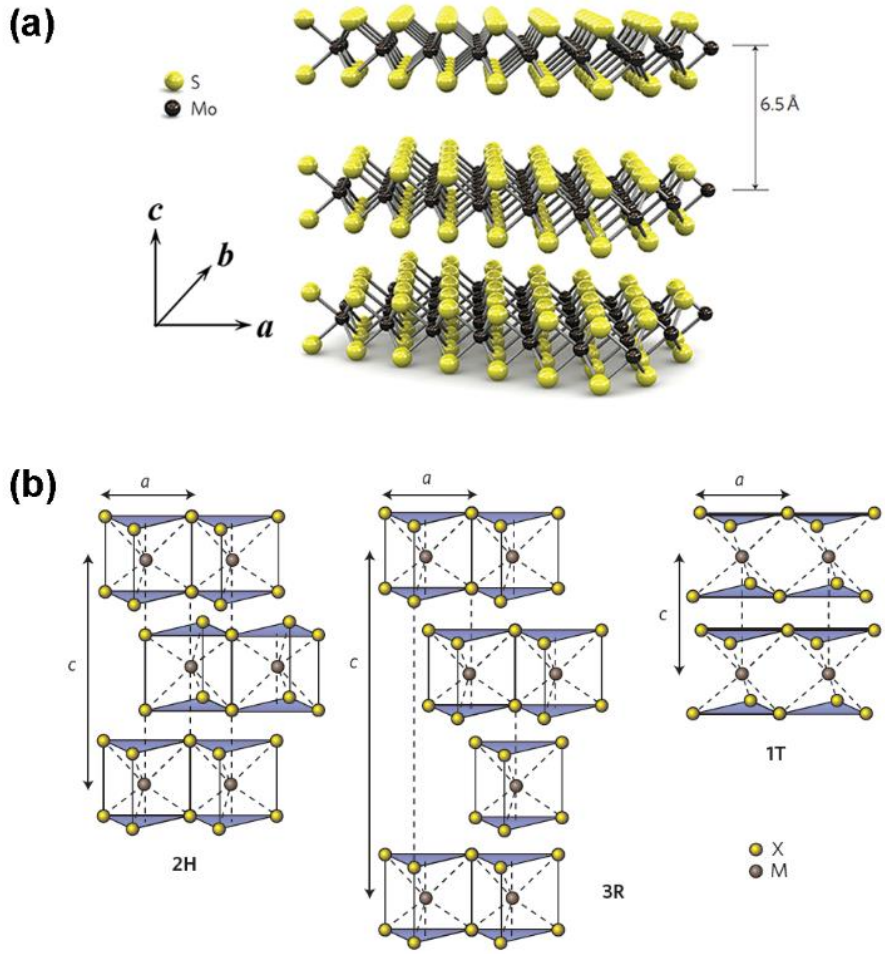

Figure 1.1: (a) Crystal structure of MoS_2. (b) Schematics of the 2H-, 3R- and 1T polytypes.[8]

1.2 Properties of 2D MoS_2 and WS_2

1.2.1 Band Structure

Unlike metallic graphene, MoS_2 and WS_2 are indirect band gap semiconductors with an energy gap of 1.2 eV and 1.4 eV respectively in bulk form.[8,12] When reduced to a monolayer, quantum confinement effects give rise to an indirect-to-direct transition such that single layer MoS_2 and WS_2 possess direct gaps of 1.9 eV and 2.0 eV respectively.[8] The band structures of bulk and monolayer MoS_2 and WS_2 calculated from first principles are shown in Figure 1.2. The valence band maximum is located at the Γ point, while the conduction band minimum is located almost halfway along the Γ-K direction, which constitutes the indirect band gap transition.[13] For MoS_2, density functional theory (DFT) calculations show that the conduction band states at the K-point are mainly due to localized d orbitals on the Mo atoms and are relatively unaffected by interlayer interaction. Thus when layer number decreases, the direct band gap at the K point only increases by about 0.05-0.1 eV.[14] However, the states near the Γ point on the conduction band are due to hybridization between p_z-orbitals of S atoms and the d-orbitals of Mo atoms, and are affected by interlayer interactions. Thus the bands at Γ are more affected by a decrease in layer number.[14] With decreasing layer number, the lowest conduction band (indirect) moves upward, increasing the overall band gap. In the monolayer, the indirect transition gap is larger than the direct transition gap, and the smallest band gap is thus the direct band gap at the K point of about 1.9 eV.

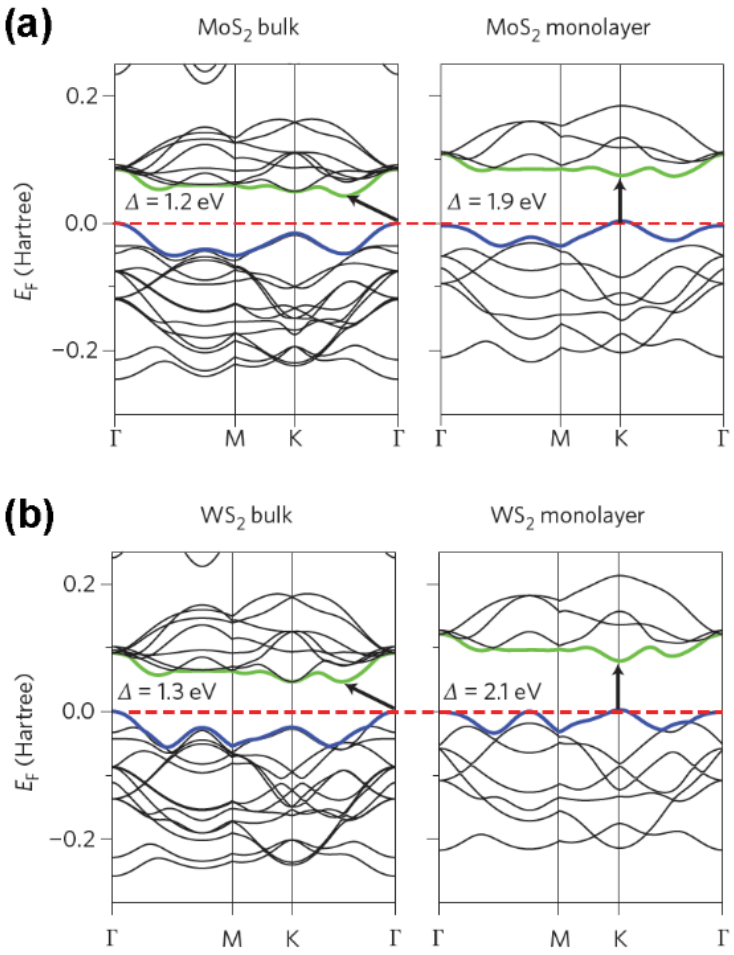

Figure 1.2: Band structures calculated from first-principles DFT for bulk and monolayer (a) MoS_2 and (b) WS_2. The dashed lines indicate the Fermi level. The arrows indicate the fundamental bandgap (direct or indirect). The blue and green curves represent the top of the valence band and bottom of the conduction band respectively.[8]

1.2.2 Electronic Properties

In 2D TMD layers, the mobility of carriers is affected by (i) acoustic and optical phonon scattering, (ii) Coulomb scattering at charged impurities, (iii) surface interface phonon scattering, and (iv) roughness scattering.[8] Carrier mobility is increasingly affected by phonon scattering with increasing temperature. At higher temperatures, the optical component dominates whereas at lower temperature it is the acoustic component that dominates.[15] Based on first principle calculations, the phonon-limited room-

temperature mobility of MoS_2 is predicted to be ~410 $cm^2\ V^{-1}\ s^{-1}$, with similar values expected for other single-layer TMDs. Coulomb scattering, which is caused by the presence of charged impurities within the TMD layers or on their surfaces, is the dominant scattering effect at low temperatures.[8] One way to screen the Coulomb scattering on charged impurities and thus enhance carrier mobilities is by dielectric engineering. For example, high-*k* dielectric HfO_2 was found to assist in improving the room temperature mobility of monolayer MoS_2 transistors from ~0.5–3 $cm^2\ V^{-1}\ s^{-1}$ in earlier reports[16] to ~200 $cm^2\ V^{-1}\ s^{-1}$ in more recent works[17]. For very thin materials such as 2D TMDs, the contribution from surface phonon scattering and roughness scattering can also be very significant. It is known that for graphene, Coulomb scattering is dominant over short-range and surface roughness scattering in the form of ripples.[18] Freestanding MoS_2 has been shown to have similar ripples[19] that may limit ballistic transport and thus reduce mobility.

The first implementation of a top-gated transistor based on monolayer MoS_2 was reported by Kis et al.[17]. The device demonstrated an excellent on/off current ratio of ~10^8 and a room-temperature mobility of >200 $cm^2\ V^{-1}\ s^{-1}$. Thin-film transistors made of MoS_2 from liquid exfoliation have similar electrical performance,[20] suggesting possibilities for flexible, transparent, 2D electronic applications. Theoretical simulations of transistor performance[21] have also shown that top-gated MoS_2 transistors with gate lengths of 15 nm could operate in the ballistic regime with an on-current as high as 1.6 mA μm^{-1} and a current on/off ratio of 1010. More recently, Radisavljevic et al.[22] demonstrated functional electronic circuits based on multiple 2D MoS_2 transistors capable of performing digital logic operations. Wang et al.[23] also reported the fabrication of complex integrated circuits built on bilayer MoS_2 such as an inverter, a logical NAND gate, static random access memory and five-stage ring oscillator.

Furthermore, ambipolar transport was demonstrated in a 10 nm-thick MoS_2 double-layer transistor[24] using an ionic liquid as the gate to reach extremely high carrier concentrations of 1×10^{14} cm^2. The ability to engineer n- and p-type transport in MoS_2 is immensely useful for applications in CMOS logic and p–n-junctions.

Although the electronic properties of WS_2 layers have been less extensively studied, theoretical models predict that among the semiconducting 2D TMDs.[21] WS_2 should have the highest mobility due to its reduced effective mass. Early reports on liquid-gated multilayer[25] and single-layer[26] WS_2 indicated a carrier mobility of 44 cm^2 V^{-1} s^{-1} for the material. Recently however, Ovchinnikov et al.[27] fabricated transistors based on monolayer and bilayer WS_2 that exhibited n-type behaviour with a high room-temperature on/off current ratio of $\sim 10^6$. The devices also demonstrated higher carrier mobilities of ~60 cm^2 V^{-1} s^{-1} single-layer WS_2 at room temperature that saturates at 140 cm^2 V^{-1} s^{-1} when the temperature drops to ~83 K.

1.2.3 Optical Properties

The evolution of the electronic structures of MoS_2 and WS_2 with decreasing thickness directly influence their optical properties. For both materials, the change from an indirect to direct bandgap and increase in bandgap energy is detected as changes in photoconductivity, absorption spectra and photoluminescence (PL).[12,13] One consequence of the indirect-to-direct transition is an increase in PL quantum yield from bulk to monolayer MoS_2 by a factor of 10^4, with even higher quantum yield for regions of the monolayer flake suspended over holes in the substrate. Single-layer WS_2 has also been reported to exhibit extraordinary room temperature PL from flake edges that surpasses all known 2D layered TMDs.[28] Single-layer MoS_2 and WS_2 sheets are

extremely thin and demonstrate high optical transparency (>90 %) in the visible light range.[29] This combination of high transparency, high conductivity and band gap tunability based on layer thickness makes 2D MoS_2 and WS_2 highly suitable for optoelectronic applications such as sensors,[30] phototransistors,[31] and organic light emitting devices (OLED)[32] for next-generation solid-state lighting panels and high-resolution displays.

1.2.4 Mechanical Properties

Castellanos-Gomez et al.[33] measured the elastic properties of freely suspended MoS_2 nanosheets, with thicknesses ranging from 5 to 25 layers by using an AFM tip. It was found that the average Young's modulus of the MoS_2 sheet is exceptionally high at 0.33 ± 0.07 TPa, which is comparable to that of graphene oxide and higher than the Young's modulus of bulk MoS_2 (0.24 TPa). Furthermore, the crystalline nanosheets could withstand elastic deformations of up to tens of nanometers without breaking. In another study,[34] monolayer MoS_2 was reported to have an effective Young's modulus of 270 ± 100 GPa, which was lower than that of multi-layers but higher than that of the bulk. Individual MoS_2 monolayers can also be deformed by up to 11% without fracturing, and be bent to a radius of curvature of 0.75 mm without degrading their electronic properties.[35] The excellent elastic properties of 2D MoS_2 nanosheets make them a highly promising material for flexible electronic devices as well as for composite films.

1.3 Fabrication Techniques for 2D MoS_2 and WS_2

One significant challenge in current MoS_2 and WS_2 research is the fabrication of high quality ultrathin films. Atomically thin flakes of TMDs can be extracted from the bulk crystals by micromechanical cleavage using adhesive tape,[12,33] applied to SiO_2 substrates of certain thickness and optically identified by light interference. While such mechanical exfoliation produces single-crystal flakes of high purity and cleanliness that are suitable for fundamental characterization, the technique is time consuming and not scalable, thereby making it unsuitable for industrial use.

For obtaining large quantities of nanosheets, solvent-based exfoliation of MoS_2 and WS_2 is frequently used. This technique is also promising because it permits the fabrication of composites and hybrids by simple mixing of dispersions of different materials.[36,37] Most commonly, liquid exfoliation is done by intercalation of TMDs by ionic species such as Li.[38,39] The procedure typically involves submerging powders of MoS_2 or WS_2 in a solution of a Li-containing compound such as n-butyllithium. This is followed by exposure to water, which reacts vigorously with the Li inserted between the TMD layers to evolve H_2 gas that pushes the layers apart. Lithium intercalation techniques are capable of producing gram quantities of submicrometre-sized monolayers,[40] but the exfoliated flakes suffer from physical and electronic changes to the crystal structure. In particular, MoS_2 and WS_2 undergo a phase change from the semiconducting 2H-polytype to the metallic 1T-polytype. This phase transformation can be reversed by annealing the exfoliated flakes at 300 °C.[39] TMDs can also be exfoliated by ultrasonication in organic solvents, aqueous surfactant solutions, or solutions of polymers in solvents.[36,37] The exfoliated nanosheets are stabilized against re-aggregation either by solvation or by steric or electrostatic repulsion due to the

adsorption of molecules from solution.[8] Ultrasonication usually yields flakes of a few hundred nanometre in size, which is too small for device fabrication. In addition, all of the above liquid exfoliation techniques do not allow for rational control over the shape and thickness of the resulting flakes, which is crucial for materials such as MoS_2 and WS_2 in which their properties vary below a critical thickness of 100 nm down to a single monolayer.[39]

Chemical vapour deposition (CVD), which has been very successful at growing high quality graphene, was recently found to be effective at producing large area MoS_2 and WS_2 thin films on insulating substrates such as SiO_2, mica and sapphire.[41-45] However, the technique requires high process temperatures in the range of 650-1000 ^oC and long growth times. Furthermore, compared to graphene, it is more challenging to obtain highly crystalline atomically thin TMDs with controlled number of layers by CVD. This is because the geometry, thickness, and crystallinity of graphene can be regulated by suitable catalyst design, but no catalyst is involved in the growth of MoS_2. Current CVD methods for MoS_2 commonly utilize thin film precursors such as Mo[42], MoO_3,[43] and $(NH_4)_2MoS_4$,[45] which are first deposited on silicon substrates, followed by sulfurization or thermal decomposition of these precursors at elevated temperatures to produce 2D MoS_2. Similarly, CVD WS_2 is performed by sulfurization of WO_3 thin films[46] or powders[47,48] deposited on a substrate. In many of these methods, the final film thickness is dependent on the concentration or thickness of the initial precursor, although precise control of the number of layers over a large area has not yet been achieved.

Chemical preparation of MoS_2 and WS_2 have also been demonstrated using hydrothermal synthesis,[49,50] which involves the growth of crystals from an aqueous

solution in an autoclave at high temperature and pressure. Such methods give reasonably good-quality flakes with sizes in the hundreds of nanometres to a few micrometres, but the flake thickness is not typically more than one layer.

1.4 Field Emission Theory

Field emission is the extraction of electrons from the surface of a condensed phase into vacuum under an applied electric field by quantum-mechanical tunnelling through the surface potential barrier.[51] There are several ways to obtain electron emission from material. The first involves heating the metal up to high temperatures, usually above 1000°C, and is known as thermionic emission.[52] If sufficient energy is gained by the electrons in the material they will be able to surmount the potential barrier at the material/vacuum interface and be emitted. In contrast, cold or field emission involves applying an external electric field that reduces the potential barrier at the material/vacuum interface. This allows the electrons to escape the material by quantum tunnelling through the barrier. It is possible to combine the two types of electron emission, such as in the Schottky emission process where both a high electric field and high temperature are applied to the material.[52] Out of the different methods to obtain emission electrons, field emission has several advantage such as low power consumption, fast response time, high brightness and efficiency, as well as a narrower spread of the emitted electrons that that render it preferable for use in vacuum electronics.

1.4.1 Electron Emission from Metals

The phenomenon of field emission is based on the effect of quantum-mechanical tunnelling[51] of electrons via a thin potential barrier at an ideal clean and flat metal surface. Under an externally applied electric field, E, the vacuum level outside the metal bends. Combined with image charge effects, the work function potential barrier height, ø, is reduced by an amount Δø. At sufficiently high fields, the width of the barrier becomes small enough that the electrons from the Fermi level, E_F, of the metal have a non-zero probability to pass through the barrier to vacuum. Figure 1.3 presents a schematic illustration of the field emission mechanism in metals.

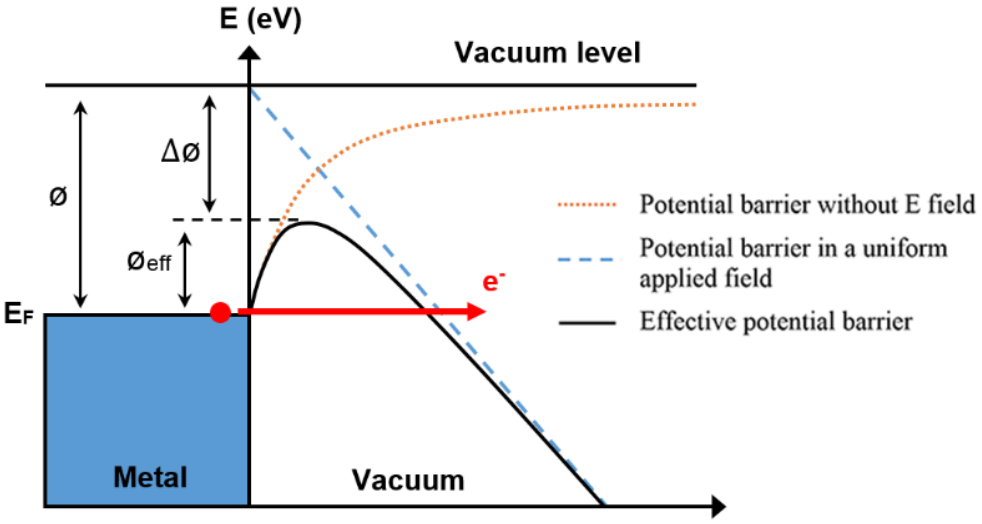

Figure 1.3: Schematic diagram of the field emission mechanism in metals.

The first approximate explanation of the field emission phenomenon was developed by W. H. Schottky. In 1928, Fowler and Nordheim made improvements to the theory to correlate it with the experimental results.[53] Although the Fowler-Nordheim (F-N) model was proposed for metal surfaces at low temperatures, it has

nevertheless been widely used to interpret of field emission from graphitic materials such as CNTs. The simplified F-N equation for an ideal flat and clean metal surface with a constant external electric field is described as,[54]

$$J = \left(\frac{A(\beta E^2)}{\text{ø}}\right) \exp\left(-\frac{B\varphi^{\frac{3}{2}}}{\beta E}\right) \tag{1.1}$$

where J is the macroscopic current density, E is the applied field, β is the geometrical field enhancement factor, φ is the work function, A = 1.54 × 10^{-6} A eV V^{-2} and B = 6.83 × 10^3 $eV^{3/2}$ V μm^{-1}. The electric field E between ideally clean and flat metallic electrodes is homogeneously distributed and can be calculated as $E = V/d$, where V is the applied voltage and d is the gap between the electrodes. By taking natural logarithm, equation 1.1 can be rewritten as the following linear relationship,

$$\ln\left(\frac{\mathrm{J}}{E^2}\right) = \ln\left(\frac{A\beta^2}{\varphi}\right) - \frac{B\varphi^{3/2}}{\beta E} \tag{1.2}$$

This standard F-N equation can be used for field emission studies of a single emitter or large-area field emitters such as Spindt arrays. The field enhancement factor, which reflects the ability of the emitters to enhance the local electric field and is often used as a qualitative measure of field emission performance, can be calculated from the slope (Δ) of the linear plot of $\ln\left(\frac{J}{E^2}\right)$ against $\left(\frac{1}{E}\right)$ for a sample of known work function using,

$$\beta = -\frac{B\text{ø}^{\frac{3}{2}}}{\Delta} \tag{1.3}$$

As can be seen from equation 1.2, the field emission current depends strongly on three factors: the applied electric field, the field enhancement factor, and the work function of the material. Therefore, a slight change in the values of these parameters leads to significant changes of FE current.

1.4.2 Electron Emission from Semiconductors

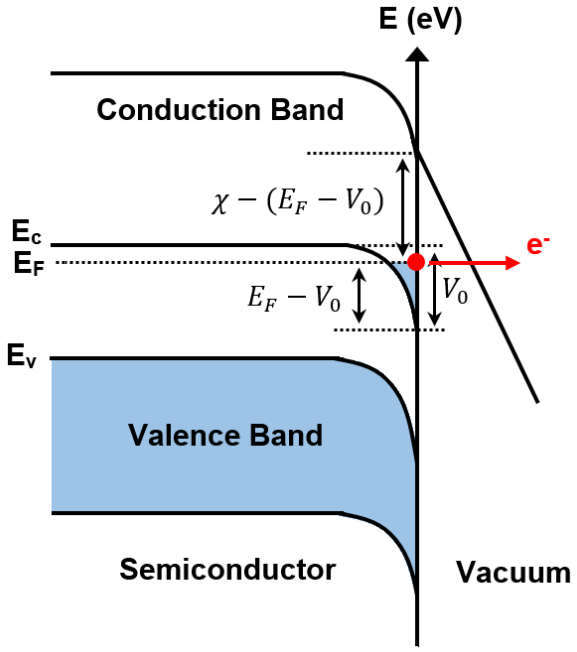

Figure 1.4: Schematic diagram of the field emission mechanism in semiconductors.

In semiconductors, electrons can emit from both the conduction (E_c) and valence (E_v) bands and sometimes from surface states.[55] Given that E_c and E_v are separated by band gap E_g, the barrier height in the conduction band is denoted by χ whereas for the valence band, the barrier height is $\chi + E_g$. The emission current density and electric field relationship for both cases may also be described using equation 1.2 by replacing of the work function with χ or $\chi + E_g$ where appropriate. Field emission from the valence band is often ignored because the top of this band is a few eV below the vacuum level.[56] If the surface states are also ignored, then electron emission occurs only from the conduction band and depends on the tunnelling probability through the potential barrier. In contrast to metals, semiconductors have a much lower density of electrons that result in deeper penetration of an applied electric field.[55] This field

penetration causes bending of both the conduction and valence bands at the emitter surface by an amount V_0 below the Fermi level so that electrons collect in the dip. Consequently, the effective height of the barrier becomes smaller and is given by $\emptyset_{eff} = \chi - (E_F - V_0)$. Figure 1.4 presents a schematic illustration of the field emission mechanism in semiconductors.

1.4.3 Field Emitters based on 2D MoS_2 and WS_2

With their excellent electrical conductivity and mechanical robustness, 2D TMDs such as MoS_2 and WS_2 are promising candidates for next generation field emitters. Compared to conventional field emitters such as CNTs and graphene, MoS_2 and WS_2 both demonstrate similar high field enhancement capabilities in addition to better long term stability.[57-59] MoS_2 nanotubes for example, demonstrate consistent reproducibility in field emission current characteristics and appear to be very inert and unsusceptible to intermediate exposure to air.[58] Transport measurements on individual bundles of MoS_2 nanotubes also suggest they demonstrate metallic behaviour for electron transport along the tube axis,[58] which is advantageous for field emission applications. In addition, 2D MoS_2 and WS_2 layers are relatively easier to fabricate and process compared to graphene. Between the two TMD materials, WS_2 is more inert, particularly in oxidizing environments, which would translate to better field emission stability over longer durations. However, MoS_2 is generally easier and cheaper to fabricate. Although theoretical models predict that semiconducting 2D WS_2 should have the highest mobility of all TMDs,[21] in practice the mobilities of single layer WS_2 and MoS_2 on Si/SiO_2 at room temperature and high vacuum conditions are similar, ranging between 40 to 60 $cm^2\ V^{-1}\ s^{-1}$ for WS_2[26,27] and ~60 $cm^2\ V^{-1}\ s^{-1}$ for MoS_2.[60] The

similar carrier mobilities of the two materials mean that neither WS_2 nor MoS_2 have an obvious advantage in terms of field emission current characteristics.

Although a number of field emission studies has been conducted for 2D carbon-based materials such as graphene,[1,61] research on 2D MoS_2 and WS_2 as potential field emitters remains largely undeveloped. Some early works include the fabrication of MoS_2 nanoflowers by reducing a tin film of MoO_2 on Mo foil with sulfur vapour at high temperatures of 950–1000 ºC.[57] The nanoflowers exhibited excellent field emission performance with a turn-on field of 4.5–5.5 V μm^{-1} at 10 $\mu A\ cm^{-2}$, which is comparable to free-standing graphite sheet[62] (~4.7 V μm^{-1}) and graphene films[63] (2–6 V μm^{-1}). In contrast, WS_2 nanoflowers synthesized by atmospheric pressure CVD[64] at 650 ºC demonstrated a much higher turn-on field of 6.1 V μm^{-1}. Other nanostructured morphologies such as nanotubes[58,59] and nanosheets[65] have also been investigated for their field emission properties. For example, Nemanič et al.[58] demonstrated that an individual MoS_2 nanotube is capable of producing currents in excess of 10 μA that remained stable for up to 70 h. The single-walled nanotubes were grown by a catalysed transport method using C_{60} as a catalyst and Iodine as a transport agent in a reaction that was ran for 22 days at 1010 K. Another example of field emission from TMD nanotubes was demonstrated by Viskadouros et al.[59] who generated WS_2 nanotubes by the high temperature reaction between H_2S and H_2 gases with tungsten oxide nanoparticles. The as-prepared nanotubes were then dispersed into a poly(3-hexylthiothene) (P3HT) matrix, dissolved in acetone, and further solution-casted on both flat Si substrates and Si microspike arrays. The nanotubes on microspike arrays had the lowest turn-on fields of ~2.6 V μm^{-1}, which was comparable to that of vertically oriented CNTs.[66] In addition, Kashid et al. used liquid exfoliation in hexane to fabricate MoS_2 planar nanosheets with lower turn-on fields of 3.5 V μm^{-1} than MoS_2

nanoflowers.[64] The good field emission performance was attributed to a high field enhancement factor associated with the nanometric sharp edges of the MoS_2 sheets.

Generally, the flat profile and smooth surface of layered TMD sheets prevents good field enhancement. This complicates the application of 2D MoS_2 and WS_2 as field emitters due to the fact that most fabrication methods, including CVD and exfoliation, results in precisely such flat layers oriented parallel to the substrate surface. Although Late et al.[67] demonstrated that it is possible for MoS_2 thin films to achieve low turn-on fields of 2.8 V μm^{-1}, this was mainly attributed to the presence of nanometric protrusions on the MoS_2 film. Thus, in order to fully exploit the capabilities of 2D MoS_2 and WS_2 as a field emitter, the nanosheets should be oriented perpendicular to the substrate surface to expose the sharp edges and so that the planes of highest conductivity are along the direction of electron emission. Aside from forming nanostructures such as nanotubes and nanoflowers, orientation of the TMD nanosheets can also be tuned by fabrication on a microtip array. One example of this is the fabrication of MoS_2 films on W tip substrates by PLD.[68] The resulting structure was found to deliver a large emission current density of ~30 mA cm^{-2} at a relatively lower applied voltage of ~3.8 kV, which makes it promising as an intense point source for electrons.

More recently, interests have shifted to exploring the field emission properties of MoS_2 and WS_2-based composites[68-70]. Using a hydrothermal method, Rout et al.[68] synthesized layered WS_2-RGO composites that exhibited much improved field emission performance over that of pristine WS_2 and RGO sheets. Fu et al.[69] also fabricated both MoS_2- and TiO_2-based MoS_2/TiO_2 heterojunctions that possess lower turn-on fields compared to the bare TiO_2 and MoS_2 structures. Similarly, MoS_2/ZnO

composites were shown to demonstrate lower turn-on field values than that of pure MoS_2 nanoflowers.[70] These results clearly show that hybridizing MoS_2 or WS_2 with other materials can produce a synergistic effect that leads to improved field emission performance. It is also clear that 2D MoS_2 and WS_2 have amazing potential for FE applications. However, current research in this area is still very limited and further progress would be needed before practical implementation can be achieved.

1.5 Motivations and Objectives

It can be seen from the above literature that despite numerous studies on MoS_2 and WS_2 fabrication, the controlled synthesis of highly crystalline atomic layers is still a challenge for commonly utilized exfoliation and chemical synthesis methods. In addition, information on the effectiveness of physical vapour deposition techniques such as pulsed laser deposition (PLD) and sputtering for growth of ultrathin TMDs is still greatly lacking, and there is inadequate understanding of the growth mechanism of MoS_2 and WS_2 using these synthesis methods. Such fundamental knowledge on the growth mechanisms is crucial to developing new methods and fine-tuning processes to produce MoS_2 and WS_2 flakes of the highest quality and appropriate dimensions. In terms of applications, some efforts have been channelled into investigating MoS_2- and WS_2-based materials as novel field emitters. However, there are still many gaps in the research and the potential of MoS_2 and WS_2 in field emission applications have yet to be fully explored. As such, there are six objectives that this project seeks to achieve:

(1) Fabricate highly crystalline 2D MoS_2 and WS_2 using physical deposition methods of PLD.

(2) Understand the growth mechanism of MoS_2 and WS_2 by PLD.

(3) Investigate the field emission properties of MoS_2- and WS_2-based emitters grown by PLD.

(4) Fabricate MoS_2-CNT and WS_2-CNT heterostructures by sputtering.

(5) Understand the growth mechanism of MoS_2 and WS_2 on CNT arrays by sputtering.

(6) Study the field emission properties of MoS_2-CNT and WS_2-CNT heterostructures grown by sputtering.

By achieving the above objectives, this work presents alternative pathways for the fabrication of high quality 2D MoS_2 and WS_2 and also contributes to a deeper understanding of the growth mechanisms of MoS_2 and WS_2 synthesized by PLD and sputtering. Through the fabrication and investigation of MoS_2- and WS_2-based field emitters, this work also contributes to current efforts to develop next generation field emitters for practical applications.

References

1. Castro Neto, A. H.; Guinea, F.; Peres, N. M. R.; Novoselov, K. S.; Geim, A.K. *Rev. Mod. Phys.* **2009**, 81, 109–162.
2. Lee, C.; Wei, X.; Kysar, J. W.; Hone, J. *Science* **2008**, 321, 385-388.
3. Christy, R. I. *Thin Solid Films* **1980**, 73, 299–307.
4. Zhang, C.; Wang, Z.; Guo, Z.; Lou, X. W. *ACS Appl. Mater. Interfaces* **2012**, 4, 3765–3768.
5. Guo, G.; Hong, J.; Cong, C.; Zhou, X.; Zhang, K. *J. Mater. Sci.* **2005**, 40, 2557–2559.
6. Fontana, M.; Deppe1, T.; Boyd, A. K.; Rinzan, M.; Liu, A. Y.; Paranjape, M.; Barbara, P.; *Sci. Rep.* **2013**, 3, 1634.
7. Zhou, W.; Yin, Z.; Du, Y.; Huang, X.; Zeng, Z.; Fan, Z.; Liu, H.; Wang, J.; Zhang, H.; *Small* **2013**, 9, 140–147.
8. Wang, Q. H.; Kalantar-Zadeh, K.; Kis, A.; Coleman, J. N.; Strano, M. S. *Nature Nanotechnol.* **2012**, 7, 699–712.
9. Enyashin, A. N.; Yadgarov, L.; Houben, L.; Popov, I.; Weidenbach, M.; Tenne, R.; Bar-Sadan, M.; Seifert, G. *J. Phys. Chem. C* **2011**, *115*, 24586−24591.
10. Chhowalla, M.; Shin, H. S.; Eda, G.; Li, L. J.; Loh, K. P.; Zhang, H. *Nature Chem.* **2013**, 5, 263–275.
11. Lin, Y.-C.; Dumcenco, D. O.; Huang, Y.-S.; Suenaga, K. *Nature Nanotech.* **2014**, *9*, 391−396.
12. Mak, K. F.; Lee, C.; Hone, J.; Shan, J.; Heinz, T. F. *Phys. Rev. Lett.* **2010**, 105, 136805.
13. Ganatra, R.; Zhang, Q. ACS Nano 2014, 8, 4074–4099.
14. Kuc, A.; Zibouche, N.; Heine, T. *Phys. Rev. B* **2011**, 83, 245213.
15. Kaasbjerg, K.; Thygesen, K. S.; Jacobsen, K. W. *Phys. Rev. B* **2012**, 85, 115317.
16. Ayari, A.; Cobas, E.; Ogundadegbe, O.; Fuhrer, M. S. *J. Appl. Phys.* **2007**, 101, 014507.
17. Radisavljevic, B.; Radenovic, A.; Brivio, J.; Giacometti, V.; Kis, A. *Nat. Nanotechnol*. **2011**, 6, 147–150.

18. Chen, J-H.; Jang, C.; Xiao, S.; Ishigami, M.; Fuhrer, M. S. *Nature Nanotech.* **2008**, 3, 206–209.
19. Brivio, J.; Alexander, D. T. L.; Kis, A. *Nano Lett.* **2011**, 11, 5148–5153.
20. Lee, K.; Kim, H.-Y.; Lotya, M.; Coleman, J. N.; Kim, G. T.; Duesberg, G. S. *Adv. Mater.* **2011**, 23, 4178–4182.
21. Liu, L.; Kumar, S. B.; Ouyang, Y.; Guo, J. *IEEE Trans. Electron Devices* **2011**, 58, 3042–3047.
22. Radisavljevic, B.; Whitwick, M.B.; Kis, A. *ACS Nano* **2011**, 5, 9934-9938.
23. Wang, H.; Yu, L.; Lee, Y.-H.; Shi, Y.; Hsu, A.; Chin, M. L.; Li, L.-J.; Dubey, M.; Kong, J.; Palacios, T. *Nano Lett.* **2012**, 12, 4674–4680.
24. Zhang, Y.; Ye, J.; Matsuhashi, Y.; Iwasa, Y. *Nano Lett.* **2012**, 12, 1136–1140.
25. Braga, D.; Lezama, I. G.; Berger, H.; Morpurgo, A. F. *Nano Lett.* **2012**, 12, 5218–5223.
26. Jo, S.; Ubrig, N.; Berger, H.; Kuzmenko, A. B.; Morpurgo, A. F. *Nano Lett.* **2014**, 14, 2019–2025.
27. Ovchinnikov, D.; Allain, A.; Huang, Y.-S.; Dumcenco, D.; Kis, A. *ACS Nano* **2014**, 8, 8174–8181.
28. Gutiérrez, H.R.; Perea-López, N.; Elías, A.L.; Berkdemir, A.; Wang, B.; Lv, R.; López-Urías, F.; Crespi, V.H.; Terrones, H.; Terrones, M. *Nano Lett.* **2013**, 13, 3447−3454.
29. Park, J.; Choudhary, N.; Smith, J.; Lee, G.; Kim, M.; Choi, W. *Appl. Phys. Lett.* **2015**, 106, 012104.
30. Zhang, W.; Chuu, C.-P.; Huang, J.-K.; Chen, C.-H.; Tsai, M.-L.; Chang, Y.-H.; Liang, C.-T.; Chen, Y.-Z.; Chueh, Y-L.; He, et al. *Sci. Rep.* **2014**, 4, 3826.
31. Yin, Z. Y.; Li, H.; Jiang, L.; Shi, Y. M; Sun, Y. H.; Lu, G.; Zhang, Q.; Chen, X. D.; Zhang, H. *ACS Nano* **2012**, 6, 74–80.
32. Frey, G. L; Reynolds, K. J.; Friend, R. H.; Cohen, H.; Feldman, Y. *J. Am. Chem. Soc.* **2003**, 125, 5998–6007.
33. Castellanos-Gomez, A.; Poot, M.; Steele, G. A.; van der Zant, H. S.; Agrait, N.; Rubio-Bollinger, G. *Adv. Mater.* **2012**, 24, 772–775.
34. Bertolazzi, S.; Brivio, J.; Kis, A. *ACS Nano* **2011**, 5, 9703–9709.
35. Pu, J.; Yomogida, Y.; Liu, K. K.; Li, L. J.; Iwasa, Y.; Takenobu, T. *Nano Lett.* **2012**, 12, 4013–4017.

36. Coleman, J. N.; Lotya, M.; O'Neill, A.; Bergin, S. D.; King, P. J.; Khan, U.; Young, K.; Gaucher, A.; De, S.; Smith, R. J. et al. *Science* **2011**, 331, 568-571.
37. Smith, R. J.; King, P. J.; Lotya, M.; Wirtz, C.; Khan, U.; De, S.; O'Neill, A.; Duesberg, G. S.; Grunlan, J. C.; Moriarty, G. et al. *Adv. Mater.* **2011**, 23, 3944–3948.
38. Zeng, Z.; Yin, Z.; Huang, X.; Li, H.; He, Q.; Lu, G.; Boey, F.; Zhang, H. *Angew. Chem., Int. Ed.* **2011**, 50, 11093–11097.
39. Eda, G.; Yamaguchi, H.; Voiry, D.; Fujita, T.; Chen, M.; Chhowalla, M. *Nano Lett.* **2011**, 11, 5111–5116.
40. Tsai, H-L.; Heising, J.; Schindler, J. L.; Kannewurf, C. R.; Kanatzidis, M. G. *Chem. Mater.* **1997**, 9, 879–882.
41. Lee, Y. H.; Zhang, X. Q.; Zhang, W.; Chang, M. T.; Lin, C. T.; Chang, K. D.; Yu, Y. C.; Wang, J. T. W.; Chang, C. S.; Li, L. J. et al. *Adv. Mat.* **2012**, 24, 2320–2325.
42. Zhan, Y.; Liu, Z.; Najmaei, S.; Ajayan, P.M.; Lou, J. *Small* **2012**, 8, 966–971.
43. Lin, Y. C.; Zhang, W.; Huang, J. K.; Liu, K. K.; Lee, Y. H.; Liang, C. T.; Chud, C. W.; Li, L. J. *Nanoscale* **2012**, 4, 6637-6641.
44. Ji, Q.; Zhang, Y.; Gao, T.; Zhang, Y.; Ma, D.; Liu, M.; Chen, Y.; Qiao, X.; Tan, P.; Kan, M. et al. *Nano Lett.* **2013**, 13, 3870−3877.
45. Liu, K. K.; Zhang, W.; Lee, Y. H.; Lin, Y. C.; Chang, M. T.; Su, C. Y.; Chang, C. S.; Li, H.; Shi, Y.; Zhang, H. et al. *Nano Lett.* **2012**, 12, 1538–1544.
46. Zhang, Y.; Zhang, Y.; Ji, Q.; Ju, J.; Yuan, H.; Shi, J.; Gao, T.; Ma, D.; Liu, M.; Chen, Y. et al. *ACS Nano* **2013**, 7, 8963–8971.
47. Peimyoo, N.; Shang, J.; Cong, C.; Shen, X.; Wu, X.; Yeow, E. K. L.; Yu, T. *ACS Nano* **2013**, 7, 10985–10994.
48. Cong, C.; Shang, J.; Wu, X.; Cao, B.; Peimyoo, N.; Qiu, C.; Sun, L.; Yu, T. *Adv. Optical Mater.* **2014**, 2, 131–136.
49. Peng, Y.; Meng, Z.; Zhong, C.; Qian, Y. *Chem. Phys. Lett.* **2001**, 30, 772–773.
50. Cheng, L.; Huang, W.; Gong, Q.; Liu, C.; Liu, Z.; Li, Y.; Dai, H. *Angew. Chem.* **2014**, 126, 7994–7997.

51. Liang, S. D. *Quantum Tunneling and Field Electron Emission Theories*; World Scientific: Singapore, 2014.
52. Raju, G. G. *Dielectrics in Electric Fields*; Marcel Dekker: New York, 2003.
53. Fowler, R. H.; Nordheim, L. *Proc. R. Soc. A* **1928**, 119, 173–181.
54. Xu, C. X.; Sun, X. W.; Chen, B. J. *Appl. Phy. Lett.* **2004**, 84, 1540–1542.
55. Bolozdynya, A. I. *Emission Detectors*; World Scientific: Singapore, 2010.
56. Huang, Q.; Qin, M.; Zhang, B. *J. Appl. Phys.* **1997**, 81, 7589.
57. Li, Y. B.; Bando, B.; Golberg, D. *Appl. Phys. Lett.* **2003**, 82, 1962.
58. Nemanič, V.; Žumer, M.; Zajec, B.; Pahor, J.; Remškar, M.; Mrzel, A.; Panjan, P.; Mihailovi, D. *Appl. Phys. Lett.* **2003**, 82, 4573.
59. Viskadouros, G.; Zak, A.; Stylianakis, M.; Kymakis, E.; Tenne, R.; Stratakis, E. *Small* **2014**, 10, 2398–2403.
60. Jariwala, D.; Sangwan, V. K.; Late, D. J.; Johns, J. E.; Dravid, V. P.; Marks, T. J.; Lauhon, L. J.; Hersam, M. C. *Appl. Phys. Lett.* 2013, 102, 173107.
61. Chen, J. H.; Jang, C.; Xiao, S.; Ishigami, M.; Fuhrer, M. S. *Nature Nanotech.* **2008**, 3, 206–209.
62. Wang, J. J.; Zhu, M. Y.; Outlaw, R. A.; Zhao, X.; Manos, D. M.; Holloway, B. C.; Mammana, V. P. *Appl. Phys. Lett.* **2004**, 85, 1265.
63. Uppireddi, K.; Rao, C. V.; Ishikawa, Y.; Weiner, B. R.; Morell, G. *Appl. Phys. Lett.* **2010**, 97, 062106.
64. Li, X.-L.; Ge, J.-P.; Li, Y. D. *Chem. Eur. J.* **2004**, 10, 6163 – 6171.
65. Kashid, R. V.; Late, D. J.; Chou, S. S.; Huang, Y. K.; Joag, M. D. D. S.; More, M. A.; Dravid, V. P. *Small* **2013**, 9, 2730.
66. Bonard, J. M.; Weiss, N.; Kind, H.; Stockli, T.; Forro, L.; Kern, K.; Chatelain, A. *Adv. Mater.* **2001**, 13, 184.
67. Late, D. J.; Shaikh, P. A.; Khare, R. K.; Kashid, R. V.; Chaudhary, M.; More, M. A.; Ogale, S. B. *ACS Appl. Mater. Interfaces* **2014**, 6, 15881−15888.
68. Rout, C. S.; Joshi, P. D.; Kashid, R. V.; Joag, D. S.; More, M. A.; Simbeck, A. J.; Washington, M.; Nayak, S. K.; Late, D. J. *Sci Rep.* **2013**, 3, 3282.
69. Fu, H.; Yu, K.; Li, H.; Li, J.; Guo, B.; Tan, Y.; Song, C.; Zhu, Z. *Dalton Trans.* **2015**, 44, 1664–1672.
70. Tan, Y.-H.; Yu, K.; Li, J.-Z.; Fu, H.; Zhu, Z.-Q. *J. Appl. Phys.* **2014**, 116, 064305.

Chapter 2

Experimental Techniques

In this chapter, the principles behind each experimental technique used will be described. The techniques used for thin film deposition will be detailed in section 2.1, whereas section 2.2 describes the method used to fabricate vertically aligned multi-walled CNTs. Lastly, material characterization techniques will be detailed in section 2.3.

2.1 Thin Film Deposition Techniques

2.1.1 Magnetron Sputtering

Sputtering is a physical vapour deposition (PVD) method used to make films of metals, semiconductors, alloys and other compounds. This involves the ejection of material from a target (cathode) by bombarding it with energetic ions and transporting the material to condense onto a substrate (anode) such as a silicon wafer. The ions are typically argon (Ar^+) and are produced in a glow discharge plasma within a vacuum chamber at a base pressure of 10^{-6} Torr. Secondary electrons produced as part of the bombardment process also play a part in sustaining the plasma.[1] The technique can be used with a direct current (DC) or radio frequency (RF) voltage source. DC sputtering is unsuitable for insulators as it causes positive charge to accumulate on the target, which repels the positively charged Ar^+ ions and thus halts the sputtering process.[22] Switching to an RF source however, allows the sputtering of insulators and operation at lower Ar pressures, leading to less collisions and better line-of-sight deposition.[3]

Unlike conventional sputter deposition, magnetron sputtering uses an applied magnetic field to increase the sputtering rate.[2] The magnetic field, which is applied perpendicularly to the electric field, constrains the motion of the electrons to around the surface regions of the target. This increases the probability of electron-atom collision, resulting in higher ionization ratios and the production of a dense plasma near the target surface, all of which contribute to higher deposition rates. A schematic diagram of a magnetron sputtering system is shown in Figure 2.1. In this work, a Denton-Discovery-18 RF magnetron sputtering was used to deposit metal films and grow semiconductor nanostructures.

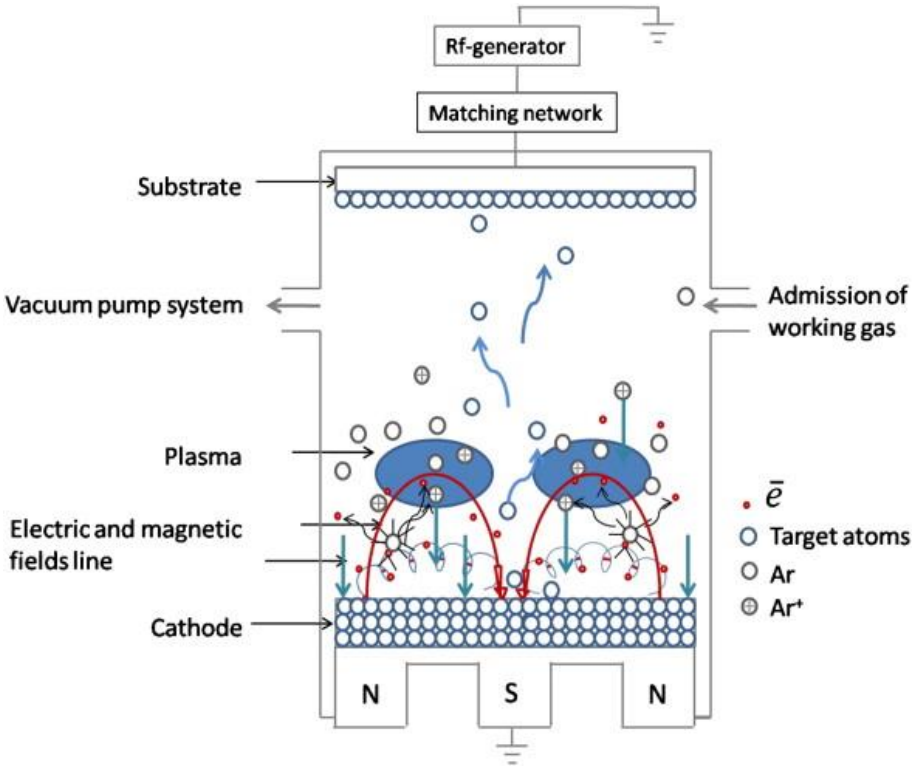

Figure 2.1: Schematic diagram of a typical RF magnetron sputtering system.[4]

2.1.2 Pulsed Laser Deposition (PLD)

Pulsed laser deposition is a type of PVD technique that has been effectively used to fabricate thin films of technological interest such as diamond-like carbon, ceramics, superconductors and nanostructured materials.[5-7] It owes its versatility to the many laser parameters such as substrate temperature, target-to-substrate distance, as well as laser fluence and repetition rate, that can be tuned and which exert great influence on the properties of the resulting products.[8] Among the advantages to using PLD for thin film deposition is the ability to grow high quality films, to ablate any material and to obtain a stoichiometric transfer of target material onto the substrate,[8] which is especially useful in the case of composite materials such as MoS_2 and WS_2. In addition, PLD offers relatively high deposition rates, typically ~100 Å/min, while the use of an external energy source results in very clean processes that allow for deposition to in either inert or reactive background gases.[9]

PLD technology is based on the irradiation of a solid target by a focused pulsed laser beam. If the energy density is sufficiently high, decomposition of the target occurs and results in the formation of a plasma cloud (plume) composed of electrons, atoms, ions, molecules, and in some cases, droplets and target fragments[4]. The plasma cloud then expands, either in vacuum or in a gaseous environment, and condenses on a substrate. Common laser sources include ArF (λ = 193 nm), KrF (λ = 248 nm) and Nd:YaG (λ = 355 nm).[10-12] The typical pulse duration of such lasers is in the nanosecond range. However, the use of femtosecond PLD, which utilizes a laser wavelength of 800 nm, has recently been explored due to its higher ablation efficiency and ability to eliminate the formation of droplets that commonly occur in the nanosecond regime, resulting in higher quality films.[13]

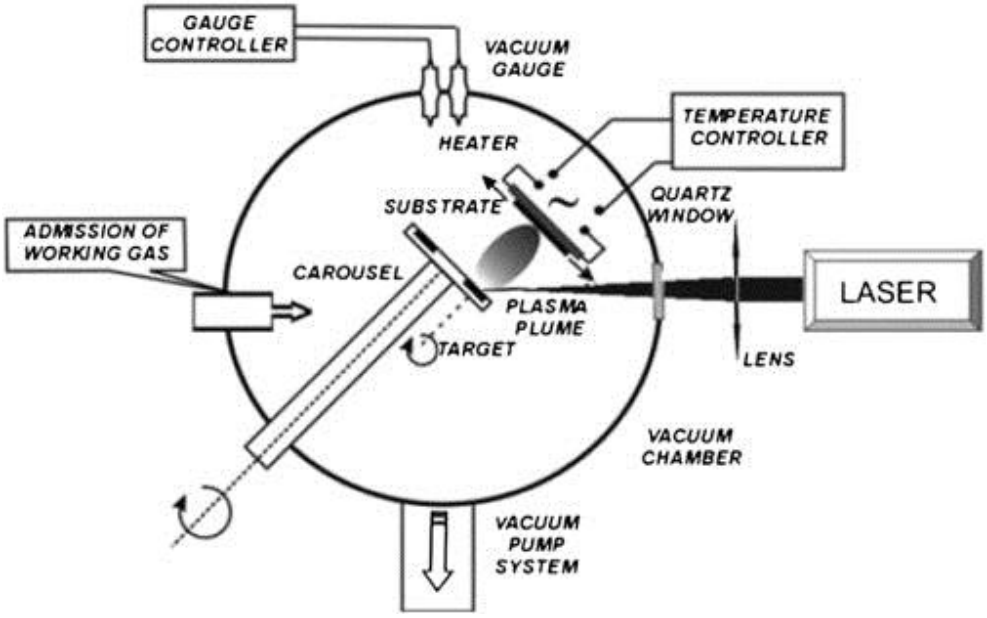

Figure 2.2: Schematic diagram of PLD.[4]

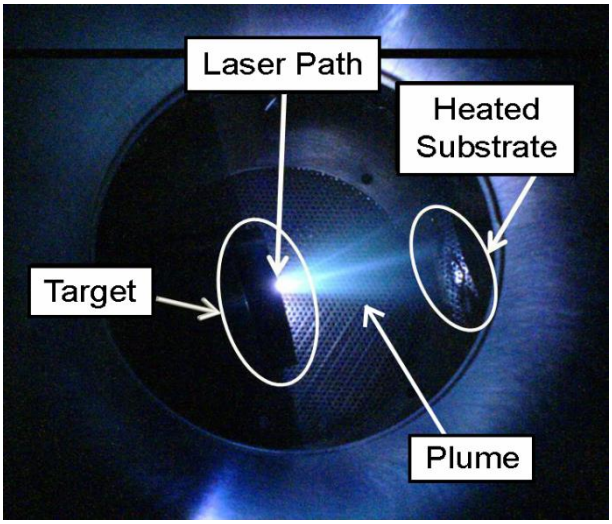

Figure 2.3: Top-view image of the PLD chamber during laser ablation.

The PLD system is shown schematically in Figure 2.2, with the major components including an excimer laser source, an ultrahigh (UHV) vacuum deposition chamber equipped with a rotating target and a fixed substrate holder, and vacuum pumps. The laser pulses are guided by several optical lenses before entering the chamber through the window and striking the target. In this study, a KrF Lambda

Physik Compex 205 laser was used. The substrates were attached with the surface parallel to the target at a separation distance of 5 cm. Figure 2.3 depicts a top-view image of the PLD chamber, in which the plasma cloud formed during laser ablation can clearly be seen.

2.2 Carbon Nanotube Fabrication Methods

2.2.1 Plasma Enhanced Chemical Vapour Deposition (PECVD)

Plasma enhanced chemical vapour deposition (PECVD) is a process used to deposit thin films on a substrate by transformation from a gaseous to a solid state. As with all CVD techniques, chemical reactions are involved in the process. The plasma is generally created by RF or DC discharge between two electrodes at pressures of a few mTorr to a few Torr. Due to energy supplied from the created plasma, decomposition of the reacting gases and subsequent growth of the films can occur at much lower temperatures compared to conventional CVD.[14] The technique also provides the advantages of good adhesion and uniformity of thin films, in addition to good step coverage and low pinhole density.[15] Aside from thin films, PECVD has also been used to fabricate nanostructures such as CNTs. The application of an electric field in PECVD allows the growth of individual, free-standing, and vertically-oriented CNTs, whereas in thermal CVD, any marginal alignment observed is simply due to nanotubes supporting each other by van der Waals forces.[15] In this work, PECVD was used to grow vertically aligned multi-walled CNTs.

2.3 Materials Characterization

2.3.1 Scanning Electron Microscope (SEM)

The scanning electron microscope (SEM) is an imaging technique for surface and subsurface analysis of solid materials. Images of a sample are produced by raster-scanning it with a focused beam of electrons, which interact with atoms in the sample to produce signals that contain information about the sample's surface topography and composition. The electron source is either a tungsten filament (thermionic emission), Lanthanum Hexaboride (LaB_6) or a field emission gun (FEG).[16] In this work, surface images were obtained via a Zeiss Supra 40 field emission SEM.

In standard detection mode, secondary electrons are emitted from very close to the specimen surface.[17] Consequently, SEM can produce very high-resolution images of a sample surface, revealing details less than 1 nm in size.[18] The images appear 3-dimensional due to the small angular aperture of the electron probe that results in a large depth of field. In addition, a setup that is equipped with energy dispersive spectroscopy (EDX) capabilities is able to provide information on the elemental composition of a sample by analysis of the characteristic X-rays emitted when the sample is irradiated by an electron beam.[17]

SEM imaging is typically carried out under vacuum because the presence of gas molecules results in the rapid spreading and attenuation of electron beams. Samples must also be electrically conductive to avoid charging, which often results in distortion of the acquired images. This is achieved by pre-sputtering non-conductive samples with a thin layer of gold.

2.3.2 Transmission Electron Microscope (TEM)

Transmission electron microscopy (TEM) is an imaging technique in which a beam of electrons is transmitted through an ultra-thin sample. The electrons interact with the 3-dimensional sample as they pass through it to form a 2-dimensional projected image that is magnified and focused onto a fluorescent viewing screen.[19] Darker areas of the generated image indicate areas that allow fewer electrons to transmit i.e. regions of greater thickness or density. Aside from an electron gun, a TEM also requires an electromagnetic lens to focus and accelerate the generated electrons, an objective lens to focus the generated image, and a sensor such as a charge-coupled device (CCD) camera. The point-to-point resolutions of TEM is typically reported to be 0.2 nm, but recent advances in aberration correction have resulted in higher resolutions of up to 0.5 Å.[20] This enables the user to examine fine details, even ones as small as the arrangement of individual atoms.

As with SEM, TEM imaging is carried out in a vacuum environment. In addition, samples must be thin enough to transmit electrons. Loose powder samples such as nanotubes are supported on specially designed copper grids and can be viewed directly without need for other preparation. Other samples such as thin films however, require mechanical polishing and ion milling to achieve a suitable thickness before viewing can be conducted.

2.3.3 Atomic Force Microscopy (AFM)

Atomic-force microscopy (AFM) is a type of scanning probe microscopy with resolutions on the order of fractions of a nanometre. It consists of a cantilever with a sharp tip (probe) that is raster-scanned over the sample surface to obtain a 3-

dimensional surface map. The vertical and lateral deflections of the cantilever are measured by reflecting a laser beam off the back of the cantilever, which then strikes a position-sensitive photodetector, as shown in Figure 2.4. The probe tip is typically 15-40 nm in diameter and made from silicon or silicon nitride.[21] The AFM can be operated under ambient conditions and in a number of modes, such as contact or tapping mode. In tapping mode, the cantilever is oscillated at or near its resonance frequency and only contacts the sample intermittently. Tapping mode generally lessens the damage done to the sample surface and probe tip compared to contact mode due to the shorter duration of applied force.[21] In this work, a Digital Instruments, Nanoscope III, Multimode AFM was used to characterize the thin films produced.

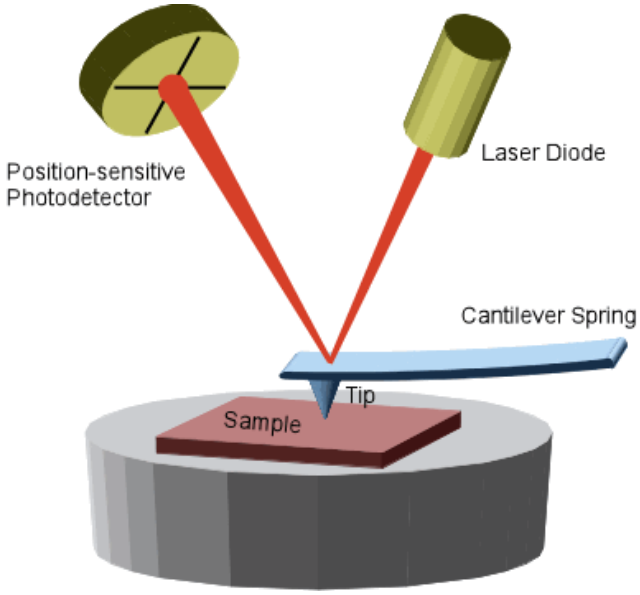

Figure 2.4: Typical AFM schematic.[22]

2.3.4 Raman Spectroscopy

Raman spectroscopy is a technique used to obtain information on molecular vibrations that can be used for sample identification and quantitation.[23] It is fast, non-destructive and can be conducted under ambient conditions for solids, liquids, powders and films. The technique involves irradiating a sample with a monochromatic light source or laser in the visible, near infrared, or near ultraviolet range, which interacts with the sample to cause excitation of the molecules to a virtual energy state. When the molecules relax, they emit photons that are then collected by a detector. Depending on the nature of the interaction, either Rayleigh or Raman scattering can occur.[24] In the former, no exchange of energy occurs and both the incident and scattered photons have the same frequency. If the molecules relax to a different vibrational state however, the energies of the scattered photons are shifted either up or down compared to their initial states. This is known as Raman scattering. In the case where the final vibrational state of the molecule is higher, the scattered photon has lower frequency (Stokes shift). Conversely, if the final vibrational state of the molecule is lower, then the scattered photon will have a higher frequency (Anti-Stokes shift). The different types of light scattering are illustrated in Figure 2.5.

The energy difference between the incident and scattered photon corresponds to the energy difference between two resonant states of the material and provides information on the sample. Plotting the intensity of this scattered light as a function of its frequency difference to the incident photons results in a Raman spectrum. In this project, two Raman setups were utilized: a Renishaw Raman spectrometer 2000 and a Horiba MicroRaman HR Evolution System, both using an Argon laser beam with excitation wavelength of 514.5 nm.

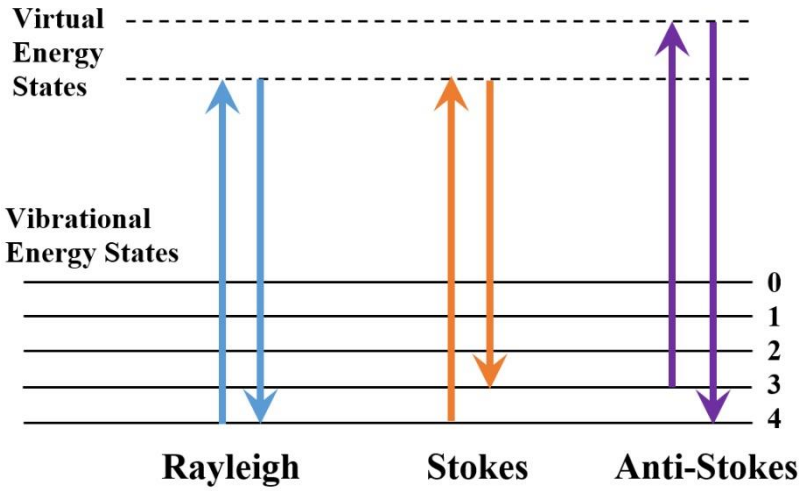

Figure 2.5: The three possible types of light scattering that occur during the interaction of photon and matter in Raman spectroscopy.

2.3.5 Photoluminescence (PL) Spectroscopy

Photoluminescence (PL) is a non-destructive optical technique used for probing the electronic structure of materials. It is also sensitive to impurities and defects that affect material quality and device performance. The technique involves the excitation of electrons to higher electronic states by photon absorption and the subsequent spontaneous light emission when a sample is irradiated with photons.[25] PL can be divided into two categories based on the time period between absorption and emission of photons. Fluorescence is typically a fast process, with the average lifetime of an electron in the excited state lasting only 10^{-5}-10^{-8} s, whereas for phosphorescence the average lifetime can be up to minutes or hours.[26]

Photoluminescence spectra are recorded by measuring the intensity of emitted radiation as a function of either the excitation wavelength or the emission wavelength. An emission spectrum is obtained by using a fixed wavelength to excite the sample while monitoring the intensity of emitted radiation as function of wavelength.[26] In this

project, a Perkin-Elmer fluorescence spectrometer LS 55 with excitation wavelength of 514 nm was used.

2.3.6 Laser Induced Breakdown Spectroscopy (LIBS)

Laser-induced breakdown spectroscopy (LIBS) is an atomic emission spectroscopy technique that uses highly energetic laser pulses to induce sample excitation.[27,28] The interaction between the focused laser pulses and the sample creates a plasma plume composed of ionized matter that can provide chemical information on virtually any kind of material, be it solid, liquid or gas. If the composition of a sample is known, LIBS can be used to analyse the relative abundance of each constituent element, or to detect the presence of impurities. In principle, LIBS can detect all elements, limited only by the laser power and the sensitivity and wavelength range of the spectrometer.

The working principle of LIBS is shown schematically in Figure 2.6. In (1), a pulsed laser beam is focused onto a small area on the surface of the sample. When the laser is discharged, radiation energy is locally coupled on the sample surface (2) and the material starts to evaporate (3), generating a plasma plume with temperatures in excess of 100,000 K (4). This leads to excitation of the ablated material and their spontaneous emission of radiation. The plasma then breaks down and emits element-specific radiation (5)–(7) that is resolved spectrally and is detected by a spectrometer. If the sample is solid, a crater is formed (8).[28] In this work, the laser beam pulses were supplied by the PLD system (KrF Lambda Physik Compex 205) whereas the optical emission spectra of the laser induced plasma were measured using a multichannel Ocean Photonics USB4000 spectrometer.

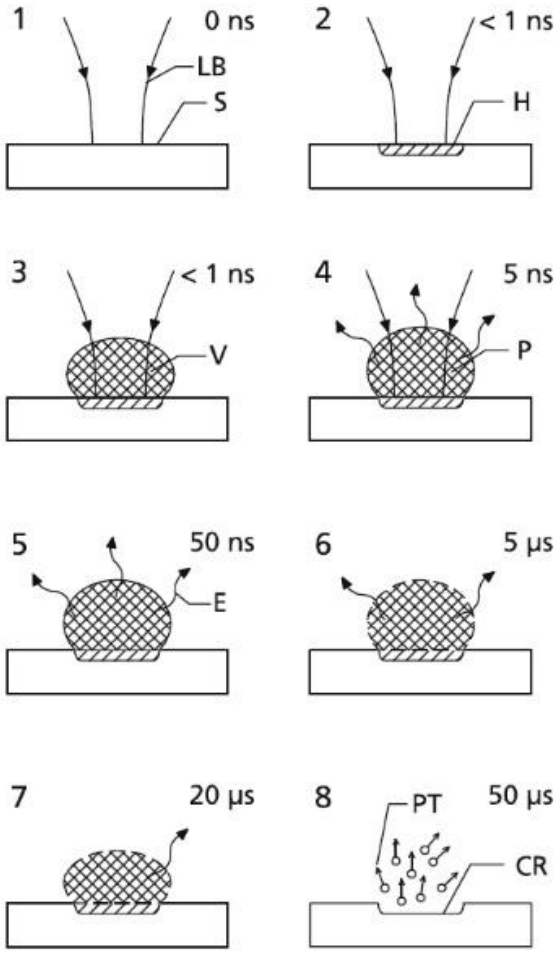

Figure 2.6: Principle of laser-induced breakdown spectroscopy. LB = incoming laser beam, S = sample, H = region of energy deposition, V = material vapour, P = plasma, E = element-specific emission, CR = crater, PT = particles.[28]

2.3.7 X-ray Photoelectron Spectroscopy (XPS)

X-ray photoelectron spectroscopy (XPS) is a surface-sensitive spectroscopic technique that measures the elemental composition and chemical state of the elements that exist within a material. It has a detection limit of approximately 0.5 at%.[29] The technique is capable of detecting all elements except helium and hydrogen because both elements have only valence electrons (XPS is optimized towards core electrons) and both have photoelectron cross-sections that are too small for emission.[30] XPS spectra

are obtained by bombarding the surface of a material with a beam of X-rays. With sufficient energy, the X-ray photon can excite the core electrons of the atoms in the sample and result in the ejection of photoelectrons. The kinetic energy of these escaping photoelectrons are then measured and converted to binding energy using the formula,[29]

$$E_B = hv - E_K - \emptyset_{spec} \quad (2.1)$$

where E_B is the binding energy of the photoelectron, h is Planck's constant, υ is the frequency of the X-ray photon, E_K is the kinetic energy of the photoelectron and $\emptyset_{spec}$ is the work function of the spectrometer. This binding energy is characteristic of an element and its oxidation state.

XPS experiments must be conducted in an ultra-high vacuum environment to avoid adsorption of gaseous molecules on the sample surface and to prevent scattering of the ejected photoelectrons, which results in loss of analytical information. It is also possible to pre-clean the sample surface by argon sputtering to remove any oxides or contaminants. When irradiated by X-rays at a take-off angle of 90º, the photoelectrons are detected from a depth of approximately 10 nm.[31] This sampling depth can be decreased by reduction of the take-off angle, thus providing depth profile information on the material. This technique is known as angle-resolved XPS (ARXPS) and can give a sampling depth as low as 1 nm for a take-off angle of 15° (Figure 2.7). In this project, a Kratos Analytical Axis Ultra^{DLD} UHV spectrometer with a monochromatised Al Kα x-ray source (1486.6 eV) was used for XPS measurements.

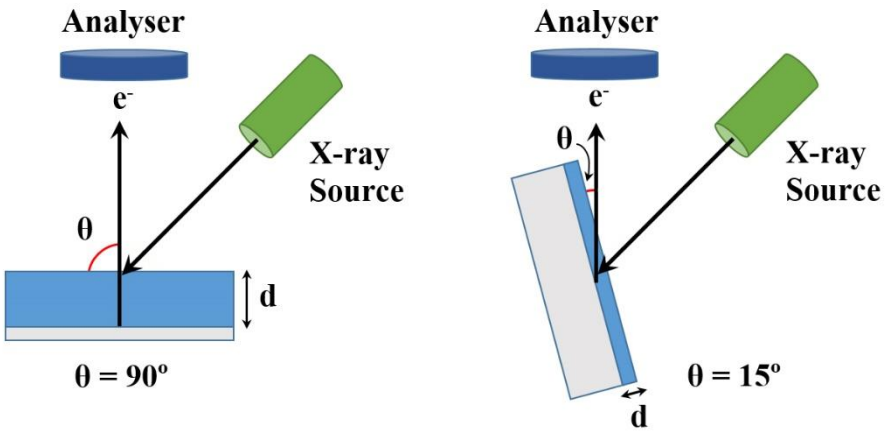

Figure 2.7: Difference in sampling depth between XPS and angle-resolved XPS.

2.3.8 X-ray Diffraction (XRD)

X-ray diffraction (XRD) is a rapid analytical technique primarily used for phase identification of a crystalline material and analysis of unit cell dimensions. It can also provide other material information such as the degree of residual stress and strain. XRD is still the chief method by which the atomic structure of new materials are characterised.

Diffraction effects are observed when X-rays impinge upon a crystalline material because the wavelengths of X-rays are typically the same order of magnitude (1–100 Å) as the spacing between planes in a crystal.[32] Of the different interactions between X-rays and matter, three types play an important role: the photoelectric effect, the inelastic Compton scattering, and the elastic Thomson or Rayeigh scattering.[32] In the photoelectric interaction, a photon transfers all of its momentum and energy to one of the bound electrons of an atom, which is then ejected as a free electron. Another inelastic process, the Compton interaction, occurs when only a portion of the photon energy is transferred to the electrons in an atom. In the third type of interaction, the

electrons in the crystal oscillate at the frequency of the incoming X-ray and emits dipole radiation in an elastic scattering process termed Thomson scattering. It is the Thomson component that is utilised in XRD analysis. In principle, the waves are scattered in all directions and peaks are observed only when the scattered X-rays interfere constructively according to Bragg's law,[32]

$$n\lambda = 2d \sin\theta \qquad (2.2)$$

where d is the spacing between planes, θ is the incident angle, n is any integer, and λ is the wavelength of the beam.

XRD analysis is divided into two primary types: powder diffraction and single-crystal XRD. In the former, a finely ground and homogenized sample is required for structural characterization, most commonly for phase and compositional identification.[33] As its name suggests, single-crystal XRD works best with single, well-ordered crystals and is most commonly used for precise determination of unit cell dimensions and positions of atoms within the lattice. In this work, a Bruker AXS 8 Advance powder diffractometer and Bruker D8 Advanced thin film diffractometer, both with a Cu Kα x-ray source ($\lambda_{CuK\alpha}$ = 1.54056Å), was used.

2.4 Device Testing

2.4.1 Field Emission (FE)

(1) Parallel Plate Setup

Field emission studies of MoS_2-CNT samples were carried out using a parallel-plate device at room temperature and at a base pressure of 3×10^{-6} Torr. The sample is clamped between an aluminium cathode and a glass slide coated

with indium tin oxide (ITO), which functions as the anode. The cathode and anode are separated by a 100 μm thick polymer film spacer on which a hole with fixed area was fashioned to define the total emission area. Actual emitter-to-anode distance was calculated by subtracting the height of the CNTs from 100 μm. During testing, the voltage was incrementally increased until the current produced is above a pre-defined limit. In this setup, the turn-on field is defined as the electric field strength required to produce a current density of 10 μA cm^{-2}. The current-voltage relationship was obtained by applying a DC voltage across the sample and anode. Readings were taken using a Keithley 237 voltage source and current measurement unit. A schematic diagram of the setup is shown in Figure 2.8.

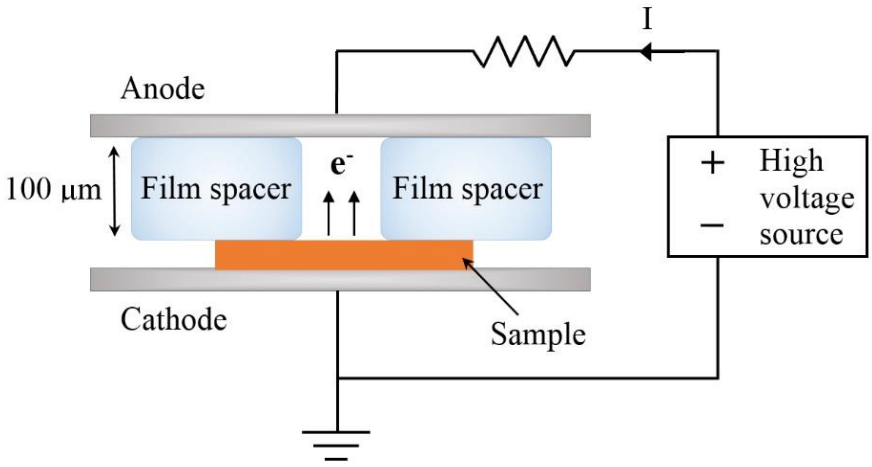

Figure 2.8: Schematic of parallel plate field emission setup.

(2) Probe Tip Setup

Field emission studies of all other samples were carried out using a probe tip setup. Compared to the parallel plate arrangement, the anode used in a probe tip field emission tester is a tungsten tip. In addition, the anode-cathode distance can be varied within the range of 0–100 μm. In this setup, the turn-on

voltage is defined as the voltage required to produce a current of 1 μA. A schematic diagram of the setup is shown in Figure 2.9.

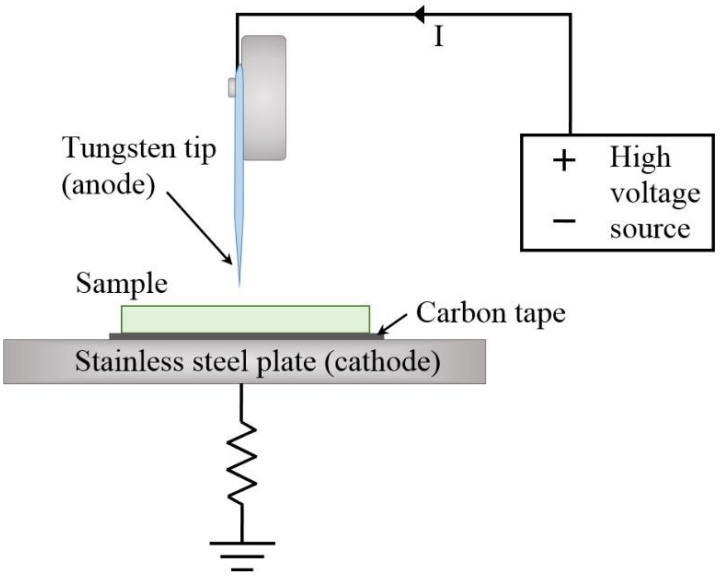

Figure 2.9: Schematic of probe tip field emission setup

References

1. Kuncser, V.; Miu, L., Ed.; *Size Effects in Nanostructures: Basics and Applications*; Springer-Verlag: Berlin Heidelberg, 2014.
2. Wasa, K.; Kanno, I.; Kotera, H. Eds.; *Handbook of Sputter Deposition Technology: Fundamentals and Applications for Functional Thin Films, Nanomaterials and MEMS*, 2nd ed.; Elsevier: New York, 2012.
3. Groza, J. R.; Shackelford, J. F.; Lavernia, E. J.; Powers, M. T., Eds.; *Materials Processing Handbook*; CRC Press: New York, 2007.
4. Surmenev, R. *Surf. Coatings Tech.* **2012**, 206, 2035–2056.
5. Choi, E.-M.; Jung, S.-G.; Lee, N. M.; Kwon, Y. S.; Kang, W. N.; Kim, D. H.; Jung, M.-H.; Lee, S.-I.; Sun, I. *Appl. Phys. Lett.* **2009**, 95, 062507.
6. Jayatissa, A. H.; Sato, F.; Saito, N.; Hirano, Y.; Takizawa, K. *Carbon* **2000**, 38, 1145.
7. Bailini, A.; Di Fonzo, F.; Fusi, M.; Casari, C. S.; Li Bassi, A.; Russo, V.; Baserga, A.; Bottani, C. E. *Appl. Surf. Sci.* **2007**, 19, 8130–8135.
8. Kramer, B., Ed.; *Advances in Solid State Physics*; Springer-Verlag: Berlin Heidelberg, 2003.
9. Martin, P. M. *Introduction to Surface Engineering and Functionally Engineered Materials*; John Wiley & Sons: New Jersey, 2011.
10. Grigorescu, S.; Carradó, A.; Ulhaq, C.; Faerber, J.; Ristoscu, C.; Dorcioman, G.; Axente, E.; Werckmann, J.; Mihailescu, I. N. *Appl. Surf. Sci.* **2007**, 254, 1150.
11. Jedyński, M.; Hoffman, J.; Mróz, W.; Szymanski, *Z. Appl. Surf. Sci.* 2008, 255, 2230.
12. Suda, Y.; Kawasaki, H.; Ueda, T.; Ohshima, T. *Thin Solid Films* **2004**, 453–454, 162–166.
13. Shen, J.; Gai, Z.; Kirschner, J. *Surf. Sci. Rep.* 2004, 52, 163–218.
14. Jones, A. C.; Hitchman, M. L., Eds; *Chemical Vapour Deposition: Precursors, Processes and Applications*; RSC Publishing: Cambridge, UK, 2009.

15. Meyyappan, M.; Delzeit, L.; Cassell, A.; Hash, D. *Plasma Sources Sci. Technol.* **2003**, 12 205–216.
16. Postek, M. T. The Scanning Electron Microscope. In *Handbook of Charged Particle Optics*; Orloff, J., Ed.; CRC Press: New York; 1997; pp 363–402.
17. Goldstein, J. I.; Newbury, D. E.; Echlin, P.; Joy, D. C.; Romig, Jr., A. D.; Lyman, C. E.; Fiori, C.; Lifshin, E. *Scanning Electron Microscopy and X-Ray Microanalysis: A Text for Biologists, Materials Scientists and Geologists*, 2nd ed.; Plenum Press: New York and London, 2012.
18. Reimer, L. *Scanning Electron Microscopy: Physics of Image Formation and Microanalysis*, 2nd ed.; Springer-Verlag: Berlin Heidelberg, 1998.
19. Reimer, L.; H. Kohl. *Transmission Electron Microscopy: Physics of Image Formation*, 5th ed.; Springer Science: New York, 2008.
20. Erni, E.; Rossell, M. D.; Kisielowski, C.; Dahmen, U. *Phys. Rev. Lett.* **2009**, 102, 096101.
21. University of Guelph, Department of Chemistry. http://www.chemistry.uoguelph.ca/educmat/chm729/afm/firstpag.htm (accessed March 20, 2016)
22. University of Greifswald, Department of Physics. http://www.physik.uni-greifswald.de/arbeitsgruppen/helm/methoden/afm-atomic-force-microscope.html (accessed March 20, 2016)
23. Ferraro, J. R.; Nakamoto, K.; Brown, C. W. *Introductory Raman Spectroscopy*, 2nd ed.; Academic Press, Amsterdam, 2003.
24. Colthup, N. B.; Daly, L. H.; Wiberley, S. E. *Introduction to Infrared and Raman Spectroscopy*, 3rd ed.; Academic Press: New York, 1990.
25. Bergman, L.; McHale, J. L., Eds.; *Handbook of Luminescent Semiconductor Materials*; CRC Press: New York, 2012.
26. University of California, Davis, Department of Chemistry. http://chemwiki.ucdavis.edu/Core/Analytical_Chemistry/Analytical_Chemistry_2.0/10_Spectroscopic_Methods/10F%3A_Photoluminescence_Spectroscopy (accessed 20 March 2016).
27. Radziemski, L. J.; Cremers, D. A. *Handbook of Laser-induced Breakdown Spectroscopy*; John Wiley & Sons: New York, 2006.
28. Noll, R. *Laser-induced Breakdown Spectroscopy: Fundamentals and Applications*; Springer-Verlag: Berlin, 2012.

29. Hoffmann, S. *Auger and X-ray Photoelectron Spectroscopy in Materials Science: A User Oriented Guide*; Springer-Verlag: Berlin Heidelberg, 2013.
30. Heide, P. v. d. *X-ray Photoelectron Spectroscopy: An introduction to Principles and Practices*; John Wiley & Sons: New Jersey, 2012.
31. Artyushkova, K.; Fulghum, J. E.; Reznikov, Y. *Mol. Cryst. Liq. Cryst.* **2005**, 438, 205/[1769]-213/[1777].
32. Birkholz, M. *Thin Film Analysis by X-ray Scattering*; Wiley-VCH Verlag: Weinham, 2006.
33. Eastern Michigan University. Integrating Research and Education, Geochemical Instrumentation and Analysis. http://serc.carleton.edu/research_education/geochemsheets/browse.html (accessed 21 March 2016).

Chapter 3

Pulsed Laser Fabricated Few-Layer MoS_2 on Metal Substrates

In this chapter, pulsed laser deposition (PLD) is used to fabricate few-layer MoS_2 on metal substrates. The influences of cooling rate and laser energy on MoS_2 growth on Ag metal are investigated in Section 3.2. In Section 3.3, the feasibility of Ag, Al, Ni and Cu as templates for MoS_2 synthesis by PLD is explored and growth mechanism of MoS_2 on these metals elucidated. In section 3.4, the field emission properties of PLD-grown MoS_2 on Ag and Al nanocones are studied.

3.1 Introduction

One significant challenge in current MoS_2 research is the fabrication of high quality ultrathin films. While mechanical exfoliation using adhesive tape[1,2] produces single-crystal flakes of high purity and cleanliness that are suitable for fundamental characterization, the technique is time consuming and not scalable, thus making it unsuitable for industrial use. Other conventional "top-down" techniques such as solvent based exfoliation[3,4] produce flakes that are too small for device fabrication, whereas lithium intercalation techniques[5] suffer from physical and electronic changes to the crystal structure. In addition, all the above mentioned techniques do not allow for rational control over the shape and thickness of the resulting flakes, which is crucial for a material such as MoS_2 in which its properties vary with thickness.[6] The most common bottom-up technique used to fabricate 2D TMDs such as MoS_2 is chemical vapour

deposition (CVD), which has so far been very successful at producing large-area MoS_2 on insulating substrates such as SiO_2, mica and sapphire.[7-11] This technique generally requires elevated process temperatures in the range of 650-1000 ºC as well as long growth times, which may not be economical for large scale industry processes. And compared to CVD graphene, it is more challenging to obtain crystalline atomically thin MoS_2 with controlled number of layers by CVD.[12] This is because the geometry, thickness, and crystallinity of graphene can be regulated by suitable catalyst design, but no catalyst is involved in the growth of MoS_2. Consequently there is growing focus towards alternative synthesis methods for ultrathin MoS_2.

The majority of MoS_2 research has so far been focused on insulating substrates, and there is very limited information and studies on the synthesis of few-layer MoS_2 using alternative growth templates such as metals. While the use of insulating substrates is necessary to study the electronic properties of MoS_2, metal substrates have their own set of advantages, including but not limited to a reduction in growth temperatures[13] and the ease of producing metal-semiconductor contacts without film transfer. It has furthermore been demonstrated that the introduction of a metal support can substantially alter the H binding energy of MoS_2 in hydrogen adsorption tests,[14] enabled by charge transfer from the substrate to the overlying film and through strong metal-MoS_2 interaction at the interface. Metal supported MoS_2 could thus potentially be used as novel catalysts for hydrogen production. Certain metals such as Ti have furthermore been shown through DFT calculations to hybridize strongly with monolayer MoS_2 d-band orbitals when the two materials come into contact, resulting in destruction of the band structure of MoS_2.[15,16] This means that the region of MoS_2 beside the metal becomes metalized and the Schottky barrier at the interface disappears, leading to the

formation of low resistance Ohmic contacts that strongly favours electron transfer from the metal to MoS_2, which is very promising for future high performance electronics.

In this chapter, few-layer MoS_2 was fabricated using pulsed laser ablation (PLD) of solid targets at a relatively low temperature of 500 ºC. PLD has been effectively used to fabricate thin films material such as diamond-like carbon, ceramics, superconductors and nanostructured materials.[17-20] It owes its versatility to the many laser parameters such as laser fluence and repetition rate that can be tuned and which exert great influence on the properties of the resulting products. Among the advantages to using PLD for thin film deposition is the ability to grow high quality films, to ablate any material and to obtain a stoichiometric transfer of target material onto the substrate, which is especially useful in the case of composite materials such as MoS_2. In addition, the generation of charged energetic species that can penetrate into the substrate allows for a reduction in growth temperatures and fabrication times. For example, Koh et al.[13] utilized PLD to successfully synthesize few-layer graphene on metal substrates at much lower temperatures of 750 ºC as compared to epitaxial growth of graphene on SiC, which requires temperatures in the range of 1000-1600 ºC. But despite the effectiveness of PLD in graphene synthesis, it has yet to be explored as a technique for growing other 2D layered materials. In addition, little is known concerning the mechanism and parameters affecting film growth of MoS_2 when using energetic source atoms and physical synthesis methods. For PLD fabricated graphene, it has been found that the film is produced via segregation of carbon atoms onto the surface after being implanted into the metal,[21] but the situation is more complicated with MoS_2 due to the presence of multiple species as the source atoms, and the high chemical reactivity of sulfur with various metals.

In section 3.2, we investigate the effects of different cooling rates and laser energies on the crystalline quality and thickness of few-layer MoS_2 grown on Ag substrates by PLD. The viability of various other metals to act as the growth template for few-layer MoS_2 growth by PLD is then studied in section 3.3. The metals chosen were Al, Ag, Ni and Cu. As sapphire (α-Al_2O_3) substrates have been demonstrated[11] to successfully produce ultrathin MoS_2 by CVD, it would be interesting to see if similar results can be replicated using pure Al metal films and solid MoS_2 sources in PLD. Ag, Ni and Cu were chosen for their reactivity with sulfur to form metal sulfides, which are thought to be beneficial to the growth of highly crystalline MoS_2 due to the minimal lattice mismatch between two sulfide compounds.

The good electrical conductivity and mechanical robustness of 2D TMDs such as MoS_2 render them promising candidates for next generation field emitters. However, most bottom-up fabrication techniques result in lateral growth of MoS_2 layers whereas top-down techniques such as exfoliation produce flakes that are oriented parallel to the substrate surface. This flat profile and smooth surface prevents good external field enhancement, which can lead to extremely high turn-on fields or even no electron emission whatsoever. For example, planar surfaces have been reported to exhibit turn-on fields as high as 500–1000 V μm^{-1}.[22] Such high electric fields are undesirable as it may cause vacuum breakdown or electrical discharge.[23] Thus, in order to build effective field emitters, 2D sheets of MoS_2 should be oriented such that sharp edges are exposed, preferably perpendicularly to the substrate. For example, Kashid et al.[24] used liquid exfoliation in hexane to fabricate MoS_2 nanosheets with exposed edges that exhibited low turn-on fields of 3.5 V μm^{-1}. Synthesizing three-dimensional (3D) structures such as nanoflowers have also been shown to be effective at improving field emission performance due to the numerous exposed sharp tips.[25] Aside from the above methods,

orientation of MoS_2 nanosheets can also be tuned by fabrication on a microtip array. Late et al.[26] fabricated MoS_2 films on W tips by PLD that, due to the presence of nanometric protrusions on the surface, were able to produce a large emission current density of ~30 $mA.cm^{-2}$ at an applied voltage of ~3.8 kV.

In section 3.4, MoS_2-coated Ag and Al nanocones were fabricated by PLD and investigated for field emission capability. Due to the reduced growth temperatures used for PLD grown MoS_2 as compared to CVD, the probability of the metal nanocones undergoing significant diffusion and reflow during the heating process is lower and thus the conical structures can be preserved. In addition, the MoS_2 layers were grown directly on the metal nanocones and thus avoided the issues associated with conventional PMMA-mediated transfer technique such as incomplete transfer and failure to completely remove polymeric residues that can adversely affect the electron transport properties of MoS_2. Field emission studies were carried out on the MoS_2-coated nanocones and their field enhancing mechanisms were studied.

3.2 Few-layer MoS_2 on Silver

3.2.1 Experimental Procedure

Synthesis: Ag films of approximately 600 nm thickness were sputtered onto normal doped Si substrates using radio-frequency (RF) magnetron sputtering system Denton-Discovery-18 at a working pressure of 10^{-2} Torr and RF power of 100 W. The Ag substrates were subsequently transferred to a KrF (λ = 248 nm) Lambda Physik excimer PLD system, which was evacuated to 2×10^{-6} Torr. A MoS_2 target (99.9% purity) was ablated with a laser energy of 50 mJ, a pulse duration of 25 ns and a frequency of 10 Hz. Duration of target ablation was 10 s to limit the amount of MoS_2 supplied to the substrate to < 5 nm. The laser spot size was 1 mm^2 and the target was rotated at a speed of 6 rpm with the laser ablating a circular outline of 2 cm in radius. Substrate temperature was kept at 500 °C during ablation. After deposition, cooling was conducted at different rates of 1 ºC and 50 °C/min until the temperature reached 300 ºC, whereupon natural cooling processes took over. To compare the effects of laser energy, a cooling rate of 50 °C/min and laser energies of 30, 40, 50, 100, and 200 mJ were used. The fabrication temperature of 500 ºC was selected as it is optimal for growth of ultrathin MoS_2 films by PLD; any lower and the crystalline quality decreases because the atoms do not have sufficient thermal energy to rearrange themselves into a periodic configuration, higher temperatures only provide minimal increase in crystallinity, whereas temperatures > 700 ºC promotes the reaction of molybdenum with oxygen.

Characterization: The optical properties of as-deposited samples were characterized using a Perkin-Elmer fluorescence spectrometer LS 55 with excitation

wavelength of 514 nm, and a Renishaw Raman spectrometer 2000 with laser of wavelength 514.5 nm. The Raman laser beam had a spot size of 1 μm and was focused using an optical microscope at 50× magnification. Surface composition was analysed by XPS using a Kratos Analytical Axis Ultra^{DLD} UHV spectrometer with a monochromatized Al Kα x-ray source (1486.6eV) scanning a spot size of 700 μm by 300 μm. Core-level XPS spectra were obtained at a take-off angle of 90º and 15° measured with respect to the sample surface at a vacuum of 5×10^{-9} Torr. Cross-sectional TEM images of the samples were taken using a JEOL JEM-2010F TEM (FEG source) operated at an accelerating voltage of 200kV.

3.2.2. Cooling Rate Effects on MoS_2 Growth

Figure 3.1(a) shows the Raman spectra of as-grown samples excited by a 514.5 nm line under ambient conditions. The spectrum of bulk MoS_2 is also included for comparison. The characteristic Raman modes E^1_{2g} and A_{1g} of 2H-MoS_2 are observed for all samples, occurring at 379.1 cm^{-1} and 404.8 cm^{-1} respectively for bulk MoS_2.[6] The frequency difference between the E^1_{2g} and A_{1g} peaks can be used to reliably identify the number of layers in ultrathin MoS_2 with ≤ 4 layers.[27,28] With increasing sample thickness, the E^1_{2g} mode red-shifts while the A_{1g} vibration blue-shifts until the frequencies of both modes converge to the bulk values for films with five or more layers. Based on the values of $A_{1g} - E^1_{2g}$ for all samples as listed in Table 3.1, it can be seen that few-layer MoS_2 was formed when the laser energy used was 50 mJ or lower. The E^1_{2g} and A_{1g} peaks of our samples were consistently broad (9 ~ 12 cm^{-1}) compared to mechanically exfoliated samples, which typically have FWHMs in the range of 2 ~ 6 cm^{-1}.[6,27] This can be attributed to thickness inhomogeneity in the deposited film. The

presence of possible defects may also result in phonon confinement effects that contribute to the broad peaks.[29]

In addition to the Raman shift, atomically thin MoS_2 exhibits unique optical properties due to the transition from an indirect to direct-bandgap semiconductor. Figure 3.1(b) displays the photoluminescence (PL) spectra of our laser-fabricated few-layer MoS_2. Pronounced emissions are observed at wavelengths of approximately 670 and 615 nm, labelled A and B respectively. These two peaks have been well established to be the direct excitonic transitions of the K point of the Brillouin zone.[30] The prominent band gap photoluminescence suggests that the as-deposited MoS_2 sheets possess good structural integrity and sufficiently low density of defects that may inhibit luminescence. There is a slight red-shift of the wavelength of the A transition with fewer layers, in agreement with previous reports.[2,6] The thinnest sample (50 mJ) also exhibits the strongest PL signals, with the emission intensity gradually decreasing with an increase in the number of layers. This reduction in PL intensity is attributed to the transition from a direct to indirect bandgap as the thickness of MoS_2 increases, but can also be partially caused by the substrate effect. For metallic substrates such as Au and Ag, the overlying MoS_2 PL intensity can be affected by the presence of additional non-radiative paths for exciton recombination such as charge transfer processes and dipole-dipole interactions,[31,32] leading to a gradual reduction in PL intensity with increasing thickness as documented by Buscema et. al[33] for few-layer MoS_2 on gold. In addition, it is known that SiO_2 substrates can reduce PL emission intensity by scattering and interference effects with surface optical phonons.[34] Thus, as the number of layers increase, the interference effects from the SiO_2 substrate can lead in a greater rate of quenching of the MoS_2 PL intensity compared to metallic substrates.

The 2-3 layers in the 50 mJ sample as predicted by the Raman spectrum can be directly observed from the TEM images shown in Figure 3.2, in which the lattice fringes on the surface of the Ag film are separated by 0.65 nm, confirming the presence of MoS_2. Optical images of the sample are displayed in the inset (b), showing that the MoS_2 film has uniform coverage over the entire surface. The lattice fringes with interplanar spacings of approximately 0.27 nm present just below the Mos_2 layer can be ascribed to the (120) plane of monoclinic Ag_2S [JCPDS #14-0072].

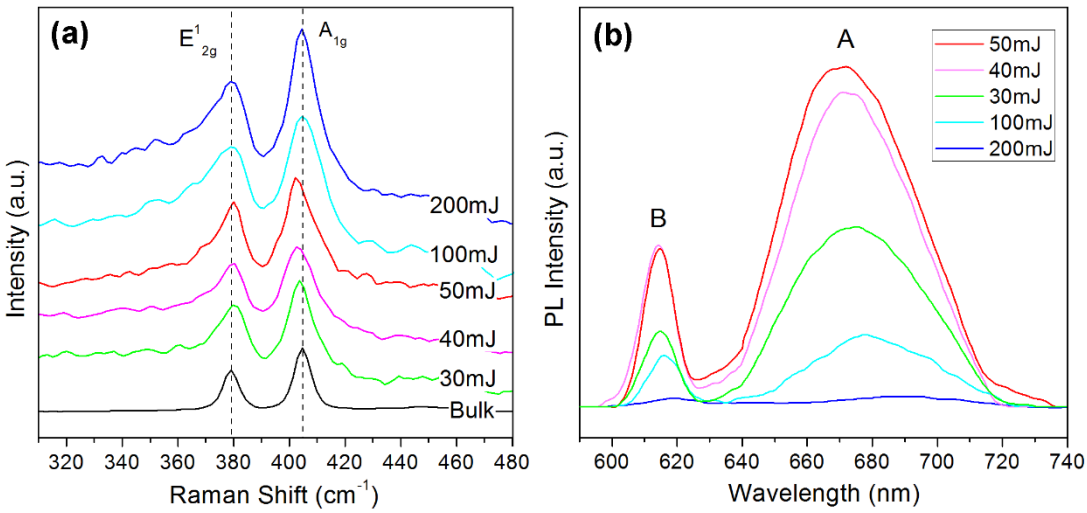

Figure. 3.1: (a) Raman and (b) photoluminescence spectra of as-grown samples fabricated using different laser energies. In (a) the left and right dashed lines indicate the positions of the E^1_{2g} and A_{1g} peaks in bulk MoS_2 respectively.

Table 3.1: Summary of the E^1_{2g} and A_{1g} peak frequencies from as-grown samples fabricated using different laser energies. A single data represents the average value from three different sampling points.

Laser Energy (mJ)	**E^1_{2g} (cm^{-1})**	**A_{1g} (cm^{-1})**	**$A_{1g} - E^1_{2g}$ (cm^{-1})**	**Estimated Number of Layers**
30	403.6	379.8	23.8	3-4
40	402.8	380.1	22.7	2-3
50	402.4	380.2	22.2	2-3

100	403.7	379	25.7	>4
200	404.7	379.1	25.6	>4
Bulk	404.8	379.1	25.7	-

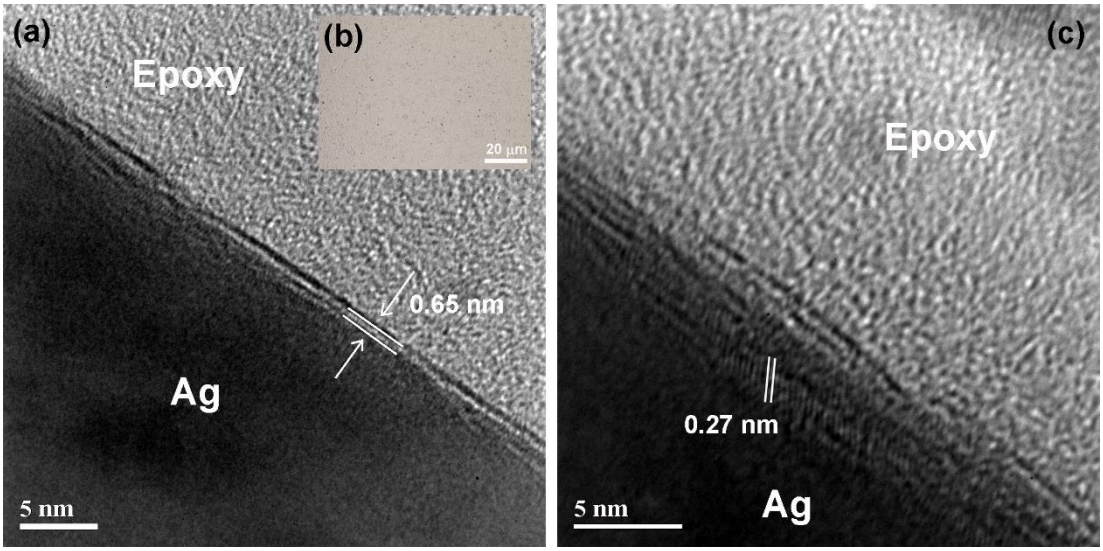

Figure 3.2: Cross-section TEM showing (a) MoS_2 layers above Ag. Inset (b) is an overview optical image showing uniform coverage of the deposited film. (c) Higher magnification TEM images showing the Ag lattice fringes.

The Mo 3d, S 2s, and S 2p regions of the XPS spectra for the 50 mJ samples cooled at 1 ºC/min and 50 ºC/min are depicted in Figure 3.3. The Mo 3d spectra of the 50 ºC/min sample shows two peaks at 228.7 and 231.9 eV that correspond to Mo^{4+} $3d_{5/2}$ and Mo^{4+} $3d_{3/2}$ of MoS_2 respectively.[7] The presence of a doublet at 231.8 and 235 eV consistent with the peaks of Mo^{6+} species indicates oxidation of Mo. In the S 2p spectra, besides the known doublet peaks of MoS_2 at 161.9 and 163.1 eV,[7] there is an additional doublet at 161.1 and 162.4 eV assigned to the S $2p_{3/2}$ and S $2p_{1/2}$ peaks of Ag_2S. This confirms the presence of an Ag_2S phase that is observed in the TEM results. Reducing the cooling rate to 1 ºC/min results in a decrease in the FWHM of the Mo 3d peaks from 1.3 to 1.1 eV, indicating increased crystallinity. The Mo^{4+} 3d doublet is also shifted to

higher binding energies by 0.3 eV, which suggests a higher degree of sulfurization of Mo. This is corroborated by an increase in the stoichiometric ratio of S : Mo from 1.81 to 1.93 as calculated from the respective integrated peak areas of the XPS spectra.

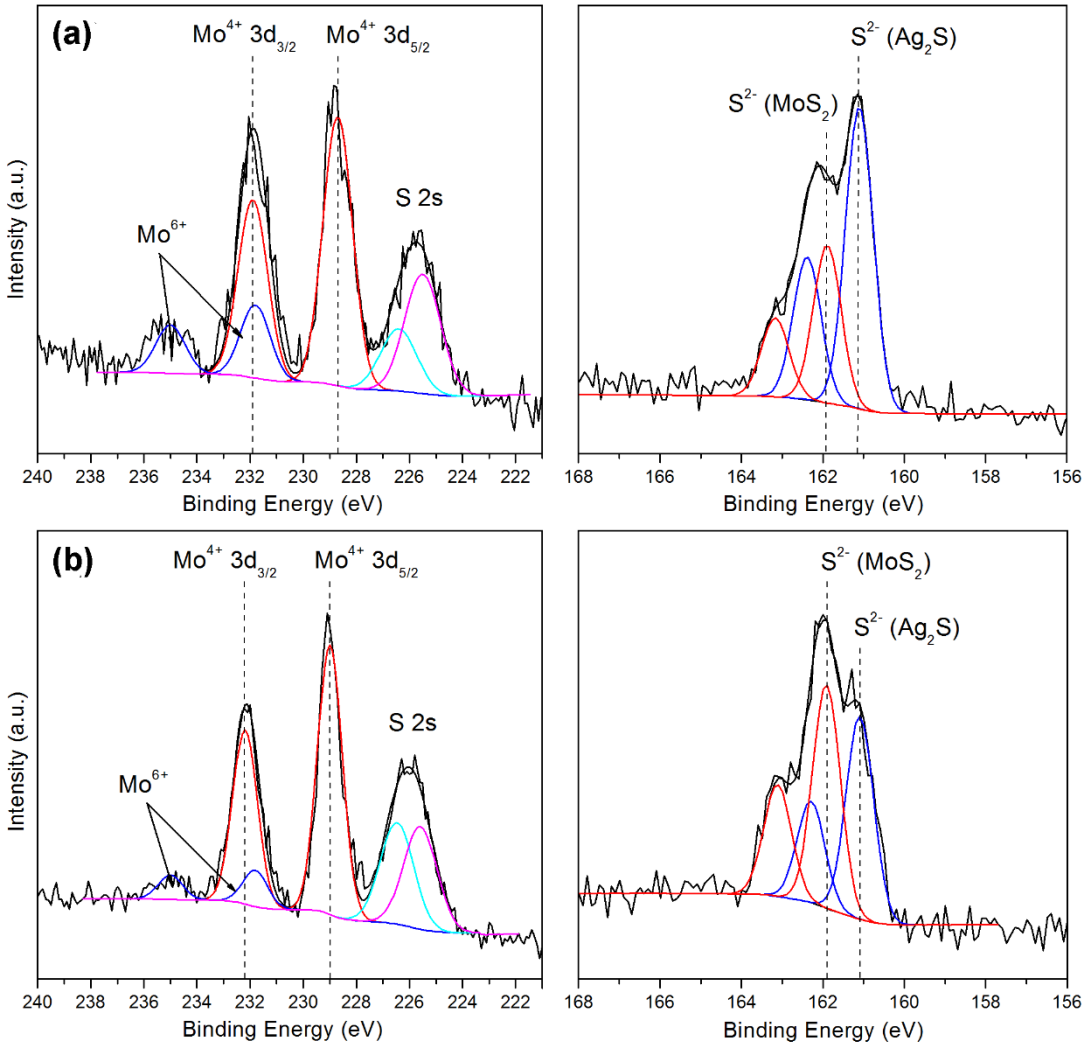

Figure 3.3: XPS spectra showing Mo 3d, S 2s, and S 2p core level peak regions for the 50 mJ sample cooled at (a) 50 ºC/min and (b) 1 ºC/min. The dashed lines indicate the positions of the Mo^{4+} 3d peaks in the 50 ºC/min sample.

The differences in the XPS spectra for samples fabricated at different cooling rates can be explained in terms of the deposition process and the subsequent cooling. When the laser ablates the target, Mo and S atoms with a certain amount of energy are ejected. These Mo and S atoms can be deposited onto the surface of the Ag substrate,

or be implanted in the near-surface regions of the film. Owing to the insolubility of Mo in solid silver,[35] any Mo atoms implanted in the Ag film will immediately precipitate onto the surface of the film. The S atoms on the other hand, react with Ag to form Ag_2S at the surface regions of the film. Remaining S atoms on the sample surface then react with Mo atoms to form MoS_2 on top of the Ag_2S layer. When cooled at 50 ºC/min, the amount of heat was quickly decreased such that the Mo and S atoms are less energetic and lacked the mobility to form highly crystalline MoS_2. For samples that were cooled at 1 °C/min however, the temperature of 500 °C was almost maintained right after laser ablation was stopped and close to equilibrium conditions were experienced. Enough heat was thus preserved such that the Mo and S atoms had sufficient mobility to rearrange themselves to form a more ordered crystalline structure. This less defective ordering translates to smaller FWHMs and a shift to higher binding energies of the Mo^{4+} 3d peaks in XPS measurements. The resulting MoS_2 film also demonstrates a higher degree of sulfurization of Mo, and less oxide is formed.

For MoS_2 grown on Ag, there are always excess Mo atoms remaining on the surface after MoS_2 formation due to the fact that some of the S atoms supplied is consumed to form Ag_2S. These excess metallic Mo species react with oxygen upon exposure to atmospheric conditions to form oxides that sit on top of the MoS_2 layer, but are not present within the MoS_2 structure itself, therefore preserving the integrity of the MoS_2 structure. This is proven by angle-resolved XPS (Figure 3.4), where the relative intensity of the oxide peaks increase significantly from 0.06% to 27% when the take-off angle is reduced from 90º to 15º. As a low take-off angle gives more surface sensitive data, this means that the oxides are present only at the surface regions of the sample. The quality of the as-deposited MoS_2 film is thus believed to be minimally affected by oxide formation.

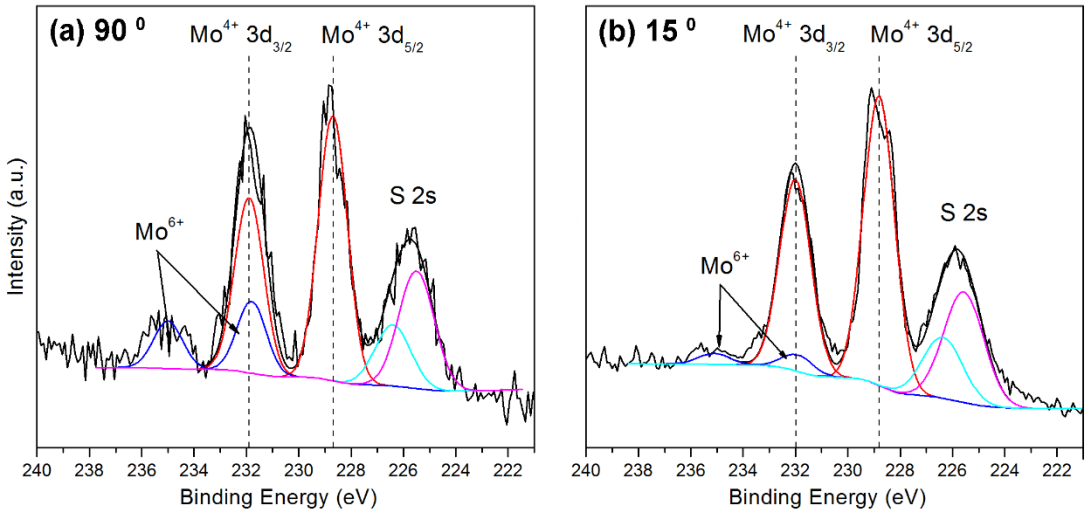

Figure 3.4: Mo 3d and S 2s spectra of the 50 mJ, 10s sample measured at take-off angles of (a) 90º and (b) 15º.

3.2.3. Laser Energy Effects on MoS_2 Growth

Improved crystallinity in the resulting MoS_2 film can also be achieved by increasing the laser energy as shown in Figure 3.5. At 200 mJ laser energy, the Mo^{4+} 3d doublet in the XPS scans is shifted to higher binding energies by 0.3 eV, and the FWHM of the peaks decreases to 1 eV. This is because in the pulsed laser process, higher laser energies give rise to more energetic Mo and S atoms, which subsequently allow the formation of a more ordered structure within a much shorter cooling time. However, the amount of Mo and S atoms supplied during the deposition process would also increase with laser energy, leading to the formation of MoS_2 films with >4 layers when the laser energy is 100 mJ and above. It is nonetheless still feasible to obtain few-layer MoS_2 at higher laser energies by simple modification of the deposition time and target-to-substrate distance.

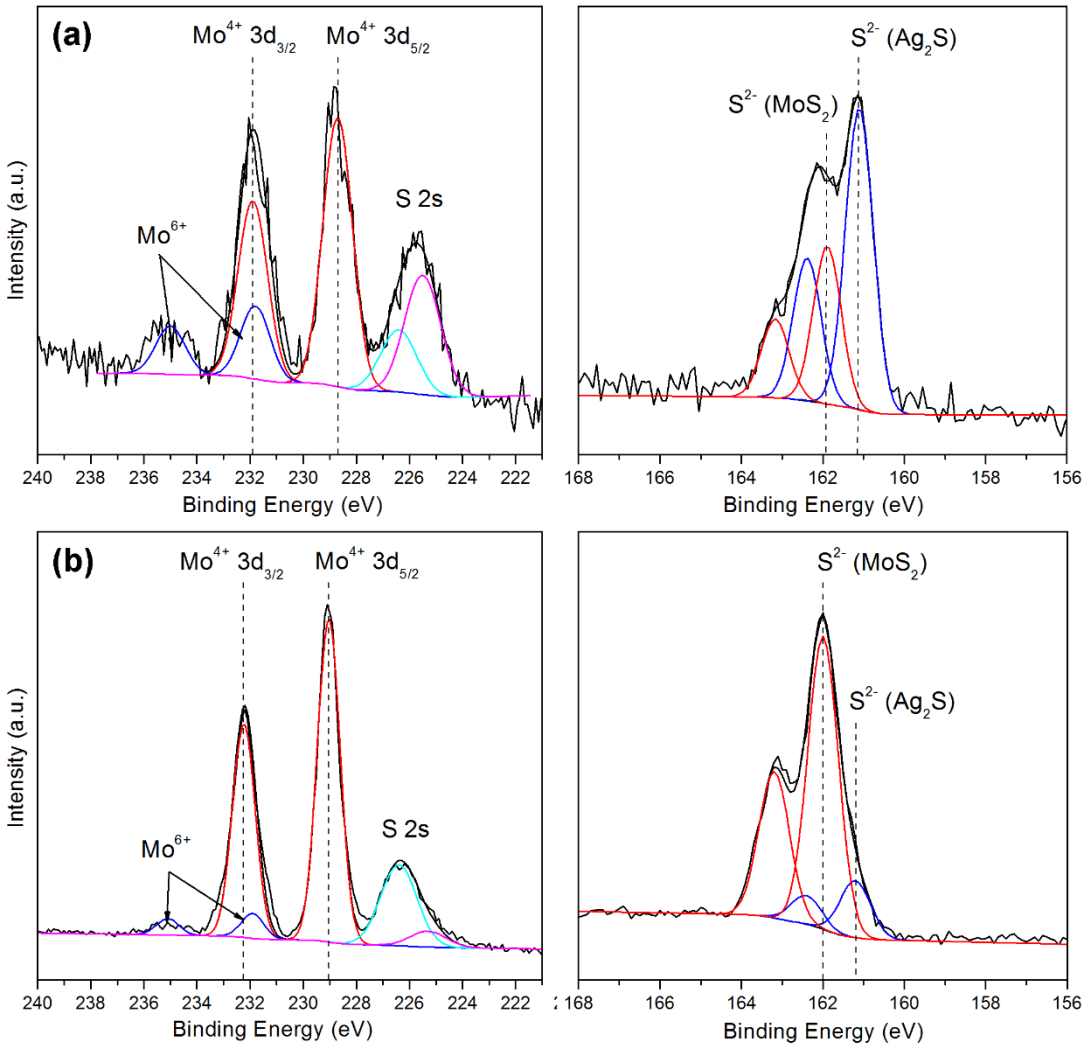

Figure 3.5: XPS spectra showing Mo 3d, S 2s, and S 2p core level peak regions for (a) 50 and (b) 200 mJ samples cooled at 50 ºC/min. The dashed lines indicate the positions of the Mo^{4+} 3d peaks in the 50 mJ sample.

It has been demonstrated that graphene[10] and mica[36] can be exploited for epitaxial growth of ultrathin thin MoS_2 layers owing to their atomically flat surface that is free of dangling bonds, in addition to their hexagonally arranged in-plane lattice characteristics. In both cases, van der Waals forces and strain relaxation effects at the substrate-adlayer interface play a crucial role in the growth of high quality MoS_2. This is particularly so for graphene due to the large lattice mismatch of ~28% with MoS_2. The growth of MoS_2 on these two substrates, graphene and mica, are thus believed to

proceed via van der Waals epitaxy. In the case of metallic substrates such as silver however, it is proposed that the growth of the MoS_2 overlayer proceeds instead by conventional epitaxy involving strong chemical bonding and lattice matching at the substrate-adlayer interface. This is deduced from in-situ formation of the monoclinic Ag_2S phase, as confirmed by the XPS results, which would facilitate the growth of the MoS_2 overlayer by chemical bonding between the sulphur atoms of both materials. And unlike with graphene, there is only a small substrate-adlayer lattice mismatch of ~2.6% between MoS_2 and Ag_2S, allowing the growth of the first MoS_2 layer on Ag_2S to be aided by lattice matching effects. Further study would be required to conclusively determine whether van der Waals epitaxy or lattice matching effects are pre-dominant for MoS_2 growth on silver and other metals.

3.3 Few-layer MoS_2 on Other Metal Substrates

3.3.1 Experimental Procedure

Synthesis: Metal films of approximately 600 nm thickness were sputtered onto normal doped Si substrate and subsequently transferred to the KrF excimer PLD chamber. The laser energies used to ablate the MoS_2 target was 50, 100, and 200 mJ, while the deposition time was set at 10 and 30 s. All other laser parameters and chamber conditions remained the same as those detailed in section 3.2.1. Substrate temperature was kept at 500 °C during ablation and subsequently decreased at a rate of 50 ºC/min until the temperature reached 300 ºC, whereupon natural cooling processes took over.

Characterization: The characterization techniques used to study the as-deposited samples are the same as those detailed in section 3.2.1.

3.3.2 Nanostructural Characterization

Figure 3.6(a) shows the Raman spectra of the as-deposited film on the various metal substrates fabricated using a laser energy of 50 mJ and a deposition time of 10 s. Also included for comparison is the spectrum of powder MoS_2, consisting of two peaks at 379.1 cm^{-1} and 404.8 cm^{-1} that correspond to the 2H-MoS_2 Raman modes of E^1_{2g} and A_{1g} respectively.[6] The in-plane E^1_{2g} mode is associated with the opposite vibration of two S atoms with respect to the Mo atom in the x-y plane, while the out-of-plane A_{1g} mode results from vibration of only S atoms in the z-direction of the unit cell.[28] The presence and intensity of these two peaks are indicators of the crystallinity of MoS_2. Based on the Raman spectra of our samples, only Ag was successful in forming

crystalline MoS_2 at this deposition parameters, while the Mo and S atoms on other metal substrates either form a more disordered structure or a separate compound altogether.

For ultrathin MoS_2 with ≤ 4 layers, the E^1_{2g} band blue-shifts while the A_{1g} vibration red-shifts with decreasing layer thickness.[27] The shift in the A_{1g} peak is attributed to stronger interlayer Van der Waals forces with increasing thickness, caused by the influence of neighbouring layers that suppress atom vibration.[37] For the shift in the E^1_{2g} mode, it is suggested that stacking induced changes in structure or increased dielectric screening of long-range Coulomb interactions in multilayer MoS_2 are more dominant factors. These shifts in Raman peak positions allow reliable identification of layer thickness in MoS_2 samples with less than five layers. For our MoS_2 on Ag samples, the E^1_{2g} and A_{1g} peak positions are determined to occur at 402.4 cm^{-1} and 380.2 cm^{-1} respectively, indicating an ultrathin film with 2-3 layers.

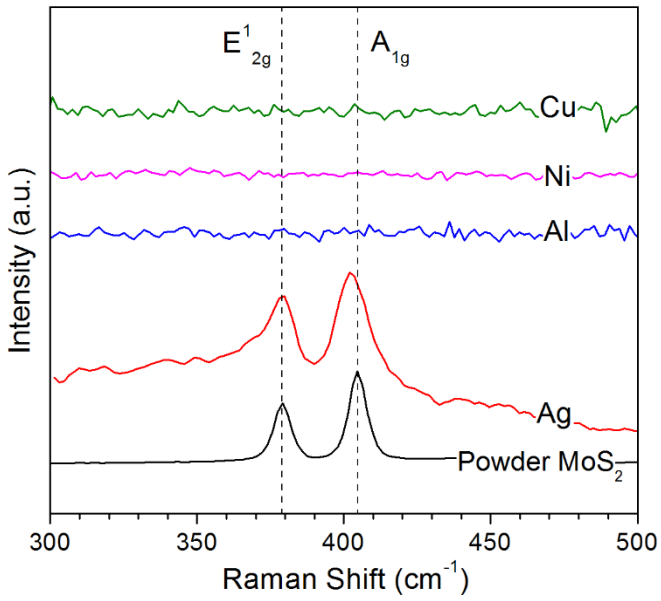

Figure 3.6: Raman spectra of (a) as-grown samples fabricated on different metal substrates at 50 mJ and 10 s. The left and right dashed lines indicate the positions of the E^1_{2g} and A_{1g} peaks in bulk MoS_2 respectively.

Crystalline MoS_2 was also formed on Al when the deposition parameters was adjusted. As shown in Figure 3.7(a), the emergence of the characteristic Raman bands at approximately 379 cm^{-1} and 404 cm^{-1} indicate that a longer deposition time and higher laser energies impart considerable crystal ordering to the MoS_2 structure. This would suggest that a larger amount of source atoms Mo and S are required for formation of a crystalline structure on Al than is needed for Ag substrates. Compared to MoS_2 on Ag, the Raman peak intensities are much lower and the FWHM slightly wider for MoS_2 on Al, both indicators of multiple defects that degrade film quality. The weak Raman signal also makes quantitative analysis of the number of layers in the as-deposited film difficult, particularly in the sample grown at 100 mJ laser energy. For the 50 mJ, 30s sample, a slight blue-shift of the E^1_{2g} band can be observed, suggesting the formation of a MoS_2 film with approximately 3-4 layers. Though neither Ni nor Cu is capable to producing even weakly crystalline MoS_2, it was observed that at higher laser energies, the obtained film on Ni appears to exhibit aggregation or clustering. This is supported by the development of broad peak centred at 403 cm^{-1} when the laser energy reaches 100 mJ in the Raman spectra of Ni samples, as shown in Figure 3.7(b).

TEM images of the Ag and Al samples are shown in Figure 3.8. Highly crystalline MoS_2 of 2-3 layers is imaged as lattice fringes with interlayer spacing of 0.65 nm on top of Ag in Figure 3.8(a), confirming the results from Raman spectroscopy. The interplanar spacings of approximately 0.27 nm present just underneath the layer of MoS_2 can be ascribed to the (120) plane of monoclinic Ag_2S [JCPDS #14-0072]. For the Al sample in Figure 3.8(b), which was fabricated at 50 mJ and 30 s, we observe the presence of broken lattice fringes of MoS_2 on top of an amorphous aluminium native oxide coating. The film is clearly only weakly crystalline and appears to be composed of 3-4 layers, which is in line with the predictions from the Raman analysis.

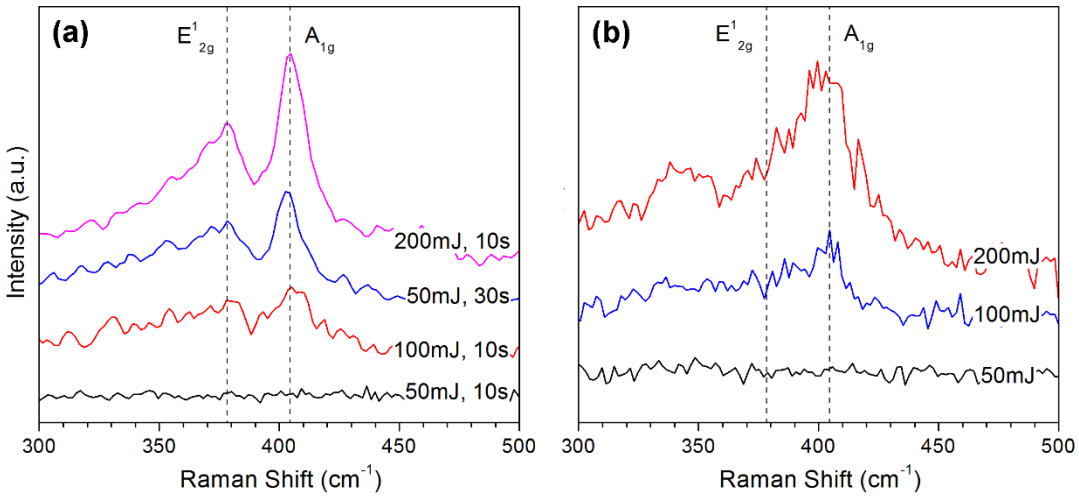

Figure 3.7: Raman spectra of (b) Al samples fabricated using different laser energies and deposition times, and (c) Ni samples fabricated using different laser energies. The left and right dashed lines indicate the positions of the E^1_{2g} and A_{1g} peaks in bulk MoS_2 respectively.

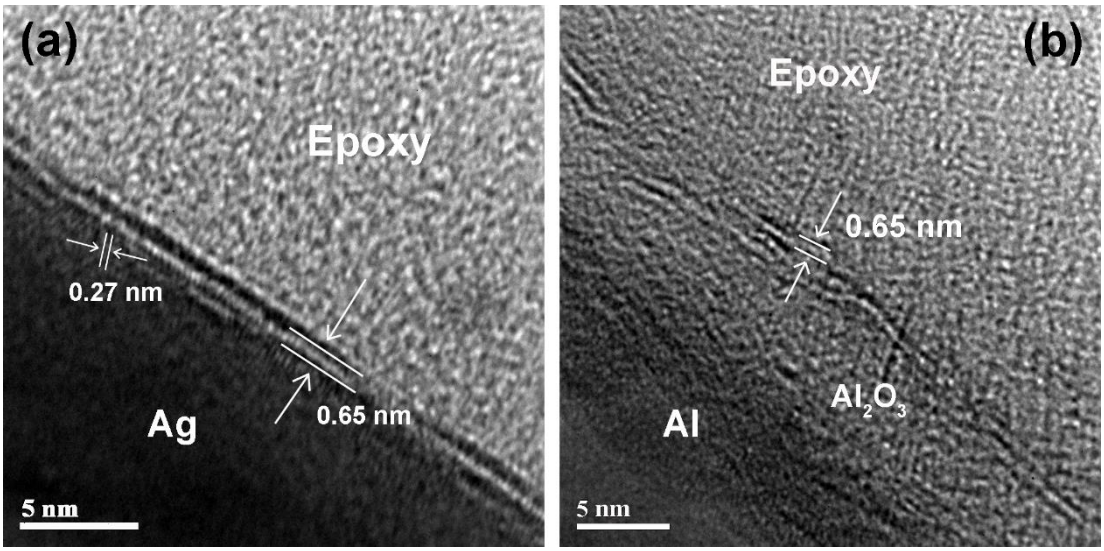

Figure 3.8: (a) Cross-section TEM of (a) Ag sample fabricated at 50 mJ and 10 s. (b) Cross-section TEM of Al sample fabricated at 50 mJ and 30 s.

Figure 3.9 depicts the high resolution XPS scans of Mo and S for films deposited at 50 mJ and for 10 s on Ag, Al and Ni substrates. Two peaks at approximately 228.7 and 231.9 eV that correspond to Mo^{4+} $3d_{5/2}$ and Mo^{4+} $3d_{3/2}$ of MoS_2 respectively are present for all three substrates. In the S 2p spectra, the known doublet peaks of the S^{2-} species in MoS_2 occurs at 161.9 and 163.1 eV, and is similarly present for all metals. This independently confirms that MoS_2 and not a different compound forms on Ag, Al and Ni. There is an additional S 2p doublet in the Al sample located at 163 and 164.2 eV, assigned to the binding energies of apical S^{2-} or bridging disulfide S_2^{2-} ligands,[38] and can essentially be attributed to the presence of amorphous sulfur that significantly reduces the crystalline quality of MoS_2. This pattern of two doublets in the S 2p spectrum of MoS_2 deposited on Al is consistent throughout different growth conditions, and is similar to that of MoS_3.[38,39] The obtained film is also considerably oxidized, judging by the presence and high relative intensity of peaks consistent with Mo^{5+} and Mo^{6+} oxidation states. Compared to the Al samples, the MoS_2 on Ag substrates are of superior crystalline quality; the S 2p doublet of amorphous sulfur is absent and the degree of Mo oxidation is much lower, with the stoichiometric ratio of S atoms to Mo calculated to be close to the ideal value of 2. The additional S 2p doublet for the Ag sample occurs at binding energies of 161.1 and 162.4 eV, which matches well with that of the S^{2-} species in Ag_2S, confirming the presence of an Ag_2S phase that is observed in the TEM results.

The Ni samples exhibit Mo 3d scans that are similar to that of Al, but with lower relative intensities of Mo^{5+} and Mo^{6+} peaks indicating a lower degree of oxidation. Its S 2p high resolution scans on the other hand is a combination of the spectra from Al and Ag samples, consisting of three doublets; the first pair contributed by amorphous sulfur, the second due to S^{2-} species of MoS_2 and the final doublet appearing at 161.1

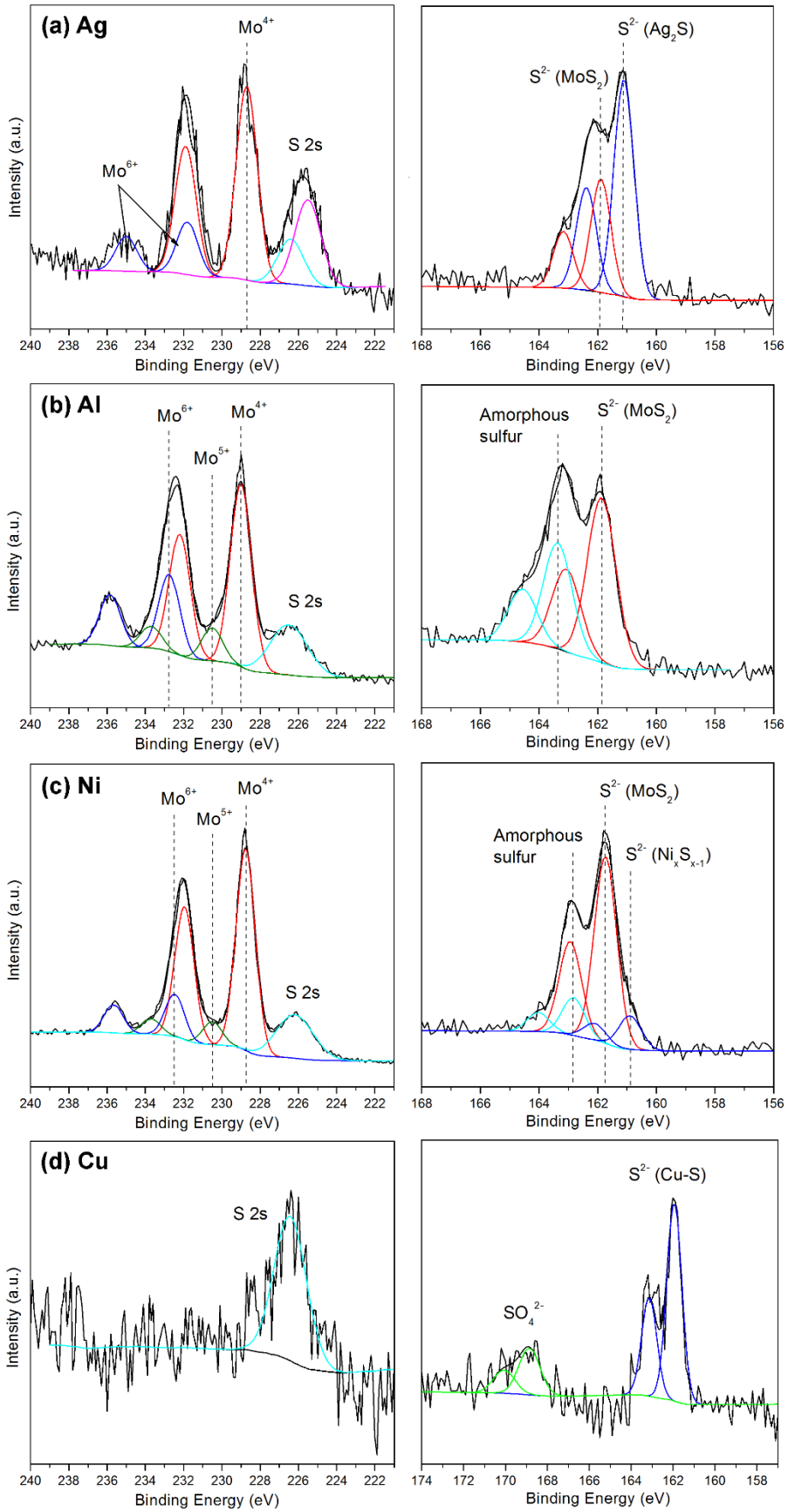

Figure 3.9: XPS spectra showing Mo 3d, S 2s, and S 2p core level peak regions for (a) Ag, (b) Al, (c) Ni and (d) Cu samples fabricated at 50 mJ and 10 s.

and 162.3 eV is within the range for metal sulfide groups. It can thus be concluded that a small amount of Ni-S phase was formed at the growth temperature of 500 ºC. In the XPS scans of Cu shown in Figure 3.9(d), we observe that no Mo is detected in the sample, with the peak at 226 eV in the Mo 3d scan attributed to S 2s. The S 2p spectra contains two doublets, one occurring at binding energies of 161.7 and 162.9 eV and in the absence of Mo is matched to S^{2-} a Cu-S phase that forms in-situ. The second doublet occurs at 168.5 and 169.7 eV, signifying the presence of oxidized sulfur species SO_4^{2-}.

3.3.3 Discussion

Across the four metals tested, highly crystalline few-layer MoS_2 was formed only on Ag, but not on Al, Ni and Cu. To understand this phenomenon, we must take into account the solubility and chemical reactivity of Mo and S atoms with these metals. We consider also that with PLD, the supplied source atoms are energetic and can penetrate into the metal layer rather than simply being deposited onto the surface. In the case of silver, Mo is insoluble in solid Ag at any temperature,[35] while S reacts with Ag to form a silver sulphide phase. During the initial growth process, chemisorption of S atoms into Ag gives rise to the formation of Ag_2S at the surface regions of the substrate. The relatively intense XPS signals from the S^{2-} species of Ag_2S suggests that MoS_2 is strongly interacting with the silver substrate through the formation of sulfide bonds; Mo atoms that segregate out of silver bind to the sulfur species in Ag_2S, in addition to unreacted S atoms. The energy supplied by the pulsed laser and by heating imparts mobility to the Mo and S atoms that allow them to rearrange into an orderly configuration during the subsequent cooling process. Small crystallites of MoS_2

nucleating in the first part of crystallization process are supported and surrounded by a soft Ag_2S phase matrix, which grants further mobility to the atoms and thus promotes grain growth. A schematic diagram of the growth process is shown in Figure 3.10. Minimal lattice mismatch (~2.6%) between the (120) plane of Ag_2S and the b-axis of the MoS_2 unit cell (Figure 3.11) further facilitates periodic ordering that gives the obtained film its high crystallinity. As laser energy can be increased and cooling rate decreased to provide more energetic source atoms, the degree of crystallinity in the resulting MoS_2 film can be tuned as desired to achieve the optimum value. As mentioned in section 3.2.2, it also known that the structural integrity of the as-deposited MoS_2 film is only minimally affected by the presence of Mo oxides. This was deduced from angle-resolved XPS measurements and the fact that the calculated stoichiometric ratio of S : Mo in the sample is close the ideal value of 2.

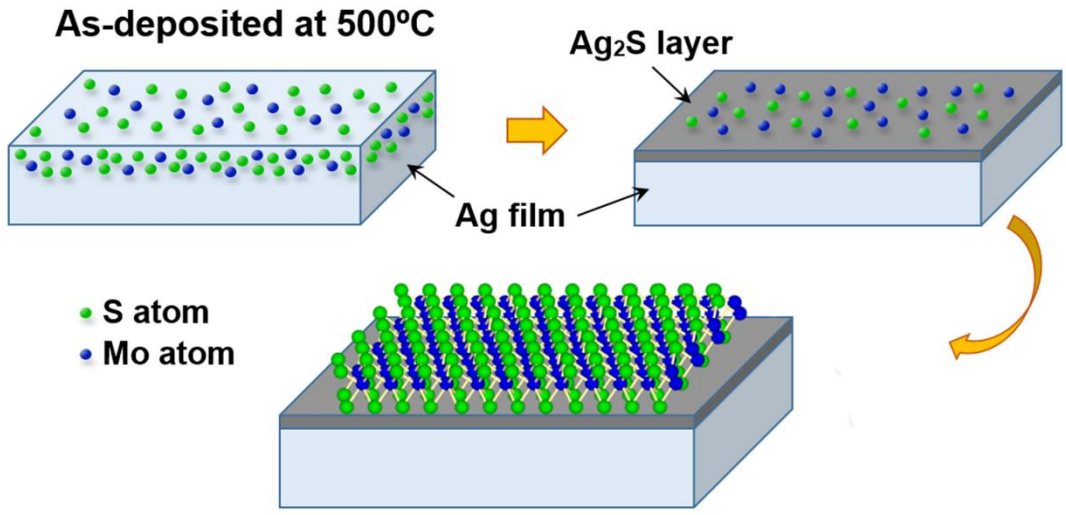

Figure 3.10: Schematic diagram of the growth of MoS_2 on silver substrates by PLD.

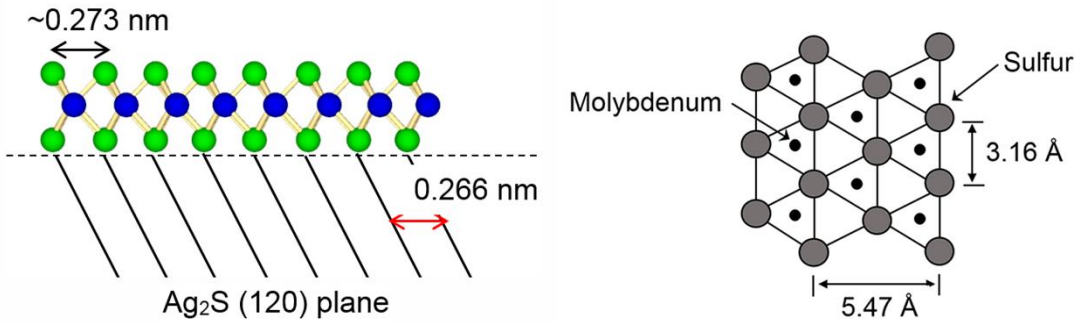

Figure 3.11: MoS_2 film on top of (120) plane of Ag_2S. Lattice misfit between the two phases is calculated to be ~2.6%.

Under atmospheric conditions, Al forms a passivating oxide layer with chemical formula Al_2O_3, which can be clearly observed as a bright amorphous layer in the TEM images of Al samples. Mo atoms implanted into the Al substrate subsequently interact strongly with the oxide layer through bond formation with oxygen atoms, as shown by the prominent peaks from Mo^{5+} and Mo^{6+} states in the XPS scans. As Mo atoms are initially consumed by oxide formation, there are always excess S atoms on the substrate surface that bond to each other to form elemental sulfur. Furthermore, the relatively large amounts of molybdenum oxide produced compared to the Ag substrates necessitates that greater quantities of Mo and S atoms be supplied before crystalline MoS_2 can be formed on Al. Hence the reason why the characteristic Raman peaks of crystalline MoS_2 only appear after longer deposition times of 30s on Al as compared to Ag substrates. However, the MoS_2 film formed on Al is of poor quality due to the uneven surface of the substrate oxide layer and its mostly amorphous nature, which creates a high energy barrier to crystallization. On such amorphous substrates nuclei are randomly oriented, and there is competition among crystallites that nucleate in various orientation during film growth. Consequently coalescence does not occur as it is more favourable for crystallites to remain as islands embedded in an amorphous

matrix rather than form a continuous crystalline film. This leads to the formation of a broken, semi-crystalline MoS_2 film on top of aluminium. An increase in deposition time improves the crystallinity of the film slightly because the first layer of semi-crystalline MoS_2 becomes part of the support/template for succeeding layers, lowering the energy barrier to crystallization. Increasing the laser energy gives rise to the same effects, in addition to imparting enhanced mobility to the atoms.

Both Cu and Ni develop native oxide coatings in air, similar to Al. Oxides of molybdenum are formed when Mo atoms are embedded in the Ni substrate because of the low solubility of Mo in NiO, but the adlayer-substrate interaction through the oxygen bonding is much weaker than in the Al substrate, as deduced from the lower relative intensity of the XPS peaks from Mo oxidation states. A lower degree of oxidation means that more Mo atoms are available for reaction with sulfur, and thus the relative intensity of the XPS peaks from amorphous sulfur are also significantly lower in comparison to the Al samples. According to the Ni-S phase diagram,[40] a Ni_xS_{x-1} phase can be in equilibrium with the solid phase with increasing sulfur content. While a Ni-S phase does form in-situ, the S 2p peaks corresponding to this phase are very weak, as opposed to the intense signal from S^{2-} of Ag_2S in the Ag sample. This suggests that the amount of Ni-S phase present in the sample is very low, and insufficient to act as a template for thin film growth. Ni/NiO (d_{Ni} = 0.352 nm,[41] d_{NiO} = 0.417 nm[42]) thus makes up the bulk of the surface upon which MoS_2 grows, and the resulting film is amorphous at low laser energies. With an increase in the laser energy, the MoS_2 film begins to exhibit signs of clustering due to enhanced atomic mobility and some order in the arrangement of atoms is achieved, marked by the emergence of a broad peak at ~403 cm^{-1} in the Raman spectra. Increasing the deposition time makes little to no difference however, as clustering requires energy that must be provided by heating or

from the laser. Crystallization is unable to take place owing to the relatively large lattice mismatches between the template and MoS_2, which creates large stresses in the obtained film that must be released by breaking the periodic arrangement of atoms. In the case of Cu, the formation of its characteristic patina, composed of a mixture of sulfates, carbonates and sulfides, dominates over any other reaction. This is inferred from the presence of oxidized sulfur species SO_4^{2-} in the XPS scans, and an observable colour change in the film from reddish to cyan. Mo has near-zero solubility in Cu, and as it is unable to bind to oxygen, all of which is consumed by the formation of the patina, the Mo atoms exists only as adsorbates on the Cu film. They are thus easily released by desorption with the thermal energy provided by heating during the deposition process, and consequently no Mo species are detected in XPS scans.

In both section 3.2 and 3.3, the growth of MoS_2 by PLD produced multiple layers of the material, with the thinnest sample possessing 2-3 layers. This raises the question of whether a single layer of MoS_2 can be grown by PLD. Because the MoS_2 layers grow by conventional epitaxy on Ag, the first layer will always be chemically bonded to the substrate and therefore a true monolayer of MoS_2 cannot be obtained on metals. With different substrates however, it is possible to grow monolayer MoS_2. Based on supplemental experiments using sapphire, it was found that the MoS_2 layers grow by van der Waals epitaxy on these substrates and thus a true monolayer of MoS_2 can be obtained. However, one drawback of using sapphire is that the resultant film is always oxygen-rich (sulfur-deficient) and therefore has poor crystallinity. A post-deposition heat treatment with sulfur and hydrogen gas is needed to reduce the as-deposited, oxygen-rich MoS_2 to highly crystalline MoS_2 with Mo : S stoichiometric ratio close to 2.

3.4 Few-layer MoS_2 Field Emitters by PLD

3.4.1 Experimental Procedure

Synthesis: Ag and Al metal nanocones were fabricated from sputter-deposited metal films through an ion irradiation technique by bombardment with Ar^+ ions using a Kaufman type ion gun (ION TECH. INC. Ltd., model 3-1500-100FC). The ion beam was directed at an incident angle of 60 ºC to the surface of the film, with the beam diameter and energy set to 4 cm and 1000 eV respectively. Irradiation was performed at room temperature for 8 min at a working pressure of 5×10^{-2} Pa. The as-fabricated metal nanocones were then transferred to the KrF excimer PLD chamber and MoS_2 growth was carried out at deposition times of 10 s, laser energies of 50 and 200 mJ, and a cooling rate of 20 ºC/min. All other laser parameters and chamber conditions used remained the same as those detailed in section 3.2.1. The Ag and Al nanocones with MoS_2 deposited at 50 and 200 mJ will hereafter be referred to as Ag-50, Ag-200, Al-50 and Al-200 respectively.

Characterization: The nanocones before and after MoS_2 deposition were analysed with a Zeiss Supra 40 field emission SEM using an in-lens secondary electron detector. Optical properties of the as-deposited samples were characterized by a Horiba MicroRaman HR Evolution System using an Argon laser beam with an excitation wavelength of 514.5 nm. XPS spectra was obtained via a Kratos Analytical Axis Ultra^{DLD} UHV spectrometer with a monochromatized Al Kα x-ray source (1486.6eV) a take-off angle of 90º with respect to the sample surface.

Field Emission Tests: Field emission studies were carried out using a probe tip setup at room temperature and at a base pressure of 2×10^{-6} Torr. An electrochemically

etched tungsten needle with a tip diameter of 50 μm was used as the anode, while the sample acted as the cathode. The zero-distance point was determined by moving the anode with 10 V of applied voltage until it came into contact with the cathode, as indicated by a non-negligible current reading on the multimeter. The anode is then slowly moved away from the cathode until the current just drops to zero. On this same spot on the sample surface, the distance between the anode and sample was adjusted to 10 μm using a micrometer stage with an accuracy of 0.5 μm. The current-voltage relationship was obtained by applying a DC voltage across the sample and anode and emission current was measured using a Keithley 2410 source measurement unit. Several emission cycles were taken in order to verify the stability and the reproducibility of the I-V curves.

3.4.2 Nanostructural Characterization

Figure 3.12 shows the surface morphology of the as-fabricated Ag and Al metal cones. It can be seen that for both types, a mostly uniform and highly dense array of nanosized cones was produced from the ion irradiation. For Ag, the nanocone tips have a tendency to undergo fracturing and breakage, resulting in detritus scattered over the surface of the cones. The surface of the nancones are also highly textured and Ag crystallite grains can be clearly observed. The heights of the Ag nanocones are within the range of 650–900 nm, whereas the diameters are within the range of 200–300 nm, with the apex of the nanocones having an average diameter of ~50 nm. The Al nanocones are somewhat shorter, with heights within the range of 500–800 nm and diameters within the range of 200–300 nm. The apex of the Al nanocones are also slightly larger at an average diameter of ~60 nm.

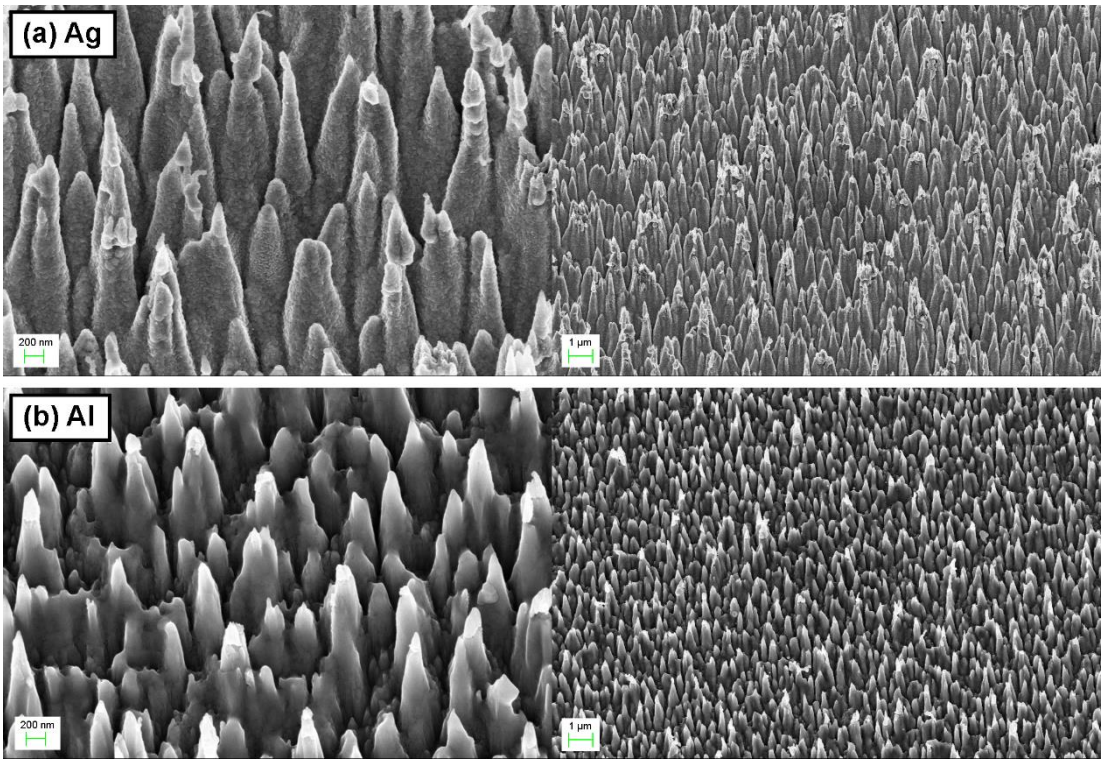

Figure 3.12: (Left) High magnification and (right) low magnification SEM images of (a) Ag and (b) Al nanocones before MoS_2 growth.

It can be observed from Figure 3.13(b) that the Al nanocones are unaffected by temperatures up to and including 500 ºC, having retained their shapes and structural integrity even after a heat treatment without MoS_2 growth. In contrast, the Ag nanocones almost completely lost their conical geometry to become a particulate film with a large density of fractured cone tips remaining on the surface [Figure 3.13(a)]. In addition, the Ag crystallites have undergone rapid recrystallization and grain growth to reach sizes of up to 1.4 µm from an average of ~50 nm before heat treatment. Figure 3.14 shows the SEM images of Ag and Al nanocones after MoS_2 growth by PLD. Both Al and Ag nanostructures are minimally affected by the bombardment of energetic species at low laser energy levels of 50 mJ. When the laser energy is increased to 200 mJ however, the Al nanocones begin to show signs of minor degradation [Figure 3.13(c) and (d)], with some of the cone tips fracturing and breaking. This indicates that

ideally, the laser energy should be kept to a minimum to prevent sputtering of the nanocones by incoming energetic species.

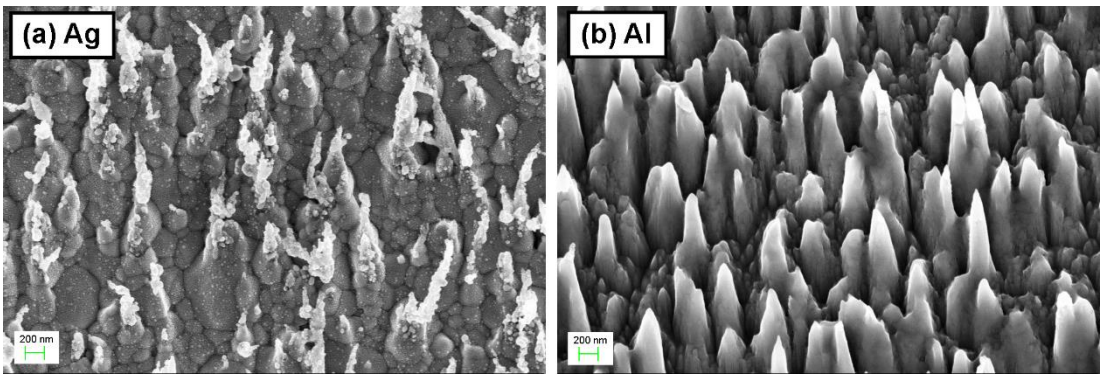

Figure 3.13: SEM images of (a) Ag and (b) Al nanocones after heating to 500 ºC without MoS_2 growth.

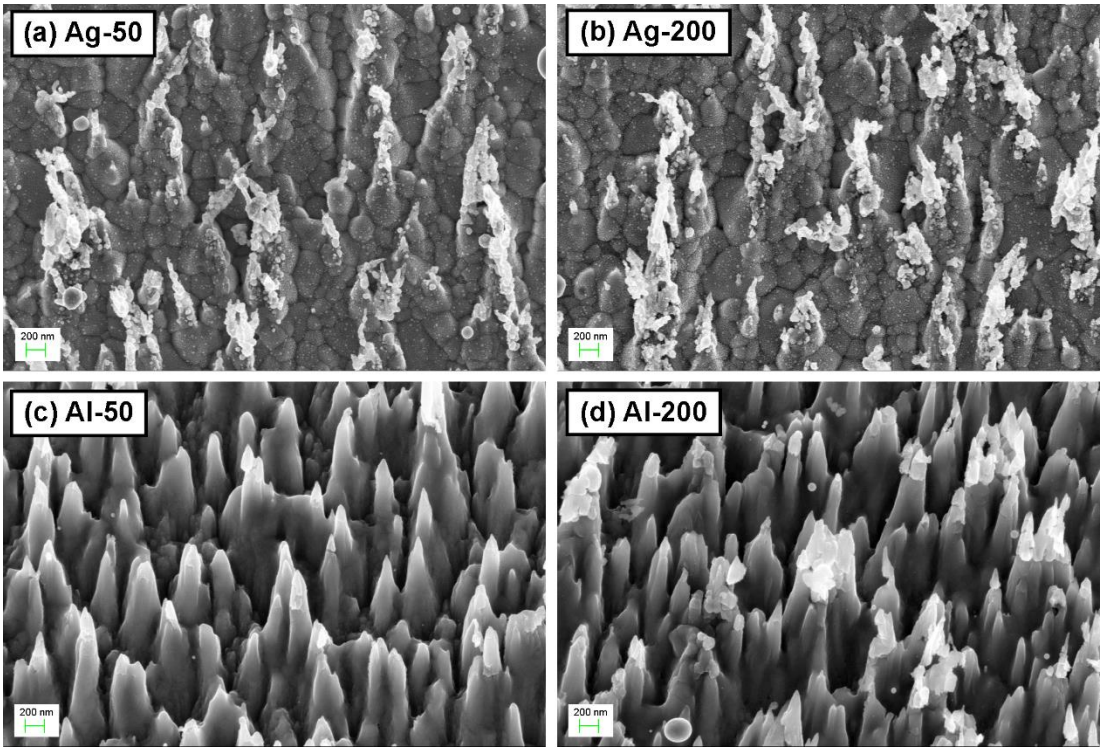

Figure 3.14: SEM images of (a)-(b) Ag and (c)-(d) Al nanocones after MoS_2 growth.

The Raman spectra of the Ag and Al cones after MoS_2 are shown in Figure 3.15(a). The two characteristic 2H-MoS_2 modes of E^1_{2g} and A_{1g} are present in all samples except for Al-50. Despite the emergence of 2H-MoS_2 Raman modes in the Al-200 sample, it can be seen from the S 2p XPS spectra in Figure 3.15(b) that the MoS_2 layers remain highly defective due to the presence of apical S^{2-} or bridging disulfide S_2^{2-} ligands (amorphous sulfur).[38] For the Ag samples, Raman and XPS measurements were conducted multiple times at different points over the entire sample surface to test for uniformity of the deposited MoS_2 film. The results were mostly consistent throughout all measurements, which indicates that the MoS_2 layers were uniformly deposited onto the nanocones.

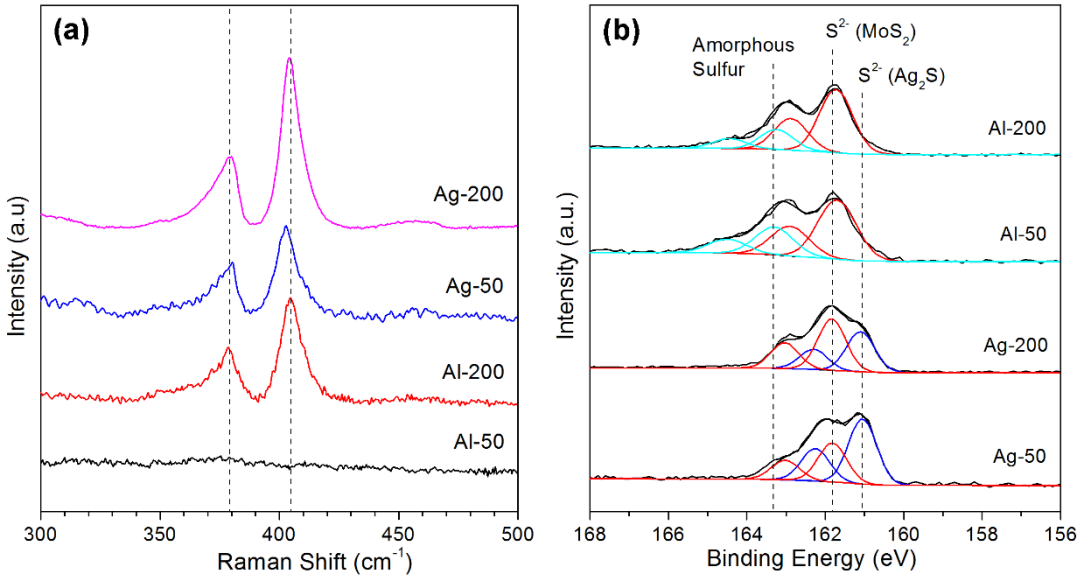

Figure. 3.15: (a) Raman spectra of as-grown MoS_2 on Ag and Al nanocones. The left and right dashed lines indicate the positions of the E^1_{2g} and A_{1g} peaks in bulk MoS_2 respectively. (b) XPS spectra showing S 2p core level peak regions for all samples.

3.4.3 Field Emission Study of Few-layer MoS_2-coated Nanocones

The field emission current versus voltage (I-V) plots for all MoS_2-coated samples are shown in Figure 3.16. In this work, the turn-on voltage was defined to be the voltage required to reach a current of 1 μA. The as-fabricated Ag and Al nanocones were not able to reach the electron emission turn-on current within the maximum limits of the voltage source (not shown in the figure). Of the MoS_2-coated nanocones, only Ag-50 and Ag-200 were able to attain the emission turn-on current, with the corresponding turn-voltages of 810 and 875 V respectively. However, it was noted that the Al-200 sample began to exhibit some degree of electron field emission at the high voltage region, reaching a maximum current of ~8.5 × 10^{-8} A at 1000 V. Fowler-Nordheim (F-N) plots of the samples depicted in Figure 3.17 reveal a linear trend between $\ln\left(\frac{I}{V^2}\right)$ and $\left(\frac{1}{V}\right)$, indicating that electron emission occurs through a quantum tunnelling process. The linear slope of the F-N plot is related to the work function of the material, ø, the field enhancement factor, β, and the distance between the electrodes, d, and can be expressed by transformation of the F-N equation as,

$$Slope = -\frac{6.83 \times 10^3 \phi^{\frac{3}{2}} d}{\beta} \tag{3.1}$$

Assuming ϕ_{MoS_2} = 4.9 eV,[43] the value of β was calculated to be 60, 36 and 70 for samples Ag-50, Ag-200 and Al-200 respectively.

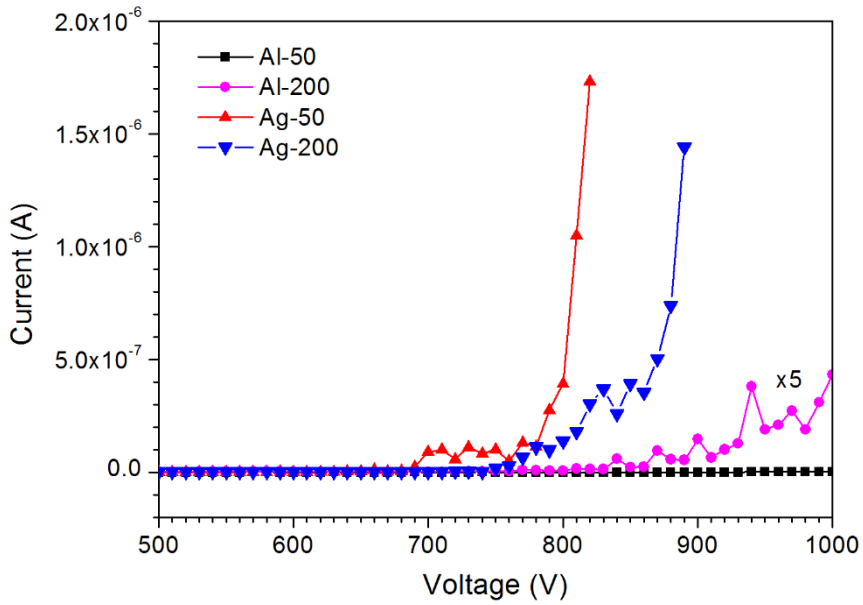

Figure 3.16: Field emission plots of current against voltage for MoS_2-coated Ag and Al nanocones. The *y*-scale of the plot for sample Al-200 is expanded by 5 times.

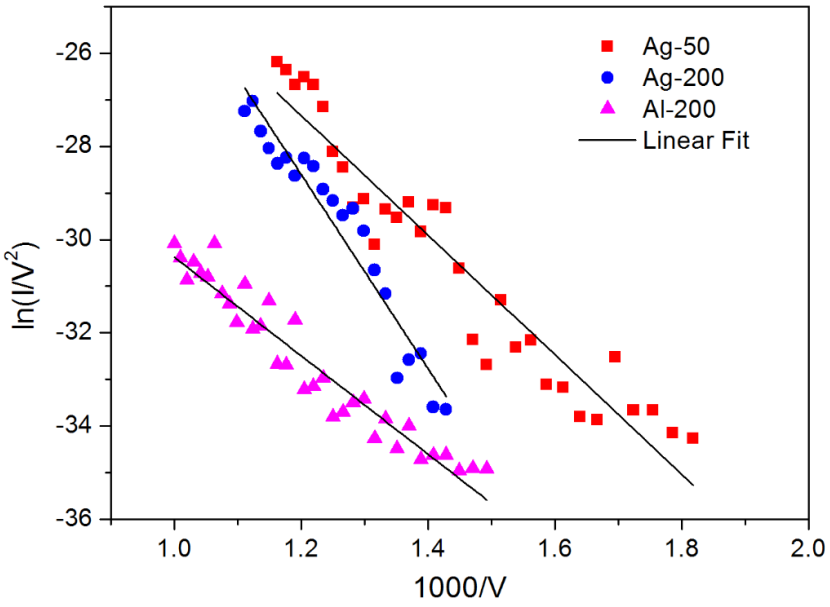

Figure 3.17: Fowler-Nordheim plots for MoS_2-coated Ag and Al nanocones.

3.4.4 Discussion

As observed from the SEM images, the Ag nanocones lost most of their definitive conical geometry after heating to 500 ºC whereas the Al nanocones remained largely unaffected. This is attributed to rapid recrystallization, grain growth and densification of the Ag structure. Grain growth usually proceeds through the motion of grain boundaries, which results in the shrinkage and elimination of small grains as well as an eventual increase in the average size of the remaining grains. Diffusivity of material is a strong function of temperature, and as such grain growth processes are expected to show similar dependency. Thin film studies of Ag has so far shown that grain boundary motion plays an important role in grain growth even at homologous temperatures (reaction temperature divided by melting temperature) as low as 0.2.[44] Given that the melting temperature of Ag is 961 ºC,[45] the temperature of 500 °C used for the growth of MoS_2 by PLD corresponds to a homologous temperature of 0.52. Although this temperature is held for only a short duration of 10 s, the nanocones are heated up and cooled to room temperature at a rate of ~20 ºC/min. This means that the Ag nanocones remain at homologous temperatures of > 0.2 for at least 30 min, which is sufficient to induce significant grain growth in Ag.[46] In addition, Ag films have a strong tendency to undergo an out-of-plane texture change from (111) orientation to (100) as a consequence of abnormal grain growth,[47] which could also contribute to the loss of the conical geometry. Interestingly, despite this change in structure, the MoS_2-coated nanocones were still able to achieve turn-on current within the maximum limits of the applied voltage. In fact, they were the only samples to do so. To understand this, we first consider the parameters and field emission mechanism.

The most commonly used parameter to characterise field emission properties is the geometric electric field enhancement, which serves as a measure of the ability of the emitter to enhance an applied field. By increasing the aspect ratio of emitters, the local field can be increased to more than a hundred-fold above the average applied field, making it possible to obtain emission with average applied fields of 1×10^5 to 1×10^6 V cm^{-1}, whereas theoretically no measurable emission would occur from a perfectly smooth surface at fields of less than 1×10^7 V cm^{-1}.[47] Another way to enhance the field emission performance of a material is by coating with an impurity-doped semiconductor that can decrease the effective barrier height for emission.[46] Because a potential barrier is formed at the metal-semiconductor interface, electrons from the metal must first tunnel through this barrier into the conduction band of the semiconductor before gaining energy from the applied field and finally escaping into vacuum.[48] Field emission performance is thus limited by the barrier at the metal-semiconductor interface rather than the barrier at the semiconductor-vacuum junction. A high carrier concentration in the conduction band of the semiconductor would lead to a relatively thin depletion layer and hence a narrower potential barrier.

For MoS_2-coated nanocones, field emission was able to take place despite the loss of the conical structure as the surface remained rough, with numerous nanometric protrusions that act as sites for electron emission. This can be seen from the β value of Ag-50 that is only slightly lower than that of the Al-200, which retained its conical structures. However, the overall low β values for all samples indicates that, rather than geometrical enhancement, the more dominant mechanism for field emission is the lowering of the effective barrier height by coating with crystalline MoS_2 layers. Both Ag ($ø_{Ag}$ = 4.3–4.6 eV)[49] and Al ($ø_{Al}$ =4.3 eV)[49] metal have work functions that are larger than the electron affinity of MoS_2 (χ = 4.0 eV)[50]. Thus upon making contact the

conduction and valence bands of MoS_2 bend upwards in order to achieve equilibrium between the metal Fermi level and the MoS_2 chemical potential, leading to the formation of a Schottky barrier. Figure 3.18 shows the schematic diagrams of the band structure of the uncoated and coated metal nanocones. Various groups[15,16.51] have used first principle calculations within density functional theory (DFT) to show that the adsorption of MoS_2 on transition metal substrates such as Ag and Ti results in a significant charge transfer from the metal to MoS_2, which ultimately leads to a net n-type doping of MoS_2. Moreover, Kang et al.[15] demonstrated that strong adhesion at the interface through covalent bonds can strongly perturb the band structure of TMDs to result in significant lowering of the Schottky barrier, in some cases to the point that the TMD regions directly adjacent to the metal becomes metalized and the Schottky barrier vanishes. Zhong et al.[16] showed that for monolayer MoS_2 adsorbed on an Ag surface, there is medium adhesion at the interface and the band structure of MoS_2 is destroyed but still identifiable. In this scenario, the Schottky barrier heights were determined experimentally to be as low as 0.212 eV and 0.138 eV for monolayer and bilayer MoS_2 respectively. In this work, the MoS_2 layers were established to bond covalently to the underlying Ag substrate (see section 3.3.3). As such, we expect the Schottky barrier heights for the MoS_2-coated nanocones to be just as low or even lower. Combined with the n-type doping of MoS_2 due to charge transfer from Ag, the probability of Fowler-Nordheim tunnelling increases greatly and samples Ag-50 and Ag-200 are able to reach the turn-on current within the limits of the applied voltage. Although a higher MoS_2 layer number favours smaller Schottky barrier heights,[16] Ag-200 was measured as having a higher turn-on voltage than Ag-50 despite its greater thickness. Because the β value is almost half that of Ag-50, it is likely that the decline in performance is due to a geometric factor. For example, the tips of the surface protrusions could be broadened

due to the thicker MoS_2 coating, or tip blunting due to breakage was caused by the higher laser energy used. In addition, a thicker coating can lead to more significant electron scattering, reducing the efficiency of electron transportation within the film.

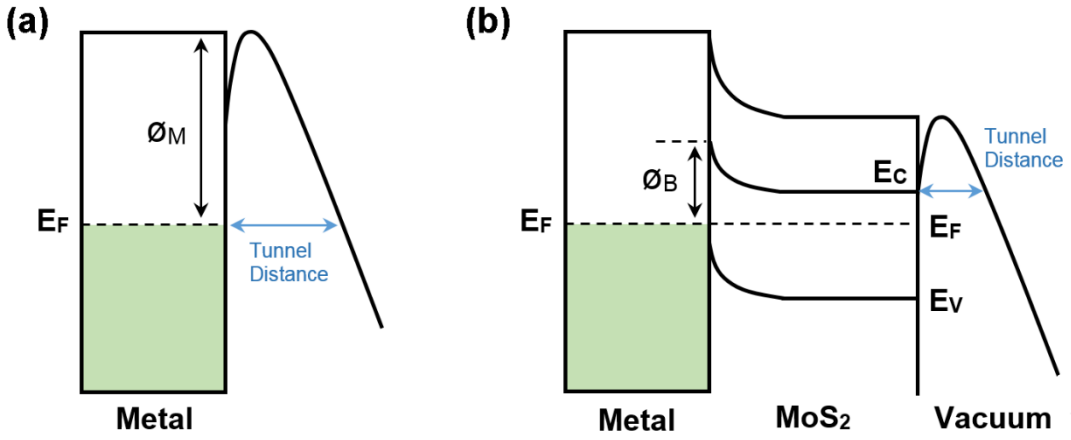

Figure 3.18: Band alignments of (a) pristine metal nanocones and (b) MoS_2-coated nanocones.

In contrast to the MoS_2-coated Ag nanocones, the corresponding Al samples did not demonstrate appreciable field emission. One possible reason for this is the unsuitability of Al as a base for Mo_2. Due to the absence of d orbitals, which can mix with the band-edge d orbitals of Mo to result in better electron injection, Al does not make good contacts for 2D TMDs.[15] Indeed, experimental results have shown that Al forms high-resistance contacts with 2D TMDs. Furthermore, the high chemical reactivity of Al leads to partial oxidation of the surface when exposed to air, which may induce a wide tunnelling barrier at the Al-MoS_2 interface. Another issue is the quality of the MoS_2 layers grown on top of Al substrates. In field emission, the conductivity of emitters is an important physical property.[52] The presence of defects within the emitters limits their conductivity by acting as sites that trap or scatter electrons, and thus adversely affects field emission performance. As discussed in section 3.3, the MoS_2

film deposited at 50 mJ on Al is highly defective and effectively amorphous. It is hence not surprising that Al-50 exhibits no field emission performance even at the maximum applied voltage of 1000 V. The MoS_2 layers in Al-200 on the other hand have appreciable crystallinity, but still contains many defects as deduced from the presence of apical S^{2-} and bridging disulfide S_2^{2-} ligands in the S 2p XPS spectra. As a result, the sample begins to emit electrons by field emission at the extreme high voltage region but does not reach the turn-on current within the maximum limits of the voltage.

Although the MoS_2-coated Ag nanocones were able to achieve turn-on current, the voltages at which this occurred were rather high. In comparison, a similar probe setup used to characterised MoS_2 nanoflowers[25] gave a turn-on voltage of ~ 760 V for an anode-cathode separation of 100 μm. This is believed to be due to the geometric shape of the Ag nanocones, which after MoS_2 deposition is completely lost. Moreover, the tip size of the original nancones were much larger (~60 nm) compared to the sharp edges of the MoS_2 nanoflowers (~3 nm). All these factors contribute to a much lower β value that limits the enhancement of the field emission properties of Ag nanocones when coated with MoS_2. Future consideration should thus be given to preserving the nanocone structure and reducing tip sizes in order to fabricate better MoS_2-based field emitters.

3.5 Summary

In section 3.2, highly crystalline few-layer MoS_2 was fabricated on Ag substrates using the PLD technique. The effects of cooling rate and laser energy of the resulting MoS_2 films were studied using Raman and Photoluminescence spectroscopy as well as XPS. The films exhibit prominent band gap PL, indicating that the as-

deposited MoS_2 sheets possess good structural integrity and a sufficiently low density of defects that may inhibit luminescence. It was observed that limiting the amount of Mo and S supplied during deposition was critical to the production of few-layer MoS_2 ($\leq$ 4 layers). Slower cooling rates and higher laser energies led to better crystallinity. Thus, by varying the parameters of deposition time, laser energy, and cooling rate, the formation of high quality few-layer MoS_2 can be precisely controlled. These results show that it is possible to produce few-layer MoS_2 using a physical deposition technique at relatively lower temperatures compared to MoS_2 growth by CVD.

In section 3.3, we presented the fabrication of crystalline few-layer MoS_2 on metal substrates using PLD. The technique involves the in-situ formation of an appropriate scaffold/template for growth and the subsequent segregation of dissolved source atoms in the metal onto the substrate surface. As such, the method is a combined physical and chemical process in which solubility and chemical reactivity of the source atoms with the underlying metal substrate are important factors affecting film growth. Of particular significance is the reaction of sulfur with the substrate; formation of a metal sulfide phase in-situ is critical to growth of highly crystalline MoS_2. Any interactions between Mo and the substrate however, is usually detrimental to the film quality as this leaves excess S atoms on the surface that bind to each other to form amorphous sulfur. Despite the formation of metal sulfides in-situ, both Ni and Cu failed to produce crystalline MoS_2. For either case, the sulfide formed was insufficient, in addition to being consumed to formed sulfates on Cu. In contrast, Ag was found to be very successful as a substrate for highly crystalline few-layer MoS_2 fabrication even at low laser energies due to the formation of substantial amounts of an Ag_2S phase. Al substrates however, could produce only semi-crystalline few-layer MoS_2 when the growth parameters was adjusted to cater to the metal. This is partly attributed to the

amorphous nature of the native oxide coating, and partly due to the energetic Mo atoms supplied by PLD that penetrate into the substrate, resulting in high levels of Mo oxides. The fact that the in-situ formation of a sulfide phase is critical for growth of good quality MoS_2 on metals indicates that conventional epitaxy and lattice matching effects are predominant over van der Waals epitaxy at the substrate-adlayer interface.

MoS_2-based field emitters were fabricated by depositing MoS_2 layers on Ag and Al nanocones and their field emission properties investigated in section 3.4. It was observed that the conical geometry of Ag nanocones was destroyed with heating to result in a particulate film covered with broken tip fragments. Nevertheless, the MoS_2-coated Ag samples still demonstrated enhanced field emission over pristine nanocones due to a reduction of the potential barrier for electron field emission by formation of a Schottky barrier at the MoS_2-Ag interface. In addition, the broken tip fragments on the surface acted as nanometric sharp edges that contributed to geometric field enhancement, and thus the MoS_2-coated Ag nanocones were able to reach the turn-on current within the maximum limits of the voltage. For MoS_2-coated Al nanocones however, the high resistance contact between MoS_2 and Al as well as the more defective structure of MoS_2 layers grown on Al prevented efficient electron transfer from the metal to the MoS_2 and from MoS_2 to vacuum. Consequently the MoS_2-coated Al nanocones did not achieve the turn-on current even at the maximum applied voltage of 1000 V.

References

1. Castellanos-Gomez, A.; Poot, M.; Steele, G. A.; van der Zant, H. S.; Agrait, N.; Rubio-Bollinger, G. *Adv. Mater.* **2012**, 24, 772–775.
2. Mak, K.F.; Lee, C.; Hone, J.; Shan, J.; Heinz, T.F. *Phys. Rev. Lett.* **2010**, 105, 136805.
3. Coleman, J. N.; Lotya, M.; O'Neill, A.; Bergin, S. D.; King, P. J.; Khan, U.; Young, K.; Gaucher, A.; De, S.; Smith, R. J. et al. *Science* **2011**, 331, 568–571.
4. Smith, R. J.; King, P. J.; Lotya, M.; Wirtz, C.; Khan, U.; De, S.; O'Neill, A.; Duesberg, G. S.; Grunlan, J. C.; Moriarty, G. et al. *Adv. Mater.* **2011**, 23, 3944–3948.
5. Zeng, Z.; Yin, Z.; Huang, X.; Li, H.; He, Q.; Lu, G.; Boey, F.; Zhang, H. *Angew. Chem., Int. Ed.* **2011**, 50, 11093–11097.
6. Eda, G.; Yamaguchi, H.; Voiry, D.; Fujita, T.; Chen, M.; Chhowalla, M. *Nano Lett.* **2011**, 11, 5111–5116.
7. Lee, Y. H.; Zhang, X .Q.; Zhang, W.; Chang, M. T.; Lin, C. T.; Chang, K. D.; Yu, Y. C.; Wang, J. T. W.; Chang, C. S.; Li, L. J. et al. *Adv. Mat.* **2012**, 24, 2320–2325.
8. Zhan, Y.; Liu, Z.; Najmaei, S.; Ajayan, P.M.; Lou, J. *Small* **2012**, 8, 966–971.
9. Lin, Y. C.; Zhang, W.; Huang, J. K.; Liu, K. K.; Lee, Y. H.; Liang, C. T.; Chud, C. W.; Li, L. J. *Nanoscale* **2012**, 4, 6637–6641.
10. Ji, Q.; Zhang, Y.; Gao, T.; Zhang, Y.; Ma, D.; Liu, M.; Chen, Y.; Qiao, X.; Tan, P.; Kan, M. et al. *Nano Lett.* **2013**, 13, 3870−3877.
11. Liu, K. K.; Zhang, W.; Lee, Y. H.; Lin, Y. C.; Chang, M. T.; Su, C. Y.; Chang, C. S.; Li, H.; Shi, Y.; Zhang, H. et al. *Nano Lett.* **2012**, 12, 1538−1544.
12. Ganatra, R.; Zhang, Q. *ACS Nano* **2014**, 8, 4074–4099.
13. Koh, A. T. T.; Foong, Y. M.; Chua, D. H. C. *Appl. Phys. Lett.* **2010**, 97, 114102.
14. Chen, W.; Santos, E. J. G.; Zhu, W.; Kaxiras, E.; Zhang, Z. *Nano Lett.* **2013**, 13, 509–514.

15. Kang, J.; Liu, W.; Sarkar, D.; Jena, D.; Banerjee, K. *Phys. Rev. X* **2014**, 4, 031005.
16. Zhong, H.; Quhe, R,; Wang, Y.; Ni, Z.; Ye, M.; Song, Z.; Pan, Y.; Yang, J.; Yang, L.; Lei, M. et al. *Sci. Rep.* **2016**, 6, 21786.
17. Benchikh, N.; Garrelie, F.; Donnet, C.; Bouchet-Fabre, B.; Wolski, K.; Rogemond, F.; Loir A. S.; Subtil, J. L. *Thin Solid Films* **2005**, 482, 287.
18. Janmohamed, R.; Steele, J. J.; Scurtescu, C.; Tsui, Y. Y. *Appl. Surf. Sci.* **2007**, 253, 7964.
19. Jayatissa, A. H.; Sato, F.; Saito, N.; Hirano, Y.; Takizawa, K.; *Carbon* **2000**, 38, 1145.
20. Voevodin A. A.; Donley, M. S.; *Surf. Coat. Techol.* **1996**, 82, 199.
21. Yu, Q.; Lian, J.; Siriponglert, S.; Li, H.; Chen, Y. P.; Pe, S. *Appl. Phys. Lett.* **2008**, 93, 113103
22. Carey, J.; Forrest, R.; Silva, S. *Appl. Phys. Lett.* **2001**, 78, 2339.
23. Charbonnier, F. M.; Bennette, C. J.; Swanson, L W. *J. Appl. Phys.* **1967**, 38, 627.
24. Kashid, R. V.; Late, D, J.; Chou, S. S.; Huang, Y. K.; Joag, M.D.D.S.; More, M. A.; Dravid, V. P. *Small* **2013**, 9, 2730.
25. Li, Y. B.; Bando, B.; Golberg, D. *Appl. Phys. Lett.* **2003**, 82, 1962.
26. Late, D. J.; Shaikh, P. A.; Khare, R. K.; Kashid, R. V.; Chaudhary, M.; More, M. A.; Ogale, S. B. *ACS Appl. Mater. Interfaces* **2014**, 6, 15881−15888.
27. Lee, C.; Yan, H.; Brus, L. E.; Heinz, T. F.; Hone, J.; Ryu, S.; *ACS Nano* **2010**, 4, 2695–2700.
28. Li, H.; Zhang, Q.; Yap, C. C. R.; Tay, B. K.; Teo, E. H. T.; Olivier, A.; Baillargeat, D. *Adv. Funct. Mater*. **2012**, 2, 1385–1390.
29. Frey, G. L.; Tenne, R.; Matthews, M. J.; Dresselhaus, M. S.; Dresselhaus, G. *Phys. Rev. B* **1999**, 60, 2883–2892.
30. Splendiani, A; Sun, L.; Zhang, Y.; Li, T.; Kim, J.; Chim, C.Y.; Galli, G.; Wang, F. *Nano Lett.* **2010**, 10, 1271–1275.
31. Kim, J.; Cote, L. J.; Kim, F.; Huang, J. X. *J. Am. Chem. Soc.* **2010**, 132, 260–267.
32. Adarsh, S.; Klaus, K.; Kannan, B. *Nanotechnol.* **2010**, 21, 015303.
33. Buscema, M.; Steele, G. A.; van der Zant, H. S. J.; Castellanos-Gomez, A. *Nano Research* **2014**, 7, 561–571.

34. Lefebvre, J.; Homma, Y.; Finnie, P. *Phys. Rev. Lett.* **2003**, 90, 217401
35. Baren, M. R.; *Bulletin of Alloy Phase Diagrams* **1990**, 11, 548–549.
36. Shi, Y.; Zhou, W.; Lu, A. Y.; Fang, W.; Lee, Y. H.; Hsu, A. L.; Kim, S. M.; Kim, K. K.; Yang, H. Y.; Li, L. J. et al. *Nano Lett*. **2012**, 12, 2784–2791.
37. Molina-Sanchez, A.; Wirtz, L. *Phys. Rev. B* **2011**, 84, 155413.
38. Shi, Y.; Wang, Y.; Wong, J. I.; Tan, A. Y. S.; Hsu, C.; Li, L.; Lu, L.; Yang, H. Y. *Sci. Rep.* **2013**, 3, 2169.
39. Chang, Y. H.; Lin, C. T.; Chen, T. Y.; Hsu, C. L.; Lee, Y. H.; Zhang, W.; Wei, K. H.; Li, L. J. *Adv. Mater*. **2013**, 25, 756–76.
40. Okamoto, H. *J. Phase Equilibria and Diffusion* **2009**, 30, 123–123.
41. Varelas, C.; Sizmann, R. *Surf. Sci.* **1978**, 71, 51-58.
42. Sasi, B.; Gopchandran, K. G. *Nanotech.* **2007**, 18, 115613.
43. An, J.; Voelkl, E.; Suk, J. W.; Li, X.; Magnuson, C. W.; Fu, L.; Tiemeijer, P.; Bischoff, M.; Freitag, B.; Popova, E. et al. *ACS Nano* **2011**, 5, 2433−2439.
44. Jung, Y. S.; Sun, Z.; Kim, H.K.; Blachere, H. *Appl. Phys. Lett.* **2005**, 87, 263116.
45. De, G.; Gusso, M.; Tapfer, L.; Catalano, M.; Gonella, F.; Mattei, G.; Mazzoldi, P.;Battaglin, G. *Appl. Phys. Lett.* **1996**, 80, 6734.
46. Seita, M.; Pecnik, C. M.; Frank, S.; Spolenak, R. *Acta Materialia* **2010**, 58, 6513–6525.
47. Geis, M. W.; Efremow, N. N.; Krohn, K. E.; Twichell, J. C.; Lyszczarz, T. M.; Kalish, R.; Greer, J. A.; Tabat, M. D. *Nature* **1998**, 393, 431–435.
48. Lantham, R. V. Vacuum **1982**, *32*, 137–140.
49. Uda, M.; Nakamura, A.; Yamamoto, T.; Fujirnoto, Y. *J. Electron Spectroscopy and Related Phenomena* **1998**, 88–91, 643–648.
50. Walia, S.; Balendhran, S.; Wang, Y.; Ab Kadir, R.; Zoolfakar, A. S.; Atkin, P.; Ou, J. Z.; Sriram, S.; Kalantar-zadeh, K.; Bhaskaran, M. *Appl. Phys. Lett.* **2013**, 103, 232105.
51. Chen, W.; Santos, E. J. G.; Zhu, W.; Kaxiras, E.; Zhang, Z. *Nano Lett.* **2013**, 13, 509–514.
52. Jeong, H. D.; Lee, J. H.; Lee, B. G.; Jeong, H. J.; Lee, G.-W.; Bang, D. S.; Cho, D.; Park, Y.-B.; Jhee, K. H. *Carbon Lett.* **2011**, 12, 207–217.

Chapter 4

Pulsed Laser Fabricated Few-layer WS_2 on Metal Substrates

In this chapter, pulsed laser deposition (PLD) is used to fabricate few-layer WS_2 on metal substrates. In section 4.2, hybrid 1T- and 2H-WS_2 layers are found experimentally to grow on Ag and the factors influencing the phasic composition are investigated. In Section 4.3, the feasibility of Ag, Au, Al and Ni as templates for WS_2 synthesis by PLD is explored and the growth mechanism of WS_2 on these metals elucidated. The origin of 1T-WS_2 and its phase stabilization on Ag and Au substrates are also discussed. In section 4.4, the field emission properties of PLD-grown WS_2 on Ag nanocones are studied.

4.1 Introduction

Within the family of layered transition metal dichalcogenides (TMD), MoS_2 has been the most widely studied, with many comprehensive and intensive studies on fabrication methods and material properties such optical and electronic performance, valleytronics, and thermal effects.[1-3] However, there remains a large body of as yet unexplored 2D layered materials that could potentially play a vital role in future nanoelectronics. One such material is WS_2, which like the related system MoS_2, is an indirect band gap semiconductor that converts to a direct gap material when thinned down to a single layer.[4] As a consequence of this indirect-to-direct transition, monolayer WS_2 exhibits extraordinary room temperature photoluminescence (PL) that

surpasses all known 2D layered TMDs.[5] Both MoS_2 and WS_2 are part of the group IV semiconducting dichalcogenides, in which a unique set of conditions gives rise to strong spin–orbit-induced electronic band splitting and spin–valley coupling,[1] which makes them promising candidates for spintronic devices. It was recently reported that atomically thin WS_2 demonstrates significantly larger spin–orbit interactions[6,7] as compared to MoS_2. Furthermore, single-layered WS_2 quantum dots have been shown to have even stronger spin-orbit coupling than WS_2 sheets, in addition to a much more blue-shifted PL emission.[8] This suggests that the optical properties and spin-orbit splitting of WS_2 can be effectively manipulated by lateral size control, which makes the material highly valuable for applications in spintronics and optoelectronics. Field effect transistors (FET) prepared from WS_2 have been demonstrated in literature with ambipolar charge carrier characteristic,[9-11] which is more frequently reported for WS_2 than for other TMD materials.[12] The ambipolar behaviour makes the material more attractive for use in device applications that involve homogenous or heterogeneous p-n junctions. Most significantly, theoretical models predict that WS_2 would produce better transistor performance than MoS_2 and even Si due to a much smaller effective electron mass.[13]

Until recently, most of the attention has been focused on the semiconducting phase of WS_2 and MoS_2, both of which possess a prismatic coordination for the metal atom (2H). Theoretical calculations predict that the 2H-polytype is more thermodynamically stable, and hence the 1T-phase converts to the former upon heating.[14] Due to this instability of the octahedral 1T-phase, it has not been found in nature. Nonetheless, WS_2 and MoS_2 layers with octahedral coordination were able to be synthesized through intercalation by alkali metals such as Li and K,[15-18] with the restacked 1T-phases in $LiMS_2$ and 1T-KMS_2 (M = Mo or W) compounds confirmed by

electron diffraction.[19,20] Free-standing layers of these 1T-polymorphs can then be engineered through solvation and reduction of the intercalate compounds.[21,22] However, 1T-$LiMoS_2$ is thermodynamically unfavourable and has been determined to gradually transform to the 2H-phase at room temperature. The 1T-phase of MS_2 compounds is also known to be stabilized by substitutional doping of Re, Tc and Mn atoms, all of which were found to act as electron donors within the MS_2 lattice.[14,23]

Both WS_2 and MoS_2 have been envisioned as efficient and earth-abundant replacements for Pt catalysts in the photocatalytic evolution of hydrogen[24-26]. Quantum-mechanical calculations have revealed that the catalytic activity of MS_2 (M = transition metal) compounds is correlated to the degree of metallic character of their edges[27,28], in addition to other factors such as density of states.[29] Given that the 1T-phase exhibits metallic behaviour, this suggest that 1T-MS_2 possesses greater catalytic ability than their 2H counterpart. Indeed, individual 1T-WS_2 nanosheets produced by lithium intercalation were found to present excellent hydrogen evolution reaction (HER) activity[30,31], the best, in fact, of any MX_2 (X = chalcogen) materials. However, they had a strong propensity for restacking and an irreversible phase transition to the 2H-phase[32], which led to significant deterioration in their electrochemical performance. There is thus a strong impetus to search for possible ways of stabilizing 1T-MS_2 compounds. Achieving this phase stabilization through the addition of an appropriate metallic species such as Ni is particularly advantageous based on increasing evidence that hybridizing MS_2 compounds with metallic materials can lead to superior catalytic performance[33-36]. For example, the introduction of a metal support has been shown to substantially alter the H binding energy of MoS_2[36]. The metal support is furthermore able to optimize the electrical contact between MoS_2 active sites and the substrate, particularly since 1T-MoS_2 layers have been reported to form low resistance contacts

to metals.[37,38] For example, Kappera et al. fabricated FETs with a 2H-MoS_2 channel and 1T-MoS_2 electrodes that demonstrated mobility values of 56 cm^2 V^{-1} s^{-1}, exceptionally large on-state currents of 110 μA $μm^{-1}$, and subthreshold swing values of 0.72 V/decade.[38] All of these values are dramatically better than metal electrodes deposited directly on top of the 2H-phase.

Despite the advantages of WS_2 over MoS_2, the material has been studied to a much lesser degree than MoS_2. This is possibly due to the difficulty in obtaining high quality single crystal WS_2 even though the chemical and atomic structures of WS_2 are similar to those of MoS_2. There are currently two main methods of preparing ultrathin WS_2: (1) top-down exfoliation and (2) bottom-up substrate growth. Exfoliation can be mechanical,[39,40] chemically assisted[41] (e.g. sonication in a good solvent) or purely chemical[42] (intercalation with e.g. lithium), but the end results remain similar: high quality flakes can be prepared but there is very little control over their size, shape or nature of their edges. On the other hand, the substrate growth technique, commonly some form of chemical vapour deposition[43-45] (CVD), is capable of producing large area monolayers with high crystallinity and good control over flake shape. However, many of these substrate growth techniques utilize different solid precursors heated to high temperatures in the range of 750-1000 ºC and require long growth times. Although pulsed laser deposition (PLD) is also a type of bottom-up substrate growth technique, it is unique in that it is a purely physical method. While PLD has found success in the fabrication of 2D materials such as few-layer graphene[46], it remains underdeveloped compared to exfoliation and CVD methods.

In section 4.2, we describe the synthesis of highly crystalline few-layer WS_2 on Ag substrates using PLD at a relatively low temperature of 450 °C. In section 4.3, the

viability of Ag, Au, Al and Ni to act as the growth template for few-layer WS_2 is investigated. Ag, and Ni were chosen for their reactivity with sulfur to form metal sulfides, which are thought to be beneficial to the growth of highly crystalline WS_2 due to the minimal lattice mismatch between two sulfide compounds. Au was selected for its high conductivity and its typical usage as an electrode in FETs, and finally Al was chosen as α-Al_2O_3 substrates have been demonstrated[47] to successfully produce ultrathin TMDs by CVD. Interestingly, a hybrid 2H-1T structure was produced on the noble metals Ag and Au, but Al and Ni gave purely 2H-WS_2. The influence of metal buffer thickness, deposition time, growth temperature, and laser energy on the phasic mixture of the WS_2 film is studied in section 4.2. The growth mechanism of the WS_2 layers on metal substrates was then discussed in section 4.3, and a possible origin of the 1T-phase was considered.

The good electrical conductivity and mechanical robustness of 2D TMDs such as WS_2 render them promising candidates for next generation field emitters. However, most synthesis techniques for WS_2 result in layers that are oriented parallel to the substrate surface. This flat profile and smooth surface prevents good external field enhancement, which can lead to extremely high turn-on fields or even no electron emission whatsoever. In order to take advantage of the beneficial properties of WS_2, the 2D sheets should ideally be oriented perpendicularly to the substrate to expose sharp edges and tips. This can be achieved by synthesizing nanostructures such as nanotubes and nanoflowers. For instance, Viskadouros et al.[48] fabricated WS_2 nanotubes with comparable field emission performance to optimized CNTs and better resistance to chemically reactive environments. Li et al.[49] synthesized WS_2 nanoflowers using atmospheric pressure CVD at 650 ºC that demonstrated a moderately low turn-on field of 6.1 V μm^{-1}. The orientation of 2D nanosheets can also be tuned by coating a microtip

array. Although, no such example for WS_2 exists, the technique has been utilized for other 2D materials such as graphene. For example, Stratakis et al.[50] spin-coated graphene sheets onto Si microtips and the resultant structure was shown to have a turn-on field of 2.3 V μm^{-1}.

In section 4.4, WS_2-coated Ag nanocones were fabricated by PLD and investigated for field emission capability. The lower growth temperatures used for PLD grown WS_2 as compared to CVD reduces the probability of the metal nanocones undergoing significant diffusion and reflow during the heating process. Furthermore, the WS_2 layers were grown directly on the Ag nanocones and thus avoided the issues associated with transfer techniques that can adversely affect the electron transport properties of WS_2. Field emission studies were carried out on the WS_2-coated nanocones before and after annealing to determine the effects of the phasic composition on the field emission performance. The field enhancing mechanisms were also investigated.

4.2 Hybrid 1T- and 2H-WS_2 Ultrathin Layers on Silver

4.2.1 Experimental Procedure

Synthesis: The synthesis of few-layer WS_2 on 500 nm thick Ag films was similar to that described in section 3.2.1. The laser energies used for ablation was kept within the range of 50–200 mJ, and the deposition time between 10–30 s. Substrate temperature was kept at 450 °C during deposition and subsequently decreased at a controlled rate of 20 ºC/min until the temperature reached 300 ºC, thereupon natural cooling processes took over.

Characterization: PL measurements as well as XPS and TEM analysis of the WS_2 films were conducted using the same instruments and conditions as detailed in section 3.2.1. Raman spectroscopy was performed in a Horiba MicroRaman HR Evolution System using an Argon laser beam with an excitation wavelength of 514.5 nm. Surface morphology and height profile were obtained with a Digital Instruments, Nanoscope III, Multimode AFM operated in tapping mode.

4.2.2 Nanostructural Characterization

Figure 4.1(a) shows the Raman spectra of the as-grown WS_2 film on Ag and sapphire excited under ambient conditions, with the spectrum of bulk WS_2 and a WS_2 sample grown on sapphire included for comparison. In the spectrum of the sapphire sample, peaks from the substrate were removed by dividing with the Raman spectrum from an uncoated sapphire sample. At this excitation wavelength of 514.5 nm, the spectrum reveals many second-order Raman peaks in addition to the first-order phonon

modes. The strongest peak at ~352 cm^{-1} can be resolved by multi-peak Lorentzian fitting into three individual contributions at 343, 351, and 355 cm^{-1} as shown in Figure 4.1(b) for the sample fabricated at 100 mJ and 10 s. These modes are assigned to the in-plane vibrational $E^{!}_{2g}$ (M) mode, the second-order mode of longitudinal acoustic phonon 2LA (M), and the in-plane vibrational $E^{!}_{2g}$ (Γ) mode respectively.[51] The other peaks at 418 and 343 cm^{-1} are attributed to the out-of-plane A^{1}_{g} mode and the in-plane vibrational E^{1}_{2g} (M) mode. Studies have previously shown that Raman characterization can provide unambiguous and non-destructive identification of the thickness of WS_2; the A_{1g} (Γ) mode softens while both the 2LA (M) and $E^{!}_{2g}$ (Γ) modes present a subtle red-shift with a decreasing number of layers.[5,52] In particular, at 514.5 nm laser excitation, the WS_2 spectrum reveals a striking increase in the intensity ratio of the 2LA (M) to A_{1g} (Γ) phonon modes due to a double resonance process.[52] Table 4.1 summarizes the frequency for the three main Raman modes A_{1g} (Γ), 2LA(M) and $E^{!}_{2g}$ (Γ), as well as the intensity ratio for the two most intense peaks in our pulsed laser fabricated samples on Ag. Based on these values, it can be concluded that atomically thin WS_2 films (≤ 5 layers) can be formed at any laser energy within the range of 50–200 mJ as long as the deposition time was capped at a maximum of 10 s. Compared to chemically derived WS_2[43,45], our samples exhibited Raman peaks with broader FWHMs such that it becomes difficult to distinguish the phonon modes in the 260–330 cm^{-1} range without multi-peak Lorentzian fitting. This indicates the presence of defects arising from disorder in the atomic arrangement of the WS_2 film. In addition, the samples fabricated at 50 mJ demonstrate much lower signal intensity, possibly indicating only partial crystallization or a large concentration of defects. As such, even though the thinnest films are formed at the lowest laser energy, for an optimal balance

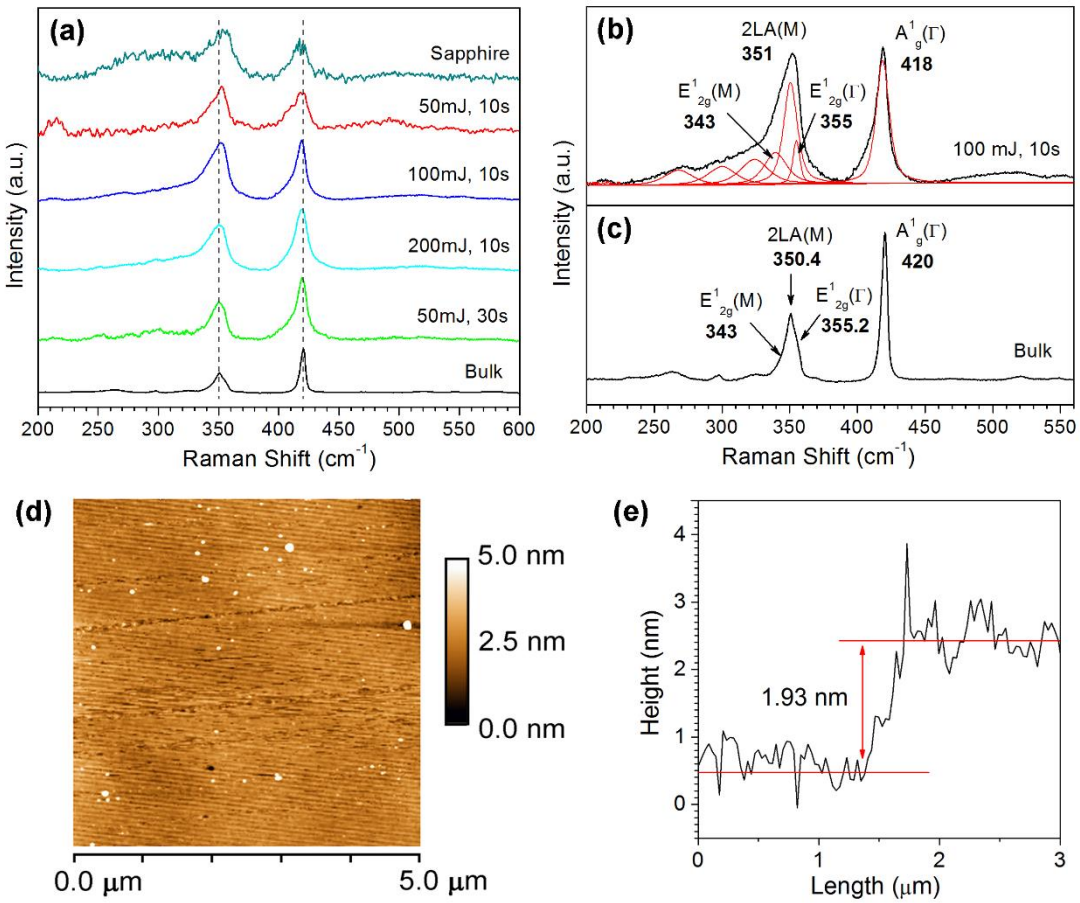

Figure 4.1: (a) Raman spectra of as-grown samples. The WS_2 film on sapphire was fabricated at 200 mJ and 10 s. The left and right dashed lines indicate the positions of the 2LA (M) and A_{1g} phonon modes in bulk WS_2 respectively. (b) Multi-peak Lorentzian fitting of Raman bands in the Ag sample fabricated at 100 mJ and 10 s. (c) Raman spectra of bulk WS_2. (d) AFM image and (d) height profile of the as-grown WS_2 film on Ag. The tri-layered WS_2 film is approximately 1.9 nm thick.

Table 4.1: Peak position for the Raman modes A_{1g} (Γ), 2LA(M) and E^{1}_{2g} (Γ), as well as the intensity ratio of A_{1g} (Γ) to 2LA(M) for the as-deposited samples on Ag.

Laser Energy (mJ)	**Deposition Time**	**A_{1g} (Γ) (cm^{-1})**	**E^{1}_{2g} (Γ) (cm^{-1})**	**2LA (M) (cm^{-1})**	**$\frac{I_{2LA}}{I_{A_{1g}}}$**	**Estimated Number of Layers**
50	10	418	351	355	0.94	~2
100	10	418.7	350.6	355	0.75	~3
200	10	419.1	350.1	354.9	0.58	4-5
50	30	419.5	350.2	355	0.51	>5
Bulk	-	420	350.4	355.2	0.46	Bulk

between film thickness and crystalline quality, a laser energy of 100 mJ would be most ideal to grow highly crystalline few-layer WS_2. It is also noted that, as with the case of PLD grown MoS_2, obtaining monolayer WS_2 by PLD is possible using sapphire but not with metal substrates. WS_2 layers on sapphire are similarly oxygen-rich and thus require post-deposition treatment to improve their crystallinity.

The as-synthesized WS_2 films on Ag was observed to display good uniformity and continuity across an area of centimetres when viewed under an optical microscope or by the naked eye. Using AFM, the surface morphology at different areas on the film was characterized and found to be similar across the entire film. A typical AFM measurement (5 μm × 5 μm) is presented in Figure 4.1(d), demonstrating an atomically smooth surface with a calculated root-mean-square (RMS) roughness of 0.55 nm, which is slightly higher than the value of the Si substrate itself (0.3 – 0.5 nm). A height profile taken at the film edge is shown in Figure 4.1(e). It reveals a film thickness of approximately 1.9 nm, which agrees well with three atomic layers of WS_2 for the sample fabricated at 100 mJ and 10 s, thus corroborating the Raman results.

Although insulating substrates such as sapphire are preferred substrates for growing 2D materials for characterization of electronic properties, it was found that such substrates do not produce good quality WS_2 films in pulsed laser synthesis. Figure 4.1(a) shows that despite the use of higher laser energies of 200 mJ to fabricate the sapphire sample, its Raman spectrum resembles the partially crystalline and highly defective spectrum of the Ag sample fabricated at 50 mJ and 10 s. At lower energies of 100 and 50 mJ, the characteristic peaks of 2H-WS_2 are completely absent. This obstacle can however, be overcome by sputtering a very thin layer of Ag on the substrate. Our investigations reveal that the minimum thickness that the Ag layer can have before it

begins to significantly affect the crystalline quality of the overlying WS_2 film is ~8 nm, as shown in Figure 4.2(a). These WS_2 films were grown on quartz, which not only permits the direct synthesis of crystalline few-layer WS_2 on insulating substrates without the need for transfer techniques, but also allows the fabrication of samples that are capable of transmitting visible light. Figure 4.2(b) reveals that the triple-layered WS_2 film on quartz has an average optical transmittance of 71% in the wavelength range between 400 and 800 nm. Reducing the buffer layer to such minimal thickness also results in in-situ consumption of most, if not all, of the pure Ag metal to form Ag_2S (a phase which was detected in the TEM, XPS and XRD analysis). This was deduced from the increase in optical transmission in the sample after deposition of WS_2, also shown in Figure 4.5(b). The high optical transmittance of our WS_2 films on quartz means that they are suitable for solar energy applications. The presence of the Ag_2S phase is also beneficial as the material appears to be a promising solar absorbing material with its narrow band gap of ~0.9 eV[52] and its unique combination of properties such as light absorbance in the near-infrared spectral regions.[53]

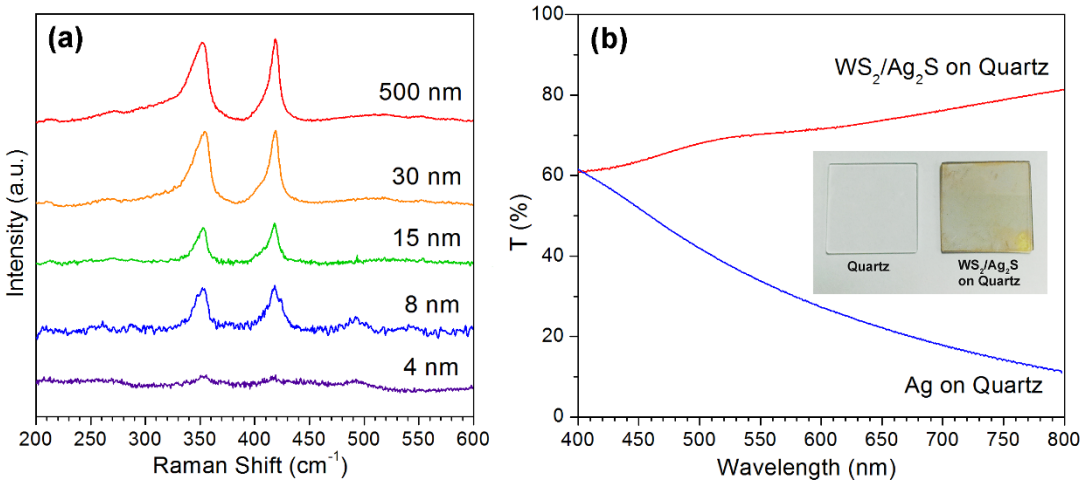

Figure 4.2: (a) Raman spectrum of as-deposited WS_2 on quartz with varying Ag buffer thickness. All samples were synthesized using the parameters of 100 mJ and 10 s. (b) Optical transmittance of a quartz substrate with Ag buffer layer of 8 nm, before and after WS_2 film growth. Inset: Photograph of the as-grown WS_2 sample and bare quartz.

High resolution TEM images of our pulsed laser fabricated samples are shown in Figure 4.3 and reveal the stacking of WS_2 (002) layers with an interplanar spacing of 0.62 nm on top of Ag [JCPDS #08-0237]. Figure 4.3(a) provides direct evidence of the successful formation of double-layered WS_2 in the sample fabricated at 50 mJ and 10 s, with the first WS_2 layer forming covalent bonds to the previously mentioned Ag_2S phase that develops in-situ on the surface of the Ag buffer. This bonding between the two layers manifests as an indistinct boundary at the interface contrary to the sharp interfaces of 2D layered materials grown by van der Waals epitaxy. The formation of the Ag_2S phase is supported by the presence of lattice fringes with interplanar spacings of 0.27 nm located underneath the WS_2 film that can be ascribed to the (120) plane of monoclinic acanthite Ag_2S [JCPDS #14-0072]. Figure 4.3(b) shows the change in the WS_2 film when the deposition time is increased to 30 s. The number of layers have increased to >5, verifying the results of the Raman measurements.

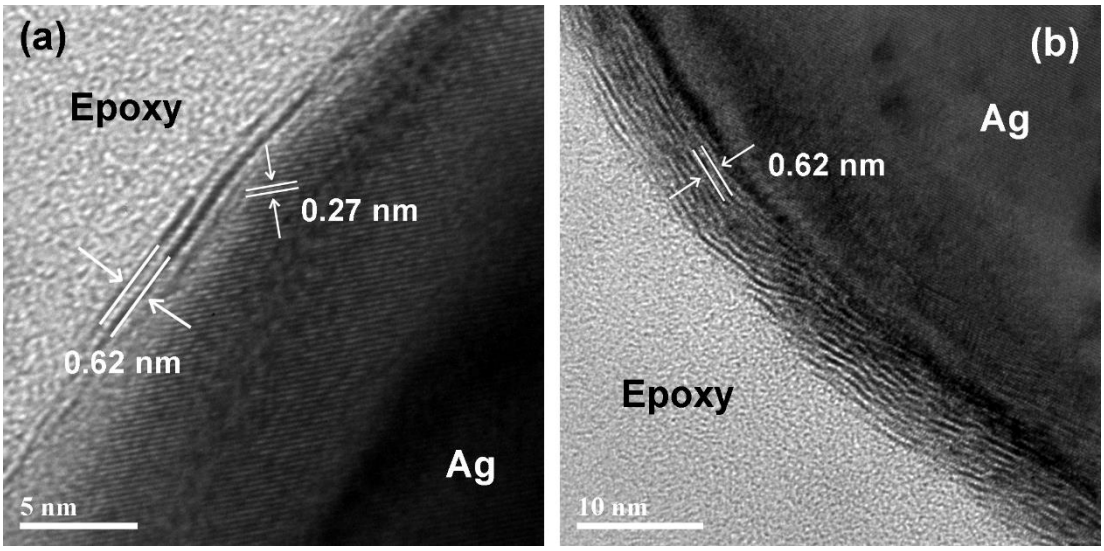

Figure 4.3: Cross-section TEM of Ag samples fabricated at a laser energy of 50 mJ and deposition times of (a) 10 s and (b) 30 s.

4.2.3 Experimental Evidence of 1T-WS_2

Figure 4.4 depicts the W 4f and S 2p core level XPS scans for the WS_2 film on Ag. Two doublets are present in the S 2p spectra, one occurring at 162.3 and 163.5 eV, consistent with the S^{2-} species of WS_2, while the second pair located at 161.1 and 162.4 eV can be assigned to the S 2p peaks of Ag_2S. The presence of both doublets confirms the successful growth of WS_2 as well as the in-situ formation of Ag_2S. For the W 4f spectra, there is a small shoulder at 35.6 eV corresponding to the W^{6+} state that indicates the formation of tungsten oxide in the as-deposited films. This oxide can arise in part from surface oxidation of the WS_2 target, and in part from unreacted W atoms remaining on the substrate surface after completion of the WS_2 film. These unreacted W atoms are always produced because some S atoms are initially consumed in the making of the Ag_2S phase. The oxide is believed to form a capping layer over the WS_2 film when it is first exposed to air, and does not negatively affect the quality of the film itself as the calculated stoichiometric ratio of S : W is very close to the ideal value of 2. It was also observed that the main W doublet peak can be deconvoluted into two separate pairs. One doublet (red curve) occurs at binding energies of 32.7 and 34.8 eV, which corresponds well with the W^{4+} species of highly crystalline 2H-WS_2.[54] The other doublet at 32.1 and 34.2 eV (blue curve) on the other hand, lies between the binding energies of metallic tungsten (W^{0+}) and W^{4+}, and appears to be due to a partially sulfided, intermediate W^{x+} state. However, calculation of the stoichiometric ratio of S : W atoms reveals that both W tungsten species (red and blue curves) have a S : W ratio of ~2, indicating that the W 4f doublet located at 32.1 and 34.2 eV is also due to a W^{4+} state. The negative shift of peak binding energies by 0.6 eV is thus believed to be attributed to the formation of the 1T-phase of WS_2, consistent with its metallic nature, and is comparable to with previous studies on 1T-MX_2 materials.[52,55]

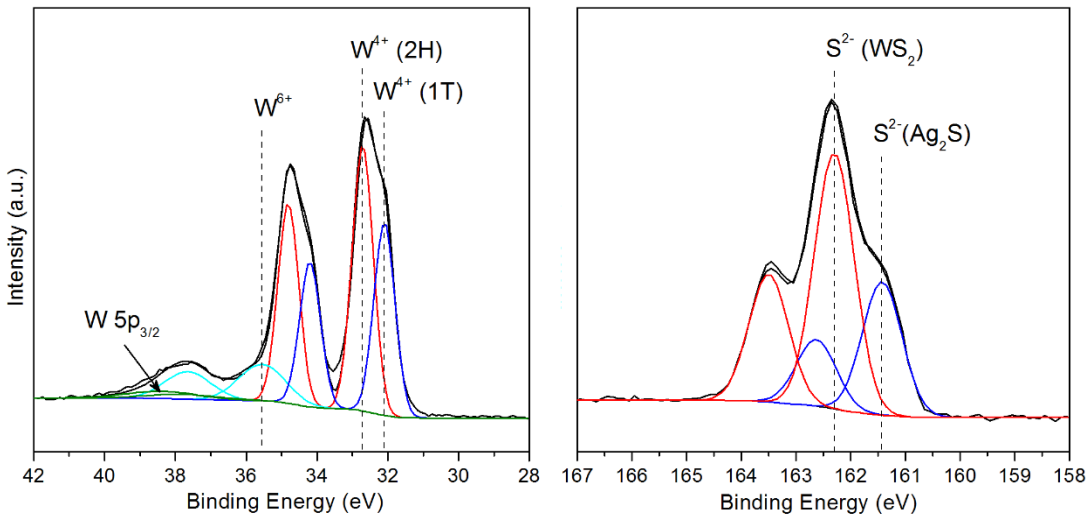

Figure 4.4: XPS spectra showing W 4f and S 2p core level peak regions for as-deposited samples fabricated at 100 mJ and 10 s.

The formation of the 1T-phase can also be established by closer inspection of the Raman spectra, as well as by powder XRD. As noted by Voiry et al,[55] the Raman spectra of 1T-WS_2 display the additional modes of J_1, J_2 and J_3 that are attributed to the superlattice structure of the distorted 1T-phase. However, these Raman modes are only readily observable when the concentration of 1T-WS_2 dominates over the 2H-phase. Figure 4.5(a) shows the Raman results from two of our as-deposited samples with widely differing concentrations of 1T-WS_2. It is apparent that the J_1, J_2 and J_3 modes are noticeable only in the sample fabricated at 50 mJ and 10 s due to the much higher 1T-to-2H ratio of 1.67. In contrast, the sample fabricated at 100 mJ and 10 s only has a 1T-to-2H ratio of 0.73, and correspondingly the typical Raman peaks of 1T-WS_2 have almost completely vanished. Included for comparison is a sample annealed at 300 ºC for 30 minutes, wherein a complete phase transformation from 1T to 2H-WS_2 was achieved as revealed by the XPS spectra shown in Figure 4.4(b). The Raman bands of 2H-WS_2 in this sample appear more distinct; in particular the combination mode of 2LA-E^2_{2g} at ~320 cm^{-1} becomes visibly noticeable. Nonetheless, the peaks still lack the

sharpness of CVD grown WS_2 sheets, and there is only a slight increase in the peak intensities while the FWHMs remained largely unchanged. This indicates that there is some degree of atomic disorder present even in the pure 2H-phase, and the crystalline quality of PLD grown WS_2 on Ag is not quite comparable to CVD grown WS_2 layers. The fact that the 1T-to-2H phase transition can be induced with thermal annealing indicates that the 1T-WS_2 produced in this work is metastable. Indeed, it was observed that partial 1T to 2H transition begins to occur even at temperatures as low as 100 ºC, which would be detrimental if the 1T-phase was intended for use at high temperatures. The ability to prepare metastable 1T-WS_2 layers at temperatures higher than the 1T-to-2H transition is rather surprising. However, this is likely to be simply due to the short deposition times and fast cooling rate, such that the 1T-structure does not have sufficient time to relax to the more stable 2H-phase.

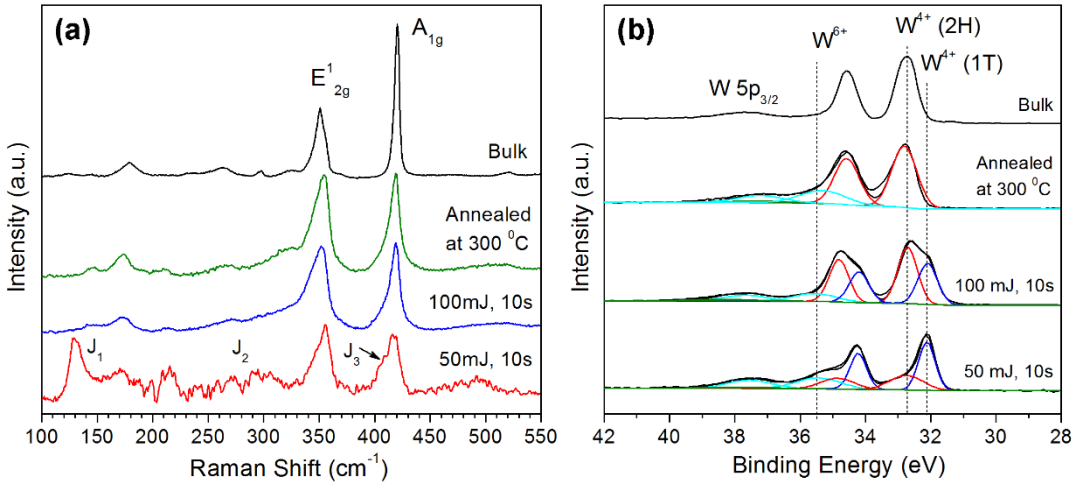

Figure 4.5: (a) Raman spectra of WS_2 films deposited on Ag. The J_1, J_2, and J_3 peaks are only active in the as-deposited sample fabricated at 50 mJ and 10s. The spectrum for WS_2 films annealed at 300 ºC more closely resembles that of bulk 2H-WS_2. (b) XPS spectra showing the W 4f core level peak regions of as-deposited, annealed, and bulk samples. As-deposited WS_2 sheets at 50 and 100 mJ have 1T-to-2H phase ratio of 1.67 and 0.73 respectively.

Unlike with 2H-WS_2, characterization of 1T-WS_2 by powder XRD is rather challenging because the 1T-phase does not exhibit a well-defined crystalline structure and well-resolved diffraction peaks.[31] This problem is exacerbated by the fact that our samples are all mixtures of 1T- and 2H-WS_2. Nonetheless, we were still able to observe differences in the XRD diffractograms obtained before and after annealing. As shown in Figure 4.6, both the as-deposited and annealed samples have peaks corresponding to the known 2H-WS_2 pattern. In the as-deposited sample, the presence of a broad peak at 14.3 ° with the highest intensity reveals the preferential growth of WS_2 sheets along the (002) direction. In contrast, the XRD pattern of the annealed sample shows a more intense (100) peak, which suggests the growth of protrusion edges along the (100) direction. The lattice spacing of the WS_2 layers can be calculated using the Scherrer equation,[56]

$$\tau = \frac{K\lambda}{\beta \cos\theta} \tag{4.1}$$

where τ is the mean size of the ordered crystalline domains, K is a dimensionless shape factor (here K = 1), λ is the X-ray source wavelength, β is the FWHM of the (002) peak in radians and θ is the Bragg angle. The lattice spacing for both the as-deposited and annealed sample is thus determined to be 0.625 nm, which indicates a slight lattice expansion of ~1.1 % compared to the value of 0.618 nm for bulk WS_2 [JCPDS #08-0237]. The annealed sample also presents additional peaks corresponding to 2H-WS_2, suggesting an improvement in crystallinity of the WS_2 film that may be attributed to a 1T-to-2H phase transformation. There is furthermore a very minor peak around 19–20º that vanishes after thermal annealing. As this peak cannot be indexed to either 2H-WS_2, Ag, Ag_2S or even WO_3, and has previously been observed to be present in 1T-WS_2,[33] we believe that it can be attributed to the presence of the 1T-phase.

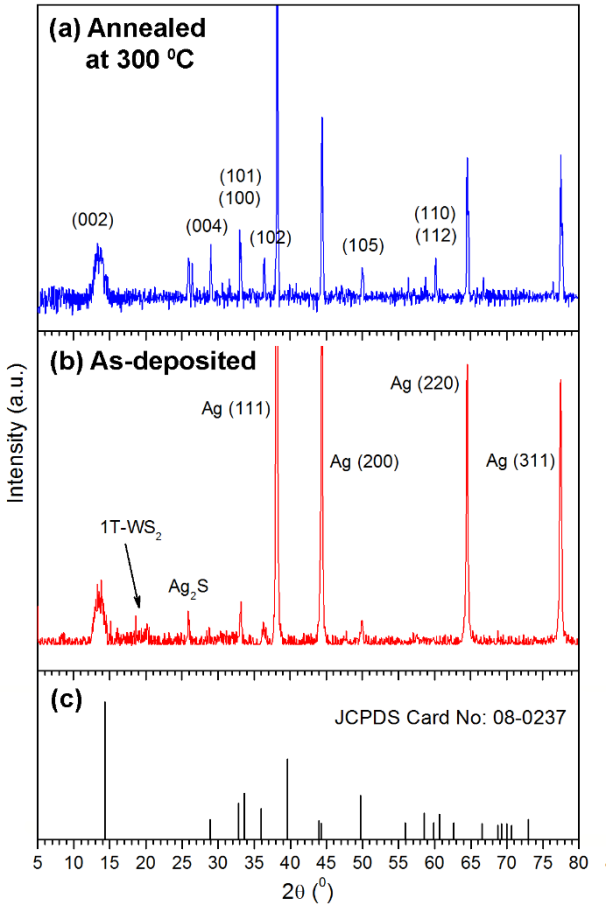

Figure 4.6: Powder X-ray diffractograms of WS_2 nanosheets (a) annealed at 300 °C and (b) as-deposited at 50 mJ and 10 s. (c) Bulk diffraction peaks of 2H-WS_2.

The presence of the 1T-phase also affects the PL measurements of our samples. Weak PL was observed in as-deposited WS_2 nanosheets, as expected from their partial metallic character. Enlarging the emission spectra allows us to see that the sample fabricated at 50 mJ and 10 s presents a major peak at ~645 nm and a shoulder peak at ~570 nm (Figure 4.7), corresponding to A and B excitonic transitions of the K point of the Brillouin zone. Curiously, the expected intensity and position dependence of the major PL peak with layer thickness can be observed even among the as-deposited samples despite the varying concentrations of 1T-WS_2. As shown in Figure 6, the major PL peak at ~640 nm quickly diminishes in intensity and gradually red-shifts with

increasing layer thickness, a trend that has been observed by other groups.[44,45,51] This is unusual as the thinnest sample also has the highest concentration of 1T-WS_2, which is expected to inhibit PL, and yet this sample gives the highest emission intensity. Because PL originates near the surface of a material, and is sensitive enough to be affected by surface adsorbates, the fact that the PL spectra of as-deposited samples appears to be largely unaffected by the presence of 1T-WS_2 suggests that the 1T-phase is located away from the surface of the film. While the origin of 1T-WS_2 in our samples is as yet unclear, we believe that it can be attributed to the capacity of Ag atoms to act as an electron donor for W (owing to Ag having more valence electrons than W). The stabilization mechanism is therefore similar to chemically exfoliated MoS_2 and WS_2, wherein the 1T-phase is stabilized by insertion of an electron donating atom such as Li. In such a case, the 1T-phase in our samples would be concentrated at the interface while 2H-WS_2 would dominate at the surface of the film, which could explain the unexpected PL results.

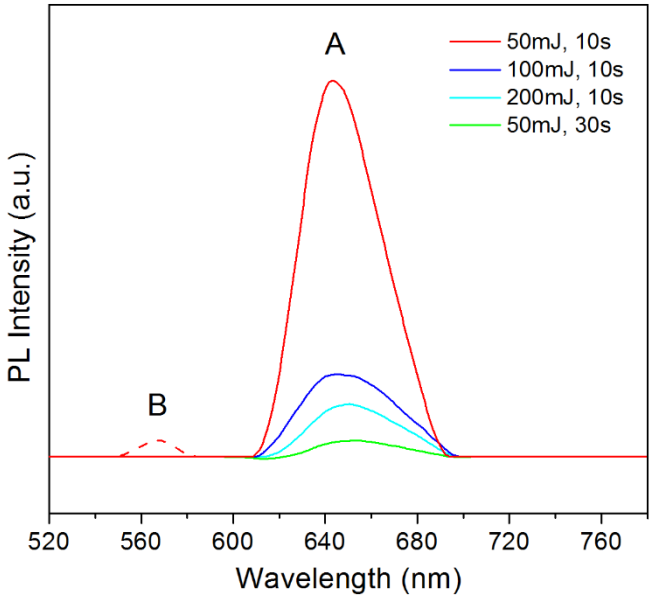

Figure 4.7: Photoluminescence spectra of as-grown samples measured using an excitation wavelength of 488 nm.

4.2.4 Factors Influencing Phasic Mixture of WS_2 Film

We further characterized the 1T-phase by investigating the influence of Ag thickness, temperature, laser energy, and deposition time on the phase and crystallinity of the resulting WS_2. As shown in Figure 4.8(a), the crystalline quality of the WS_2 sheets begins to degrade slightly when the thickness of the Ag layer is reduced to less than 30 nm. Below a thickness of 8 nm, the obtained WS_2 becomes essentially amorphous. The proportion of the two phases, 2H and 1T, is also affected, with the amount of 1T-phase gradually decreasing as the Ag thickness is reduced [Figure 4.8(b)], providing further evidence that the Ag layer is responsible for the formation and stabilization of 1T-WS_2. Higher growth temperatures also appear to negatively impact the crystallinity of the resulting WS_2 in addition to reducing the amount of 1T-phase, as illustrated in Figure 4.7(c)-(d). Above 450 ºC, the substrate temperature becomes too high, leading to the re-evaporation of adatoms from the surface and a degradation in WS_2 film quality. The optimum temperature window for WS_2 growth by PLD is therefore deduced to be around 450-500 ºC, which is much lower than CVD techniques for WS_2. This is credited to the generation and rapid deposition of energetic ablation species in PLD, which helps to raise the substrate temperature during film growth. As mentioned above, the concentration of the 1T-phase was also observed to decrease as the substrate temperature is raised, which we attribute to the metastable nature of 1T-WS_2. The 1T-phase of MoS_2 has for example been shown to begin irreversibly converting to 2H-MoS_2 even at low temperatures of 95 ºC.[57] At higher substrate temperatures of 600 ºC and 750 ºC, there is a greater driving force for the 1T-to-2H phase conversion during film growth, resulting in lower concentrations of 1T-WS_2 in the final film. However, complete phase transformation is not achieved even at 750 ºC due to the very short deposition times (in seconds) and moderately fast cooling

rate, as the 1T-structure does not have sufficient time to relax to the more stable 2H-phase. A complete 1T-to-2H phase transformation is only achieved with post-deposition annealing, which can be done in-situ.

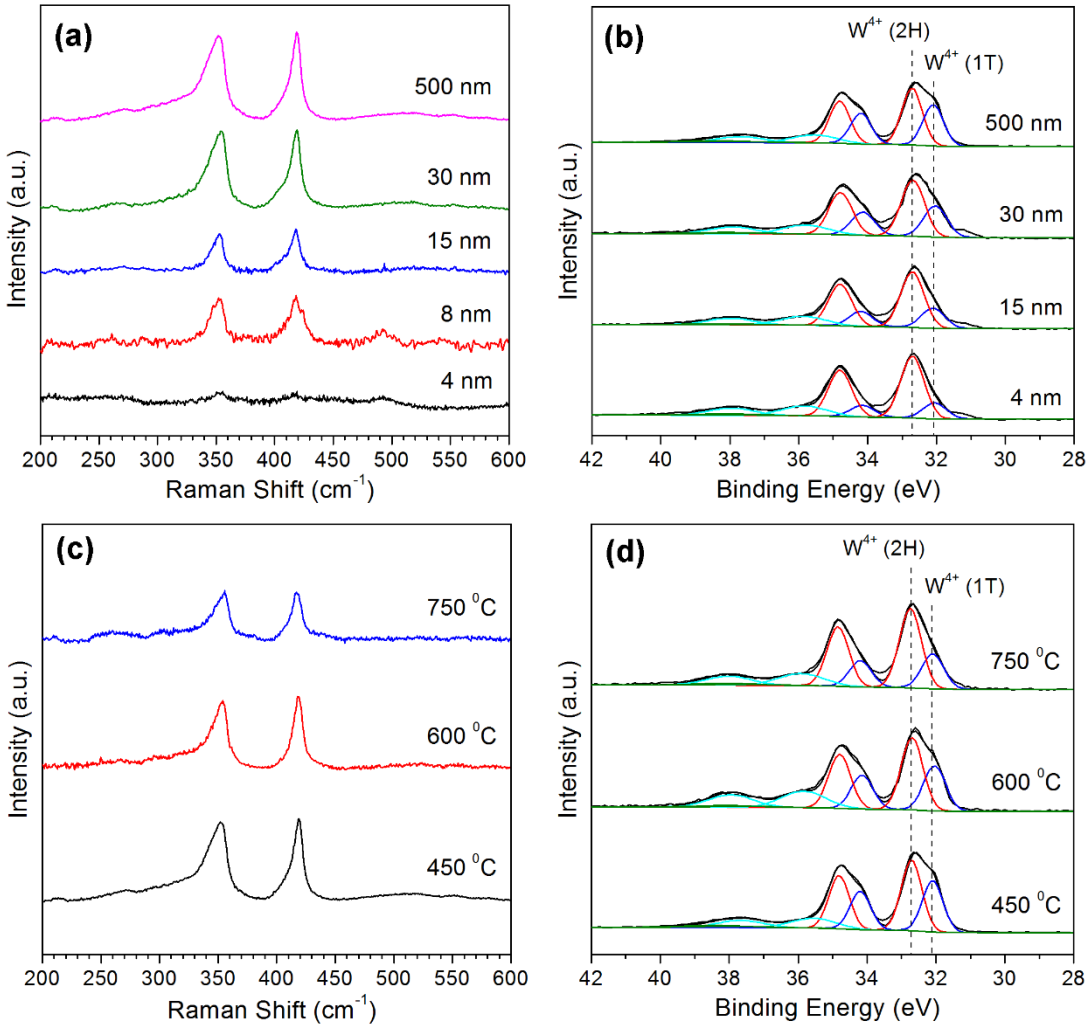

Figure 4.8: (a) Raman and (b) W 4f core level XPS spectra for Ag samples fabricated with varying buffer thickness. (c) Raman and (d) W 4f core level XPS spectra for Ag samples fabricated at different substrate temperatures. All samples were grown using a laser energy of 100 mJ and deposition time of 10 s.

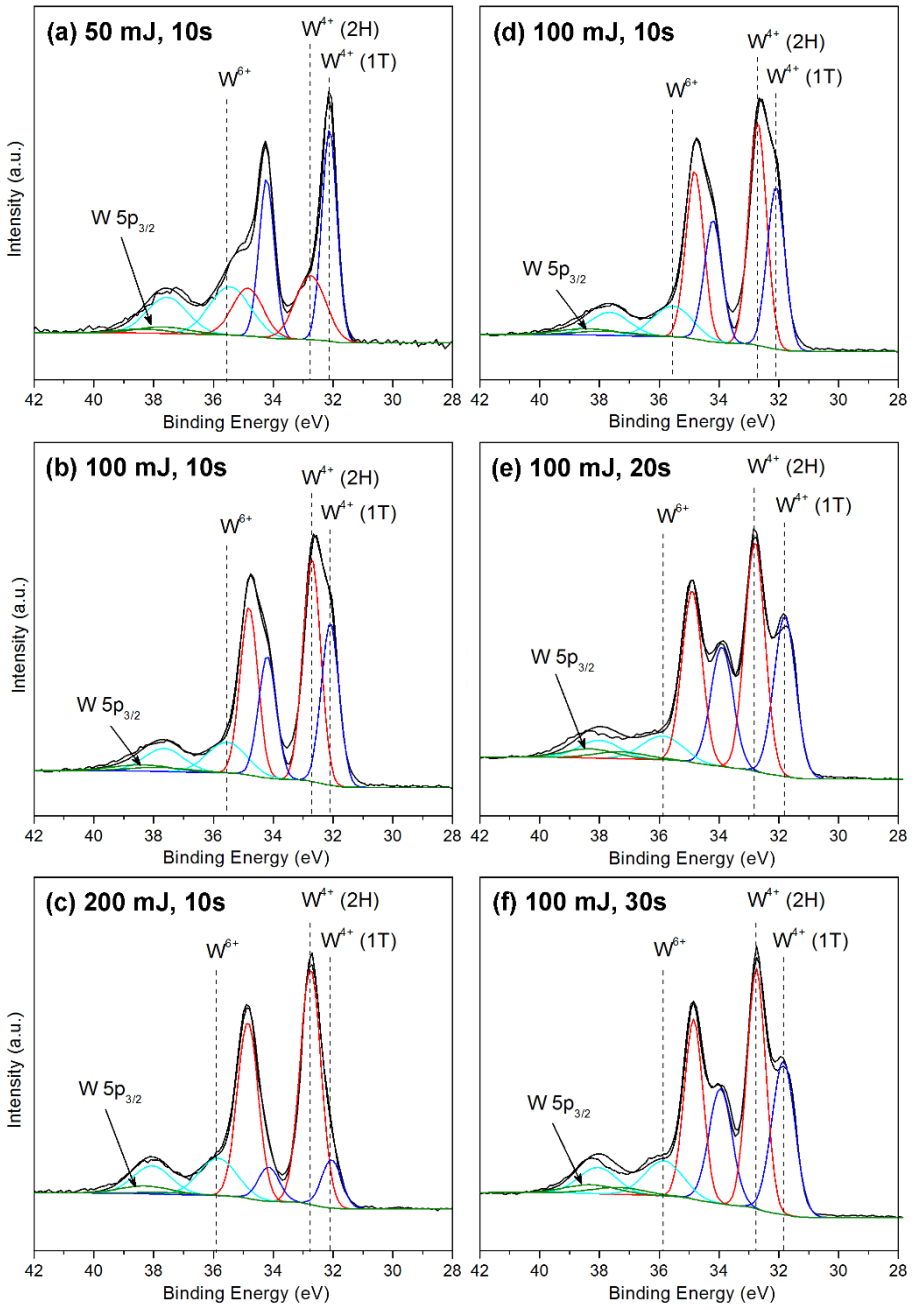

Figure 4.9: XPS spectra showing W 4f core level peak regions for Ag samples fabricated at different laser energies and deposition times.

It was observed that the concentration of the 1T-WS_2 phase appears to decrease with longer deposition times and higher laser energies as depicted in Figure 4.9. In addition, the peak position of the W 4f doublet for 1T-WS_2 continues to shift to lower binding energies with increasing deposition times, an indication of increasingly

metallic character. This phenomenon could possibly be due to bombardment of the growing film by energetic species in the PLD process, which may lead to the breaking of W-S bonds in 1T-WS_2. It is likely that with longer deposition times, the 1T-WS_2 phase would convert completely into metallic tungsten. Similarly, the formation of a metallic layer was previously observed during prolonged sputtering of WS_2,[58] another ion-assisted deposition technique. The breaking of the W-S bond appears to affect only 1T-WS_2 and not 2H-WS_2, as seen by the negligible negative shift in the W 4f peak position for the 2H polymorph. This is deduced to be a consequence of the higher thermodynamic stability of 2H-WS_2, rendering it less likely to be affected by the bombardment of energetic species during film growth.

4.3 Ultrathin WS_2 Layers on Other Metal Substrates

4.3.1 Experimental Procedure

Synthesis: Ag, Au, Al and Ni metal films of approximately 500 nm thickness were sputtered onto normal doped Si substrates and subsequently loaded in a KrF (λ = 248 nm) Lambda Physik excimer PLD system. The energies used for ablation was kept within the range of 50–200 mJ, whereas the deposition time was in the range of 10–30 s. Substrate temperature was maintained at 450 °C during deposition, after which it was decreased at a controlled rate of 20 ºC/min to 300 ºC, whereupon natural cooling processes took over. All other laser parameters and chamber conditions remained the same as those detailed in section 4.2.1.

Characterization: Optical emission spectra of the laser induced plasma were measured in the wavelength region from 350 to 1000 nm using a multichannel Ocean Photonics USB4000 spectrometer. Measurements were taken at intervals from the beginning of discharge until the disappearance of the plasma, with the interval and integration times set at 2 s and 1 s, respectively. All other characterization techniques of Raman, TEM and XPS used to study the as-deposited samples are the same as those detailed in section 4.2.1.

4.3.2 Nanostructural Characterization

Figure 4.10(a) shows the Raman spectra of the as-grown WS_2 film on different metal substrates excited under ambient conditions. The spectrum of bulk WS_2, which consists of two main peaks at ~351 and 420 cm^{-1}, can be found in Figure 4.1(c). At the

deposition parameters of laser energy = 100 mJ and growth time = 10 s, only very weak signals from the characteristic Raman bands of WS_2 at ~352 cm^{-1} and 418 cm^{-1} are obtained for Au and Ni metals. For Al, the WS_2 phonon modes only begin to emerge at longer deposition times of 30 s, suggesting that a greater amount of source atoms is necessary to achieve some degree of crystalline ordering. In contrast, the Ag metal produces WS_2 layers that exhibit intense Raman signals, indicating good crystalline quality in the obtained film. At this excitation wavelength of 514.5 nm, the Raman spectrum of the Ag sample also reveals many second-order peaks in addition to the first-order phonon modes. As shown in Figure 4.10(b), the strongest peak at ~352 cm^{-1} can be resolved by multi-peak Lorentzian fitting into three individual contributions at 343, 351, and 355 cm^{-1}, assigned to $E^{!}_{2g}$ (M), 2LA (M), and $E^{!}_{2g}$ (Γ) modes respectively.[52] It has been shown that peak shifts in the A_{1g} (Γ), 2LA (M) and $E^{!}_{2g}$ (Γ) modes can be used to identify the number of layers in WS_2 films.[5,52] However, at 514.5 nm laser excitation, the intensity ratio of the 2LA (M) to A_{1g} (Γ) phonon modes provides a much more accurate means of ascertaining the thickness of WS_2. From this, it is determined that the Ag sample gives a WS_2 film of ~3 layers. Although the weak Raman signals observed in the other metal substrates makes quantitative analysis of the number of layers in the as-deposited film difficult, the peak intensity ratios suggest that Au, Al and Ni also give ultrathin WS_2 with 2-3 layers. However, the incredibly low peak intensities indicate that these crystalline layers exist largely as tiny clusters in a predominantly amorphous matrix, rather than as a single continuous film. Increasing the laser power and deposition time does little to improve the Raman spectra of the Au, Al and Ni samples, which suggests that these metals are not at all suitable for the growth of highly crystalline WS_2 by PLD.

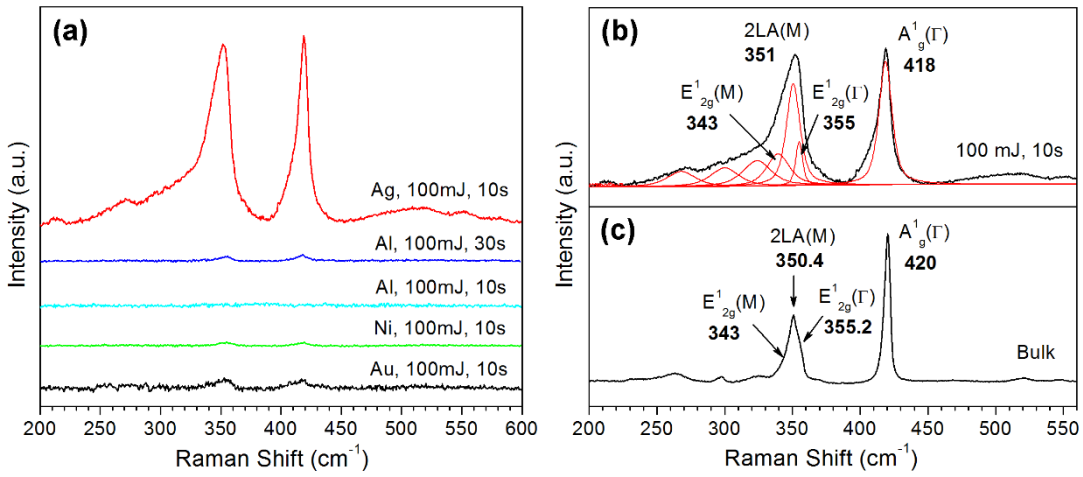

Figure 4.10: (a) Raman spectra of as-grown WS_2 films fabricated on different metal substrates. (b) Multi-peak Lorentzian fitting of Raman bands in the Ag sample fabricated at 100 mJ and 10 s, with (c) the spectra of bulk WS_2 included for comparison.

High resolution TEM images of the Ag samples are shown in Figure 4.11(a), revealing the stacking of WS_2 (002) layers with an interplanar spacing of 0.62 nm. Additional lattice fringes with interplanar spacings of 0.27 nm is observed underneath the WS_2 film, ascribed to the (120) plane of monoclinic Ag_2S [JCPDS #14-0072]. This Ag_2S phase, which develops in-situ, was previously found to promote the growth of ultrathin MoS_2 by PLD through lattice matching and conventional epitaxy (see section 3.3). Its presence here suggests that Ag_2S also fulfils a similar function for WS_2, with W atoms in the first layer of the film binding covalently to the S species in Ag_2S. These covalent bonds manifest as an indistinct boundary at the interface, contrary to the sharp interfaces of 2D layered materials grown by van der Waals epitaxy. Figure 4.11(b) depicts the TEM image of Al samples, in which the crystalline layers of WS_2 are observed as clusters on top of an amorphous aluminium native oxide. The oxide is easily differentiated from the crystalline, pure Al layer through the absence of lattice fringes. These results are in line with the Raman analysis, which previously hinted that

the WS_2 layers on Al, Au and Ni metals exist as crystalline clusters in an amorphous matrix.

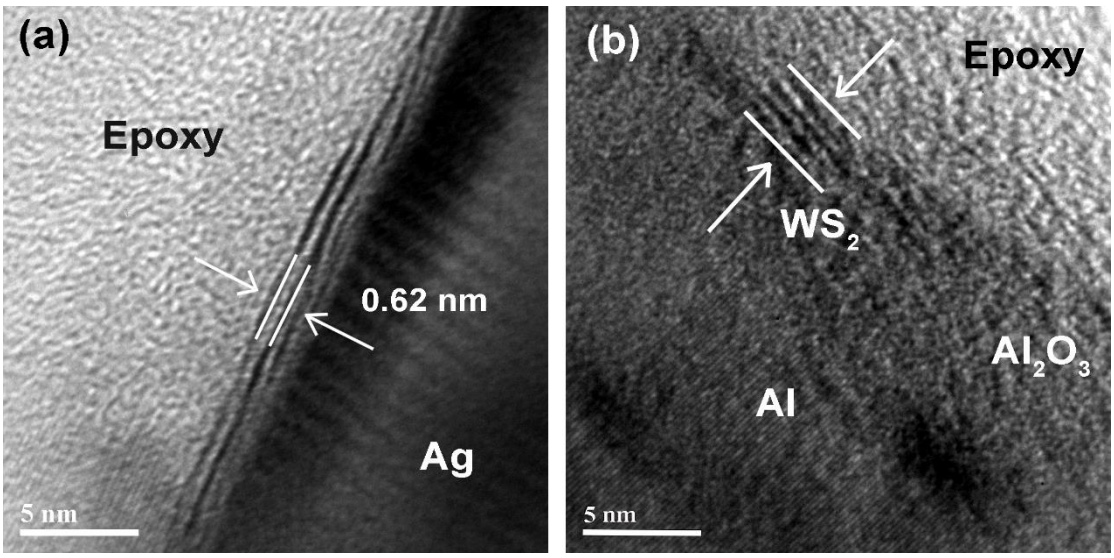

Figure 4.11: Cross-section TEM of (a) Ag and (b) Al samples fabricated at 100 mJ and 10 s.

To characterize the chemical nature and bonding state of WS_2 on metal surfaces, XPS was used to analyse the samples. Figure 4.12(a)-(d) depicts the W 4f and S 2p core level XPS scans for the WS_2 films deposited on Ag, Au, Ni and Al respectively. One S 2p doublet occurring at binding energies of 162.3 and 163.5 eV, consistent with the S^{2-} species of WS_2, is present throughout all four metal substrates. Similarly, the known 4f doublet of the W^{4+} species in 2H-WS_2 can be observed at binding energies of 32.7 and 34.8 eV for all substrates, confirming the formation of the semiconducting 2H-phase of WS_2. For Ag and Ni substrates, there is an additional S 2p doublet located at 161.1 and 162.4 eV, which is within the range of metal sulfide groups. In the case of Ag, this doublet can be assigned to the S^{2-} species of Ag_2S, which was observed beforehand in the TEM images of this sample. A third and final S 2p species, found at binding energies

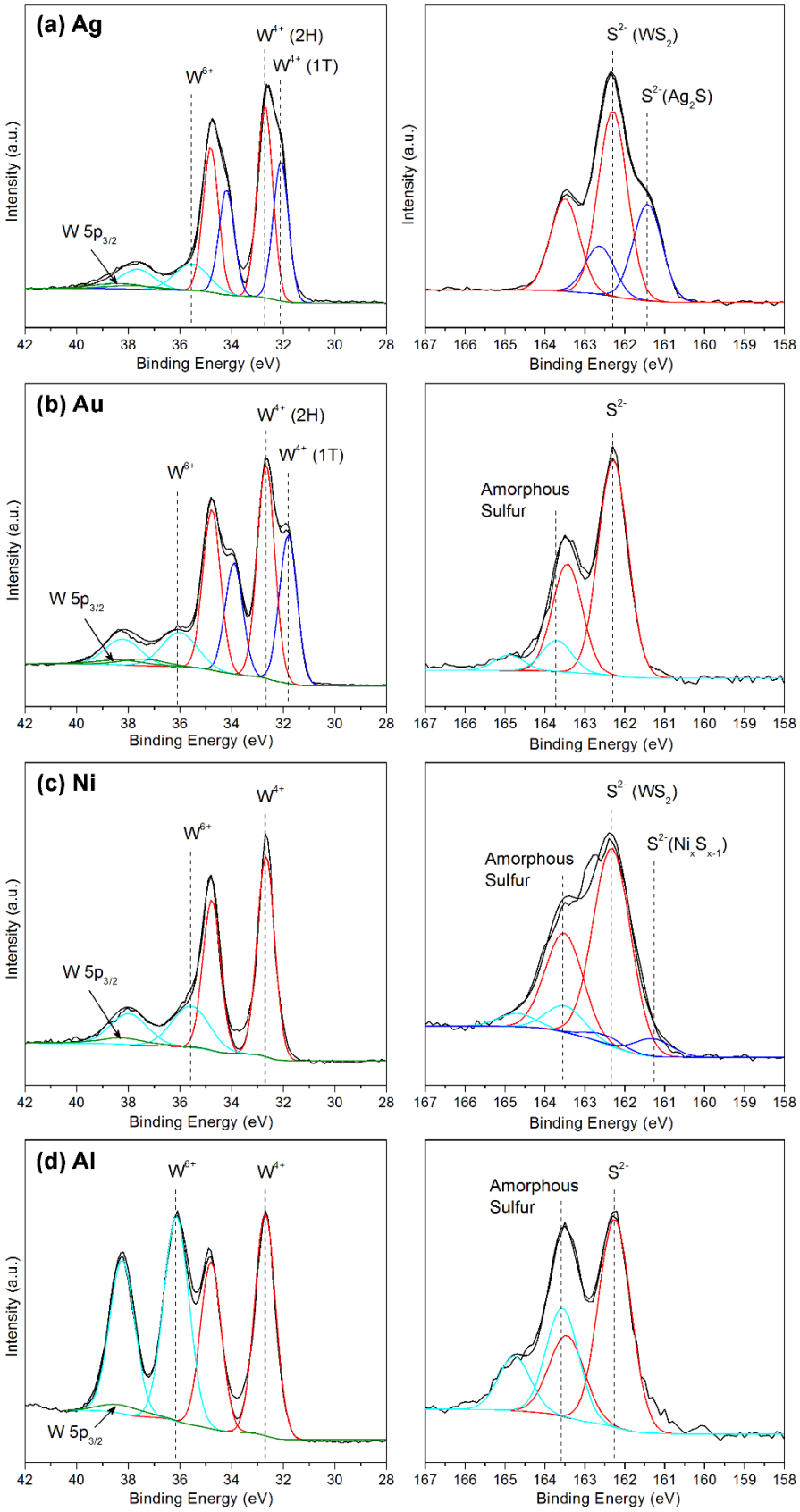

Figure 4.12: XPS spectra showing W 4f and S 2p core level peak regions for (a) Ag, (b) Al, (c) Au and (d) Ni samples fabricated at 100 mJ and 10 s.

of approximately 163.6 and 164.8 eV, is observed for all metals with the exception of Ag. This S 2p species is assigned to the apical S^{2-} or bridging disulfide S_2^{2-} ligands,[59] and can essentially be attributed to the presence of amorphous sulfur that reduces the crystalline quality of WS_2. The relative intensity of these amorphous sulfur peaks is especially high for the Al sample, indicating a much more defective WS_2 structure. The obtained film on Al is also considerably oxidized, judging by the intense peaks from the W^{6+} oxidation state. Curiously, for the noble metals Ag and Au, it was observed that there is an additional W 4f doublet at binding energies of 32.1 and 34.2 eV, as shown in Figure 4.12(a) and 4.12(b). The negative shift of 0.6 eV compared to the 2H-WS_2 doublet suggests the formation of the metallic 1T-phase of WS_2, as discussed in section 4.2.3. These results are surprising since purely 2H-WS_2 is detected in the Ni and Al samples, implying that some quality of the noble metals Ag and Au is capable of inducing the formation and stabilization of the 1T-WS_2.

4.3.3 In-situ Optical Emission Studies of WS_2 Growth

To gain more insight into the physical processes and underlying mechanism of WS_2 growth by PLD, the deposition process was monitored by laser induced breakdown spectroscopy (LIBS). This technique allows the simultaneous analysis of multiple species in all states of aggregation, in addition to having the ability to detect impurity atoms present in trace amounts. Typical optical emission spectra of the WS_2 plasma produced in vacuum using a laser energy of 100 mJ (laser fluence = 10 J cm^{-2}) for our four metal substrates are shown in Figure 4.13(a). All spectra are continuous at wavelengths from 350 to 1000 nm, and there is no apparent differentiation in emission between the four substrates, indicating that the metal layer is unaffected during laser

ablation and that no metallic species from the substrate is generated to form part of the plasma. Figure 4.13(b) gives a clearer view of the emission spectrum for the Ag substrate, which exhibit dominant spectral lines originating from transitions in neutral sulfur (S I) and tungsten (W I). Oxygen and oxide species are notably absent in the full spectrum, providing evidence that oxygen impurities are not found in significant amounts in either the WS_2 target or as adsorbed gases in the deposition chamber. The formation of tungsten oxide on the samples must therefore occur after deposition, either through the presence of oxygen on the substrates themselves or through exposure to atmospheric oxygen when the samples were unloaded. Figure 4.13(c) shows part of the visible portion of the emission spectrum in Figure 4.13(b). Close inspection reveals that this region of the spectrum is dominated by lines from singly ionized sulfur (S II), with some overlapping emission peaks from neutral tungsten (W I). The observed WI and S II transitions, which were confirmed using the NIST database,[60] are marked on the spectrum. Although ionic species of tungsten should also be present in the plasma plume, we are unable to confirm this as the strong emission lines of singly ionized tungsten (W II) fall in the deep UV region (235 nm to 265 nm), which is out of the range of our spectrometer. Nevertheless, the observable spectrum can still be divided into three distinct segments: the spectral region from 350 to 515 nm primarily showed W I transitions, the region from 515 nm to 670 nm had a mix of W I and S II lines, with the S II lines being more dominant, and the wavelength range beyond 670 nm was attributed only to S I transitions. LIBS was also employed for temporal monitoring of the plasma emission up to a deposition time of 30 s, as shown in Figure 4.13(d). The normalized optical signals of W I / S I demonstrate some scatter between individual measurements at the start of laser ablation, but stabilizes after the initial 10 s. The relative standard deviation (RSD) of the normalized optical signals is calculated to be

6.7 ± 1.5 %, which indicates good short-term stability of ablation. Due to the short deposition times needed to fabricate atomically thin WS_2, this short-term stability is imperative for depositing compositionally homogeneous layers of material.

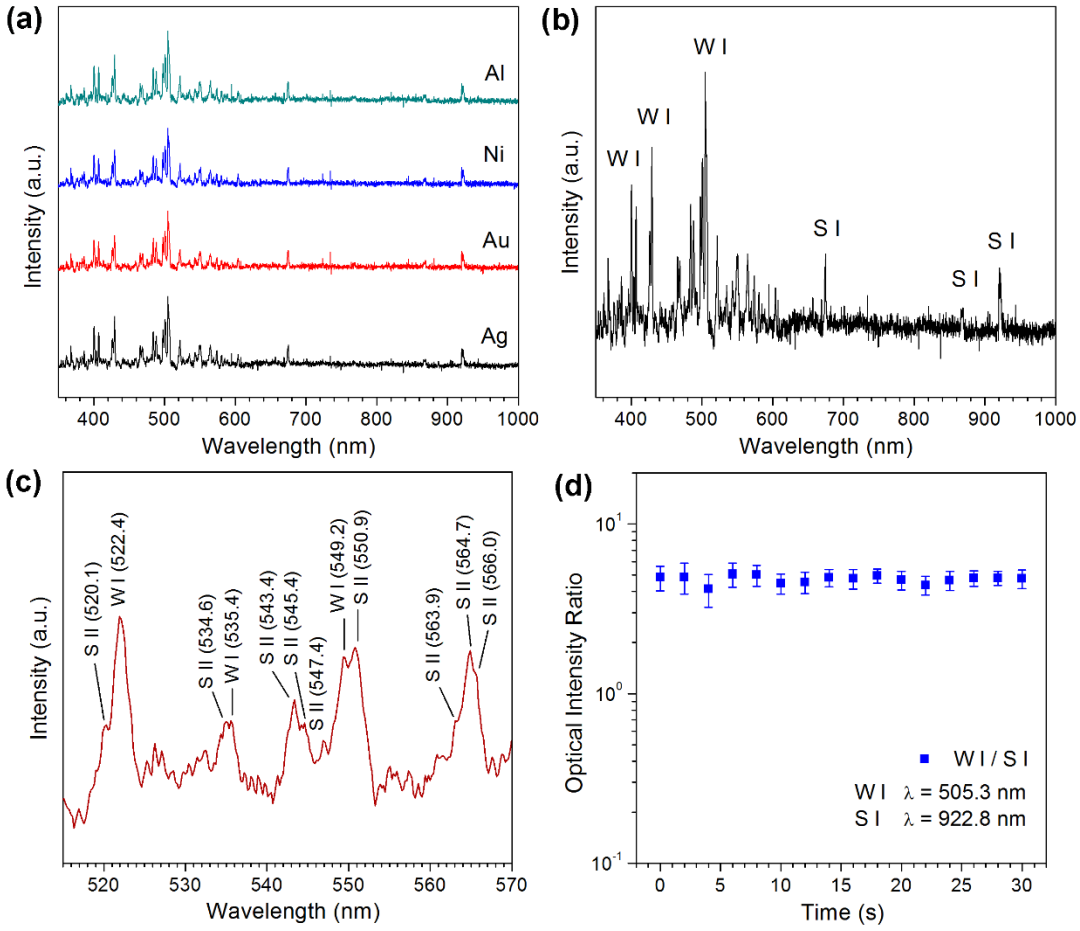

Figure 4.13: (a) Emission spectrum of laser produced plasma from the WS_2 target with different substrates loaded in the PLD chamber. (b) Enlarged emission spectrum of the Ag substrate showing dominant spectral lines originating from transitions in neutral sulfur (S I) and tungsten (W I). (c) Part of the visible radiation portion of the emission spectrum of Ag substrates demonstrating the presence of singly ionized sulfur species (S II). (d) Temporal evolution of the plasma emission signal for Ag substrates up to a deposition time of 30 s.

The LIBS spectra obtained were also used to measure electron temperature of the laser-produced plasma. For a plasma in local thermodynamic equilibrium (LTE), the population of excited states follows the Boltzmann distribution function, which is given in the following relationship,[61]

$$\ln\left(\frac{\lambda_{ij} I_{ij}}{g_i A_{ij}}\right) = -\frac{E_i}{K T_e} + \ln\left(\frac{N(T)}{U(T)}\right) \tag{4.2}$$

with λ_{ij}, I_{ij}, g_i, A_{ij} and E_i denoting the wavelength, intensity, statistical weight, transition probability and energy of the upper state *i*, respectively. *U(T)* is the partition function, *N(T)* the total number density, *K* the Boltzmann constant, and T_e the electron temperature. The relevant spectroscopic parameters of the transition lines of tungsten used in these calculations were taken from the NIST database[60] and are listed in Table 4.2. We selected the spectral range of 400–490 nm as only W I lines are present in this region and there is negligible overlap between peaks. The spectral lines at 400.88 nm and 429.46 nm were ignored due to the effects of self-absorption on the line intensity.[61] As shown in Figure 4.14, the resulting distribution of data fits reasonably well to a linear energy dependence, indicating that the plasma is indeed in effective LTE during deposition and the time of optical measurement. From the slope of the fitted line, we obtain an electron temperature of approximately 8300 ± 400 K or 0.72 ± 0.03 eV. This temperature is slightly higher than the quasi-stationary value of 0.6 eV[61] obtained from the ablation of pure tungsten in vacuum after a delay time of > 1 μs and with a laser fluence of 5 J cm^{-2}. No comparison can be made to similar experiments with WS_2, as none have been published to the best of our knowledge.

Table 4.2: Spectroscopic data used for estimation of electron temperature.

Wavelength (nm)	**Energy of lower state, E_j (eV)**	**Energy of upper state, E_i (eV)**	**Statistical weight, g_i**	**Transition probability, $(A_{ij} \times 10^8)$**
404.56	0.37	3.43	5	0.0288
406.99	0.60	3.64	5	0.0360
421.58	2.42	5.36	9	0.0370
424.14	1.92	4.84	5	0.1070
426.94	0.37	3.27	5	0.0304
430.21	0.37	3.25	7	0.0360
465.99	0.00	2.66	3	0.0100
484.38	0.41	2.97	5	0.0190

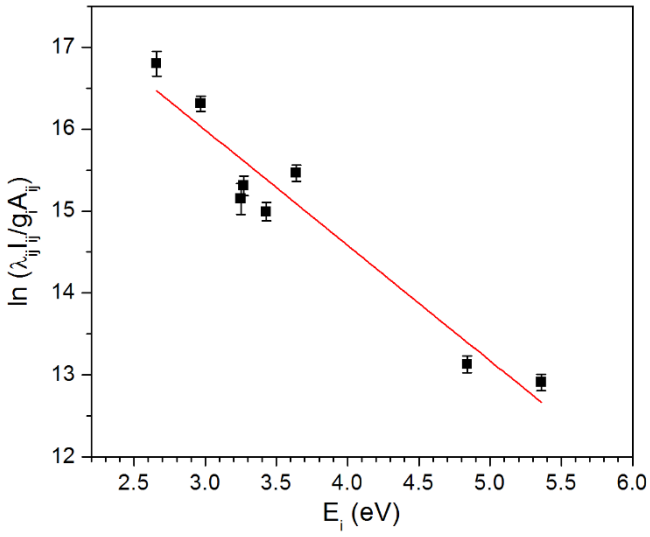

Figure 4.14: Boltzmann plot of W I emission lines used for calculation of electron temperature.

4.3.4 Discussion

The above results clearly show that only Ag was successful in producing highly crystalline and textured WS_2 layers. Ag was also the only substrate to react with the source atoms to form large amounts of a metal sulfide phase in-situ. This can altogether be interpreted as such: rather than being detrimental to the growth process as one would expect, the presence of the metal sulfide phase plays a crucial role in the development of crystalline WS_2 layers. In the initial step of the growth process, ablated S and W atoms arrive on the surface of the substrate. Since the Gibbs free energy of formation at 450 ºC for WS_2 is lower than Ag_2S,[62,63] it is WS_2 that will form first. While the WS_2 platelets are growing, S diffuses around or through the WS_2 grains to react with the Ag layer. During this process the Ag layer becomes more and more sulfur-rich, which continuously lowers the melting point of the material[41]. At approximately 33.333 at% sulfur, a phase mixture of solid βAg_2S and a liquid is stable above 178 ºC. As the substrate in this experiment was held at 450 ºC, a liquid silver sulfide film is formed at the interface that may act as a flux and thereby provide increased mobility to the source atoms and promote the growth of WS_2 crystallites in a preferred direction. Because S atoms were consumed in the making of the Ag_2S phase, some W atoms remain unreacted and sit on top of the completed WS_2 film. From the LIBS spectra, we know that no oxygen impurities are present in the chamber during film growth. And since Ag substrate itself has minimal oxygen when scanned by XPS, these unreacted W atoms only oxidize upon exposure to atmospheric conditions, forming a sort of capping layer. The as-deposited WS_2 film should thus be unaffected by the presence of the oxide, and this is confirmed by the calculated stoichiometric ratio of S : W atoms that is very close to the ideal value of 2. Time monitoring of the LIBS spectra during deposition gives indication of a stable plasma plume, even during the first 10 s of laser ablation, which

is the length of time needed to grow a tri-layered WS_2 film at a laser fluence of 10 mJ cm^{-2}. This stability allows the stoichiometric transfer of source atoms to assist in the epitaxial recrystallization of WS_2 layers. The generation of energetic ionic species, as confirmed by LIBS, also contributes to the process by ensuring high atomic mobility so that the source atoms can be quickly adsorbed onto the substrate surface and interact with each other. This allows for a significant reduction of the growth time and temperature in comparison to CVD.[44,58]

Although Ni is also capable of forming a nickel sulfide phase in-situ, the low relative intensity of the XPS peaks from this species indicates that the quantity produced is very little and likely insufficient to form a new layer over the entirety of the substrate surface. This leaves the Ni base metal as the main growth template. As WS_2 appears to grow preferentially by conventional epitaxy when fabricated using PLD, Ni is unable to produce highly crystalline WS_2 due to the large lattice mismatch at the interface. It might be feasible however, to modify the Ni substrate to make it into a suitable growth template through pre-deposition sulfurization to produce a uniform Ni-S layer. The remaining metal substrates, Al and Au, suffer from the same issue of large lattice mismatches between the substrate and overlying WS_2 film. And unlike Ni or Ag, they do not form any new phase in-situ that can act as an intermediary at the interface. Al also notably requires longer deposition times for the characteristic Raman bands of WS_2 to appear. This is attributed to the presence of a native oxide coating, as seen in the TEM images, which promotes W-O bond formation over W-S. This can be clearly deduced from the prominent peaks of W^{6+} species in the XPS scans. Because the W atoms are all initially consumed by oxide formation, more source atoms must be provided and consequently a longer deposition time is needed before WS_2 can begin to form on Al substrates. The development of large quantities of tungsten oxide also

distorts the ratio of free W to S atoms on the substrate surface, resulting in leftover S atoms that react together to form amorphous sulfur. This is reflected in the S 2p scans of the Al sample that show a much more significant contribution from amorphous sulfur as compared to the other substrates. Overall, the growth mechanism of WS_2 on metal substrates is very similar to that of MoS_2. For both materials, the growth process proceeds through conventional epitaxy and involves the in-situ formation of an Ag_2S phase, which acts as a template for formation of highly crystalline MS_2 layers (M = Mo or W).

In addition to determining the growth mechanism of pulsed laser fabricated WS_2, we consider also a possible origin of the metallic 1T-phase that is formed in the Ag and Au samples. Studies have shown that the metallic ground state in 1T-WS_2 arises from the incomplete occupation of W $4d_{xy,yz,xz}$ orbitals, which also leads to the decreased stability of this phase.[5] Electron doping the 1T-WS_2 lattice has been suggested as a method to increase the stability of the 1T-phase, as the additional electrons from the donor atom occupy the empty conduction band $4d_{xy,yz,xz}$ orbitals of W. In contrast, when such doping occurs in the 2H-phase the donor electrons that populate the higher energy bands induce a change in the electronic structure from semiconducting to metallic, destabilizing the 2H-WS_2 lattice.[23] Consequently, the formation of the 1T-phase becomes favoured over that of 2H-WS_2. For lithium intercalated MoS_2 and WS_2, the electron transfer to the TMD layers also implies the insertion of Li^+ into the van der Waals gap, with Li occupying the interlayer S–S tetrahedral site and forming the 1T-$LiMS_2$ (M = Mo or W) phase.[15,21,22] Even for a single Li atom located on top of Mo in 2H-MoS_2, there is still some charge transferred to MoS_2 according to a Lowdin charge analysis.[45] It has been noted that the 1T-phase can also achieved by the substitutional doping of Re, Tc, and Mn atoms. A 2H-to-1T

phase transition was observed by scanning TEM for Re-doped MoS_2,[14] but its origin and nature have not been addressed. It was however postulated that the 2H-to-1T phase transition was also induced by electron doping, as with TMDs intercalated with alkali metals, due to the fact that Re has one more valence electrons than Mo.

In the case of pulsed laser grown WS_2 layers, we believe that it is possible to explain the formation of the 1T-phase in terms of electron doping due to charge transfer from metallic atoms in the buffer layer. Both Ag ($4d^{10}\ 5s^1$) and Au ($5d^{10}\ 6s^1$) have more valence electrons than W ($5d^4\ 6s^2$), allowing them to potentially act as electron donors. Unlike with Re, Tc and Mn atoms however, substitutional doping of Ag/Au is not expected to occur. This is because the closed d^{10} shell of both Ag and Au atoms is very stable, which makes it difficult for these atoms to ionize to the +4 oxidation state necessary for substitutional doping of WS_2 to take place. Furthermore, once incorporated into the WS_2 lattice the Ag/Au atoms would need to donate even more electrons in order to induce the phase transition from 2H-to-1T, rendering this scenario highly unfeasible. A more viable explanation would be for the Ag/Au atoms located in the vicinity of the WS_2 sheets to donate one electron each to the WS_2 lattice, similar to how Li donates an electron during intercalation of TMDs. This would then lead to the formation of a stable d^{10} shell as well as a phase transformation from 2H- to 1T-WS_2. Because the Ag/Au atoms are confined to the interface, only the first WS_2 layer in direct contact with the metal buffer would be affected by the electron doping and be converted to the 1T-phase. The resulting tri-layered film is thus composed of a mixture of 2H- and 1T-WS_2. Although Ni ($3d^8\ 4s^2$) similarly possesses more valence electrons than W, it reacts in atmospheric conditions to form oxides. Having lost two electrons to form Ni^{2+} in nickel (II) oxide, the ability of Ni to act as electron donor for WS_2 is greatly reduced and consequently the 1T-phase is absent in WS_2 films grown on Ni. On the

other hand, Al only has 3 valence electrons compared to the 6 present in W, rendering it unsuitable as an electron donor for WS_2.

The possible formation of 1T-WS_2 by intercalation with Ag/Au raises a number of interesting questions. For example, we claimed that in our tri-layered WS_2, intercalation effects would be confined only to the WS_2 layer at the interface. Would it then be feasible to obtain purely 1T-WS_2 if a single layer is prepared on Ag/Au? We believe this is certainly possible based on the double-layered WS_2 film on Ag fabricated in section 4.2. This sample was found to possess a significantly higher concentration of the 1T-phase compared to 2H-WS_2 (the ratio of 1T-to-2H increases from 0.73 to 1.67 when tri-layered WS_2 is reduced to two layers). It is thus expected that a single layer would be composed entirely of the 1T-phase, which leads to the issue of using Au contacts for WS_2-based devices. Since these devices also utilize mono-layered WS_2, the presence of Au combined with joule heating during device testing could induce phase transformation from 2H- to 1T-WS_2. As even partial conversion to the 1T-phase would affect device performance, such a phenomenon, if it indeed occurs, would have serious implications for ongoing efforts to fabricate WS_2-based devices. It is thus imperative for further investigations into the influence of Au on pre-fabricated WS_2 sheets grown by non-PLD methods to be conducted.

4.4 Few-layer WS_2 Field Emitters by PLD

4.4.1 Experimental Procedure

Synthesis: The procedure for synthesising few-layer WS_2 on Ag nanocones is similar to that described in section 3.4.1. The laser energies used for PLD growth of WS_2 was 50 and 100 mJ, and the resulting samples will hereafter be referred to as Ag-50 and Ag-100 respectively.

Characterization: SEM, Raman and XPS analysis of the nanocones before and after WS_2 deposition were conducted using the same instruments and conditions as that detailed in section 3.4.1.

Field Emission Tests: The field emission setup, conditions and testing procedure is similar to that detailed in section 3.4.1.

4.4.2 Nanostructural Characterization

From Figure 4.15(a), it can be seen that a mostly uniform and highly dense array of nanosized cones was produced when the Ag film was irradiated with ions, with dimensions similar to that described in section 3.4.2. Figure 4.15(b) shows the nanocones after they had been heated to 450 ºC and cooled back to room temperature in the PLD chamber without depositing any WS_2. Just as was observed in section 3.4.2, the nanocones lost most of their conical shape to result in a particulate film littered with fractured cone tips. The Ag grains also underwent significant grain growth, reaching sizes of up to 1.1 μm from an average of ~50 nm before heat treatment.

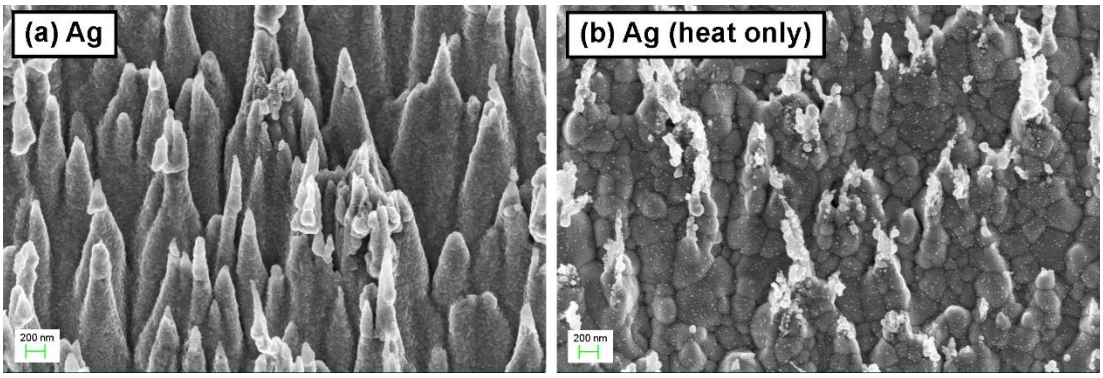

Figure 4.15: SEM images of Ag nanocones (a) before and after (b) heat treatment at 450 ºC without WS_2 growth.

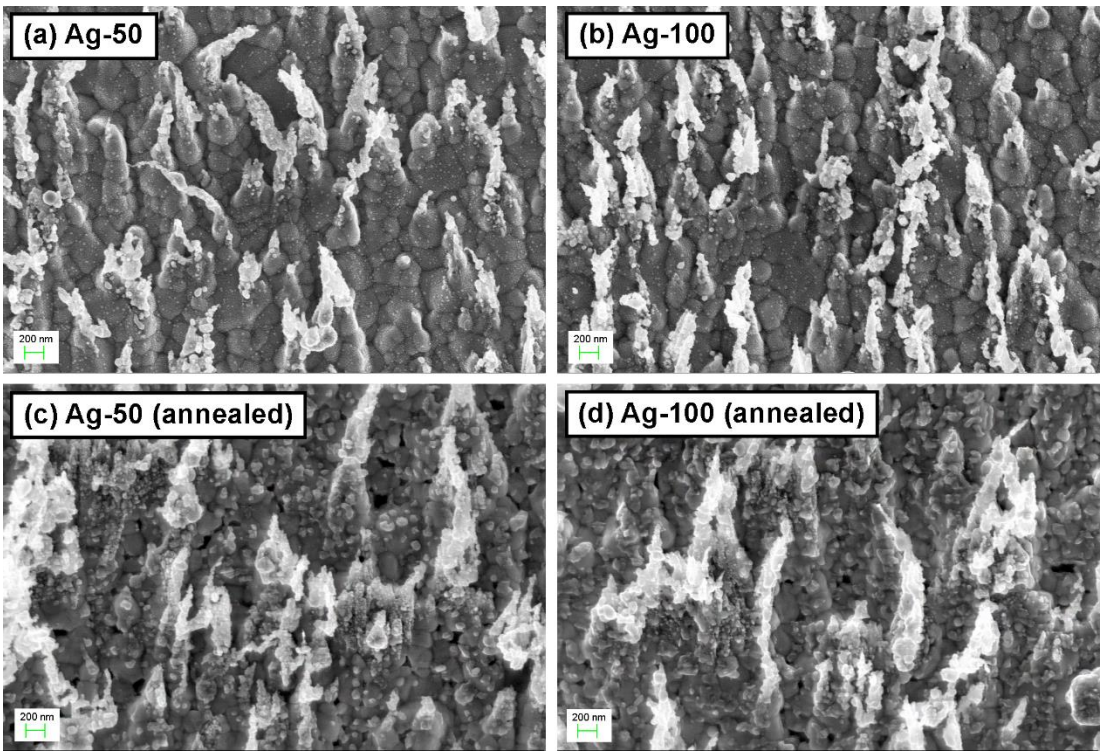

Figure 4.15: SEM images of Ag nanocones (a)-(b) after WS_2 growth and (c)-(d) after post-deposition annealing at 300 ºC for 30 min.

Figure 4.16(a) and 4.16(b) shows the SEM images of the nanocones after WS_2 growth by PLD. The bombardment of energetic species at either laser energies of 50 or 100 mJ does not appear to influence the nanostructures on the substrate surface. Post-deposition annealing of the samples at 300 ºC for 30 min however, induces further

recrystallization and growth of the Ag grains. The surface is now covered with numerous newly formed small grains and the broken tip fragments have also grown larger. The Raman and XPS spectra of the WS_2-coated nanocones before and after annealing at 300 ºC are depicted in Figure 4.17. The characteristic Raman modes of 2H-WS_2 are present in all samples. From the W 4f core level XPS spectra in Figure 4.17(b), we note also the presence of the 1T-phase in the as-fabricated samples, which completely transforms to 2H-WS_2 after annealing. As with the MoS_2-coated nanocones described in section 3.4, multiple Raman and XPS measurements conducted at different positions over the entire sample surface gave consistent results, confirming the successful and uniform coating of WS_2 layers onto the nanocones.

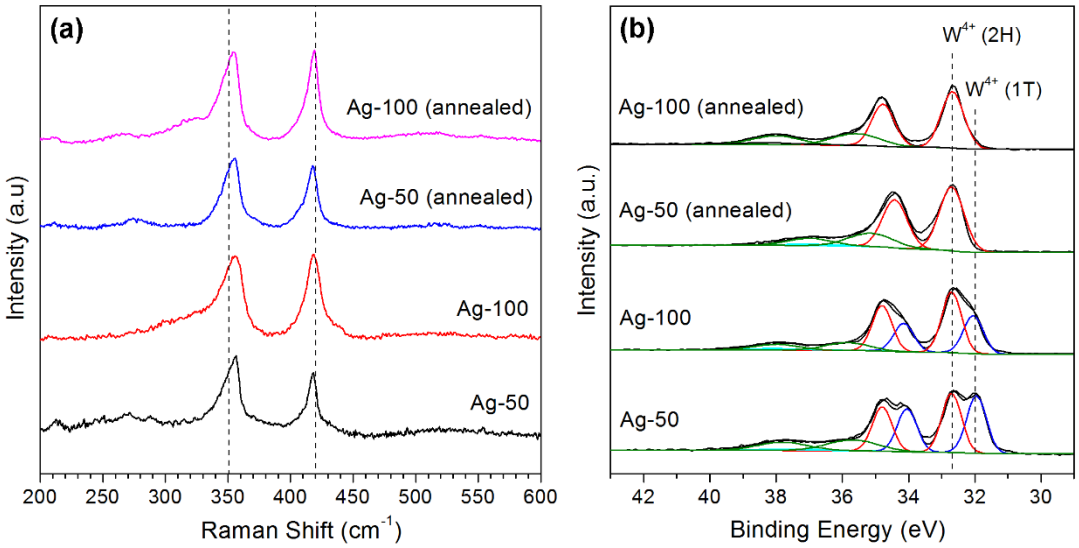

Figure 4.17: (a) Raman and (b) XPS W 4f core level spectra of as-grown WS_2 on Ag nanocones before and after annealing at 300 ºC for 30 min. The left and right dashed lines in (a) indicate the positions of the 2LA (M) and A_{1g} phonon modes in bulk WS_2 respectively.

4.4.3 Field Emission Studies of Few-layer WS_2 Coated Nanocones

The field emission I-V plots for all WS_2-coated samples are shown in Figure 4.18. With the turn-on voltage defined as the voltage required to reach a current of 1

μA, the as-fabricated Ag nanocones were not able to reach the electron emission turn-on current within the maximum limits of the applied voltage. For the WS_2-coated nanocones, samples Ag-50, Ag-100, Ag-50 (annealed) and Ag-100 (annealed) have turn-on voltages of 795, 695, 910 ad 815 V respectively. The Fowler-Nordheim (F-N) plots for all samples are shown in Figure 4.19, revealing a linear trend between $\ln\left(\frac{I}{V^2}\right)$ and $\left(\frac{1}{V}\right)$. This indicates that electron emission occurs through a quantum tunnelling process. The slight deviation from the main linear relationship at the high voltage region for samples Ag-100 and Ag-100 (annealed) can be attributed to the space charge effect.[64] It is unlikely that geometric alteration due to Joule heating is a factor as the F-N plots are generally reproducible.. Assuming $ø_{WS_2}$ = 5.1 eV,[33] the field enhancement factor, β, was calculated to be 54, 57, 32, and 33 for samples Ag-50, Ag-100, Ag-50 (annealed) and Ag-100 (annealed) respectively.

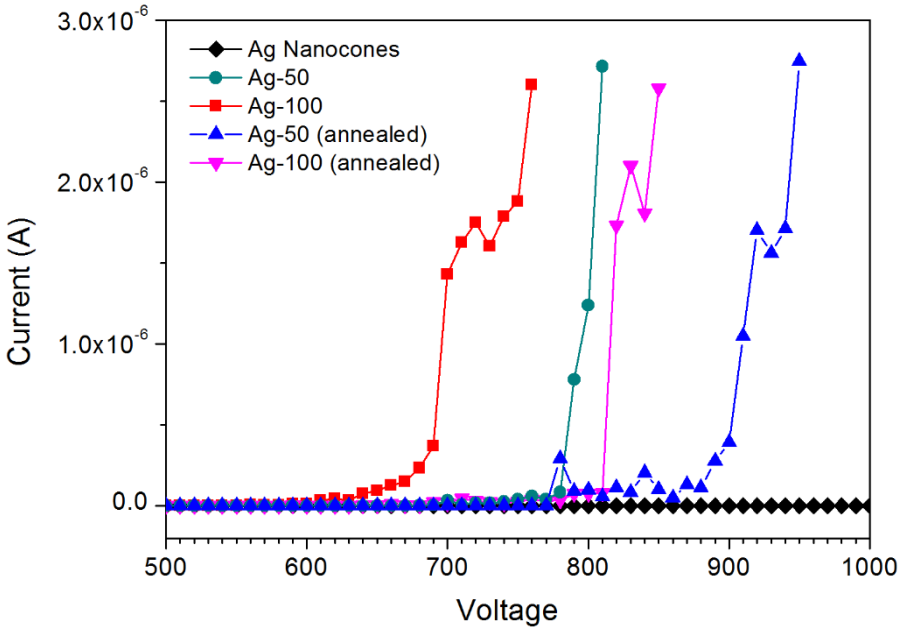

Figure 4.18: Field emission plots of current against voltage for WS_2-coated Ag nanocones.

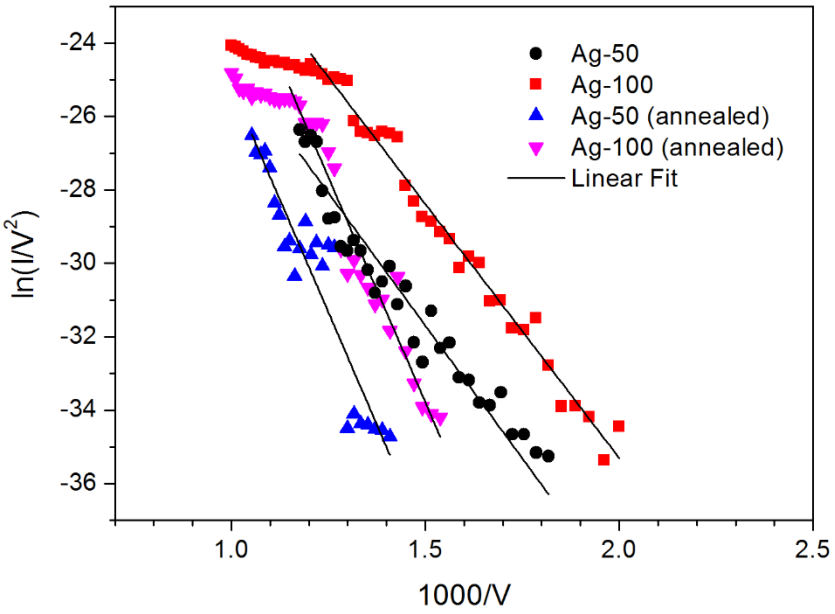

Figure 4.19: Fowler-Nordheim plots for WS_2-coated Ag nanocones.

4.4.4 Discussion

As observed from the SEM images, the Ag nanocones lost most of their definitive conical geometry after heating to 450 ºC due to rapid grain growth and densification. Ag thin films have been reported to undergo significant grain growth even at homologous temperatures (reaction temperature divided by melting temperature) as low as 0.2 K and for annealing durations as short as 5 min.[66,67] With Ag possessing a melting temperature of 961 ºC, the deposition temperature of 450 °C used for the growth of WS_2 by PLD corresponds to a homologous temperature of 0.47. Despite the short deposition time of 10 s, the heating and cooling of the Ag nanocones at ~20 ºC/min means that overall, the nanocones are held at homologous temperatures of > 0.2 for at least 30 min. Consequently, substantial recrystallization and grain growth occurs such that the conical structures lose their characteristic shape. Reflow and diffusion are not thought to play large roles in the loss of the conical shape as these

processes require higher deposition temperatures and prolonged heating to have a significant effect.

Despite the loss of the conical geometry, all WS_2-coated nanocones were still able to reach the turn-on current within the maximum limits of the voltage. This can be attributed to the surface roughness of the samples, as the numerous nanometric protrusions act as sites for electron emission. However, the overall low β values for the coated samples indicates that, rather than geometrical enhancement, the lowering of the effective barrier height is the dominant mechanism for enhanced field emission performance. Because electrons must tunnel through this barrier from the metal into the conduction band of the semiconductor before escaping into vacuum, field emission performance is limited by the barrier at metal-semiconductor junction rather than the one at the semiconductor-vacuum interface.[68] Ag ($ø_{Ag}$ = 4.3–4.6 eV)[69] has a work function that is very close to the electron affinity of WS_2 (χ = 4.5 eV),[4] leading to the formation of Schottky barriers and n-type contacts due to charge transfer from the metal to WS_2.[70,71] With the energy levels of Ag lying so close to the conduction band of WS_2, the injection of carriers from the metal into WS_2 is more efficient and thus decreases the contact resistance. Furthermore, strong adhesion at the metal-semiconductor interface through covalent bonds can perturb the band structure of TMDs to result in significant lowering of the Schottky barrier. In some instances, the perturbation is so strong that TMD regions directly adjacent to the metal becomes metalized and the Schottky barrier vanishes.[70,71] Ag demonstrates medium hybridization with TMDs such as MoS_2 and develops moderately high Schottky barriers when physically adsorbed on the surface.[70] However, in this work the WS_2 layers were established to bond covalently to the underlying Ag substrate (see section 4.2.2). As such, a lower than expected Schottky barrier is believed to form at the interface. Combined with the n-type doping

of WS_2 due to chare transfer from Ag, the probability of Fowler-Nordheim tunnelling increases such that all coated nanocones display improved field emission capability compared to the pristine nanocones.

Another interesting observation is that the field emission performance deteriorated when the samples were annealed at 300 ºC. Part of the reason can be attributed to grain growth and enlargement of the broken tip fragments, which decreases the external field enhancement as indicated by the reduction of the β value. Of more import however, is the change in structure of the WS_2 layers: the as-deposited samples consist of a mixture of 1T- and 2H-WS_2, whereas the annealed samples contain only the 2H-phase. In field emission, the conductivity of the emitters are also important contributing factors.[72] Compared to the semiconducting 2H-phase, which often forms high resistance Schottky contacts with metals, the 1T-phase of 2D TMDs are metallic and typically have much higher electrical conductivity. For example, 1T-MoS_2 is hydrophilic and 10^7 times more conductive than the semiconducting 2H-polytype,[73] with an estimated carrier concentration of $>10^{13}$ cm^{-2}.[37] This significantly higher conductivity allows for far more efficient electron transport from the substrate to the coating material. Recent studies on FETs based on 1T-MoS_2 have in fact shown that charge injection into the channel for such devices is more efficient compared to FETs based on purely 2H-MoS_2 contacts.[38] What then of the transport from the 1T-WS_2 to the surface of the coating? It was postulated in section 4.3.4 that the electron doping of WS_2 layers by Ag occurs only at the regions directly adjacent to the interface. Consequently, the resulting structure should have three distinct layers: Ag, 1T-WS_2 and 2H-WS_2. Due to the similar work function and conduction band energy relative to vacuum level between the 1T- and 2H- polytypes, a low contact resistance is formed between these two phases. For example, transistors utilizing 1T-MoS_2 contacts and a

2H-MoS_2 channel were demonstrated to have a contact resistance of ~200 Ω μm[37] versus the values of 0.7–1.5 kΩ μm typically reported for metal contacts on 2H-MoS_2.[74,75] All of these attributes come together to result in highly efficient electron transport from the Ag nanocones to 1T-WS_2 and further on to the surface of 2H-WS_2, allowing for a lower turn-on voltage compared to the annealed samples, which consists of only of the 2H-phase and thus have higher contact resistance. Figure 4.20 shows the schematic diagrams of the band structure of the uncoated and coated metal nanocones.

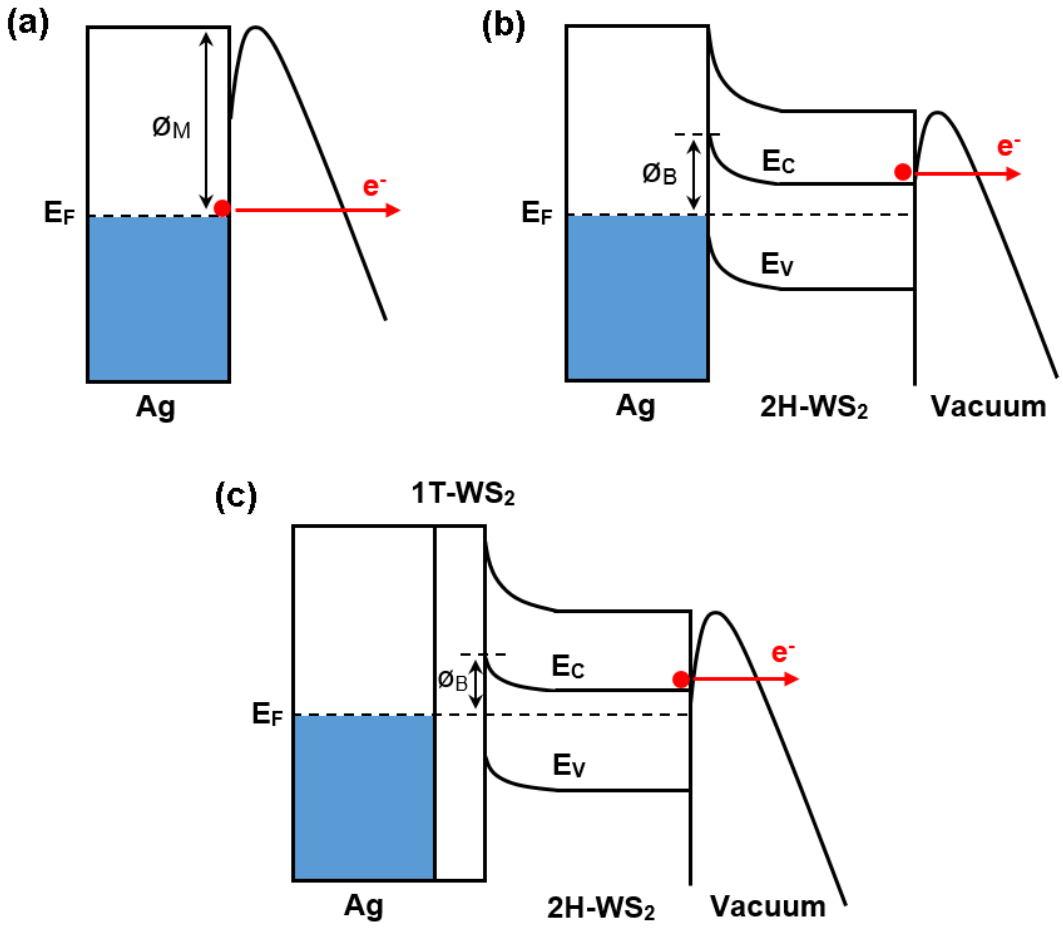

Figure 4.20: Band alignments of (a) pristine Ag nanocones, (b) 2H-WS_2-coated nanocones and (c) Ag nanocones with a hybrid 1T- and 2H-WS_2 coating.

Between Ag-50 and Ag-100, the former exhibits higher turn-on voltages due to a more defective structure as can be deduced from the Raman spectra. This characteristic of the WS_2 layers grown at 50 mJ was also discussed in section 4.2.2. The defects act as traps for electrons and also increases the probability of scattering, leading to overall lower electrical conductivity than the WS_2 layers grown at 100 mJ. After annealing, the crystallinity of the WS_2 film improves but is still not quite comparable to Ag-100 (annealed). In addition, a higher layer number generally favours smaller Schottky barrier heights,[71] hence Ag-50 (annealed) has a higher turn-on voltage compared to Ag-100 (annealed).

Although the WS_2-coated Ag nanocones were able to achieve the turn-on current, the voltages at which this occurred were rather high. This is believed to be due to the loss of the geometric shape of the Ag nanocones after WS_2 deposition. Moreover, the tip size of the original nancones were larger (~50 nm) than the typical size of nanotube tips (~30 nm)[48] and nanosheet edges (~1–5 nm).[76] All these factors contribute to a much lower β value that limits the field emission properties of WS_2-coated Ag nanocones. Future consideration should thus be given to preserving the nanocone structure and reducing the tip sizes in order to fabricate better WS_2-based field emitters.

4.5 Summary

Crystalline few-layer WS_2 on Ag were successfully fabricated by PLD in section 4.2. Samples fabricated at a laser energy of 100 mJ and deposition time of 10 s demonstrated the optimum balance between crystalline quality and film thickness. It was also found that crystalline WS_2 is able to form on Ag layers as thin as 8 nm, leading to high optical transmittance in the visible range, which is advantageous for applications

in optoelectronic devices and solar cells. Curiously, the resulting WS_2 film consisted of a hybrid 2H-1T structure. Higher Ag thickness favoured the formation of the 1T-phase, suggesting that the Ag substrate was responsible for the stabilization of 1T-WS_2 at room temperature. Other factors influencing the phasic composition of the WS_2 film was also studied. Lower growth temperatures led to a higher proportion of the 1T-phase due to the tendency of 1T-WS_2 to convert to 2H-WS_2 upon heating. On the other hand, higher laser energies favoured the 2H-phase, possibly because the 1T-phase is disrupted by bombardment of high energetic ions. These results provide a new route for the stabilization of 1T-WS_2 and could pave the way for future fabrication of purely 1T-WS_2 sheets for high performance devices.

In section 4.3, we investigated the viability of several metals as substrates for growth of 2D WS_2 by PLD. The physical processes and underlying growth mechanism was also studied, and is determined to be similar to pulsed laser fabricated MoS_2, wherein the in-situ formation of a lattice matching metal sulfide phase is crucial to the growth of WS_2. The resulting film is thus bound to the substrate through conventional epitaxy rather than the expected Van der Waals epitaxy. Ag substrates were very successful at producing highly crystalline few-layer WS_2 precisely due to the formation of substantial amounts of an Ag_2S phase. In contrast, Al, Au and Ni metal were only able to produce amorphous or at best partially crystalline WS_2 due to insufficient or a complete lack of a suitable growth template at the interface. In addition, it was found that the type of metal can affect the phase of the resulting WS_2 film. For Ag and Au, we obtained a hybrid 2H-1T structure, whereas for Al and Ni, only the 2H phase was formed. It was posited that the 1T-phase was induced by the electron doping of Ag/Au atoms located within the vicinity of the WS_2 lattice. By donating electrons, the Ag/Au atoms are able to form a stable d^{10} shell in addition to destabilizing the 2H-phase of

WS_2, which leads to the formation of 1T-WS_2. The 2H-to-1T conversion affects only the first WS_2 layer at the interface, thus resulting in a phasic mixture of 2H- and 1T-WS_2 in the final multi-layered films. Although these findings open up the possibility of Ag- or Au-doped 1T-WS_2 nanostructures as superior catalysts for HER, they also raise certain issues for device fabrication. Namely, the influence of Au contacts on monolayer WS_2 sheets during testing of WS_2-based devices. Further work would be required to conclusively resolve these issues.

In section 4.4, WS_2-based field emitters were fabricated by depositing WS_2 layers on Ag nanocones by PLD. It was observed that the conical geometry of Ag nanocones was destroyed with heating to 450 ºC due to rapid grain growth and densification. Nevertheless, the WS_2-coated samples still demonstrated improved field emission over pristine nanocones due to reduction of the potential barrier for electron field emission by formation of a Schottky barrier at the WS_2-Ag interface. In addition, the broken tip fragments on the surface of the samples acted as nanometric sharp edges that contributed to geometric field enhancement. The as-deposited WS_2-coated nanocones exhibited lower turn-on voltages compared to the corresponding annealed samples due to the phasic mixture of 1T- and 2H-WS_2 in the former compared to the pure 2H-phase in the latter. With the higher electrical conductivity and carrier concentration of the metallic 1T-WS_2, in addition to the similar work functions and conduction band energy relative to vacuum level between the 1T- and 2H- phases, there is highly efficient electron transfer from the substrate to the surface and hence a lower turn-on voltage. Finally, the Ag-50 samples demonstrated higher turn-on voltages than Ag-100 due to the higher density of defects that trap and scatter electrons.

References

1. Wang, Q. H.; Kalantar-Zadeh, K.; Kis, A.; Coleman, J. N.; Strano, M. S. *Nat. Nanotechnol.* **2012**, 7, 699−712.
2. Ganatra, R.; Zhang, Q. *ACS Nano* **2014**, 8, 4074–4099.
3. Chhowalla, M., Shin, H. S., Eda, G., Li, L. J., Loh, K. P., Zhang, H. *Nature Chem.* **2013**, 5, 263−275.
4. Lee, S. H.; Lee, D.; Hwang, W. S.; Hwang, E.; Jena, D.; Yoo, W. J. *Appl. Phys. Lett.* **2014**, 104, 193113.
5. Gutiérrez, H. R.; Perea-López, N.; Elías, A. L.; Berkdemir, A.; Wang, B.; Lv, R.; López-Urías, F.; Crespi, V. H.; Terrones, H.; Terrones, M. *Nano Lett.* **2013**, 13, 3447−3454.
6. Ramasubramaniam, A. *Phys. Rev. B: Condens. Matter Mater. Phys*. **2012**, 86, 115409.
7. Zhu, Z. Y.; Cheng Y. C.; Schwingenschl¨ogl, U. *Phys. Rev. B: Condens. Matter Mater. Phys*. **2011**, 84, 153402.
8. Lin, L. Xu, Y.; Zhang, S.; Ross, I. M.; Ong, A. C. M.; Allwood, D. A. *ACS Nano* **2013**, 7, 8214−8223.
9. Hwang, W. S.; Remskar, M.; Yan, R.; Protasenko, V.; Tahy, K.; Chae, S. D.; Zhao, P.; Konar, A.; Xing, H. G.; Seabaugh, A. et al. *Appl. Phys. Lett.* **2012**, 101, 013107.
10. Zhang, Y.; Zhang, Y.; Ji, Q.; Ju, J.; Yuan, H.; Shi, J.; Gao, T.; Ma, D.; Liu, M.; Chen, Y. et al. *ACS Nano* **2013**, 7, 8963.
11. Braga, D.; Lezama, I. G.; Berger, H.; Morpurgo, A. F. *Nano Lett.* **2012**, 12, 5218.
12. Zhang, Y.; Ye, J.; Matsuhashi, Y.; Iwasa, Y. *Nano Lett.* **2012**, 12, 1136.
13. Liu, L.; Kumar, S. B.; Ouyang, Y.; Guo, J. *IEEE Trans. Electron Devices* **2011**, 58, 3042.
14. Lin, Y.-C.; Dumcenco, D. O.; Huang, Y.-S.; Suenaga, K. *Nature Nanotechnol.* **2014**, 9, 391−396.
15. Wang, L.; Xu, Z.; Wang, W.; Bai, X. *J. Am. Chem. Soc.* **2014**, 136, 6693−6697.

16. Kan, M.; Wang, J. Y.; Li, X. W.; Zhang, S. H.; Li, Y. W.; Kawazoe, Y.; Sun, Q.; Jena, P. *J. Phys. Chem. C* **2014**, 118, 1515−1522.
17. Wang, X.; Shen, X.; Wang, Z.; Yu, R.; Chen, L. *ACS Nano* **2014**, 11, 11394−11400.
18. Eda, G.; Fujita, T.; Yamaguchi, H.; Voiry, D.; Chen, M. W.; Chhowalla, M. *ACS Nano* **2012**, 6, 7311–7317.
19. Wypych, F.; Solenthaler, C.; Prins, R.; Weber, T. *J. Solid State Chem.* **1999**, 144, 430−436.
20. Heising, J.; Kanatzidis, M. G. *J. Am. Chem. Soc.* **1999**, 121, 638−643.
21. Gordon, R. A.; Yang, D.; Crozier, E. D.; Jiang, D. T.; Frindt, R. F. *Phys. Rev. B* **2002**, 65, 125407.
22. Yang, D.; Frindt, R. F. *J. Phys. Chem. Solids* **1996**, 57, 1113−1116.
23. Enyashin, A. N.; Yadgarov, L.; Houben, L.; Popov, I.; Weidenbach, M.; Tenne, R.; Bar-Sadan, M.; Seifert, G. *J. Phys. Chem. C* **2011**, 115, 24586−24591.
24. Ran, J.; Zhang, J.; Yu, J.; Jaroniec, M.; Qiao, S. Z. *Chem. Soc. Rev.* **2014**, 43, 7787−7812.
25. Zong, Xu; Han, J.; Ma, G.; Yan, H.; Wu, G.; Li, C. *J. Phys. Chem. C* **2011**, 115, 12202–12208.
26. Voiry, D.; Salehi, M.; Silva, R.; Fujita, T.; Chen, M.; Asefa, T.; Shenoy, V. B.; Eda, G.; Chhowalla, M. *Nano Lett.* **2013**, 13, 6222−6227.
27. Kibsgaard, J.; Lauritsen, J. V.; Lægsgaard, E.; Clausen, B. S.; Topsøe, H.; Besenbacher, F. *J. Am. Chem. Soc.* **2006**, 128, 13950−13958.
28. Lauritsen, J. V.; Kibsgaard, J.; Helveg, S.; Topsøe, H.; Clausen, B. S.; Lægsgaard, E.; Besenbacher, F. *Nature Nanotechnol.* **2007**, 2, 53−58
29. Putungan, D. B.; Lin, S.-H.; Kuo, J.-L. A *Phys. Chem. Chem. Phys.* **2015**, 17, 21702−21708.
30. Lukowski, M. A.; Daniel, A. S.; English, C. R.; Meng, F.; Forticaux, A.; Hamers R. J.; Jin, S. *Energy Environ. Sci*. **2014**, 7, 2608–2613.
31. Mahler, B.; Hoepfner, V.; Liao, K.; Ozin, G. A. *J. Am. Chem. Soc.* **2014**, 136, 14121–14127.
32. Turner, J. A. *Science* **2004**, 305, 972−974.
33. Kim, J.; Byun, S.; Smith, A. J.; Yu, J.; Huang, J. *J. Phys. Chem. Lett.* **2013**, 4, 1227−1232.

34. Chang, Y. H.; Lin, C. T.; Chen, T. Y.; Hsu, C. L.; Lee, Y. H.; Zhang, W.; Wei, K. H.; Li, L. J. *Adv. Mater*. **2013**, 5, 756−760.
35. Merki, D.; Vrubel, H.; Rovelli, L.; Fierro, S.; Hu, X. *Chem. Sci.* **2012**, 3, 2515−2525.
36. Chen, W.; Santos, E. J. G.; Zhu, W.; Kaxiras, E.; Zhang, Z. *Nano Lett.* **2013**, 13, 509−514.
37. Kappera, R.; Voiry, D.; Yalcin, S. E.; Branch, B.; Gupta, G.; Mohite, A. D.; Chhowalla, M. *Nature Mater.* **2014**, 13, 1128–1134.
38. Kappera, R.; Voiry, D.; Yalcin, S. E; Jen, W.; Acerce, M.; Torrel, S.; Branch, B.; Lei, S.; Chen, W.; Najmaei, S. et al. *Appl. Phys. Lett. Mater.* **2014**, 2, 092516.
39. Zhao, W. J.; Ghorannevis, Z.; Chu, L.; Toh, M.; Kloc, C.; Tan, P.; Eda, G. *ACS Nano* **2012**, 7, 791−797.
40. Zeng, Z.; Yin, Z.; Huang, X., Li, H.; He, Q.; Lu, G.; Boey, F.; Zhang, H. *Angew. Chem., Int. Ed.* **2011**, 50, 11093−11097.
41. Coleman, J. N.; Lotya, M.; O'Neill, A.; Bergin, S. D.; King, P. J.; Khan, U.; Young, K.; Gaucher, A.; De, S.; Smith, R. J. et al. *Science* **2011**, 331, 568−571.
42. Matte, H.; Gomathi, A.; Manna, A. K.; Late, D. J.; Datta, R.; Pati, S. K.; Rao, C. *Angew. Chem., Int. Ed.* **2010**, 49, 4059−4062.
43. Peimyoo, N.; Shang, J.; Cong, C.; Shen, X.; Wu, X.; Yeow, E. K. L.; Yu, T. *ACS Nano* **2013**, 7, 10985−10994.
44. Zhang, Y.; Zhang, Y.; Ji, Q.; Ju, J.; Yuan, H.; Shi, J.; Gao, T.; Ma, D.; Liu, M.; Chen, Y. et al. Z. *ACS Nano* **2013**, 7, 8963−8971.
45. Cong, C.; Shang, J.; Wu, X.; Cao, B.; Peimyoo, N.; Qiu, C.; Sun, L.; Yu, T. *Adv. Optical Mater.* **2014**, 2, 131-136.
46. Koh, A. T. T.; Foong, Y. M.; Chua, D. H. C. *Appl. Phys. Lett.* **2010**, 97, 114102.
47. Liu, K. K.; Zhang, W.; Lee, Y. H.; Lin, Y. C.; Chang, M. T.; Su, C. Y.; Chang, C. S.; Li, H.; Shi, Y.; Zhang, H. et al. *Nano Lett*. **2012**, 12, 1538−1544.
48. Viskadouros, G.; Zak, A.; Stylianakis, M.; Kymakis, E.; Tenne, R.; Stratakis, E. *Small* **2014**, 10, 2398–2403.
49. Li, X.-L.; Ge, J.-P.; Li, Y. D. *Chem. Eur. J.* **2004**, 10, 6163–6171.

50. Stratakis, E.; Eda, G.; Yamaguchi, H.; Kymakis, E.; Fotakis, C.; Chhowalla, M. *Nanoscale* **2012**, 4, 3069−3074.
51. Zeng, H.; Liu, G.-B.; Dai, J.; Yan, Y.; Zhu, B.; He, R.; Xie, L.; Xu, S.; Chen, X.; Yao, W. *Sci. Rep.* **2013**, 3, 1608.
52. Berkdemir, A.; Gutiérrez, H. R.; Botello-Méndez, A. R.; Perea-López, N.; Elías, A. L., Chia; C.-I., Wang, B.; Crespi, V. H.; López-Urías, F.; Charlier, J.-C. et al. *Sci. Rep.* **2013**, 3, 1755.
53. Xu, Y.; Schoonen, M. A. A. *Am. Mineral.* **2000**, 85, 543−556.
54. Morrish, R.; Haak, T.; Wolden, C. A. *Chem. Mater.* **2014**, 36, 3986−3992.
55. Voiry, D.; Yamaguchi, H.; Li, J.; Silva, R.; Alves, D. C.; Fujita, T.; Chen, M.; Asefa, T.; Shenoy, V.; Eda, G. *Nature Mater.* **2013**, 12, 850−855.
56. Cullity, B. D.; Stock, S. R. *Elements of X-ray Diffraction*, 3rd ed.; Prentice-Hall: Upper Saddle River, New Jersey, 2001.
57. Jo, S.; Ubrig, N.; Berger, H.; Kuzmenko, A. B.; Morpurgo, A. F. *Nano Lett.* **2014**, 14, 2019.
58. Elias, A. L.; Perea-López, N.; Castro-Beltrán, A.; Berkdemir, A.; Lv, R.; Feng, S.; Long, A. D.; Hayashi, T.; Kim, Y. A.; Endo, M. et al. *ACS Nano* **2013**, 7, 5235−5242
59. Shi, Y.; Wang, Y.; Wong, J. I.; Tan, A. Y. S.; Hsu, C.; Li, L.; Lu, L.; Yang, H. Y. *Sci. Rep.* **2013**, 3, 2169.
60. National Institute of Standards and Technology. Atomic Spectra Database. http://www.nist.gov/pml/data/asd.cfm (accessed 18th June 2015).
61. Lissovski, A.; Piip, K.; Hämarik L.; Aints, M.; Laan, M.; Paris, P.; Hakola, A.; Karhunen, J. *J. Nucl. Mater.* **2015**, 463, 923−296.
62. Thompson, W. T.; Flengas, S. N. *J. Electrochem. Soc.* **1971**, 118, 419−425.
63. Sharma, R. C.; Chang, Y. A. *Bulletin of Alloy Phase Diagrams* **1986**, 7, 263−269.
64. Dyke, W. P.; Trolan, J. K. *Phy. Rev.* **1953**, 89, 4.
65. Yu, K.; Zhang, Y. S.; Xu, F.; Li, Q.; Zhu, Z. Q.; Wan, Q. *Appl. Phys. Lett.* **2006**, 88, 153123.
66. Jung, Y. S.; Sun, Z.; Kim, H. K.; Blachere, H. *Appl. Phys. Lett.* **2005**, 87, 263116.
67. Seita, M.; Pecnik, C. M.; Frank, S.; Spolenak, R. *Acta Materialia* **2010**, 58, 6513–6525.

68. Lantham, R. V. Vacuum **1982**, *32*, 137−140.
69. Uda, M.; Nakamura, A.; Yamamoto, T.; Fujirnoto, Y. *J. Electron Spectroscopy and Related Phenomena* **1998**, 88−91, 643-648.
70. Kang, J.; Liu, W.; Sarkar, D.; Jena, D.; Banerjee, K. *Phys. Rev. X* **2014**, 4, 031005.
71. Zhong, H.; Quhe, R,; Wang, Y.; Ni, Z.; Ye, M.; Song, Z.; Pan, Y.; Yang, J.; Yang, L.; Lei, M.; Shi, J.; Lu, J. *Sci. Rep.* **2016**, 6, 21786.
72. Jeong, H. D.; Lee, J. H.; Lee, B. G.; Jeong, H. J.; Lee, G.-W.; Bang, D. S.; Cho, D.; Park, Y.-B.; Jhee, K. H. *Carbon Lett.* **2011**, 12, 207−217.
73. Acerce, M.; Voiry, D.; Chhowalla, M. *Nature Nanotechnol.* **2015**, 10, 313–318.
74. Das, S.; Appenzeller, J. *Nano Lett.* **2013**, 13, 3396.
75. Liu, H.; Neal, A. T.; Ye, P. D. *ACS Nano* **2012**, 6, 8563.
76. Rout, C. S.; Joshi, P. D.; Kashid, R. V.; Joag, D. S.; More, M. A.; Simbeck, A. J.; Washington, M.; Nayak, S. K.; Late, D. J. *Sci Rep.* **2013**, 3, 3282.

Chapter 5

MoS_2- and WS_2-based Field Emitters by Sputtering

In this chapter, sputter deposition is used to fabricate 2D TMD-based field emitters. MoS_2 supported on multi-walled CNTs are studied in section 5.2, while hybrid WS_2 and CNT emitters are investigated in section 5.3.

5.1 Introduction

One way to control and enhance the properties of MoS_2 and WS_2 is to modify their morphology and physical structure. For example, aside from a lateral 2D film, MoS_2 and WS_2 structures that have been reported include nanoparticles,[1,2] spherical nanovesicles and fibrous floccus,[2] nanotubes,[3-5] nanorods,[6,7] microspheres,[8] and nanoflowers[5,9,10]. These unique nanosized structures are advantageous in that there is a significant increase in the surface area as compared to thin films, leading to an increase in efficiency of MoS_2- and WS_2-based sensors and photocatalytic devices.[11,12] Both nanostructured[9] and few-layer TMD nanosheets[13] have found potential applications as field emitters for their robust mechanical properties and the presence of atomically thin edges that enhance the local electric field concentration and ultimately increase the tunnelling probability of electrons. For example, Viskadouros et al.[14] reported the fabrication of WS_2 nanotubes with comparable field emission performance to optimized CNTs and better resistance to chemically reactive environments.

Another technique to enhance the properties of base MoS_2 and WS_2 is by hybridizing with other nanostructures to form composites. The synergistic effects created by combining compatible materials can result in significant improvements in field emission performance.[15-17] As demonstrated by Rout et al.,[15] layered WS_2-RGO composites synthesized using a hydrothermal method exhibited a lower turn-on field of 2 V μm^{-1} compared to the values of 3.5 V μm^{-1} and 2.3 V μm^{-1} for pristine WS_2 and RGO sheets. Fu et al.[16] fabricated both MoS_2- and TiO_2-based MoS_2/TiO_2 heterojunctions that possess lower turn-on fields compared to the bare TiO_2 and MoS_2 structures. Similarly, MoS_2/ZnO composites were shown to demonstrate better field emission performance over that of pure MoS_2 nanoflowers.[17] Among the many possibilities for hybridizing with MoS_2 and WS_2, CNTs are an excellent choice as they are themselves excellent field emitters,[18] in addition to possessing very good mechanical and electrical properties.[19,20] Another advantage of using CNTs is the ease with which atoms can bond to the nanotube surface, as chemically grown carbonaceous materials such as nanotubes possess abundant oxygen-containing groups that can facilitate the immobilization of materials grown on their surface, making them promising templates for the preparation of composites.[21] As CNTs are generally metallic and both MoS_2 and WS_2 are semiconducting, introducing a outer shell of MoS_2 or WS_2 over the nanotubes would promote field emission performance of the resulting composites through the formation of a Schottky junction at the interface. Such phenomena have been widely reported with other semiconducting shell materials such as MoO, SiO_2, ZnO and MgO.[22-24] The MoS_2 or WS_2 coating would also provide the added benefit of a protective layer for the nanotube core that can minimize emission instability caused by adsorption or ion bombardment of residual gas molecules.

Various techniques have been used to hybridize CNTs with TMD nanosheets. An L-cysteine-assisted hydrothermal method was developed by Zhou et al.[25] for the growth of MoS_2 nanosheets on acid treated CNTs using $Na_2MoO_4 \cdot 2H_2O$ as precursors. The end product was obtained by heating in a Teflon-lined stainless steel autoclave and heated at 180 °C for 48 h. Another group reported a two-step method to prepare MoS_2 sheet-coated multi-walled CNTs by first synthesizing MoS_3 on acid-treated MWCNTs by mixing $(NH_4)_2MoS_4$ and HCl in CNT suspension and then annealing the obtained product at 650 ºC for 1 h in a H_2 gas.[26] Aside from hydrothermal methods, other fabrication techniques have also been investigated for the fabrication of TMD-coated 1D carbon materials. One example is the preparation of ultrathin MoS_2 nanosheets on active carbon fibres using a simple dissolution and sintering method.[27] The as-prepared active carbon fibres were immersed in a dimethylformamide (DMF) solution containing $(NH_4)_2MoS_4$ and the obtained sample was annealed at 750 ºC for 2h in a 5% H_2/Ar atmosphere. Jeon et al.[28] also reported the growth of MoS_2-CNT composites using CVD at 850 ºC with sulfur and MoO_3 powder as the precursors.

Most of the above techniques for hybridizing CNT with TMD nanosheets are chemical in nature, often requiring high temperatures and long growth times for production of high quality crystals. This could potentially lead to degradation of the structural integrity of CNTs, thereby negatively affecting field emission performance. Many of the synthesis methods also require more than one step to obtain the final compound of MoS_2 or WS_2, which makes them time-consuming and non-economical. To overcome these limitations, we demonstrate a simple one step physical approach to obtain both MoS_2-CNT and WS_2-CNT heterostructures at room temperature via magnetron sputtering. As opposed to chemical based methods, sputtering offers greater control over the morphology and thickness of the resulting film by variation of RF

power and deposition time. The technique is also economical and suitable for large scale industrial application, as well as clean because no external catalysts or solvents were used. The unique 3D MoS-CNT and WS_2-CNT heterostructures obtained are composed of nano-petals of MoS_2 or WS_2 enveloping a CNT core and demonstrated improved field emission performance over uncoated CNTs, as detailed in section 5.2 and section 5.3 respectively. The MoS_2-CNT composites also exhibited lower turn-on fields compared to MoS_2 nanoflowers and nanosheets.

5.2 MoS_2 Nano-petals Supported on Carbon Nanotubes

5.2.1 Experimental Procedure

Synthesis: Thin film Fe catalysts were deposited on highly n-doped Silicon (100) substrates using a Denton-Discovery-18 RF magnetron sputtering system. The substrates were cut into 10 mm × 10 mm pieces, cleaned in ethanol, and blow-dried using a nitrogen gun before they were placed into the sputtering chamber. Sputter deposition was performed at a working pressure of 10^{-2} Torr and RF power of 100 W. The substrates were transferred in air to the PECVD growth chamber, which was pumped down to ~10^{-5} Torr and the substrates were heated up to 700°C. C_2H_2 and H_2 gases were used in the growth process at flow rates of 40 sccm and 60 sccm respectively. Growth of multi-walled CNTs was performed for 60 minutes at a pressure of 1.2 Torr and RF power of 100 W. MoS_2 was then deposited onto the CNTs via RF magnetron sputtering using a MoS_2 target (99.9 % purity) and a low RF power of 40 W. Sputter deposition was carried out at a working pressure of 10^{-2} Torr and deposition times of 5, 10, 15, 20, 25 and 30 min.

Characterization: Surface morphologies were characterised by Zeiss Supra 40 field emission SEM using an in-lens secondary electron detector and a JEOL JEM-2010F TEM operating at an accelerating voltage of 200 kV. Surface composition was analysed by XPS using a Kratos Analytical Axis Ultra^{DLD} UHV spectrometer with a monochromatized Al Kα x-ray source (1486.6eV). Core-level XPS spectra were obtained at a take-off angle of 90° measured with respect to the sample surface at a vacuum of 5 × 10^{-9} Torr. The optical properties of as-fabricated samples were

characterized using a Renishaw Raman spectrometer 2000 (excitation λ = 514.5 nm) and Perkin-Elmer fluorescence spectrometer LS 55 (excitation λ = 514 nm).

Field Emission Tests: Field emission studies were carried out using a parallel-plate device at room temperature and at a base pressure of 2×10^{-6} Torr. The sample was clamped between an aluminium cathode and a glass slide coated with ITO, which functions as the anode. A polymer film spacer with a thickness of 100 μm is used to maintain emitter-to-anode distance. The current-voltage relationship was obtained by applying a DC voltage across the sample and anode. Emission current was measured using a Keithley 237 source measurement unit.

The parallel plate setup, where the current is averaged over a large sample area, is the most commonly used method for investigating field emission properties. This method was initially used due to the ease of comparing obtained results with available literature (the MoS_2-coated CNTs were chronologically the first set of experiments conducted). However, when a large area anode is used the emission is usually dominated by a relatively small number of very strong emitting sites. This is especially true for CNTs as they normally consist of a few high aspect ratio emitters and a majority of low aspect ratio emitters. Consequently, subsequent field emission tests were conducted using a probe tip setup, where the sample area investigated is much smaller. With this method, regions with no strong emitters can be found and the multitude of emitters with lower aspect ratio can be probed.

5.2.1 Nanostructural Characterization

From the SEM images depicted in Figure 5.1, we observe the emergence of a film-like layer encapsulating the tips of the CNTs after 5 min sputter deposition of MoS_2. As deposition time is increased, the encapsulating shell thickens until a sputter time of 15 min, whereupon the roughness of the film demonstrates a noticeable change, with the shell layer becoming more particulate-like than film-like. Further increase in sputter time results in a drastic alteration in morphology as sharp petal-shaped flakes begin to protrude from the shell, leading to the formation of a dense nano-petal forest that completely envelops the CNTs. Still longer sputter times increase the density of the nano-petals and the thickness of the encapsulating layer such that the CNTs buckle under the added weight, as can be seen from the cross-sectional SEM images. Figure 5.2 shows the TEM images of selected samples. The pristine CNTs depicted in Figure 5.2(a) are clearly multi-walled and have diameters of approximately 40 nm. After sputtering for 5 min, the nanotubes appear to be coated with an amorphous film-like material that thickens until a sputter time of 15 min is reached. At 20 min, crystalline petal-shaped flakes are formed as protrusions from the sidewalls of the encapsulated CNTs, corroborating the results obtained from SEM. The nano-petals increase in density as sputter time is further increased. Figure 5.2(f) shows a high resolution image of a nano-petal from the 30 min sample. The lattice fringes have interplanar spacings of 0.65 nm, which is characteristic of MoS_2. These results suggests the formation of highly crystalline MoS_2 from an amorphous base after a specific threshold is reached in sputter deposition time.

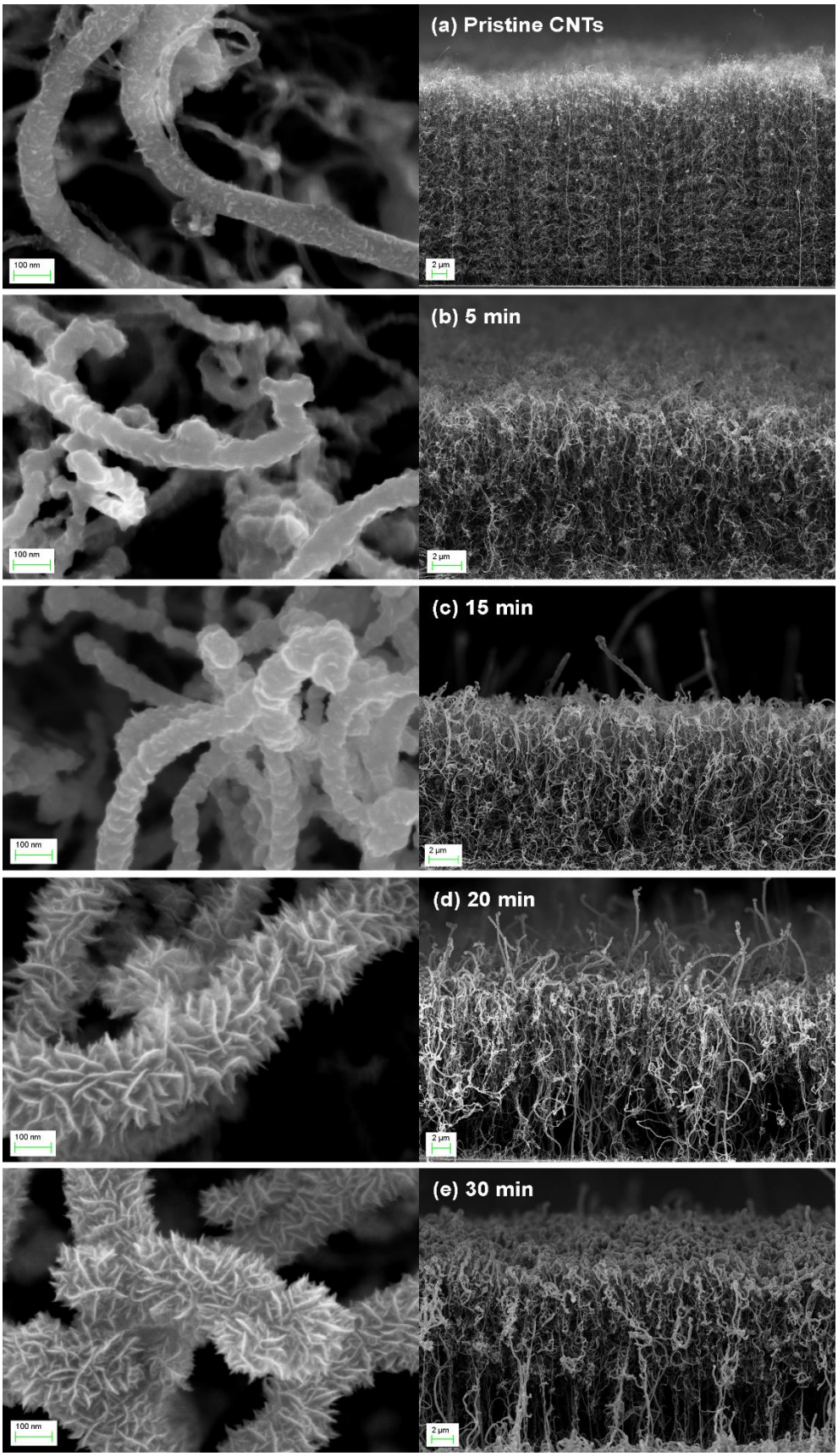

Figure 5.1: (Left) Top view and (right) cross-sectional SEM images of (a) pristine CNTs and MoS_2-CNT samples fabricated at sputter deposition times of (b) 5 min, (c) 15 min, (d) 20 min, and (e) 30 min.

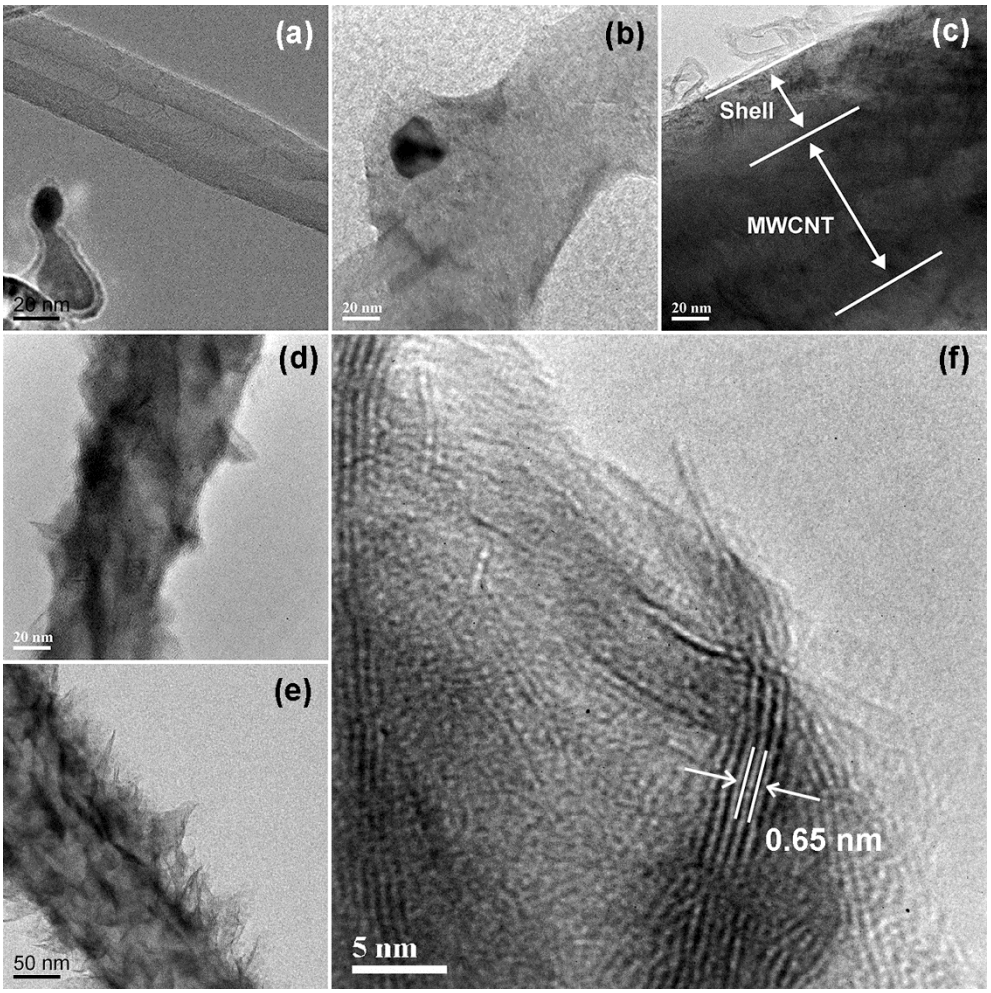

Figure 5.2: TEM images of (a) pristine CNTs and MoS_2-CNT samples fabricated at sputter deposition times of (b) 5 min, (c) 15 min, (d) 20 min, and (e) 30 min. (f) HRTEM image of nano-petals in the 30 min sample showing lattice fringes of MoS_2.

To verify the results of the SEM and TEM images, the as-grown samples were analysed by Raman spectroscopy, a technique that offers quick and non-destructive means of characterizing the crystallinity of both CNTs and MoS_2. From the Raman spectra shown in Figure 5.3 (a), we observe three distinct peaks at 1355 cm^{-1}, 1580 cm^{-1}, and 2969 cm^{-1} present across all samples, corresponding to the disorder (D), graphitic (G) and second-order disorder (2D) peak of carbon.[29] The G peak occurs due to the in-plane C-C vibrations of sp^2 hybridized carbon atoms in both chains and rings, whereas the D peak corresponds to the breathing mode of six-fold aromatic rings of sp^2 carbon

and is independent of film thickness. The D peak is activated by disorder in atomic arrangement and hence indicates the presence of amorphous carbon or defects in the CNT walls. While the D peak is absent in perfectly crystalline graphite, the 2D peak (also known as the G' peak) is present even in the absence of defects. All three Raman bands are characteristic of CNTs, and the ratio of the intensities of the D to G peak (I_D/I_G) can be used as an indicator of the quality of the nanotubes. The I_D/I_G ratio is calculated to be 0.73 across all samples, indicating that the CNTs have low crystallinity.[20,30]

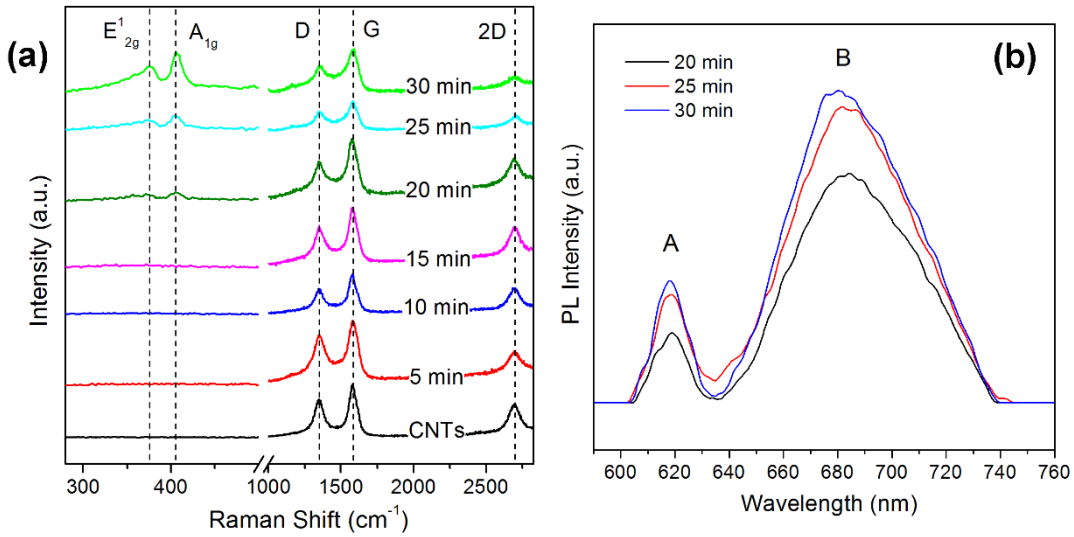

Figure 5.3: (a) Raman spectra of pristine CNTs and MoS_2-CNT samples. (b) PL spectra of as-grown MoS_2-CNT samples fabricated at 20, 25, and 30 min sputter times.

At 20 min sputter time, we observe the emergence of two peaks at approximately 376 cm^{-1} and 405 cm^{-1}, which can be attributed to the E^1_{2g} and A_{1g} Raman modes of MoS_2 respectively. The in-plane E^1_{2g} mode arises from the opposite vibration of two S atoms with respect to the Mo atom, while the out-of-plane A_{1g} mode results from opposite vibration of only S atoms.[31] Both peaks are present only in the case of crystalline MoS_2. As such, their appearance, coinciding with the formation of

nano-petals as observed in the SEM and TEM images, verify that crystalline MoS_2 does indeed form after 20 min of sputter deposition. The increase in intensity for both Raman modes as sputter time increases also points to an improvement in crystallinity of MoS_2, resulting in highly crystalline nano-petals at 30 min sputter time. For samples fabricated with sputter times of 15 min and below, the absence of the E^1_{2g} and A_{1g} Raman modes indicate that the encapsulating shell formed at these sputter times is either a disordered form of MoS_2 or an entirely different compound.

The PL spectra of 20 to 30 min samples are shown in Figure 5.3(b). Two emissions can be detected at wavelengths of approximately 684 and 615 nm, labelled A and B respectively. These two peaks have been well established to be the direct excitonic transitions of the K point of the Brillouin zone for few-layer MoS_2.[32] As thickness of MoS_2 increases in the nanoscale, the bandgap decreases from 1.9 eV to 1.2 eV in bulk MoS_2 and we thus expect to see a slight red-shift and gradual extinguishing of the direct band edge transition peak at 684 nm. Instead, we observe a blue-shift in this band edge from 684 nm to 680 nm when the sputter time is increased in direct contradiction of the quantum confinement effects of MoS_2. This is believed to be due to the incident laser beam impinging only on the topmost layer of the samples such that signal is recorded mainly from this area, with little contribution from the layers underneath. Due to the reduction in tip size as more atoms stack up along the *a*- and *b*-axis of the MoS_2 crystal, nano-petals with thinner tips are produced as the sputter time is increased. This reduction in layers at the top would then be reflected as a gradual blue-shift in the direct band edge as sputtering time is increased from 20 to 30 min, as was observed in our samples.

In order to determine the composition of the encapsulating shell, the as-grown samples were analysed by XPS. High resolution scans of Mo 3d, S 2s and S 2p core level spectra of selected samples are presented in Figure 5.4. The Mo 3d spectra for all samples were fitted with two spin-orbit doublets. For the 5 min sample, the first doublet occurs at 230 and 233.1 eV, which gradually shifts to lower binding energy as the sputter time increases until it reaches binding energies of 229.15 and 232.25 eV in the 20 min sample, which agrees well with that of Mo^{4+} in MoS_2.[33] The peak positions of this doublet thereafter remain approximately constant up to the 30 min sample. The binding energy values of 230 and 233.1 lie between those of Mo^{4+} in MoO_2 and the Mo species in Mo_2C. It is thus concluded that a Mo-O-C type bond is formed at the interface. The intensity of this doublet is much lower than the main oxide doublet, hinting that only bond formation occurs and no new phase is formed. As sputter time increases, the binding energies downshift and relative intensity of the peaks increases to indicate formation of a separate MoO_2 phase. After 20 min, the doublet reaches binding energies of 229.15 and 232.25 eV, signifying that a chemical change has taken places during the sputtering process. The other Mo 3d doublet occurring at 232.6 and 235.7 eV corresponds to the Mo^{6+} species in MoO_3, which is predominant in the 5 min sample but decreases in relative concentration as sputter time increases until it becomes a minor compound in the 20 min sample.

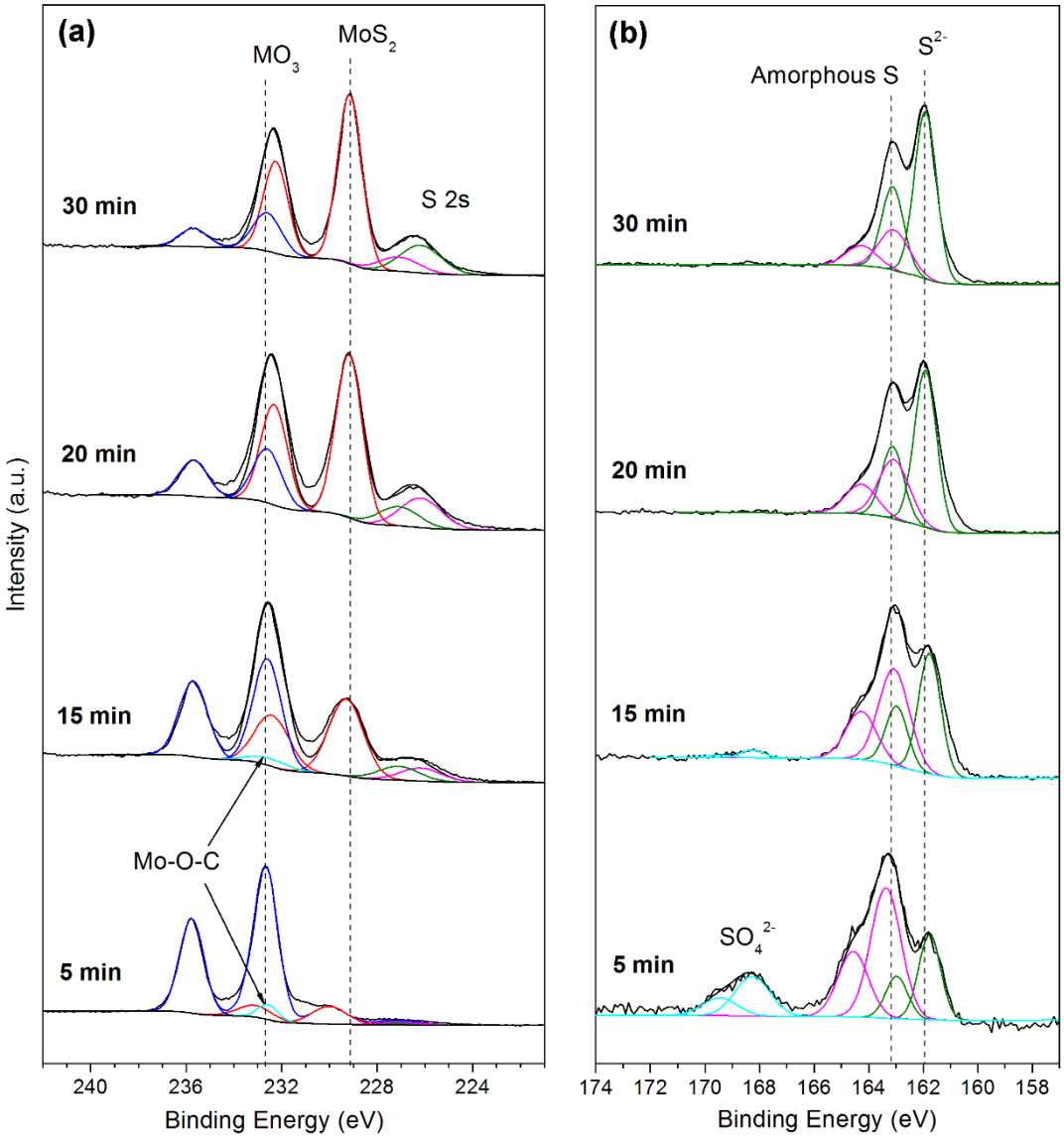

Figure 5.4: High resolution XPS scans of (a) Mo 3d, S 2s and (b) S 2p core levels for selected MoS_2-CNT samples.

The S 2p spectra of the 5 and 15 min samples are present with three doublets, the first of which occurs at 161.9 and 163.1 eV and can be attributed to the S^{2-} species in MoS_2.[33] The second doublet located at approximately 163.1 and 164.3 eV is attributed to the presence of amorphous sulfur, while the final pair occurring at 168.25 and 169.45 eV is assigned to the oxidized sulfur species SO_4^{2-}. The fact that meaningful signal from the S^{2-} species in MoS_2 is detected in all samples indicates that some degree

of Mo-S bonding occurs even at low sputter deposition times. However, as the Mo^{4+} doublet of the 5 min sample has binding energies closer to the oxidized form of molybdenum rather than its sulfurized form, we can deduce that any MoS_2 produced at low sputter deposition times are highly defective and sulfur-deficient i.e. molybdenum exists mostly as MoO_2 with only minor bonding to sulfur atoms. This is attributed to the preference of sulfur to bind to oxygen or to itself, as evidenced by the pronounced peaks from oxidized SO_4^{2-} species and amorphous sulfur. As sputter time increases to 20 min however, the relative intensity of the S^{2-} doublet increases while the SO_4^{2-} doublets disappears and the signal from amorphous sulfur is significantly reduced, all of which coincide with a downwards shift of the binding energies of the Mo^{4+} doublet. This behaviour suggests the gradual displacement of oxygen atoms by sulfur atoms in the Mo compound to form MoS_2.

5.2.3 Growth Mechanism of MoS_2 on CNTs

From the findings detailed in Section 5.2.2, we can conclude that when sputtering takes place, the first group of Mo atoms that deposit on the CNT surface bind to oxygen molecules that are physically and chemically adsorbed on the sidewalls of the nanotubes. This results in the formation of MoO_3, with some minor contributions from MoO_2, both of which exists as amorphous compounds. These molybdenum oxides make up the tubular shell that encapsulates the CNTs at low sputter times (< 20 min). The shell layer has strong adhesion to the nanotubes due to the presence of Mo-O-C bonds at the interface rather than weak Van der Waals forces. Any S atoms present on the nanotube surface at this stage prefers to bind to other S atoms or to oxygen and there is minimal interaction with Mo atoms, resulting in negligible yield of MoS_2. As

sputtering proceeds the gaseous SO_4^{2-} species most likely desorb from the nanotube surface, while the increasing concentration of S atoms on the CNT sidewalls favours the displacement of oxygen atoms in MoO_2 to form MoS_2. At 15 min sputter time, any MoS_2 phase formed is either of insufficient quantity or crystallinity to be detected by Raman spectroscopy. The lack of a crystalline layered structure (nano-petals) present in the encapsulating shell as observed via SEM and TEM suggests that the latter explanation is true, i.e. amorphous MoS_2 particles forms on top of MoO_3. As sputtering progresses beyond the 15 min mark, MoS_2 begins to form almost exclusively, and in its crystalline form.

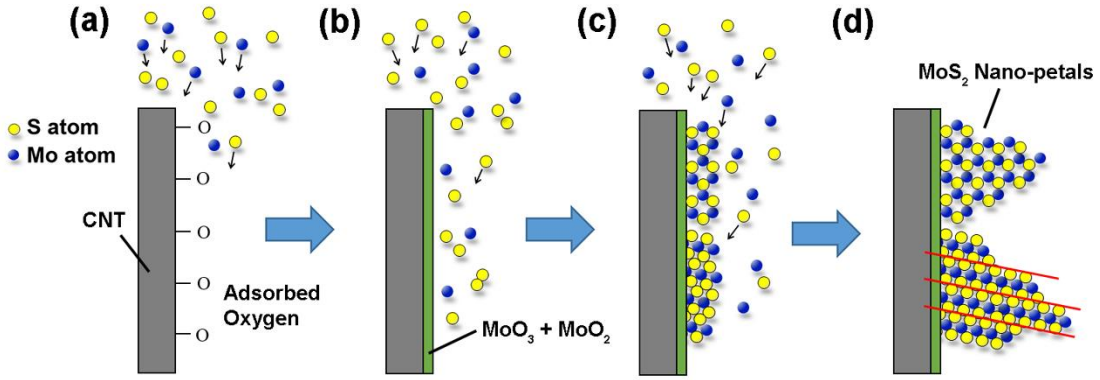

Figure 5.5: Proposed growth model of MoS_2 nano-petals on CNT. The red lines in (d) mark out the layers in crystalline MoS_2 as seen in the TEM images.

To understand the growth of MoS_2 nano-petals perpendicular to the sidewalls of CNTs, we consider first the crystal structure of MoS_2. Individual layers of MoS_2 are held together by weak van der Waals forces and stacked in a staggered arrangement along the *c*-axis. In such a layered structure, the surface energy of the planes perpendicular to the *c*-axis is much smaller than others and thus the grains of MoS_2 grow with its basal plane parallel to the substrate surface to minimize the energy of the

film. In this work, MoS_2 growth was carried out at room temperature without the use of catalysts. Thus a modified vapour-solid (VS) growth mechanism is believed to be pre-dominant instead of the typical vapour-liquid-solid (VLS) growth processes.[34,35] In the sputtering process, Mo and S atoms are removed from a solid target by bombardment with high energetic ions and subsequently deposited onto the CNTs. Ion bombardment imparts high mobility to the source atoms such that they possess enough energy to diffuse on the surface of the nanotubes to favourable sites and form nuclei. CNTs synthesized by PECVD have more defects in their structures than those grown by arc discharge and thermal CVD because of damage caused by ion bombardment.[35] Defects in PECVD grown nanotubes can take the form of "cross-struts" perpendicular to the tube axis, pentagon-heptagon pairs, vacancies and ion impurities.[36-38] These defect sites are more reactive than the planar surface region, which could attract arriving source atoms during the initial stage and act as the first nucleation centres for MoS_2 growth. Grain boundaries of the graphene layers that comprise the nanotube walls can also act as nucleation sites due to the presence of dangling bonds that attract adsorbates.[39] As such, MoS_2 crystals will prefer to nucleate on these defective sites. In the initial growth process, the presence of adsorbed oxygen on the CNT surface leads to significant oxidation of the Mo species to form an oxide base layer. Once most of the oxygen is consumed and the concentration of sulfur atoms at the surface reaches a critical value, clusters of pure MoS_2 begin nucleating on top of the oxide layer. Energetics favour the lateral growth of MoS_2 islands, but the rate at which these nuclei grow is slower than the rate at which Mo and S atoms are reaching the surface of the oxide base layer. Consequently, fresh MoS_2 nuclei accumulates on top of previously formed islands, resulting in a fast stacking of atoms along the direction perpendicular to the *c*-axis of MoS_2 to form vertically standing petal-shaped nanoflakes. The growth

process thus follows the mixed island and layer growth model, also known as the Stranski-Krastanov mode. As more atoms stack up, the surface areas of the nano-petal edge are reduced, leading to the formation of needle-sharp tips. A schematic diagram of the proposed growth process is shown in Figure 5.5.

5.2.4 Field Emission Study of MoS_2-CNT Composites

In order to examine the effective functionality of the MoS_2-CNT core-shell structures, their electron field emission property was measured. Figure 5.6 and Figure 5.7 shows the current density versus electric field (J-E) and Fowler-Nordheim (F-N) plots respectively for the MoS_2-CNT samples. The turn-on field is defined as the electric field strength required to produce a current density of 10 μA cm^{-2}. The measured turn-on field for pristine CNTs used in this work is 2.5 V μm^{-1}. For the 5, 10, 15, 20, 25, and 30 min samples, the measured turn-on fields are 1.65, 1.40, 1.30, 1.15, 1.05, and 0.80 V μm^{-1} respectively, demonstrating that the MoS_2-CNT heterostructures have markedly improved field emission performance over that of as-grown CNTs and that this improvement increases with sputtering time. The turn-on fields of our MoS_2-CNT samples are also much lower as compared to MoS_2 nanoflowers[9] (4.5–5.5 V μm^{-1}) and MoS_2 nanosheets[13] (3.5 V μm^{-1}), indicating that the as-prepared MoS_2-CNT nanostructured composites are, in fact, excellent field emitters. Assuming $\varphi_{CNT} = 5.0\ eV$,[24] $\varphi_{MoO_3} = 5.3\ eV$,[40] and $\varphi_{MoS_2} = 4.9\ eV$,[41] the field enhancement factor, β, which is determined primarily by sample morphology, can be calculated from the slope of the F-N plot. For pristine CNTs and samples 5 to 30 min, the value of β is calculated to be 2410, 2820, 2800, 2870, 3240, 3350, and 6500 respectively.

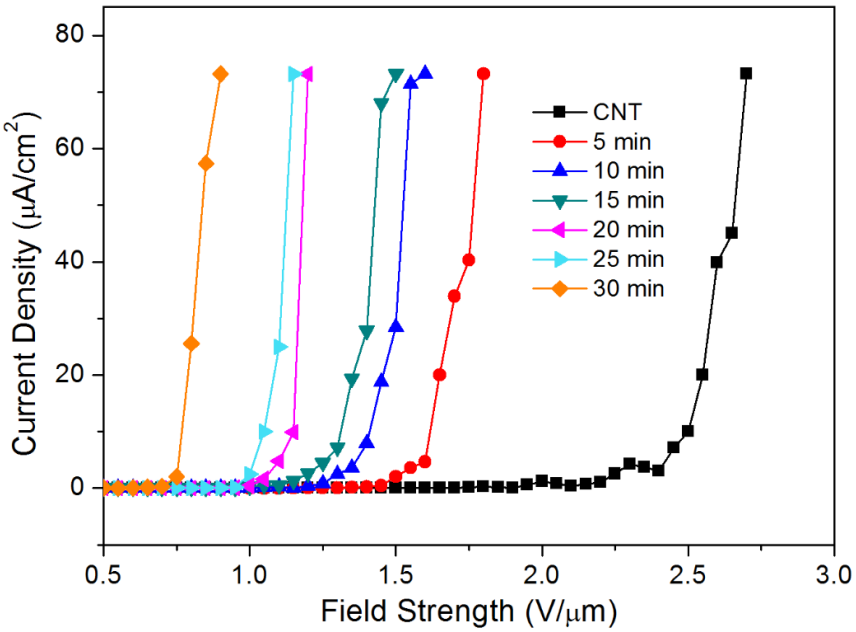

Figure 5.6: Field emission plots of current density against electric field for MoS_2-CNT samples.

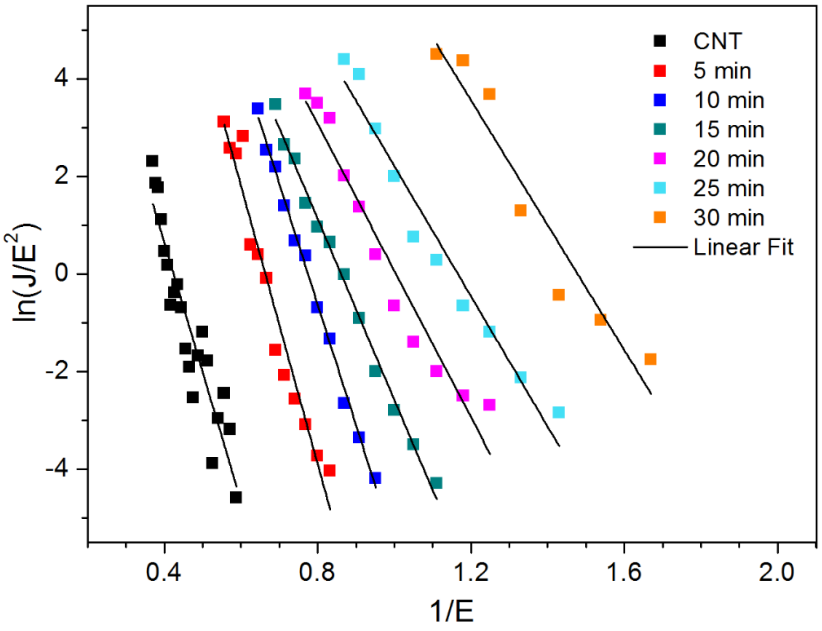

Figure 5.7: Fowler-Nordheim plots for MoS_2-CNT samples.

The widely accepted field emission mechanism for CNTs is that electrons are emitted mainly from the CNT tips. The CNT sidewalls contribute little to the field emission, as the geometric shape of the flat side wall gives low local field strength compared to the sharp CNT tips.[24] An enhancement in field emission property of any CNT heterostructures can thus be induced by physical changes at the side walls, such as the formation of multiple additional emission sites that significantly increase the field enhancement factor, β. Alternatively, if the encapsulating layer is a semiconductor such as MoO_3 or MoS_2, a Schottky junction is formed at the interface with the metallic CNTs that lowers the energy barrier for electron emission. For our MoS_2-CNT samples, all demonstrate an enhancement in β as compared to pristine CNTs, indicating that both the tubular and nano-petal forest encapsulation provide additional sites for electron emission that would result in lower turn-on fields. Interestingly, the β values for the 5, 10 and 15 min samples are very similar despite a consistent decrease in turn-on field as sputter time increases. We can therefore conclude that the physical changes on the CNT surface play a minor role in enhancing field emission for these three samples. Instead, the formation of a CNT-MoO_3 Schottky barrier at the interface is believed to be the dominant enhancement mechanism that results in more effective field emission properties. In contrast, the 20, 25, and 30 min samples show a marked increase in the value of β, particularly for the 30 min sample. This is attributed to the emergence of the nano-petal structures at a sputtering time of 20 min and their subsequent increase in density in addition to a reduction in tip size as sputter time increases. As sharper tips induce higher local field concentration, they result in a reduction of the height of the electron tunnelling barrier from the sample to vacuum. Thus when combined together, both trends produce effects that reinforce each other and that lead to a large improvement in the field enhancement factor of the 30 min sample. The formation of a

Schottky junction at the interface likely still playsa considerable role in lowering the turn-on field for the 20 and 25 min samples, but is not as important in the 30 min sample on account of its much larger β value.

The Schottky effect refers to a phenomenon where a positive voltage is applied to the anode with respect to the cathode, generating an electric field at the cathode that aids the emission process by lowering the potential energy barrier. Since MoO_3 is a wide bandgap n-type semiconductor with E_g = 3.15 eV,[42] a Schottky barrier was predicted to be obtained between MoO_3 and CNTs. Under an applied electric field, electrons and holes separate, inducing band bending and resulting in a potential drop, ΔV, across the coating material. Electrons tunnel from the Fermi level of the CNTs into the conduction band of MoO_3, and subsequently into MoS_2. The accumulation of electrons in MoS_2 in turn generates the space charge effect, which is essentially a downward shift of the vacuum level relative to the Fermi level of the back contact i.e. CNTs. Such a lowering of the vacuum level reduces the emission barrier height with respect to pristine CNTs, allowing electrons to tunnel more effectively into vacuum. This would then translate to lower turn-on fields for MoS_2-CNT heterostructures. A schematic diagram of the proposed field emission mechanism is shown in Figure 5.8.

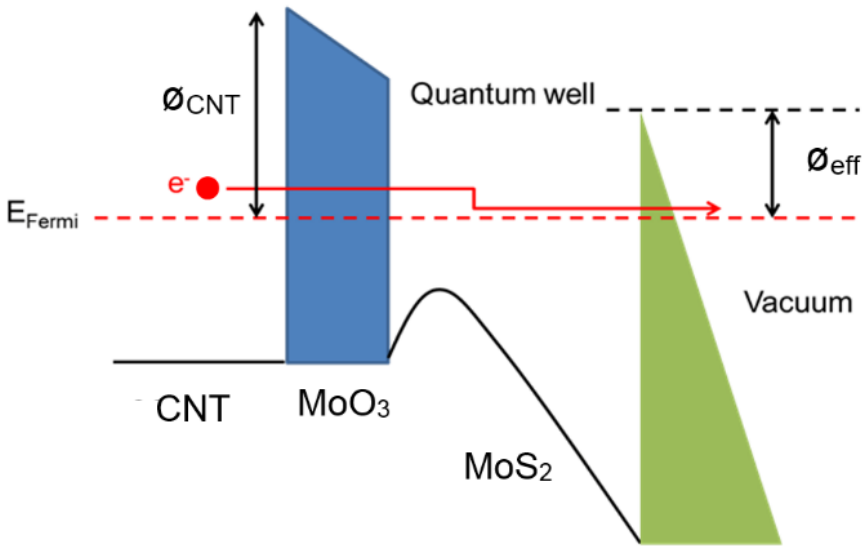

Figure 5.8: Schematic diagram of the CNT/MoO_3 and MoO_3/MoS_2 heterojunctions under an applied electric field.

5.3 WS_2 Nano-brushes Supported on Carbon Nanotubes

5.3.1 Experimental Procedure

Synthesis: The growth of MWCNTs by PECVD on highly n-doped Si substrates with a thin layer of sputter deposited Fe catalyst is the same as that detailed in section 5.2.1. The CNTs were tip-coated with WS_2 via RF magnetron sputtering using a WS_2 target (99.9 % purity) at room temperature, a low RF power of 40 W, a working pressure of 10^{-2} Torr and deposition times of 10, 20, 25, 30, 35, 40, 50, and 60 min.

Characterization: SEM and XPS analysis of the samples were conducted using the same instruments and conditions as that detailed in section 5.2.1. TEM images were obtained using a JEOL JEM-3010 TEM operating at an accelerating voltage of 300 kV. Crystallographic data were obtained through a Bruker D8 Advanced Thin Film XRD system using a Cu Kα source ($\lambda_{CuK\alpha}$ = 1.54056 Å). The optical properties of as-fabricated samples were characterized using a Horiba MicroRaman HR Evolution System with 514.5 nm excitation wavelength.

Field Emission Tests: Field emission studies were conducted using the same probe tip setup and experimental conditions as first detailed in section 3.4.1.

5.3.2 Nanostructural Characterization

The SEM images of the samples are depicted in Figure 5.9, in which we observe the emergence of a film of angular particulates encapsulating the CNTs after 10 min sputter deposition of WS_2. As the deposition time is increased, the particulate film

thickens until sharp flakes begin to emerge from the surface at a sputter time of 30 min [Figure 5.9(e)]. These nanoflakes lengthen and increase in concentration when the sputtering time is increased to 35 min, leading to the formation of a dense forest of triangular flakes that completely envelops the CNTs [Figure 5.9(f)]. Still longer sputter times give rise to a drastic change in the sample morphology, as seen in Figure 5.9(g), whereupon new nanoflakes begin to grow over pre-existing ones. These new nanoflakes appear to be much sharper and narrower, and quickly become so numerous as to give the impression of "bristles on a brush". Any increase in the deposition times from this point forth only serves to thicken the encapsulating layer, but induces little change in the morphology of the samples. This transformation of the WS_2-CNT hybrid nanostructures is corroborated by the TEM images of the samples, which is shown in Figure 5.10. Pristine multi-walled CNTs with diameters of approximately 20 nm are depicted in Figure 5.10(a). After sputtering with WS_2 for 10 min, the nanotubes become coated with angular particulates that thicken to become a film at a sputter time of 30 min [Figure 5.10(c)]. Thin sheets of material can also be seen extending outward from the sidewalls of the encapsulated CNTs, similar to the results obtained from SEM. These thin sheets increase in density and length as sputter time is increased to form triangular nanoflakes that eventually begin stacking on top of each other. The topmost flakes appear to preferentially roll themselves into a narrow and highly curved geometry, as illustrated in Figure 5.10(f). Higher magnification images in Figure 5.11(a) and 5.11(b) gives a clearer view of the differences in morphology between the nanoflakes formed at a sputter time of 35 min versus 60 min respectively. To differentiate the two types of nanoflakes, we dub the former "petals" and the latter "bristles" in keeping with their unique shapes. Both the nano-petals and nano-bristles were found to be crystalline, with high resolution TEM images of the 35 min sample

[Figure 5.11(c)] exhibiting the presence of lattice fringes with interplanar spacings of 0.64 nm, which is characteristic of 2H-WS_2 [JCPDS #08-0237].

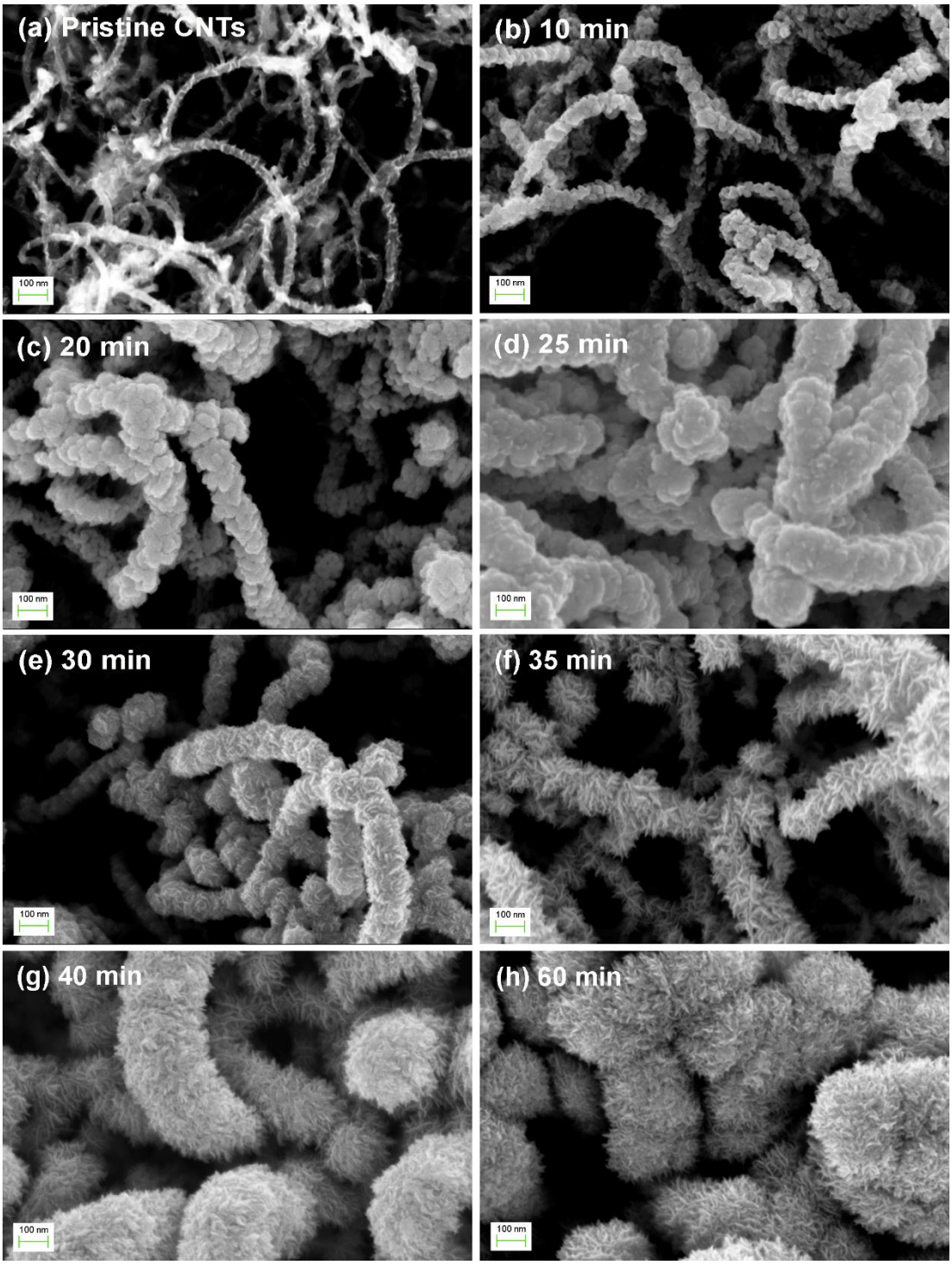

Figure 5.9: Top view SEM images of (a) pristine CNTs and WS_2-CNT samples fabricated at sputter deposition times of (b) 10 min, (c) 20 min, (d) 25 min, (e) 30 min, (f) 35min, (g) 40 min and (h) 60 min.

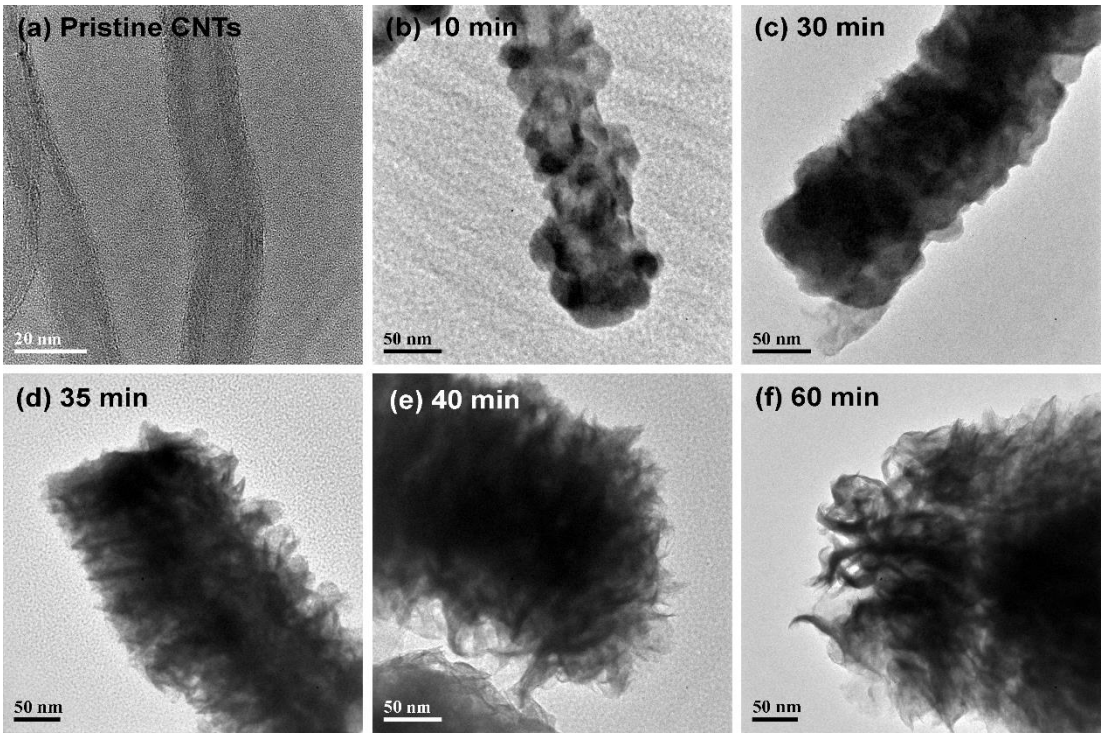

Figure 5.10: TEM images of (a) pristine CNTs and WS_2-CNT samples fabricated at sputter deposition times of (b) 10 min, (c) 30 min, (d) 35 min, (e) 40 min and (f) 60 min.

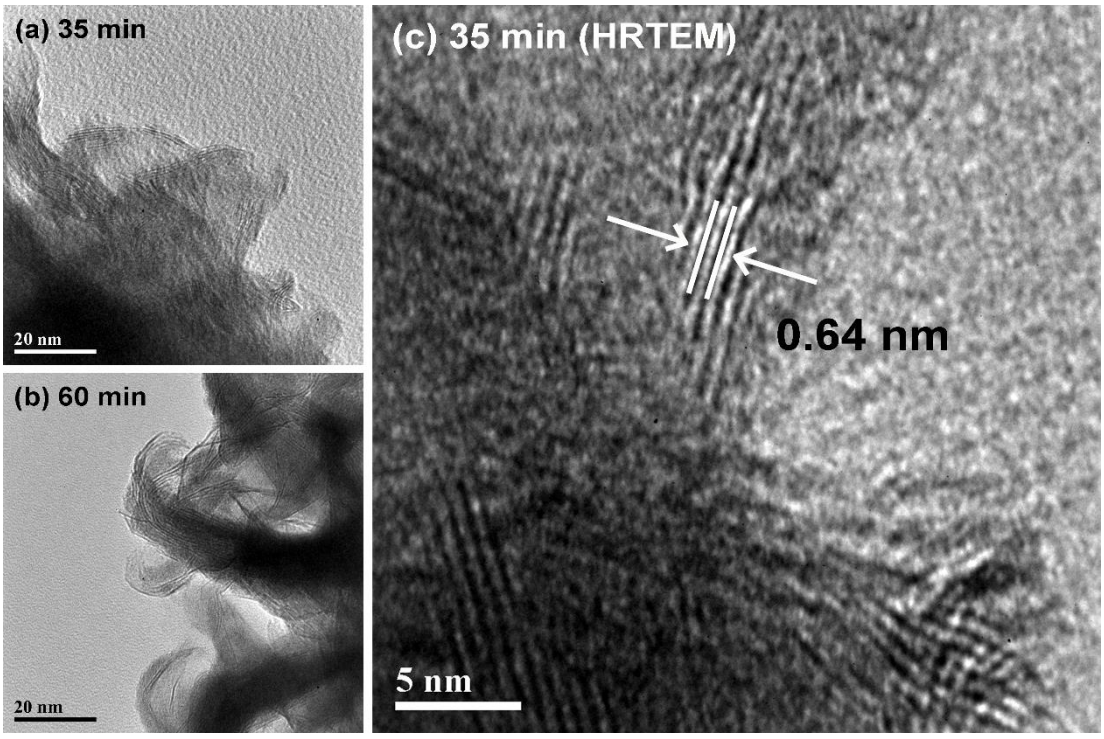

Figure 5. 11: TEM images of (a) nano-petals in 35 min sample and (b) nano-bristles in 60 min sample. (c) HRTEM image of nano-petals in the 35 min sample showing lattice fringes of WS_2.

The optical properties of our as-grown samples were also analysed by Raman spectroscopy (Figure 5.12). Three distinct peaks at 1350 cm^{-1}, 1575 cm^{-1}, and 2969 cm^{-1} were observed for all samples, corresponding to the disorder (D), graphitic (G) and second-order disorder (2D) peak of carbon. The G peak is due to the E_{2g} mode at the Γ-point.[42] It arises from the stretching of C-C bonds in graphitic material, and is common to all sp^2 hybridized carbon systems. The D peak on the other hand corresponds to the breathing mode of six-fold aromatic rings of sp^2 carbon and is activated by disorder in the graphitic structure.[43] The 2D band is excited by a double-resonant Raman process that, unlike the D band, is present even in the absence of defects. The carbon region of the Raman spectra remains unchanged even after prolonged deposition of WS_2, indicating that the coating does not interact strongly with the nanotubes. At a sputter time of 20 min, we observe a small broad peak at approximately 800 cm^{-1}, which gradually intensifies until two distinct peaks at 704.1 cm^{-1} and 804.9 cm^{-1} emerge at 30 min sputter time. Both peaks are matched to the O-W-O stretching modes in tungsten (VI) oxide.[44] A shoulder at approximately 300 cm^{-1} can also be observed in the Raman spectra at 20 min. With increasing deposition times, this feature transforms into a definite peak at 263.1 cm^{-1} and another weak shoulder appears at 325.9 cm^{-1}. Both bands correspond to the O-W-O bending modes of WO_3.[44] This trend suggests that the particulate film formed during initial deposition is composed of amorphous WO_3 that then crystallizes with longer sputter times. There appears to be no contribution whatsoever from WS_2 regardless of sputtering duration, which is curious as the TEM images depict the distinctive crystalline 2D flakes of WS_2. It is possible that the contribution from the underlying WO_3 film is so strong that it overwhelms the WS_2 signals, resulting in non-detection of the characteristic Raman modes of WS_2.

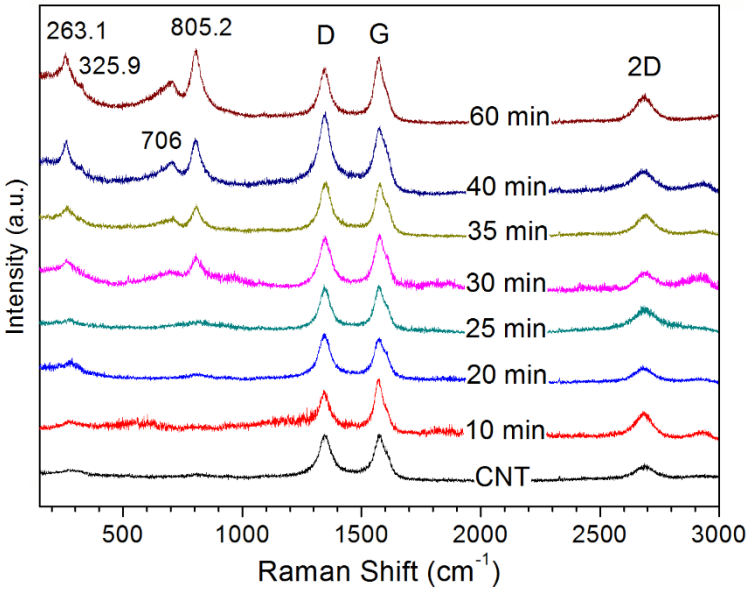

Figure 5.12: Raman spectra of pristine CNTs and WS_2-CNT samples.

Further analysis of the composition and crystallinity of the as-grown samples were conducted by thin film XRD (Figure 5.13). Two slightly distinguishable peaks at 2θ = 42.7 º and 43.9, indexed to the (100) and (101) reflections of graphitic carbon respectively [JCPDS #65-6212], is observed for pristine CNT and all WS_2-CNT composites except for the sample sputter deposited at 60 min [Figure 5.13(a)]. At such prolonged sputtering times, the deposited coating is thick enough that incident X-rays are unable to penetrate into the CNT layer. No other peaks are observed in the XRD profile for pristine CNTs and the 20 min sample, not even from a WO_3 phase, which tallies with the Raman results indicating that the WO_3 particulate film is still amorphous or poorly crystalline at this sputtering time. After 30 min however, a small hump centred at 2θ = 33.9 º begins to emerge, and by 60 min, it is joined by three additional peaks with broad FWHMs due to the overlapping of signals from the WS_2 and WO_3 phase. Despite the strong overlap, it can be seen from Figure 5.12(b) that the reflections at 2θ = 54.6 º, 55.3 º and 71.4 º arise solely from the WO_3 phase [JCPDS #05-0388].

The first two peaks begin to emerge at sputter times of 30 min [Figure 5.13(a)], which matches with the Raman results indicating that crystallization of the amorphous WO_3 phase occurs from this sputter time onwards. On the other hand, the reflections at 2θ = 33.9 º, 55.8 º and 60.5 º can be indexed to hexagonal 2H-WS_2 [JCPDS #08-0237], confirming its presence in the samples sputter-deposited for 30 min or longer. This corroborates the results from the SEM and TEM images, from which we observed the emergence of sharp flakes at a sputter time of 30 min.

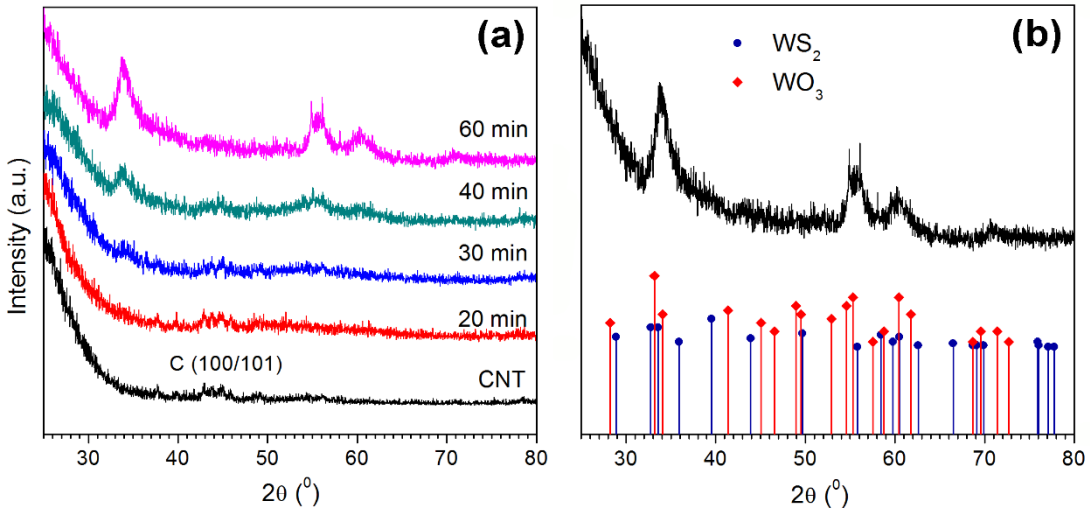

Figure 5.13: (a) X-ray diffractograms of WS_2-CNT samples. (b) X-ray diffractogram of 60 min sample with bulk diffraction peaks of 2H-WS and WO_3.

High resolution XPS scans of W 4f and S 2p core level spectra for selected samples are presented in Figure 5.14. For each sample, there is a W 4f doublet at binding energies of 36.0 and 38.1 eV (blue curve) owing to the W^{6+} oxidation state of WO_3, thus confirming the presence of the WO_3 phase. For the samples sputter deposited at 10, 20 and 25 min, there is an additional doublet at binding energies of 34.8 and 36.9 eV (cyan curve), which can be assigned to a W^{5+} state in WO_y where $2 < y < 3$.[45.] Beginning from the 20 min sample, a third W 4f doublet emerges (red curve). This doublet first occurs at binding energies of 33.6 and 37.7 eV, then gradually shifts to

lower energies with increasing sputtering duration until it stabilizes at around 32.7 and 34.8 eV when a sputter time of 30 min is reached. These values of binding energies corresponds well a W^{4+} species in an intermediate O-W-S state that undergoes chemical change to form highly crystalline 2H-WS_2 at 30 min sputter time. Although the relative proportions of this phase increase with sputter time, WS_2 remains the minor compound compared to WO_3 even at the longest sputter time of 60 min. This dominance of the oxide phase could explain the difficulty in detecting the characteristic Raman peaks of WS_2 as previously discussed. Figure 5. 14(b) depicts the S 2p spectra of the WS_2-CNT samples. At 10 min sputter time, there are two S 2p doublets, one located at 163.2 and 164.4 eV due to the presence of amorphous sulfur and the other pair at 168.25 and 169.45 eV due to the oxidized sulfur species SO_4^{2-}. Although the SO_4^{2-} vanishes at longer sputtering times, the peaks from amorphous sulfur remain present throughout all samples. From 20 min onwards, a new doublet at binding energies of approximately 161.6 and 162.8 eV begins to appear and gradually shifts to slightly higher binding energies with longer sputter times. They eventually stabilize after 30 min of sputtering at values of 162.0 and 163.2 eV, which agrees well with the S^{2-} species in WS_2.[46] This gradual shift can be attributed to increasing electron withdrawing character of the W species bonded to S, thus complementing the chemical change we observed in the W 4f spectra where the O-W-S bond converted to the S-W-S bonds at 30 min sputter time. These results collectively indicate that the WS_2 phase produced at low sputter deposition times (< 30 min) are highly defective and sulfur-deficient. One possible reason for this is the preference of sulfur atoms to bind to oxygen or to itself, as evidenced by the pronounced peaks from oxidized SO_4^{2-} species and amorphous sulfur. As sputter time increases beyond 30 min however, the SO_4^{2-} peaks disappears in conjunction with a reduction of the amorphous sulfur signal intensity relative to the S^{2-}

species, all of which coincide with a downwards shift of the binding energies of the W^{4+} doublet. This behaviour suggests that longer deposition times favours the gradual displacement of oxygen atoms by sulfur in the W compound to form WS_2.

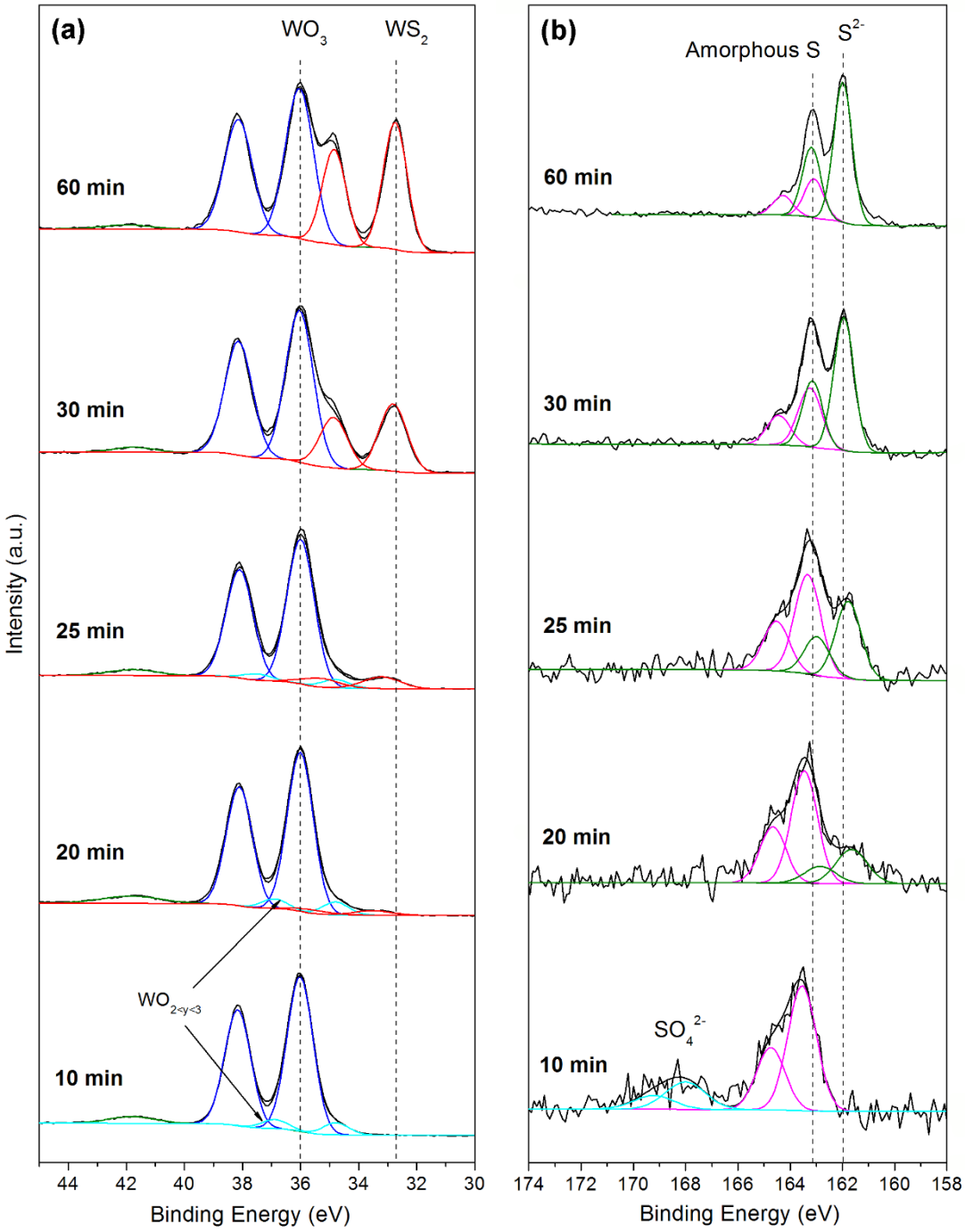

Figure 5.14: High resolution XPS scans of (a) W 5d and (b) S 2p core levels for selected WS_2-CNT samples.

5.3.3 Growth Mechanism of WS_2 on CNT

Figure 5.15 shows the proposed schematic growth process of the core-shell WS_2-CNT nanostructures. In the synthesis of WS_2 on CNTs, no external catalysts or metal seeds were involved, which makes the process simple and clean. The lack of catalysts or seeds also suggests that a modified vapour-solid (VS) growth mechanism is pre-dominant instead of the typical vapour-liquid-solid (VLS) growth processes.[33,34] In the sputtering process, W and S atoms are removed from a solid target by bombardment with high energetic ions that imparts high mobility to the source atoms, allowing them to quickly reach the CNTs and move along the surface of the nanotubes despite the lack of heat supplied. The source atoms are attracted to the defective areas in CNTs, which due to their higher reactivity compared to the surface plan regions, act as favourable sites for nucleation and subsequent crystal growth. In PECVD grown CNTs, these defects can take the form of "cross-struts", pentagon-heptagon pairs, vacancies and ion impurities.[36-38] Other important defects include grain boundaries in the graphene layers of the nanotube wall that can act as nucleation sites due to the presence of dangling bonds that attract adsorbates.[39]

In the initial growth process, the W and S atoms that reach the surface of the substrate do not interact with each other. Instead, the presence of adsorbed oxygen on the CNT walls leads to significant oxidation of the W and S species to form an amorphous WO_3 base layer with adsorbed gaseous SO_4^{2-} species. Excess S atoms then bind to each other to form amorphous sulfur. Once most of the oxygen is consumed and the concentration of S atoms at the surface reaches a critical value (sputter time > 10 min), sulfurization of the as-formed WO_3 phase begins to take place. The process is most likely analogous to the CVD growth of 2D WS_2 layers involving the reaction of

sulfur vapour with a pre-deposited WO_3 thin film at high temperatures.[47,48] In our samples, we are able to determine that initial sulfurization proceeds via the displacement of oxygen atoms in WO_3 with S atoms to form, first O-W-S bonds, and then finally S-W-S. These clusters of pure WS_2 crystals nucleate on top of the oxide layer, with kinetics initially favouring the lateral growth of WS_2 islands due to minimization of energy. This can be deduced from the layered structure of WS_2, wherein the surface energy of the planes perpendicular to the *c*-axis is much smaller than others due to the weak van der Waals forces holding the layers along this axis together. However, the rate at which the WS_2 nuclei grow is much slower than the rate at which W and S atoms reach the surface of the oxide layer. As with the growth of MoS_2 on CNT, the rapid deposition of W and S atoms causes the crystal orientation to change such that the *c*-axis is parallel to the surface, resulting in vertically standing, triangular-shaped nanoflakes reminiscent of flower petals. These nano-petals proliferate with increasing sputter time until a critical density is reached at 40 min. At this point, the nano-petal forest encapsulating the nanotube is too dense to allow additional flakes to develop as quickly as during the initial stage of sputtering. The continued transport of source atoms at the same rate thus leads to the vapour conditions around the nano-petals becoming even more supersaturated, triggering secondary branching in a process resembling dendritic outgrowth.[49] Incoming source atoms thus begin to form nuclei and islands on the surface of the nano-petals. TMD layers are known to be unstable towards bending and have a high propensity to roll into curved structures.[50] Combined with the strict space constraints between each nano-petal, the secondary nanoflakes that form eventually begin to roll and twist into the curved structures with needle-sharp tips seen in the TEM images. Hence the term nano-bristles.

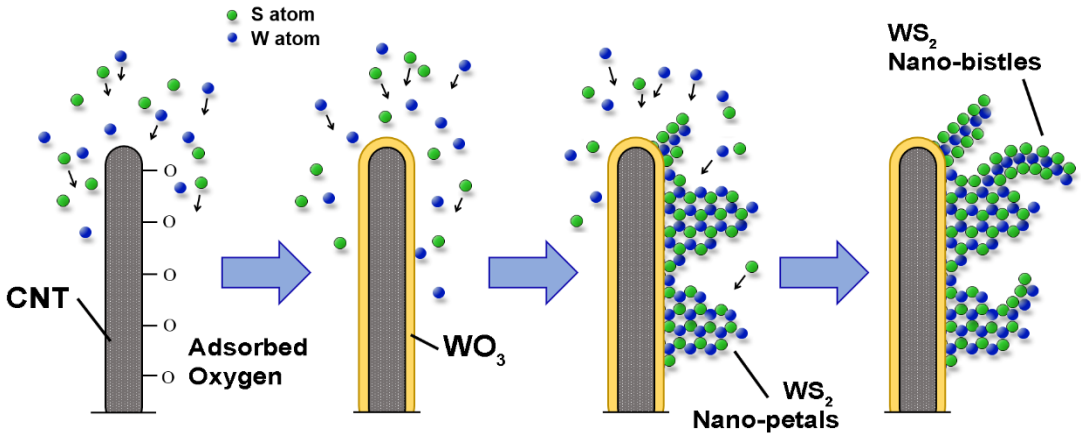

Figure 5.15: Proposed schematic growth process of WS_2 nano-petals and nano-bristles supported on CNT.

5.3.4 Field Emission Study of WS_2-CNT Composites

In order to investigate the field emission properties of the films, I-V curves were obtained at an anode-to-cathode distance of 10 μm. Figure 5.16 shows the I-V plots of selected WS_2-CNT samples. The turn-on voltage, defined as the voltage required to produce a current of 1 μA, is determined to be 425 V for pristine CNTs used in this work. For the 10, 20, 30, 40, 50 and 60 min samples, the measured turn-on voltages are 348, 295, 232, 355, 356, and 376 V respectively, demonstrating an improvement in field emission performance that peaks at the 30 min sample. These results indicate that both the WO_3 coating and WS_2 nanoflakes are capable of enhancing the ability of CNTs to emit electrons. In addition, that the turn-on voltage increases beyond a sputter time of 30 min despite there being no change in chemical state suggests that morphological transformation is responsible for the diminishing field emission performance in these samples. Fowler-Nordheim (F-N) plots of the samples were also obtained (Figure 5.17), revealing a linear trend between $\ln\left(\frac{I}{V^2}\right)$ and $\left(\frac{1}{V}\right)$ that indicates that the electron emission occurs through a quantum tunnelling process. In addition, the observed current

saturation phenomenon with a smaller line slope of each plot at the high voltage region has been known to be caused by adsorbates on the emitter surface.[51] The slope of the linear region of the F-N plot is a function of the work function of the material, ø, the field enhancement factor, β, and the distance between the electrodes, d, which can be expressed by transformation of the F-N equation as,

$$Slope = -\frac{6.83 \times 10^3 ø^{\frac{3}{2}} d}{\beta}$$

Assuming $\varphi_{CNT} = 5.0\ eV$,[24] $\varphi_{WO_3} = 4.8\ eV$,[52] and $\varphi_{WS_2} = 5.1\ eV$,[53] the value of β for pristine CNTs and samples 10 to 60 min is to be 39, 71, 85, 124, 334, 360 and 395 respectively.

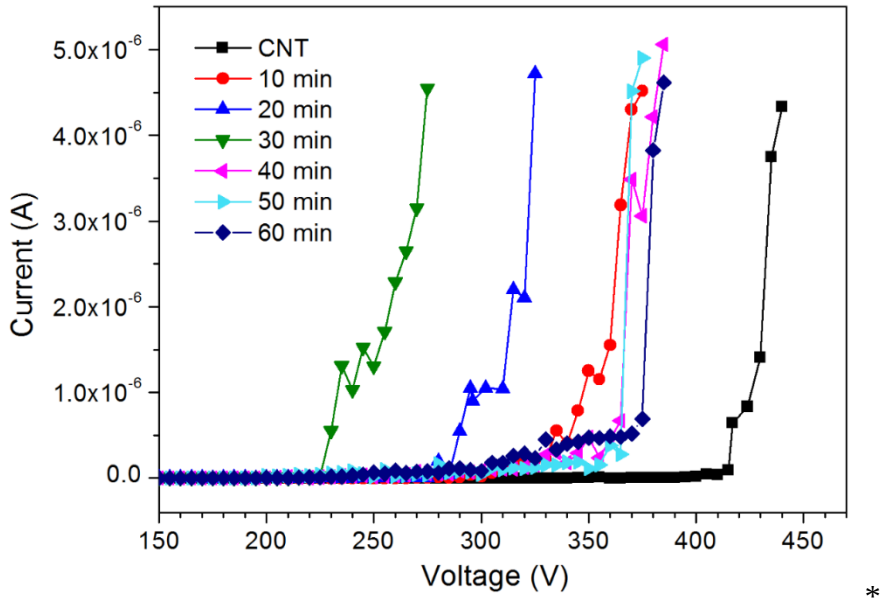

Figure 5.16: Field emission plots of current versus voltage for WS_2-CNT samples.

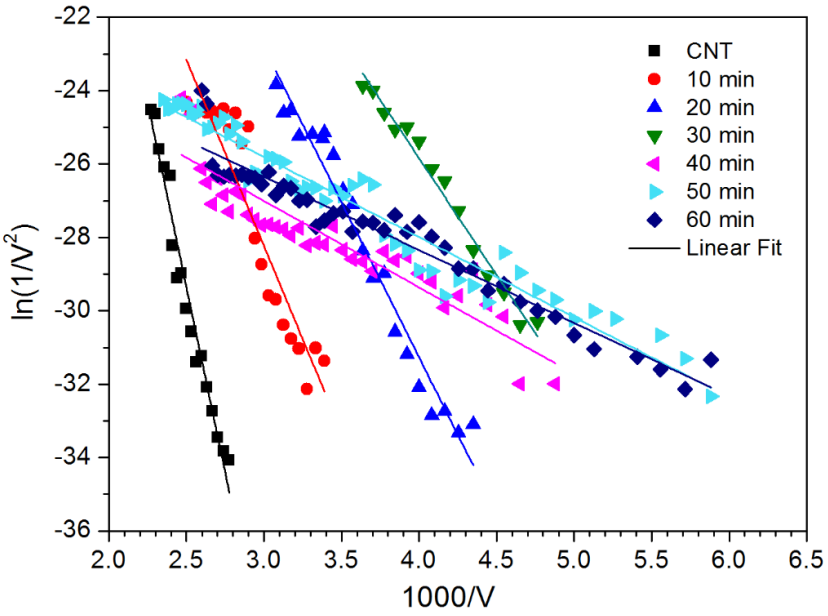

Figure 5.17: Fowler-Nordheim plots for WS_2-CNT samples.

As explained in section 5.2.4, the influence of the physical geometry and dimension of emitters is reflected in F-N equation through the field enhancement factor, β. For the sputter coated CNTs in this work, all demonstrated an enhancement in β as compared to pristine CNTs, indicating that all three different morphologies of a WO_3 particulate film, WS_2 nano-petal forest, and WS_2 nano-bristle forest provide additional sites for electron emission compared to the uncoated nanotubes. In particular, the samples with the nano-bristle morphology (40, 50 and 60 min) exhibit the highest β values, which is not surprising considering that they have both a higher density of sharp edges and tips as well as smaller average tip diameter compared to the nano-petals due to rolling of the flakes into the bristle geometry. What is unusual however, is that despite the having the highest β values, these samples also have the lowest turn-on fields of the coated CNTs. One possible reason for this is poor electrical contact between the nano-petals and nano-bristles when the latter stacks on top of the former. This would cause a substantial voltage drop to occur between the nano-petals and nano-

bristles at large emission currents because of the large contact resistance, leading to current saturation. The thicker coating could also result in greater electron scattering, reducing the efficiency of electron transportation within the nanoflakes. The end result is a field performance that is comparable to the sample with WO_3 nanoparticle coated CNTs (10 and 20 min).

Aside from the improvement in field enhancement factor of the emitters, it is believed that the lower turn-on voltages for the composite nanostructures are also correlated with the decrease in potential energy barrier because of band bending and the presence of defects at the interface between WO_3 and WS_2. A schematic energy band diagram of the CNT/WO_3 and WO_3/WS_2 heterojunction under an applied electric field is shown in Figure 5.18. Owing to the fact that the band gap of CNTs is quite narrow, about a few hundred meV at room temperature,[54] whereas WO_3 is an n-type semiconductor with a band gap of 2.6–2.9 eV,[55] it is assumed that the heterojunction formed is similar to a metal/semiconductor junction. Consequently, the electrons are injected from the Fermi level of CNTs into the conduction band of WO_3 by tunnelling through the Schottky barrier and then emitted from WO_3 into vacuum. WO_3 has a smaller electron affinity of 3.2 eV[56] as compared to the value of 4.8 eV for CNTs.[57] This leads to much lower energy threshold for the electrons escaping from the conduction band of WO_3 into vacuum, and thus they are more easily emitted from WO_3 than CNTs. For samples deposited for 30 to 60 min wherein a layer of WS_2 nanoflakes grows over WO_3, the electrons would tunnel further into the conduction band of WS_2. The band bending at this junction is beneficial to the movement of electrons from the WO_3 to WS_2 and holes from WS_2 to WO_3, which effectively reduces the recombination of electron-hole pairs.[58] If vacancies and defects are present at the interface, they can induce defect energy bands ($E_{defects}$) between the energy bands of WO_3 and WS_2. The

electrons on the WO_3 conduction band can thus easily jump into these defect energy bands and then jump further into the WS_2 bands. Hence, a large number of electrons gather on the surface of WS_2 nanoflakes and are easily emitted into the vacuum through subsequent F–N tunnelling.

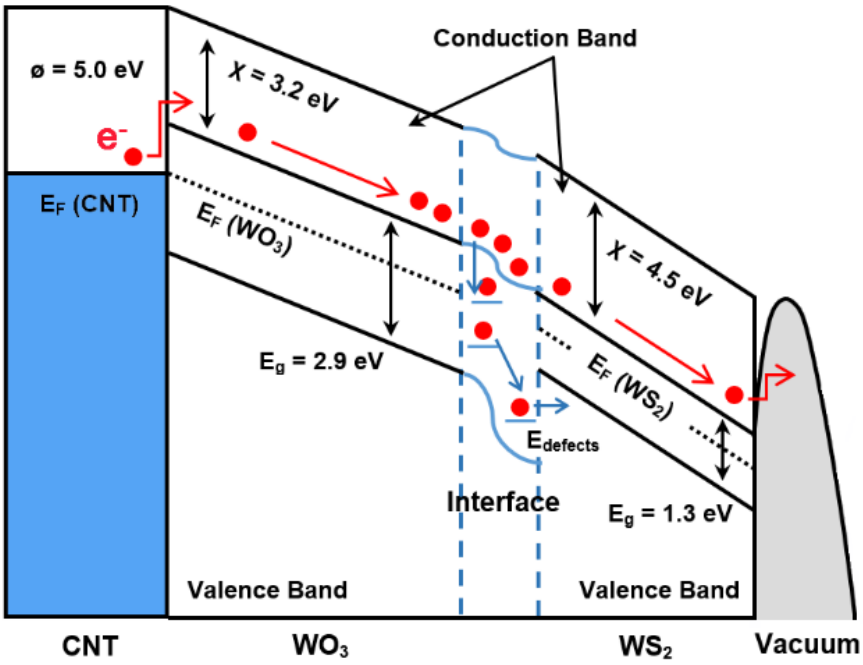

Figure 5.18: Schematic diagram of the CNT/WO_3 and WO_3/WS_2 heterojunctions under an applied electric field.

5.4 Summary

In summary, core-shell MoS_2-CNT hybrid structures were synthesized by RF magnetron sputtering at room temperature in section 5.3. It was established that MoO_2 and MoO_3 were initially formed with strong adhesion to the CNT core through Mo-O-C chemical bonding. Increasing the amount of source atoms supplied beyond a certain threshold results in a chemical change from MoO_2 to MoS_2, which then crystallizes and forms vertically standing nano-petals on the side walls of the CNTs. Both the tubular

MoO_3 coating and the MoS_2 nano-petal forest imparted improved field emission properties to the nanotubes, the former mainly through the formation of a Schottky junction at the interface and the latter mainly due to the geometric enhancement of needle-tipped nano-petals that act as additional emission sites. Both phenomena established a lower energy barrier for electrons to escape from the coating material to vacuum, resulting in a lower turn-on field as compared to pristine CNTs. Resonance PL was obtained for the 20, 25 and 30 min samples at approximately 684 nm and 615 nm, demonstrating the dual functionality of the MoS_2-CNT heterostructures. The observed blue-shift in the direct band edge at 684 nm with increased sputtering time is attributed to formation of sharper and thinner nano-petal tips, and the fact that the incident laser beam impinges only on the topmost layer of the samples. The successful fabrication of MoS_2-CNT hybrids with both photoluminescence and field emission properties has great potential for application in multi-functional nanodevices.

In section 5.4, sputter deposition was also used to fabricate core-shell WS_2-CNT heterostructures at room temperature. An amorphous WO_3 particulate film was initially formed over the nanotubes. Increasing the amount of source atoms eventually results in sulfurization of the WO_3 film to form intermediate O-W-S bonds before complete transformation to S-W-S bonds take place. The crystalline WS_2 nanostructures on CNT take the form of vertically standing nano-petals for the 30-35 min samples, while in the 40-60 min samples they adopt a rolled and curved geometry (nano-bristles). All three morphologies of a WO_3 particulate film, WS_2 nano-petals and WS_2 nano-bristles result in enhanced field emission performance over that of uncoated CNTs. The lowest turn-on voltage of 232 V was obtained for the 30 min sample. This is attributed to the combined effects of the formation of a Schottky barrier at the CNT/WO_3 interface, the possible presence of defects at the WO_3/WS_2 interface, and the geometric enhancement

of sharp-tipped nano-petals that act as additional emission sites. The observed increase in turn-on voltages of the 40-60 min samples despite the much higher field enhancement factors is deduced to be due to poor electrical contact between the nano-petals and nano-bristles. The large voltage drop across this interface at high emission currents thus results in current saturation and poorer field emission performance. The successful synthesis of such hybrid structures open up a range of possibilities for new materials for nanodevices.

References

1. Li, Y.; Wang, H.; Xie, L.; Liang, Y.; Hong, G.; Dai, H. *J. Am. Chem. Soc.* **2011**, 133, 7296.
2. Li, X.-L.; Li, Y.-D. *J. Phys. Chem. B.* **2004**, 108, 13893.
3. Nath, M.; Govindaraj, A.; Rao, C.N.R. *Adv. Mat.* **2001**, 13, 283.
4. Remskar, M.; Mrzel, A.; Virsek, M.; Godec, M.; Krause, M.; Kolitsch, A.; Singh, A.; Seabaugh, A. *Nanoscale Res. Lett.* **2011**, 6, 26.
5. Deepak, F. L.; Mayoral, A.; Yacaman, M. J. *Mater. Chem. Phys.* **2009**, 118, 392.
6. Albiter, M. A.; Huirache-Acuña, R.; Paraguay-Delgado, F.; Rico, J, L.; Alonso-Nuñez, G. *Nanotech.* **2006**, 17, 3473.
7. Wang, S.; Li, G.; Du, G.; Li, L.; Jiang, X.; Feng, C.; Guo, Z.; Kim, S. *Nanoscale Research Lett.* **2010**, 5, 1301.
8. Zhou, W.; Yin, Z.; Du, Y.; Huang, X.; Zeng, Z.; Fan, Z.; Liu, H.; Wang, J.; Zhang, H. *Small* **2013**, 9, 140.
9. Li, Y. B.; Bando, B.; Golberg, D. *Appl. Phys. Lett.* **2003**, 82, 1962.
10. Zhu, H.; Du, M. L.; Zhang, M.; Zou, M. L.; Yang, T. T.; Fuab, Y. Q.; Yao, J. M. *J. Mater. Chem. A* **2014**, 2, 7680.
11. Frame, F. A.; Osterloh, F. E. *J. Phys. Chem. C* **2010**, 114, 10628.
12. Zong, X.; Yan, H. J.; Wu, G. P.; Ma, G J.; Wen, F. Y.; Wang, L.; Li, C. *J. Am. Chem. Soc.* **2008**, 130, 7176.
13. Kashid, R. V.; Late, D, J.; Chou, S. S.; Huang, Y. K.; Joag, M.D.D.S.; More, M. A.; Dravid, V. P. *Small* **2013**, 9, 2730.
14. Viskadouros, G.; Zak, A.; Stylianakis, M.; Kymakis, E.; Tenne, R.; Stratakis, E. *Small* **2014**, 10, 2398–2403.
15. Rout, C. S.; Joshi, P. D.; Kashid, R. V.; Joag, D. S.; More, M. A.; Simbeck, A. J.; Washington, M.; Nayak, S. K.; Late, D. J. *Sci Rep.* **2013**, 3, 3282.
16. Fu, H.; Yu, K.; Li, H.; Li, J.; Guo, B.; Tan, Y.; Song, C.; Zhu, Z. *Dalton Trans.* **2015**, 44, 1664–1672.
17. Tan, Y.-H.; Yu, K.; Li, J.-Z.; Fu, H.; Zhu, Z.-Q. *J. Appl. Phys.* **2014**, 116, 064305.

18. Nilsson, L.; Groening, O.; Emmenegger, C.; Kuettel, O.; Schaller, E.; Schlapbach, L.; Kind, H.; Bornard, J. M.; Kern, K. *Appl. Phys. Lett.* **2000**, 76, 2071–2073.
19. Iijima, S. *Nature* **1991**, 354, 56.
20. Popov, V. N. *Mater. Sci. Eng. R.* **2004**, 43, 61.
21. Tan, C.; Zhang, H. *Chem. Soc. Rev.* **2015**, 44, 2713–2731.
22. Yue, G. Z.; Qiu, Q. Qiu; Gao, B.; Cheng, Y.; Zhang, J.; Shimoda, H.; Chang, S.; Lu, J. P.; Zhou, O. *Appl. Phys. Lett*. **2002**, 81, 355–357.
23. Rosen, R.; Simendinger, W.; Debbault, C.; Shimoda, H.; Fleming, L.; Stoner, B.; Zhou, O. *Appl. Phys. Lett.* **2000**, 76, 1197–1199.
24. Tan, Z.; Chua, D. H. C. *J. Electrochem. Soc.* **2011**, 158, K112–K116.
25. Zhou, K.; Liu, J.; Shi, Y.; Jiang, S.; Wang, D.; Hu, Y.; Gui, Z. *ACS Appl. Mater. Interfaces* **2015**, 7, 6070−6081.
26. Tai, S. Y.; Liu, C. J.; Chou, S. W.; Chien, F. S. S.; Lin, J. Y.; Lin, T. W. *J. Mater. Chem.* **2012**, 22, 24753–24759.
27. Wang, C.; Wan, W.; Huang, Y. H.; Chen, J. T.; Zhou, H. H.; Zhang, X. X. *Nanoscale* **2014**, 6, 5351–5358.
28. Jeon, I.; Kutsuzawa, D.; Hashimoto, Y.; Yanase, T.; Nagahama, T.; Shimada, T.; Matsuo, Y. *Organic Electronics* **2015**, 17, 275–280.
29. Graf, D.; Molitor, F.; Ensslin, K.; Stampfer, C.; Jungen, A.; Hierold, C.; Wirtz, L. *Nano Lett.* **2007**, 7, 238–242.
30. Dresselhaus, M. S.; Dresselhaus, G.; Jorio, A. *Annu. Rev. Mater. Res.* **2004**, 34, 247–278.
31. Li, H.; Zhang, Q.; Yap, C. C. R.; Tay, B. K.; Teo, E. H. T.; Olivier, A.; Baillargeat, D. *Adv. Funct. Mater*. **2012**, 2, 1385–1390.
32. Splendiani, A; Sun, L.; Zhang, Y.; Li, T.; Kim, J.; Chim, C. Y.; Galli, G.; Wang, F. *Nano Lett.* **2010**, 10, 1271–1275.
33. Liu, K. K.; Zhang, W.; Lee, L. H.; Lin, Y. C.; Chang, M. T.; Su, C. Y.; Chang, C. S.; Li, H.; Shi, Y.; Zhang, H. et al. *Nano Lett.* **2012**, 12, 1538–1544.
34. Pan, Z. W.; Dai, Z. R.; Wang, Z. L. *Science* **2001**, 291, 1947–1949.
35. Yan, B.; Zheng, Z.; Zhang, J. X.; Gong, H.; Shen, Z. X.; Huang, W.; Yu, T. *J. Phys. Chem.* **2009**, C113, 20259–20263.

36. Jianga, J.; Feng, T.; Zhana, J. H.; Cheng, X. H.; Chao, G. B.; Jiang, B. Y.; Wang, Y. J.; Wana, X.; Liu, X. H.; Zou, S. C. *Appl. Surf. Sci.* **2006**, 252, 2938–2943.
37. Merkulov, I. A.; Merkulov, V. I.; Melechko, A. V.; Klein, K. L.; Lowndes, D. H.; Simpson, M. L. *Phys. Rev. B.* **2007**, 76, 014109.
38. Mielke, S. L.; Troya, D.; Zhang, S.; Li, J.-L.; Xiao, S.; Car, R.; Ruoff, R. S.; Schatz, G. C.; Belytschko, T. *Chem. Phys. Lett.* **2004**, 390, 413–420.
39. Terrones, M. *Annu. Rev. Mater. Res.* **2003**, 33, 419–50.
40. An, J.; Voelkl, E.; Suk, J. W.; Li, X.; Magnuson, C. W.; Fu, L.; Tiemeijer, P.; Bischoff, M.; Freitag, B.; Popova, E. et al. *ACS Nano* **2011**, 5, 2433−2439.
41. Yu, J.; Sow, C.H.; Wee, A. T. H.; Chua, D. H. C. *J. Appl. Phys*. **2009**, 105, 114320.
42. Ferrari, A. C. *Solid State Comm.* **2007**, 143, 47–57.
43. Mohiuddin, T. M. G.; Lombardo, A.; Nair, R. R.; Bonetti, A.; Savini, G.; Jalil, R.; Bonini, N.; Basko, D. M.; Galiotis, C.; Marzari, N. et al. *Phys. Rev. B* **2009**, 79, 205433.
44. Kalantar-zadeh, K.; Vijayaraghavan, A.; Ham, M.-H.; Zheng, H.; Breedon, M.; Strano, M. S. *Chem. Mater.* **2010**, 22, 5660-5666.
45. Vasilopoulou, M.; Soultati, A.; Georgiadou, D. G.; Stergiopoulos, T.; Palilis, L. C.; Kennou, S.; Stathopoulos, N. A.; Davazogloua, D.; Argitis, P. *J. Mater. Chem. A* **2014**, 2, 1738–1749.
46. Morrish, R.; Haak, T.; Wolden, C. A. *Chem. Mater.* **2014**, 36, 3986–3992.
47. Zhang, Y.; Zhang, Y.; Ji, Q.; Ju, J.; Yuan, H.; Shi, J.; Gao, T.; Ma, D.; Liu, M.; Chen, Y. et al. *ACS Nano* **2013**, 7, 8963–8971.
48. Cong, C.; Shang, J.; Wu, X.; Cao, B.; Peimyoo, N.; Qiu, C.; Sun, L.; Yu, T. *Adv. Optical Mater.* **2014**, 2, 131–136.
49. Bunn, C. *Crystals: Their Role in Nature and in Science*, 2nd ed.; Academic Press: New York, 1966.
50. Rao, C. N. R.; Nath, M. *Dalton Trans.* **2003**, 1, 1–24.
51. Yu, K.; Zhang, Y. S.; Xu, F.; Li, Q.; Zhu, Z. Q.; Wan, Q. *Appl. Phys. Lett.* **2006**, 88, 153123.
52. Tao, C.; Ruan, S.; Xie, G.; Kong, X.; Shen, L.; Meng, F.; Liu, C.; Zhang, X.; Dong, W.; Chen, W. *Appl. Phys. Lett.* **2009**, 94, 043311.

53. Kim, J.; Byun, S.; Smith, A. J.; Yu, J.; Huang, J. *J. Phys. Chem. Lett.* **2013**, 4, 1227−1232.
54. Wilder, W. G.; Venema, L. C.; Rinzler, A. G.; Smalley, R. E.; Dekker, C. *Nature* **1998**, 391, 59.
55. Ou, J. Z.; Balendhran, S.; Field, M. R.; McCulloch, D. G.; Zoolfakar, A. S.; Rani, R. A.; Zhuiykov, S.; O'Mullane, A. P.; Kalantar-Zadeh, K. *Nanoscale* **2012**, 4, 5980–5988.
56. Walter, C. W.; Hertzler, C. F.; Devynck, P.; Smith, G. P.; Peterson, J. R. J. *Chem. Phys.* **1991**, 95, 824.
57. Kazaoui, S.; Minami, N.; Matsuda, N.; Kataura, H.; Achiba, Y. *Appl. Phys. Lett.* **2001**, 78, 3433.
58. Tan, Y.-H.; Yu, K.; Li, J.-Z.; Fu, H.; Zhu, Z.-Q. *J. Appl. Phys.* **2014**, 116, 064305.

Chapter 6

Conclusions and Future Work

6.1 Conclusions

The primary objective of this work was to fabricate MoS_2- and WS_2-based materials for field emission applications. In order to achieve the aforementioned goals, two parallel series of experiments were conducted. In the first, MoS_2 growth at elevated temperatures using pulsed laser ablation of a solid target and subsequent transport of ablated atoms to an Ag substrate was conducted. Slower cooling rates and higher laser energies result in higher MoS_2 crystalline quality as the more energetic source atoms are able to rearrange themselves into a more orderly configuration. The thickness of the MoS_2 film can be controlled by varying the parameters of deposition time and laser energy, with the thinnest sheets possessing 2-3 layers as determined by Raman spectroscopy and TEM.

MoS_2 growth by PLD was subsequently studied on various different metal substrates such as Ag, Al, Ni, and Cu. Highly crystalline few-layer MoS_2 was successfully grown on Ag, but is absent in Al, Ni and Cu under specific deposition conditions. The growth mechanism involves the in-situ formation of a metal sulfide phase that acts as a scaffold/template for growth and subsequent segregation of dissolved source atoms in the metal onto the surface. This inability of the metals Al, Ni and Cu to produce crystalline MoS_2 was thus due the absence of such a growth template. In the case of Al, the absence of template can be partially offset by increasing the amount of source atoms supplied, thereby producing semi-crystalline few-layer MoS_2.

The results show that despite PLD being a physical vapor deposition technique, both physical and chemical processes play an important role in MoS_2 growth on metal substrates.

Using the information gained from PLD growth of MoS_2 on metals, Ag and Al nanocones were fabricated and coated with MoS_2 for field emission purposes. Despite loss of the conical structures after heating, the field emission properties of Ag nanocones were greatly enhanced with the MoS_2 layer coating due to charge transfer interactions and the formation of a low Schottky barrier at the metal-MoS_2 interface. This led to a reduced electron tunnelling barrier height that manifested as a lower turn-on voltage. For the Mos_2-coated nanocones however, no discernible field emission property was obtained due to the high resistance contact between Al and MoS_2 as well as the high density of defects present in MoS_2 layers grown on Al. The overall conductivity of the emitter was thus reduced, resulting in much higher turn-on voltages that were beyond the limit of the voltage source.

In the final part of this series, atomically thin MoS_2 flakes were fabricated by sputter deposition at room temperature on CNTs. With longer deposition times, the particulate film consisting mostly of MoO_3 transforms to a dense nano-petal forest of crystalline MoS_2. Both the MoO_3 coating and the MoS_2 nano-petal forest significantly enhanced the field emission properties of CNTs, with the sample deposited at 30 min exhibiting the lowest turn-on fields. The mechanism for improvement in field emission performance for both structures is different; in the case of the MoO_3 coating it is due to the formation of a Schottky junction at the interface, whereas for the MoS_2 nano-petal forest it is mainly due to the geometric enhancement of needle-tipped nano-petals that

act as additional emission sites. The addition of 2D MoS_2 flakes onto CNT also imparts photoluminescence properties to the resulting hybrid structure.

In the second series, the success of PLD at growing 2D TMDs was extended to WS_2. In contrast to MoS_2, the optimum balance between crystalline quality and film thickness was obtained at a laser energy of 100 mJ and a deposition time of 10 s. The crystalline WS_2 layers are able to grow on Ag layers as thin as 8 nm, resulting in high optical transmittance in the visible range for the final product. The final film was composed of a hybrid 2H-1T structure, suggesting that the Ag substrate was capable of stabilizing 1T-WS_2. Lower growth temperatures, thicker Ag layers and lower laser energies favoured a higher proportion of the 1T-phase.

Next, WS_2 growth by PLD on the metal substrates Ag, Au, Al, and Ni was investigated. The underlying growth mechanism involved the in-situ formation of a lattice matching metal sulfide phase, similar to pulsed laser fabricated MoS_2. Consequently, only Ag was successful at producing highly crystalline few-layer WS_2 due to the formation of substantial amounts of Ag_2S. The 1T-phase was observed to be present in the film grown on the noble metals Ag and Au, but was absent in Ni and Al. It was deduced that the 1T-phase arises due to electron doping of the WS_2 lattice by Ag/Au atoms, leading to the formation of a stable d^{10} shell and a phase transformation in the WS_2 structure from 2H-to-1T. Neither Ni nor Al are capable of such electron doping processes for different reasons; in Ni, the surface oxides inhibits its ability to donate electrons, whereas Al is chemically unsuitable to act as electron donor for WS_2.

Using PLD, WS_2-based field emitters were similarly fabricated by depositing WS_2 layers on Ag nanocones. Despite loss of the conical geometry after heating, all WS_2-coated samples demonstrated improved field emission over pristine nanocones,

This was attributed to a reduction of the potential barrier for electron field emission by formation of a Schottky barrier at the WS_2-Ag interface. The as-fabricated WS_2-coated nanocones exhibited lower turn-on voltages compared to the annealed samples due to the presence of the metallic 1T-phase, which exhibits much higher electrical conductivity and carrier concentration than the semiconducting 2H-WS_2. This results in very efficient electron transfer from the substrate to the sample surface and hence a lower turn-on voltage is obtained for the as-deposited samples. The samples fabricated at lower laser energies consistently demonstrated higher turn-on voltages than those synthesized at higher laser energies due to a higher density of defects that reduces the overall electrical conductivity of the emitter.

In the final part of the second series, ultrathin WS_2 flakes were coated onto CNTs at room temperature by sputtering. Longer deposition times resulted in the initial particulate film of WO_3 converting first to a dense nano-petal forest of crystalline WS_2, and then finally to a thick nano-bristle morphology. All three morphologies lead to enhancement of the field emission performance over that of pristine CNTs, with the lowest turn-on voltage of 232 V obtained for the 30 min sample. The mechanisms behind this enhancement include the formation of a Schottky at the CNT/WO_3 interface, the possible presence of defects at the WO_3/WS_2 interface, and the geometric enhancement of sharp-tipped nano-petals/nano-bristles that act as additional emission sites. The higher turn-on voltages for the samples with deposition times longer than 30 min is believed to be due to poor electrical contact between the nano-petals and nano-bristles, which prevents efficient transport of electrons from substrate to the sample surface.

From the studies carried out in this dissertation, ultrathin and high quality MoS_2 and WS_2 layers were able to be synthesized using physical methods such as PLD and sputtering, and at much lower temperatures than is typical for these materials. A major contribution of this work is the revelation of the growth mechanisms of MoS_2 and WS_2 by these physical methods, as well as the discovery of a new route for the stabilization of 1T-WS_2, both of which can serve as a guideline for the development of high quality TMD materials with structures and properties tailored for specific applications. In addition, this work demonstrated that effective MoS_2- and WS_2-based field emitters can be fabricated by PLD and sputtering. The performance of these emitters can be enhanced by tuning their geometrical shape as well as the crystalline quality and thickness of the TMD sheets. For WS_2, control of the phasic composition is another important aspect affecting field emission property.

6.2 Future Work

It was demonstrated that few-layer MoS_2 and WS_2 can be grown by PLD directly onto nano-patterned substrates for various applications. However, the propensity of Ag to undergo rapid recrystallization and grain growth even at temperatures as low as 200 ºC means that the Ag substrates often lose their definitive shapes after TMD growth. As lowering of the temperature is not feasible in this case, it would be beneficial to explore patterning of the Si substrate instead, and then coating of the Si nanostructures with a thin Ag film. This would then preserve the structures even after TMD growth by PLD. In addition, the shape of the nanostructures should be further fine-tuned so that much smaller tips that increase the field enhancement are produced.

Another issue is the stabilization of the 1T-WS_2 phase, which was speculated to occur by electron doping of Ag and Au. Conclusive evidence through DFT calculations should be conducted to confirm this. Furthermore, as Ag and more so Au are often used as contacts in TMD-based transistors, it is important that further investigations be carried out on the influence of Ag and Au on pre-fabricated WS_2 sheets grown by other methods such as exfoliation. This is to ensure that no phase change occurs at the metal-TMD interface, which would significantly affect device performance. If a phase change does occur, then it would be interesting to study the kind of devices that can be formed with such a hybrid structure seeing as the 1T-phase of WS_2 is metallic and possesses much better electrical conductivity. Finally, it would also be interesting to carry out studies to understand the reasons why MoS_2 is not similarly affected by the electron doping to form the 1T-phase.

In closing, it is clear that the development of TMD-based materials for field emission applications is still in the stages of infancy. As the field emission properties of MoS_2 and WS_2 are highly affected by their geometrical configuration and structure, fabrication techniques play a critical role in realizing their full potential as field emitters. Currently, many challenges remain in terms of fabrication and structure optimization before MoS_2 and WS_2 field emitters can be employed in practical applications. Even so, as further progress is achieved in the synthesis and tailoring of their properties, TMDs such as MoS_2 and WS_2 can will be able to play a pivotal role in the advancement of field emission devices.